University of California
Santa Barbara

The Quantum Brain: Explorations and Adventures with Posner molecules

A dissertation submitted in partial satisfaction
of the requirements for the degree Doctor of Philosophy

in
Physics

by

Joshua Sidney Straub

Committee in charge:

Professor Matthew P.A. Fisher, Chair
Professor Matthew E. Helgeson, Co-Chair
Professor Songi Han
Professor Zvonimir Dogic

The Dissertation of Joshua Sidney Straub is approved.

Professor Songi Han

Professor Zvonimir Dogic

Professor Matthew E. Helgeson, Committee Co-Chair

Professor Matthew P.A. Fisher, Committee Chair

August 2023

The Quantum Brain: Explorations and Adventures with Posner molecules

For all my loved ones who have supported me in this journey.

Acknowledgements

There are so many people that I would like to thank for making this thesis possible. First, I want to thank both of my advisors. Matthew E. Helgeson, thank you for accepting me into your lab when I didn't even know how to use a pipette, and for your patience and guidance over the years. Your passion for science and deep knowledge of experimental research have both been important resources for me during my PhD.

Matthew P.A. Fisher, I still recall my excitement when I first received your email in January 2017, telling me I had been accepted to UCSB and asking if I would be interested in working on the Quantum Brain project with you. I now cannot imagine having spent my time in graduate school on any other project. Thank you for having such a brilliant and fun idea for me to focus my PhD on. And mostly, thank you for your human kindness, friendship, and support over the past six years, without which I do not think this thesis would have been possible.

I express my gratitude to my many lab mates and collaborators during my PhD. Thank you to all of the scientists in shared facilities at UCSB who have helped me, and in particular Dr. Hongjun Zhou. To the Helgeson group members past and present, I am grateful for your support and patience as I rambled on about quantum mechanics and dynamic light scattering to no end. To all my collaborators on the Quantum Brain project, I have very much enjoyed going down this wild scientific journey together. Particular thanks to Mesopotamia Nowotarski, Manisha Patel, Yaodong Li, Jiaqi Lu, Marshall Deline, Nick O'Dea, Songi Han, Alexej Jerschow, Stuart Licht, Tobias Fromme, and Jeff Sczechowski from whom I have learned so much and with whom I have had so many positive conversations.

There are also so many wonderful loving friends in my life that have been sources of inspiration, guidance, and joy. From Harvey Mudd, thank you Hannah Welsh, Sakshi

Shah, Madi Pignetti, Rebecca Harman, Nick Bailey, and Rohan Nagpal. From UCSB, thank you Dariya Ignatenko, Noah Swimmer, William Schultz, Sarah Steiger, Iman Salty, Serena Seshadri, Tanvi Sheth, Zoe Ö'Conor, Mark Turiansky, Remi Boros, Cloe Gentile, Joe Costello, Seamus O'Hara, Aleksei Khindalov, and Sergio Hernandez-Cuenca. I love you all dearly and you each hold a special place in my heart.

Finally, I would like to thank my parents, John and Mary, and my brother Philip. Ema and Aba, thank you for your unwavering love and support and wisdom in good times and bad, and for always encouraging me to trust and believe in myself. Thank you Philip for understanding and supporting me in the way that only a brother can. I love you so much.

Curriculum Vitæ

Joshua Sidney Straub

Education

2023	Ph.D. in Physics (Expected), University of California, Santa Barbara.
2020	M.A. in Physics, University of California, Santa Barbara.
2017	B.S. in Physics, Harvey Mudd College.

Publications

- **Joshua S. Straub**, M.S. Nowotarski, J. Liu, T. Sheth, S. Jiao, M.P.A. Fisher, M.S. Shell, M.E. Helgeson, A. Jerschow, S. Han. Phosphates form spectroscopically dark state assemblies in common aqueous solutions. Proc. Natl. Acad. Sci. U.S.A., 120(1), 2023. DOI
- M.L Deline, M. Grashei, F.H.A. van Heijster, F. S., **Joshua S. Straub**, T. Fromme. Adenylate kinase derived ATP shapes respiration and calcium storage of isolated mitochondria. Biochim Biophys Acta Bioenerg, 1862(7), 2021. DOI
- M.L. Deline, **Joshua S. Straub**, M. Patel, P. Subba, M. Grashei, F.H.A. van Heijster, P. Pirkwieser, V. Somoza, J.D. Livingstone, M. Beazely, B. Kendall, M.J.P. Gingras, Z. Leonenko, C. Hoeschen, G. Harrington, K. Kuellmer, W. Bian, F. Schilling, M.P.A. Fisher, M.E. Helgeson, T. Fromme. Lithium affect mitochondrial amorphous calcium phosphate aggregation in a tissue and isotope dependent manner. Front. Physiol., 2023. DOI
- M.S. Nowotarski, L. R. Potnuru, **Joshua S. Straub**, R. Chaklashiya, T. Shimasaki, B. Pahari, H. Coffaro, S. Jain, S. Han. DNP enhanced multiple quantum solid state NMR spin counting of molecular assemblies in vitrified solutions. *Submitted 2023*
- J. Lu, **Joshua S. Straub**, M.S. Nowotarski, S. Han, X. Xu, A. Jerschow. Spectroscopically dark phosphate features revealed by chemical exchange saturation transfer. *Submitted 2023*
- **Joshua S. Straub**, M. Patel, M.S. Nowotarski, L. R. Potnuru, M.P.A. Fisher, M.E. Helgeson. A differential lithium isotope effect on the *in vitro* formation of calcium phosphate. *In preparation*
- **Joshua S. Straub**, M. Patel, M.S. Nowotarski, M.P.A. Fisher, M.E. Helgeson. Direct evidence for free calcium phosphate prenucleation species in solution. *In preparation*

Abstract

The Quantum Brain: Explorations and Adventures with Posner molecules

by

Joshua Sidney Straub

The brain's computational functions, from information synthesis and memory recall to consciousness, remain largely enigmatic. Despite great scientific effort, the mechanisms behind information storage, computation, and readout within the brain are still not well understood. Because of the warm, crowded nature of biological systems, it has traditionally been thought that quantum states would rapidly decohere and be unsuitable for biological information storage. Recently, the "Quantum Brain theory" has proposed the potential for a quantum information network in the brain that could maintain and process quantum information on timescales relevant to brain function. Within the framework of this theory, quantum information is stored in the collective phosphorus spin states of nanometric calcium phosphate clusters known as Posner molecules. The pair binding of these Posner molecules is postulated to be impacted by the collective phosphorus spin states, allowing for a unique quantum state to biochemical signal transduction mechanism. Given that this theory puts forward a uniquely possible method for quantum information processing in the brain, experimental validation or refutation of the theory would be an important step towards an understanding of brain function. This thesis presents experimental results aimed at testing the possibility of this Quantum Brain theory. We show that Posner molecules are stable in simulated body fluids, and uncover a differential lithium isotope effect on the growth of calcium phosphate. This isotope effect provides a link between nuclear spin states and calcium phosphate binding dynamics, and can be connected to *in vivo* lithium isotope effects in mitochondria. We

also uncover spectroscopically 'dark state' phosphate assemblies after measuring unexpected ^{31}P NMR signals, revealing that phosphate solution behavior and ^{31}P nuclear spin dynamics are much more complex than previously predicted. These results verify key predictions of the Quantum Brain theory, indicating the possibility of quantum information processing in the brain, while also progressing our understanding of the complex solution phase space of calcium phosphate.

Contents

Chapter 1

The Quantum Brain theory

1.1 Introduction

The brain's computational functions, such as synthesizing complex information or memory recall, as well as the experiential aspect of the human brain that we refer to as consciousness, remain largely mysterious despite scientific and philosophical efforts to understand its workings dating back thousands of years. While we have made great strides in our understandings of neuroscience over the last 75 years, many problems remain open or only partially solved. From a computing perspective, information storage, processing, and readout are still not fully understood, while from a mixed neuroscientific/philosophical perspective, consciousness- our ability to be aware of the world and our own mind/thoughts- remains enigmatic.

Since we all experience our own minds, the awareness of which seems fundamental to our existence, the problem of understanding the human brain naturally appeals to scientific curiosity. Given the complexity and interdisciplinary nature of the problem - including but not limited to cellular biology, network analysis, biochemistry, information science, and psychology - progress towards understanding the human brain requires

multi-scale efforts across diverse scientific communities. Additionally, bold proposals and rigorous experimental research are required to progress our current understanding of the brain and begin to unravel the fundamental questions of neuroscience.

Since the discovery of quantum mechanics at the onset of the 20th century, the theory has been successfully applied to a myriad of scientific problems at the microscopic scale. Quantum mechanics allows for descriptions of molecular, atomic, and subatomic interactions that cannot be captured with "classical" physics (physical theories that don't include quantum mechanics). In addition to the quantization of energy and other physical variables (hence the name), quantum mechanics introduces new principles of superposition (a system existing in multiple states at the same time, as described by its wave function), entanglement (where the state of a particle cannot be described independently from other particles), and measurement (the collapse of the wave function into a single state when a system is observed). These features of quantum mechanics allow for quantum systems to function in ways that classical systems cannot.

One such example is quantum information science, where the classical concept of a bit (a two level system that is either a 0 or 1) is expanded into the qubit, which can take on a superposition between 0 and 1. This concept is often visualized using the Bloch sphere, a geometric representation of the state space for a qubit. While a classical bit can only take on the 2 points at the top or bottom of the sphere, a qubit can be anywhere along the surface of the sphere, allowing for effectively infinite possible states as compared to 2. Multiple qubits can then also become entangled, allowing for quantum computations that are not impossible or intractably wrong using classical computers. Note that this concept can be expanded to the "qutrit," in which there is a three level system as opposed to a two level system.

While a number of remarkable physical (and philosophical) consequences result from quantum mechanics, one particularly stunning result is the nature of wave function col-

lapse upon measurement. This discovery has led to a number of different interpretations of what this result means for the universe, from the many-worlds hypothesis (the universe is deterministic, but there are many worlds which encompass all possible outcomes for wave-function measurement and we happen to exist in the one where the measurement outcome was what we observed) to the Copenhagen interpretation (the universe is non-deterministic and probabilistic). Regardless of the philosophical interpretation of quantum mechanics, there is rigorous experimental evidence that the universe is fundamentally quantum.

Given, then, the extreme precision with which evolution has tuned biological functions, it seems very possible quantum mechanics might be leveraged in biological systems. Over the past three decades, there has been a growing interest in this area of "quantum biology," where quantum mechanics is non-trivially utilized to perform biological functions. Non-trivial utilization here refers to the idea that a classical physical system would be unable to achieve the same function or efficiency in the absence of quantum mechanics. Evidence of quantum biological effects exist in a number of systems, ranging from proton tunneling in proteins [1, 2] to olfaction [3] to photosynthesis [4, 5, 6] to magnetoreception in birds [7, 8, 9, 10]. However, uncovering new cases of quantum biological effects is a significant challenge, as the warm, crowded environments found in biology are juxtaposed to the cold, isolated environments favorable for discovering and understanding quantum mechanical behavior. Thus, while there are a few cases with evidence of quantum biological functions, there are likely many more that exist but have so far been experimentally or conceptually inaccessible.

When considering the mysterious and unintuitive nature of both consciousness and quantum mechanics, it seems natural that scientists and philosophers might ask whether the two may be interconnected in some way. Indeed, a number of theories have been put forward that attempt to utilize quantum mechanics to describe brain function and

consciousness. However, such attempts can often deviate from serious biophysics to philosophy when they fail to rigorously provide testable hypotheses (which may not be problematic in and of itself, but is when it refuses to properly acknowledge this distinction). Thus, while theories that utilize quantum mechanics to propose a description of human consciousness are almost always grandiose by nature, the real quality of such theories lies in their proposal of experimental tests that can provide proof- or disproof- of their hypotheses.

In this chapter, we will provide some basic background on modern neuroscience to give a sense of the state of the field as it pertains to the bulk of the chapter, where we discuss the possibility of quantum computation in the brain and introduce Matthew Fisher's "Quantum Brain theory."

1.2 A brief overview of classical neuroscience

We will make no attempt here to address the full scope of the vast field of neuroscience. Rather, we will focus on a couple areas- both current knowledge and open questions - that will be helpful in contextualizing the Quantum Brain theory introduced later in this chapter. We begin by reviewing the role of calcium ions in neuronal cells and then discuss current ideas of how memory functions, with a brief note on the state of consciousness in neuroscience.

1.2.1 Calcium signaling in the brain

Calcium ions (Ca^{2+}) play a number of important roles in neuronal signaling and regulation [11]. Calcium regulates neurotransmitter release, impacting synaptic plasticity by strengthening and weakening synapses via long-term potentiation [12] and long-term depression [13], respectively. Calcium is also a secondary messenger throughout neuronal

cells, meaning that intracellular calcium ions relay signals received from extracellular receptors. In this sense, calcium ions have been shown to play numerous roles in neuronal cells, ranging from regulation of gene expression [14] to dendrite growth [15] to memory functions via the endoplasmic reticulum (ER) [16] and mitochondria [17], two organelles with important roles in intracellular calcium storage. Thus, calcium is fundamental to neuronal cell function.

Given that calcium plays roles as both signaler and messenger in neurons, controlling calcium concentrations within the cell is crucial. Plasma membranes control the influx of calcium ions in neurons via both voltage-dependent and receptor-operated channels [11]. There are several different voltage dependent calcium channels, each serving distinct roles, but all operating under the same principle of altering the electrical potential across the plasma membrane for ion-specific transport [18, 19]. Additionally, a number of different receptor-operated channels regulate calcium import, by undergoing conformational changes after ligand binding and opening pores that allow for calcium ions to cross the plasma membrane [20, 21].

After a rapid influx of calcium into the cytosol across the plasma membrane, it is important to rapidly regulate local calcium concentrations after signal transduction. The endoplasmic reticulum and mitochondria serve this role as two key intracellular stores for calcium. The endoplasmic reticulum is a continuous network of folded membranes that exist throughout neuronal cells, from axons to presynaptic terminals to dendrites, that has been shown to play a key role in calcium homeostasis and neuronal plasticity, with disruptions in function leading to a number of neuropathologies [16, 22, 23, 24]. Mitochondria are organelles that play a fundamental role in a range cellular functions, including energy productive via ATP hydrolysis, and also intracellular calcium buffering in the brain and other cells [25, 26, 27]. Mitochondria also play a fundamental role in Fisher's Quantum Brain theory as the location for a potential biological qutrit and will

be discussed in more detail below. Here we note though that mitochondria and the endoplasmic reticulum are closely related, with several studies showing that the endoplasmic reticulum transports calcium into mitochondria as ionic species and in the form of calcium phosphate clusters [28, 29, 30], indicating that mitochondria are intimately related to any form of intracellular calcium buffering within neuronal cells.

1.2.2 Memory function

The question of memory storage and retrieval remains an open question in neuroscience [31]. Memory is often thought of in the form of the engram, which are lasting changes- at a biophysical/biochemical level- within the brain that allow for the imprinting of memories in response to an event. Our modern understanding of the engram builds off the work of Donald Hebb, who first proposed the ideas of neuronal "cell assemblies" whose connections are strengthening by learning events in 1949 [32]. This theory, with the colloquial description "neurons that fire together wire together," is still the basis of our modern understanding of neuroscience and the engram. Experimental studies have confirmed the importance of synaptic plasticity in memory growth via long-term potentiation and long-term depression [33, 34, 35].

In regards to the physical location of information, it has recently been shown that certain populations of neuronal cells- the engram cells noted above- are responsible for memory storage and retrieval [36, 37]. However, it does not appear that the cell is the unit of information, but rather that smaller sub-cellular entities encode information. In particular, dendrites, branch or spine like protrusions from neuronal cells and are the location of synaptic connections, seem to be a potential location for the engram. Studies have shown that long-term potentiation leads to the growth of dendritic spines [38], and that the ablation of spines can lead to the loss of previously learned information [39].

Thus, we have a sense of the spatial location of engrams within the cell, but the basic unit of information storage is still unknown.

The specific mechanisms of storage and retrieval are also still under investigation. Studies have shown that protein synthesis is required for long-term memory but not short term memory [40]. Other studies on mice that have undergone amnesic treatment have shown that synaptic potentiation, but not protein synthesis, is necessary for retrieving memories but not for storing them [41, 42]. Thus, while storage and retrieval are certainly physiologically related, this evidence suggests that they are fundamentally different in their biological encodings and time-scale dependent. Taken all together, the information network in the brain appears to be a complex interplay between different systems and functions.

Additionally, consciousness has no current neuroscientific explanation- which is perhaps not surprising given that this problem seems less well-defined than the still open problem of memory and learning. The present approach to the problem of consciousness deals with neuronal correlates of consciousness [43, 44], but this proposal is far from providing a fully coherent explanation and will require great deal of experimental work to test and develop.

Thus, given the number of open questions in the neuroscience of the mammalian brain, and the clear complexity of the information network (at both the physical cellular and subcellular level but also the experiential level), it does not seem unreasonable to consider the idea of a quantum information network within the brain. This quantum information network could coexist alongside a classical information network, serving either distinct or complementary roles. In the following section we consider how this quantum information network could be realized, focusing on Fisher's Quantum Brain theory.

1.3 Quantum Brains: from microtubules to Posners

1.3.1 Historical ideas of biological quantum computing

The idea that quantum mechanics could be utilized for brain function dates back to Wigner in the 1960s [45], and the potential mechanisms and implications have been debated since. From a physical perspective, the fundamental problem with quantum mechanics operating in the human brain is the issue of quantum decoherence due to environmental interaction. Biological systems are "wet" (i.e. crowded, with many molecules bumping into each other) and "warm" (i.e. human body temperatures are around 310 K), whereas many experimental realizations of quantum information storage occur at the scale of a few Kelvin or less in isolated systems. The wet and warm nature of biology lead to strong environmental interaction with any quantum degrees of freedom in the system which could encode quantum information. Strong interactions would result in quantum decoherence, and the loss of any quantum information encoded within the states. Proposals for the rates of decoherence in a biological environment such as the brain have generally put information lifetimes at the scale of picoseconds to nanoseconds, which appears far too short for any interesting quantum information processing that could result in brain functions. Thus, it is imperative for a serious theory for quantum information within the brain to propose a system that can hold coherent quantum information for timescales that allow for some form or processing and output.

Perhaps the best-known theory that attempts a full physical picture was the "orchestrated objective reduction" theory of Hameroff and Penrose [46, 47, 48, 49, 50]. Their theory utilizes ideas of Penrose that a quantum superposition of states with different geometries (such as an enzyme with two distinct conformations) would create a "bubble" in spacetime curvature. These bubbles are unstable and would eventually collapse into classical states, in a process called "objective reductions." The timescale for such

events is set by $t = \hbar/E$, where t is the coherence time until objective reduction collapse, and E is the gravitational energy of the superposed mass. Hameroff and Penrose considered objective reductions occurring within microtubules, self assembling tubes of protein which are components of the cytoskeleton and which have a variety of biological roles, including the formation of synaptic connections and the growth of axons and dendrites. They proposed that coherent quantum superpositions could form between billions of tubulins (monomers of microtubules) that could exist for tens to hundreds of milliseconds. This is much longer than previous proposed limits on quantum information in biology, potentially allowing quantum processing in the brain on physiologically relevant timescales. These quantum states could then evolve to perform quantum computations during these coherent periods, eventually collapsing via objective reduction into classical tubulin states that control synaptic and neural events.

While an extremely ambitious theory, a success of this theory is in its connection to real experimental evidence (anesthetic function appears related to hydrophobic pockets such as those found in tubulin) and put forward testable hypotheses [50]. However, these experimental tests are difficult to perform in controlled experiments, as quantum correlations or coherences are difficult to detect in any system, and biological systems involving billions of proteins make for a particularly complex experiment. Therefore, work towards realizing some of these proposed experimental systems is still ongoing today. Nevertheless, the theory of Hameroff and Penrose was one of the first and strongest serious scientific proposals aimed at tackling the possibility that quantum mechanics may be non-trivially operational in the human brain and consciousness.

1.3.2 Reverse engineering a "quantum brain"

Recently, another proposal has been put forward by Matthew P.A. Fisher, where he utilized a reverse-engineering approach to construct a model of how quantum information processing in the brain could feasibly function [51]. As a first requirement, he considered what quantum degrees of freedom would have the environmental isolation required to store and process quantum information on relevant timescales. Spin offers an excellent potential vehicle, in particular spin $\frac{1}{2}$ nuclei. Spin is an inherent form of angular momentum possessed by particles such as atomic nuclei and electrons and can take the values $I = 0, \frac{1}{2}, 1, \frac{3}{2}, 2, ...,$ with corresponding spin angular momentum of $\sqrt{I(I+1}\hbar$. While spins are fundamentally quantum, they can be thought of in a classical analogue as tiny magnets because of their interactions with magnetic fields. Spins with magnitude $> \frac{1}{2}$ will also couple with electric field gradients via their electric quadrupole moment, often leading to rapid spin decoherence as compared to spin $\frac{1}{2}$ particles. Electrons are also spin $\frac{1}{2}$ particulars, but have a much greater magnetic dipole moment than nuclear spins, and therefore also have strong environmental interactions and relatively rapid decoherence, on the order of microseconds or nanoseconds. In contrast, spin $\frac{1}{2}$ nuclei in solution can have spin relaxation times - equivalent to decoherence times - on the order of seconds and sometimes even minutes, even without any "special" forms of environmental isolation. Therefore, spin $\frac{1}{2}$ nuclei offer an intriguing potential vehicle for quantum information that could stay coherent long enough for computation even in a biological system.

When considering spin relaxation for spin $\frac{1}{2}$ particles, the primary contribution generally come from dipolar coupling, the interaction between two magnetic dipoles, particularly in the case of symmetric species such as the Posner molecule. While a full discussion of spin relaxation can be found elsewhere [52, 53], here we briefly describe this mechanism in order to consider what sort of molecular structure might allow for long spin relaxation

times- thereby allowing adequate time for quantum computation. "Small" here is defined by $\tau_c >> \omega_0$, where $\tau_c = \frac{4\pi\eta r^3}{3kT}$ is the rotational correlation time of a molecule with radius r in a solvent with viscosity η at temperature T. ω_0 is the Larmor frequency of our spin, defined as $\omega_0 = \gamma B$ with γ the gyromagnetic ratio of the spin and B the magnetic field strength. The dipolar relaxation rate for a spin a ($R_{dip,a}$) then scales as $R_{dip,a} \propto \frac{\gamma_a^2 \gamma_b^2 \tau_c}{d^6}$ where γ_a is the gyromagnetic ratio of spin a, γ_b is the gyromagnetic ratio of the dipolar coupled spin, and d is the distance between the two spins. Notably, spins with smaller gyromagnetic ratios and spatial separation from other magnetic dipoles which tumble rapidly in would have the slowest dipolar relaxation rates. (Electrons have a gyromagnetic ratio at least three orders of magnitude greater than nuclei, which leads to much faster spin relaxation).

1.3.3 Posner molecules: a biological qutrit?

Given these requirements, we can consider what nuclear spin could be a good candidate as our putative quantum information encoder. Protons (^{1}H) are spin $\frac{1}{2}$, but have a large gyromagnetic ratio for a nucleus. Additionally, protons are generally in rapid exchange within the body, and are so ubiquitous in the form of water that they would appear unlikely to be carriers of quantum information. When considering the most abundant nuclei within biology, the other spin $\frac{1}{2}$ nucleus is phosphorus (^{31}P), which is biologically plentiful (1% of the body by mass) and has a lower gyromagnetic ratio than a proton. Phosphorus is also generally found in the form of phosphate, where a central phosphorus atom is bound to four oxygen atoms. Given that ^{16}O, the most common isotope of oxygen at 99.8% abundance, is a spin 0 particle, these oxygens provide spatial separation between the phosphorus nuclei and other spins that could induce relaxation. However, phosphates are generally found in protonated states at biological pHs, meaning

that protons are bonded to these oxygens, leading to spin relaxation on the order of a few seconds in water (Phosphate spin relaxation is discussed in detail in Chapter 3). While a few seconds may still be a long coherence for most quantum states at 310 K, it still seems short on the timescales required for consciousness and cognition.

Interestingly, though, there is another abundant biological atom that can out-compete protons in binding to phosphates at biological pHs - calcium. Calcium is another atom whose primary isotope (^{40}Ca at 96.9 % abundance) has a spin 0 nucleus, and makes up $\sim$1.5% of the body's mass. Calcium phosphate, in the form of the solid phase hydroxyapatite, is the main constituent of bones and teeth within the body, but can also be found within cells. While the physical chemistry of calcium phosphate will be explored in detail in Chapter 2, here we note that researchers have previously proposed the existence of the "Posner cluster," (used interchangeably with Posner molecule) a $\sim$ 1 nm spherical and symmetric calcium phosphate species with stoichiometry $Ca_9(PO_4)_6$. Thus, the phosphorus nucleus is surrounded by spin 0 atoms, creating spatial separation between phosphorus and other magnetic dipoles that could induce dipolar relaxation. Because of its small size (and thus large rotational diffusion rate), the Posner cluster would tumble rapidly in solution, with a rotational correlation time in water at 310 K of $\propto$ 85 picoseconds. While there have been a number of conflicting calculations on just how long the spin relaxation time of a Posner molecule would be, estimates range from minutes to days. Even at the lower limit of these estimations, this timescale for quantum information storage (and thus computation and processing) is far beyond the limits of what had originally been considered possible in a wet, warm biological environment, indicating that the Posner molecule is worth investigation for its potential role as biological quantum information carrier.

1.3.4 From nuclear spin states to biochemistry

While storage of quantum information is important for biological quantum computing, it is also key that the quantum states can be "read out" in some form that can lead to neuronal signaling. This conversion of quantum states to biochemical signals is often at the crux of theoretical proposals for quantum information in the brain or other forms of quantum mechanical effects in biology. In the case of Fisher's theory, he proposed a novel hypothesis, termed "quantum dynamical selection," which links the spins states in a small symmetric molecule with binding reactions [54]. Quantum dynamical selection (QDS) offers a means to go from phosphorus nuclear spin states within Posner molecules to actual biochemical outputs.

QDS utilizes the fact that indistinguishable particles will have their wave functions transform in a known way upon exchange. For fermionic particles, those with half-integer spin, the particle statistics state that the wave function for the system will acquire a factor of -1 when two particles are exchanged - an antisymmetric wave function. For bosonic particles, those with integer spin, the particle statistics result in the wave function remaining unchanged upon exchange- a symmetric wave function. These exchange statistics are the reason for the Pauli exclusion principle - two fermions cannot be in the exact same state, as then upon exchange their wave functions would be identical, and not antisymmetric, unless the wave function was zero, in which case the particles do not exist. Similarly, the symmetric nature of bosonic wave functions is why exotic materials like Bose-Einstein Condensates can exist, since all of the bosons are able to access the same ground state. As we describe in detail below, the fermionic exchange statistics couple the collective spin states of a symmetric molecule with the allowed orbital angular momentum states, resulting in spin state restrictions on potential molecular binding.

To better understand QDS, it is instructive to consider a planar molecule composed

of fermionic nuclei with n-fold symmetry for $n > 3$. The operator $\hat{C}_n$ will then perform a $\frac{2\pi}{n}$ rotation of the molecule, swapping the positions of the fermionic nuclei but leaving the molecule in an indistinguishable state. We then consider the nuclear spin states in the eigenbasis of $\hat{C}_n$, so that they acquire the phase factor (eigenvalue) of ω_n^τ, where $\omega_n = e^{\frac{2\pi}{n}}$ and the "pseudospin" $\tau = 0, 1, 2, ..., n-1$. Because of the fermionic particle statistics, the full wave function for the molecule - which includes the nuclear spin states but also the orbital states of the nuclei and the electronic wave functions - must pick up a sign of $(-1)^{n-1}$. Since the electronic wave functions would be expected to be identical under this rotation, the particle statistics then imply that the orbital angular momentum- which will dictate whether binding can occur- of the molecule will be constrained by the value of the pseudospin.

We can see the exact constraint on the orbital angular momentum by considering the orbital wavefunction, $\psi_\tau(\phi)$ under a $\frac{2\pi}{n}$ rotation,

$$\psi_\tau(\phi + \frac{2\pi}{n}) = (-1)^{n-1}\omega_n^{-\tau}\psi_\tau(\phi) \tag{1.1}$$

Therefore the pseudospin τ is coupled to the orbital angular momentum states. Expanding these orbital angular momentum states ψ_τ via their eigenstates, $e^{iL\phi}$, with $L \in \mathbb{Z}$, we see that the allowed angular momentum values

$$L = n\mathbb{Z} - L_{quasi} \tag{1.2}$$

where $L_{quasi} = \tau$ for odd n and $\tau + \frac{n}{2}$ for even n, in order to account for both the phase ω_n and the $(-1)^{n-1}$ terms. QDS thus predicts that the nuclear spin states of the molecule are coupled to the orbital motion of the molecule. In particular, the value of pseudospin (as determined by the collective nuclear spin state) dictates whether a molecule is able to stop rotating.

It is important here to define what it means for a molecule to be "not rotating." Following Fisher and Radzihovsky, we define "non-rotating" to mean that a real wave function describes the orbital motion. Since a real wave function is a solution to the time independent Schrödinger equation, such a wave function is then in a steady state. This consideration is why QDS does not apply to molecules with two-fold symmetry. In that case, the pseudospin phase factor would be real ($e^{i\pi}$ for the singlet state or e^0 for the triplet state) and thus there is no constraint on which pseudospin states can access a non-rotating state.

A couple of case studies show the resulting impact of QDS on chemical reactions. First, we consider a symmetric substrate molecule binding to an enzyme to catalyze a reaction such as bond breakage or formation. In this case, the substrate is often thought to bind in a pocket of the enzyme to undergo the catalyzed reaction. The substrate must then stop its rotation in this enzyme pocket, requiring a real wave function (equivalent here to a state of zero orbital angular momentum). From equation (2), we note that this can only be accessed by a single pseudospin sector ($\tau = 0$ for odd n and $\tau = -\frac{n}{2}$ for even n). Thus, when the substrate approaches the enzyme and attempts to bind, a projective measurement will be made onto the pseudospin sector. A failure to project onto the proper pseudospin state will mean that the substrate is prohibited from binding to the enzyme. The quantitative implications on enzyme-catalyzed reaction rates and experimental exploration of a model system with 3-fold symmetry is explored in Chapter 6.

Second, we consider the case of two Posner molecules attempting to bind one another. This case is treated in detail by Fisher and Radzihovsky, but we summarize the result here. Posner molecules are predicted to have 3-fold symmetry, and their binding is energetically favorable for anti-parallel $\hat{C}_3$ axes [55]. The formation of a chemical bond between two Posner molecules implies that the relative rotation of the molecules is zero.

To fulfill this requirement in the anti-parallel state, the total pseudospin of the two Posners must sum to zero. Therefore, an attempted binding event between the molecules makes a projective measurement onto the pseudospin sum of the pair, and the Posners are restricted from binding unless in a state where $\tau_1 + \tau_2 = 0$. Thus, an attempted binding event- whether successful or unsuccessful- will entangle the pseudospin states of the two Posner molecules. Such entanglements are fundamental for a quantum system to be able to perform non-classical computations. Thus, pseudospin acts as the quantum degree of freedom for Posner molecules that can be entangled or read out during binding events. Since the Posner molecule has 3-fold symmetry, there are three pseudospin sectors, so that a Posner molecule pseudospin state is a qutrit.

Additionally, in the bound state, depending on solution conditions, the Posners may be more likely to either chemically dissociate into ionic constituents or to undergo further aggregation events (and be less likely to dissociate). In both cases, the phosphorus spin states of the molecule, via their pseudospin, are now dictating chemical reactions that could modulate the biochemistry of a cell. Posner dissolution would also release free calcium ions, which we have established to be fundamental to neuronal signaling and regulation. Thus, increasing or decreasing the likelihood of Posner dissociation could impact downstream neuronal behavior.

1.3.5 Mitochondria: a home for Posners

Thus far, we have introduced a potential carrier for biological quantum information (phosphorus nuclear spin states within Posner molecules), and a putative means for transducing these spin states to measurable biochemical events (QDS). The next question then is where within cells would these Posner clusters be stable?

It is known that non-local synchronous neuronal firing is a feature of higher order

mammalian brains. As introduced, one feature of quantum mechanics (and quantum computation) is the ability to create non-local entanglements that can cause non-local correlated events. In the context of Fisher's Quantum Brain theory, this would require two Posner molecules that are pseudospin entangled to then become spatially separated within the brain. Therefore, wherever Posners are present, there should also be some mechanism of transporting Posner molecules between cells.

Mitochondria provide a possible solution to these requirements. For one, mitochondria are organelles that are found within almost all cells, colloquially known as "the powerhouse of the cell" due to their role in adenosine triphosphate (ATP) formation, storage, and hydrolysis to produce chemical energy for cellular functions [56, 57]. ATP hydrolysis occurs via the breaking of a bond to form adenosine diphosphate (ADP) and a phosphate ion, and ADP can be additionally hydrolyzed into adenosine monophosphate (AMP) and another phosphate ion. Mitochondria therefore have a high abundance of phosphate.

Another important cellular function of mitochondria is in the sequestration and release of calcium ions [25, 26]. As established, mitochondria uptake calcium from the cytoplasm via the mitochondrial calcium uniporters when there is a high concentration of calcium in the cell. Within mitochondria, calcium play a number of different roles, including in metabolic function, ATP hydrolysis and cell death [58, 59]. When the calcium load of mitochondria surpasses their buffering ability, an event known as the mitochondrial permeability transition occurs, leading to a number of correlated events, including a depolarization of the mitochondrial membrane and a large efflux of accumulated calcium ions [60]. It has been shown that in the lead up to these events, calcium is stored in the form of amorphous calcium phosphate granules, which can reach sizes as large as 30 nm in diameter [61]. As will be detailed in the next chapter on the physical chemistry of calcium phosphate, amorphous calcium phosphate has been hypothesized to take the

form of a "glass" of Posner molecules. Posner clusters are thus considered prenucleation clusters for amorphous calcium phosphate, so that the presence of amorphous calcium phosphate within the mitochondria is a sign that Posner clusters could exist there as well.

Now, mitochondria appear to be an excellent location to find biological Posner molecules, and given their relationship with calcium ions- a key neuronal signal- mitochondria are also intimately connected with neuronal function. However, we have established that there is also a need for a method to transport Posner molecules between neuronal cells. Again, mitochondria seem uniquely suited for this role due to the presence of complicated intercellular networks of mitochondria[62]. Because of their importance as cellular sources of energy, it is critical to be able to transport mitochondria amongst cells to supply energy to different regions of the body. Therefore, molecular motors in the body move mitochondria both within and between cells.

Additionally, mitochondria regularly undergo fission and fusion events, both splitting and combining as they undergo their intercellular transport [63]. Such events mix/split the inner matrix constituents of mitochondria, where Posners would be putatively present. Thus, a fission event could cause two pseudospin entangled Posner molecules to be split between different mitochondria. These mitochondria could then be transported through intercellular networks to different regions of the brain and produce non-local entanglements.

We can also consider two mitochondria where the Posner molecules have all reached a single pseudospin sector (say one where $\tau = 1$ for each Posner and one where $\tau = -1$ for each Posner). Within the mitochondria, the Posners are in a steady state where all two Posner binding events are prohibited. However, when these two mitochondria undergo a fusion event, the Posners from each pseudospin sector mix, and suddenly a number of binding events are possible. Therefore, a fusion event could result in a rapid change

of Posner dynamics and downstream calcium phosphate formation, potentially leading to mitochondrial permeability transition events and/or release of calcium signals. While these networks of fissioning and fusioning mitochondria are not strictly required for the Quantum Brain theory, it is still interesting to consider such events and their potential impacts.

In full, the Quantum Brain theory offers a physically feasible mechanism for quantum information storage and processing within a biological environment. Quantum information is encoded within the collective nuclear spin states of Posner molecules via a pseudospin. QDS then links these pseudospin quantum numbers with binding events, altering downstream calcium phosphate dynamics that could be converted into biochemical signals. Mitochondria could house these Posner molecules, creating non-local entanglements via fission events followed by intercellular mitochondrial transport, and potentially downstream fusion events could mix pseudospin sectors and lead to rapid aggregation events. Particularly of note in the theory as opposed to previous proposals are the long coherence times for the quantum information, and the novel mechanism for transduction of quantum states into biochemical signals.

We do not discuss specific means of what sort of computation would be possible within this thesis. Rather, we will focus on experimental efforts to test different elements of the theory in order to explore whether such a proposal could be physically feasible. While all the work presented in this thesis will be *in vitro* studies, we will regularly return to this Quantum Brain theory to connect the *in vitro* results with possible *in vivo* implications.

In Chapter 2, we will introduce the current understanding of calcium phosphates, focusing on phases with biological relevance as well as calcium phosphate nanoclusters. In Chapter 3, we present evidence for spectroscopically 'dark state' assemblies of phosphates that form in aqueous solutions, and investigate their solution behavior. In Chapter 4, we investigate calcium phosphate nanoclusters in simulated body fluids, and confirm the

existence of Posner molecules in these solutions. In Chapter 5, we discover a lithium isotope effect on the formation of calcium phosphate, and propose that this effect is related to QDS. In Chapter 6, we present a framework for investigating QDS in a model enzymatic system with a three-fold symmetric substrate. In Chapter 7, we summarize our findings, and propose future research directions building off of the results in this thesis.

1.4 Permissions and Attributions

1. The content of Chapter 3 and Appendix B is the result of a collaboration with Mesopotamia Nowotarski, Jiaqi Lu, Tanvi Sheth, and Sally Jiao and has previously appeared in Proceedings of the National Academy of Sciences [64].

2. The content of Chapter 5 and Appendix C is the result of a collaboration with Manisha Patel and Mesopotamia Nowotarski.

3. The content of Chapter 6 is the result of a collaboration with Manisha Patel.

Chapter 2

Calcium Phosphates

2.1 Introduction

Calcium phosphates are key biominerals as the primary component of bones and teeth [65, 66, 67, 68, 69, 70], as well as being abundant natural resources as a source and recycling method of phosphorus for industrial purposes [71, 72]. The basic units of calcium phosphates are calcium (Ca^{2+}) and phosphate (PO_4^{3-}) ions, as well as protons (H^+) and hydroxides (OH^-). Additional ions may also incorporate into structures depending on the conditions of mineral formation, including but not limited to fluoride, chloride, magnesium, and carbonate.

Calcium phosphates have complex solution phase behavior with a number of different species forming depending on the pH and concentrations of calcium and phosphate. The pH of the solution will modulate the protonation state of the phosphate groups, and have a heavy impact on the resulting mineral species that form. The amount of water molecules incorporated into the crystalline phase also impacts the structure.

At lower pHs (below ~ 6), the preferred thermodynamic phases of brushite ($CaHPO_4 \cdot 2H_2O$) and monetite ($CaHPO_4$) form, whereas above this pH the phases hydroxyapatite

($Ca_{10}(PO_4)_6(OH)_2$; HAp), octacalcium phosphate
($Ca_8H_2(PO_4)_6 \cdot 5H_2O$; OCP), and β tricalcium phosphate (β-$Ca_3(PO_4)_2$; β-TCP) are thermodynamically preferred [73]. A number of other thermodynamically stable phases incorporating additional ions exist as noted above (in particular with fluoride or chloride replacing a hydroxide group), or more heavily protonated forms of phosphates, can also form under the proper solution conditions [73].

Calcium phosphates can also form metastable phases in solution as an intermediary before transitioning into the thermodynamically preferred phases. The most heavily studied of such phases is amorphous calcium phosphate (ACP), a kinetically stable phase that forms between pH 6.5 and pH 10.5 [74, 73] en route to hydroxyapatite formation. The stoichiometry of ACP can vary heavily depending on the solution conditions, with Ca/P ratios ranging from 1.1-1.7 [73], but the mostly commonly reported value is a Ca/P ratio of 1.5, where the charge balance is complete between Ca^{2+} and $PO_4{}^{3-}$ ions. As will be explored in more detail, ACP is generally considered a glass-like structure of Posner molecules, and therefore is of particular interest in the context of the Quantum Brain theory.

From a biological perspective, calcium phosphates are primarily studied for their fundamental in bone and teeth growth [68, 65, 70]. Synthetic calcium phosphates are promising biomaterials for bone regeneration or in combination with other healing bio-agents [66, 67]. However, calcium phosphates also play a number of other biological roles. Pathological calcification often occurs via the deposition of calcium phosphates [75, 76]. As noted in Chapter 1, calcium phosphates form in mitochondria and the endoplasmic reticulum after calcium uptake for intracellular calcium buffering. And, of course, nanometric calcium phosphate in the form of Posner molecules are proposed biological carriers of quantum information.

In biological systems, the dominant species of calcium phosphate are amorphous cal-

cium phosphate and hydroxyapatite, as these phases are preferential at biological pHs. Therefore in this chapter we focus on the physical chemistry of these two closely linked phases of calcium phosphate, as well as the Posner molecule, which has historically been thought of in terms of a prenucleation cluster for ACP. We begin by discussing hydroxyapatite, focusing on its nucleation and growth, and then transition into the formation of ACP. The experimental characterization of these phases is closely linked and such discussions are intermingled in both sections. Finally, we will go in depth into calcium phosphate nanoclusters, in particular the Posner molecule, surveying experimental and theoretical work on the energetics and dynamics of these molecules to contextualize the open questions that must be answered to test the Quantum Brain theory.

2.2 Hydroxyapatite

Hydroxyapatite is the primary mineral component of bone and teeth, making it an important biomineral as the thermodynamically stable phase of calcium phosphate at biological pHs. As such, a number of studies have aimed to explore the formation and stabilization of hydroxyapatite [77, 78, 65, 79, 80]. A primary focus for such work is in the transition of ACP into HAp, given that ACP is generally considered a precursor to the formation of HAp. However, given HAps importance as a biomaterial, there have also been a number of bioengineering studies focusing on controlling the morphology of HAp or inhibiting its growth via proteins or other biomolecules [81, 82, 83, 84, 85].

The nucleation and growth of hydroxyapatite is complex in that it can proceed via both classical and nonclassical nucleation pathways [77]. The former pathway can be thought of through the framework of homogeneous classical nucleation theory. In this case, we consider the free energy of a homogeneous spherical crystal nucleus of radius r relative to its ionic constituents, which we express as

$$\Delta G = \frac{-4\pi r^3}{3\nu} K\,T\,ln\,S + 4\pi r^2 \sigma \tag{2.1}$$

where ν is the volume of an individual molecule, S is the supersaturation ratio, and σ is the surface energy of the between the solid and solution [86]. Assuming ideal mixing, the supersaturation ratio can be calculated by $S = \frac{C}{C^*}$ where C is the solute concentration in the solution and C^* is the solubility. This concept can easily be extended via ionic activity products for species that contain multiple species of ions (e.g. hydroxyapatite has an ionic activity product of $[Ca^{2+}]^{10}[PO_4^{3-}]^6[OH^-]^2$).

We see from equation (1) that there is a trade-off between a negative volumetric energy in the first term and a positive surface energy in the second term. Since these terms have different radial dependence, at a critical radius of $r^* = \frac{2\sigma}{KTlnS}$ ΔG reaches a maximum, and thus the probability of nucleus formation will be minimized. However, above this critical radius the growth of the nucleus will be energetically favorable, so the nucleation rate will be primarily limited by overcoming the energetic barrier associated with forming the critical nucleus size. Assuming Arrhenius-like kinetics of growth, the rate R of nucleation (in terms of number of nuclei) can then be expressed by [86]

$$R = A\,exp\left(\frac{-16\pi\sigma^3\nu^2}{3K^3T^3(ln\,S)^2}\right) \tag{2.2}$$

where A is the Arrhenius prefactor that depends on the kinetics of the specific system. Once these nuclei have formed past the critical radius, they can they continue their growth via both agglomeration of monomers or the coalescence of multiple nuclei. This classical nucleation process has been demonstrated to be one route for the formation of hydroxyapatite in solution [77], although most studies on classical nucleation have used surface-induced growth i.e. heterogeneous nucleation [87, 88].

However, much of the focus on hydroxyapatite growth has investigated the nonclas-

sical nucleation pathway where amorphous calcium phosphate is formed as a metastable phase before transitioning into crystalline hydroxyapatite. This pathway is the primary route for hydroxyapatite formation [89, 90], with the classical nucleation of hydroxyapatite in bulk solution only having been observed in the last few years [77]. In nonclassical nucleation, the free energy barrier to nucleus formation is smaller for a metastable phase as opposed to the thermodynamically stable phase. Therefore, the crystallization process occurs in two (or more) stages- first the formation of these metastable nuclei, and then the conversion of these intermediate nuclei - generally some amorphous, glassy form- into the crystal [86]. Such nonclassical processes have been found to be widespread in crystallization in a number of systems, such as proteins [91], metals [66], minerals [77, 89], and polymers [92].

During the second stage of nonclassical nucleation, the glassy intermediate phase must undergo some type of rearrangement in order to form the crystal phase. For the transformation of hydroxyapatite from amorphous calcium phosphate, a number of mechanisms have been observed, including nucleation of crystals on the surface of ACP [93, 94], internal rearrangement [95, 78], and dissolution of ACP followed by rapid reprecipitation of HAp [89, 96]. However, several of these studies used additives such as nanoparticles or surfaces that could impact the nucleation of ACP and following transformation to HAp as compared to a bulk solution. Recently, multiple studies have used transmission electron microscopy to directly visualize this transformation process, and found evidence supporting the dissolution/reprecipitation mechanism [77, 79].

Experimentally, a number of techniques are used to identify and characterize hydroxyapatite. Because hydroxyapatite is generally formed via amorphous calcium phosphate, a key component of these experimental methods is being able to identify between glassy ACP and crystalline HAp. A commonly used technique here is X-ray diffraction on powdered samples, where the well-defined inter-atomic structure of the crystalline lat-

tice of HAp will lead to sharply resolved peaks. The location of these peaks also allows for the differentiation between other crystalline calcium-phosphate phases. ACP, on the other hand, will have broad peaks due to its glassy nature that leads to distribution of interatomic distances. Similarly, electron microscopy techniques, which can be sued to visualize ACP and HAp in both solid and solution forms, can differentiate between the two phases due to the presence of electron diffraction patterns for the crystalline phase. Raman spectroscopy has also been used to study the evolution of amorphous calcium phosphate into hydroxyapatite by looking at different modes of P-O-P bonds between the two phases, with the advantage that such experiments can occur in solution to observe this transition over time [80]. ^{31}P solid-state nuclear magnetic resonance has also been used to study both the ACP-HAp transition [97] and HAp structures [98].

In summary, we see that the nucleation and growth of hydroxyapatite is quite complex, with both classical and nonclassical nucleation processes occurring, at times simultaneously. A number of experimental techniques are used to identify and study hydroxyapatite, with a key feature being the ability of such techniques to differentiate crystalline HAp from its glassy ACP precursor. We now turn our attention specifically towards ACP and its solution phase growth and characterization, due to its importance both as a HAp precursor and in the framework of the Quantum Brain theory.

2.3 Amorphous calcium phosphate

While hydroxyapatite is biologically more abundant as the actual calcium phosphate phase found in bone and teeth, amorphous calcium phosphate is often the first phase to form in solution. Thus, because of its role as a biomineral precursor, the formation and stabilization of amorphous calcium phosphate has been a focus of investigation *in vivo* and *in vitro*. While the formation of solid ACP under high temperature/pressure

conditions has also studied for its potential use as a ceramic, [74], a majority of research has focused on the solution phase behavior of ACP.

The formation of ACP was introduced above as the first step of the two-stage non-classical nucleation of hydroxyapatite. However, ACP formation itself also occurs via a multi-stage mechanism, the current understanding of which is demonstrated in Fig. 2.1 (we will add in additional "vertical" equilibrium within stages in this thesis as we uncover additional phases that occur in solution). In stage I, calcium and phosphate ions exist free in solution. At sufficient ionic concentrations, temperature, and pH, these solutions will become saturated and the ions will form calcium phosphate prenucleation clusters(stage II). The details of these prenucleation clusters will be discussed in detail in the following section, but there is general agreement that these clusters are calcium phosphate species ~ 1 nm in size, although their stoichiometry is still debated [89, 99, 100, 101, 102]. These clusters then rapidly aggregate into amorphous calcium phosphate colloids with diameters in the range of $50 - 100$ nm (stage III) [90, 93]. ACP colloids then agglomerate into larger ACP aggregates at the scale of several hundreds nanometers up to a few microns (stage IV). The exact size of these clusters will be determined by solution conditions such as temperature, pH, ionic concentrations of calcium and phosphate, and other species in solution that will impact the balance between negative volumetric free energy and positive surface energy to dictate a most energetically favorable size (analogously to our discussion of classical nucleation theory above).

The conventionally reported calcium/phosphate ratio in ACP is 1.5, in which case charge balance is achieved by the calcium and phosphates alone. However, different ratios can be formed at different solution conditions, with the incorporation of protons or hydroxide ions in the case of lower/higher Ca/P ratios, respectively [73]. Additionally, other ions can incorporate into the ACP if present during the solution growth, with magnesium, carbonate, and pyrophosphate the most commonly studied additives, all

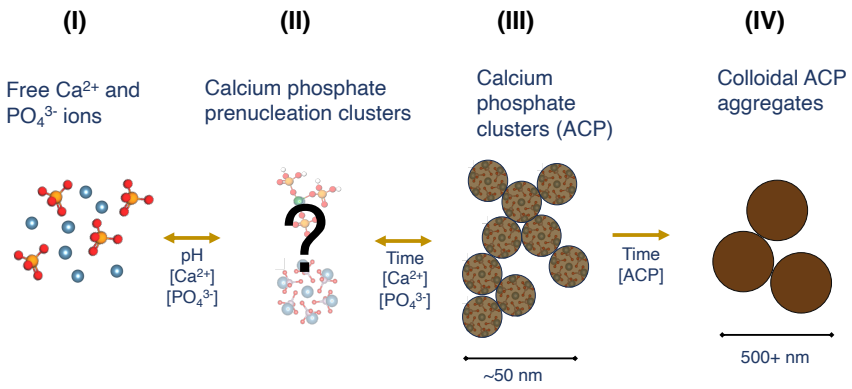

Figure 2.1: Proposed nucleation and growth pathway for the formation of amorphous calcium phosphate (ACP), showing four proposed stages and the transitions between them. Soluble calcium and phosphate ions (I) initially form prenucleation nanoclusters (II), although the identity of these prenucleation clusters is still an open question. These nanoclusters then then rapidly form calcium phosphate clusters at 50-100 nm in diameter (III). These ACP clusters then aggregate into larger colloidal strcutures at several hundred nanometers in size (IV)). Over time, these metastable ACP aggregates undergo phase transformation to hydroxyapatite.

of which can impact the solution phase behavior of ACP formation and its subsequent transition into HAp [103, 104, 105, 106, 107]. Water molecules are also often incorporated into ACP in solution, with studies showing that ACP is approximately 20% water by weight (primarily in the interstices between calcium phosphate clusters [108]), although the presence of water does not shift the Ca/P ratio [65].

While ACP is generally reported to transition into hydroxyapatite on the time scale of minutes to hours, depending on exact solution conditions, amorphous calcium phosphate can also be stabilized and isolated. To form solid ACP, one can precipitate ACP out of solution and isolate it via filtration and lyophilization before the phase has time to transform to hydroxyapatite. Biologically, amorphous calcium phosphate has been found in milk and dental enamel, where proteins are able to stabilize ACP clusters and prevent the transition to hydroxyapatite [109, 110, 111, 112]. In blood and saliva, calcium phosphate is in a supersaturated state, but proteins are able to prevent the formation of

pathological calcium phosphate particles (fetuin [113, 114, 115] and slatherin [116, 117], respectively). In all of these cases, the proteins interact directly with ACP, either forming a coating around small particles to stabilize them (sometimes at sizes as small as a few nanometers [112, 114] or create protein-ACP complexes that alter morphology and aggregation. *In vitro*, polymers such as polyethylene glycol [118, 119] and hyaluronic acid [120], and even ATP [121], have all been investigated for their roles in altering ACP growth and stabilization.

Taken altogether, it is clear that while ACP is generally thought of as a metastable phase when studied in *in vitro* solutions, in a biological setting this may not be the case. The presence of proteins that interact directly with ACP can stabilize particles at a range of sizes. While some such proteins have been uncovered, no comprehensive proteomics study has been done that investigates all regions of the body where ACP is found. The polymer studies show that even indirect interactions such as crowding effects (which will certainly occur in a cellular environment) can have a large impact on ACP behavior.

In addition to the biological fluids noted above, ACP has been found to form after calcium loading events in mitochondria and the endoplasmic reticulum at sizes up to $\sim$ 30 nm [61, 30]. In these cases, the ACP appears stable and does transition into a crystalline phase. Current research is investigating the calcium phosphate-interacting proteome of the mitochondria to better understand this stabilization. However, ACP is transient in these cases because loading of mitochondria with ACP eventually will induce enough stress to cause the mitochondria permeability transition pore to open, leading to a number of correlated events that include ACP dissolution [60].

A number of the techniques for characterization of ACP were introduced in the previous section, as these techniques often have to differentiate between ACP and HAp. X-ray scattering, electron microscopy, Raman spectroscopy, and NMR are all important techniques in ACP characterization. Historically, X-ray diffraction has been used since

the 1970s, with Posner and Betts conducting the first experiments to note that within ACP there is short-range order on the scale of 0.95 nm [99, 89]. This led to the proposal of the Posner molecule, a spherical calcium phosphate nanocluster with stoichiometry $Ca_9(PO_4)_6$ and diameter of $\sim$ 1 nm, as the basic building block of ACP. These experiments led to our modern understanding of ACP formation that is shown in Fig. 2.1 by introducing the concept of the prenucleation cluster to ACP growth. A full description of experimental and theoretical work aimed at investigating Posner molecules (and other potential calcium phosphate nanoclusters) is provided below, because of the central importance of Posner molecules as the putative biological qutrit in the Quantum Brain theory.

Another technique that allows for the monitoring of solution ACP behavior *in situ* is dynamic light scattering (DLS). DLS has been used to study Stages II-IV of ACP growth [78, 100, 122], and will be used throughout this thesis because of its ability to rapidly screen different solution conditions and provide information on not only particle size but also concentrations and growth kinetics when used properly. A full discussion of dynamic light scattering theory can be found in Appendix A.

In summary, the formation and growth of ACP is a multistage process that has been studied extensively in both biological and *in vitro* systems. We now understand that ACP proceeds via the four stage mechanism presented in Fig. 2.1, but a number of questions remain about this process. In particular, the identity of prenucleation clusters and the dynamics of their formation are still debated. Additionally, stages 3 and 4 of ACP growth are modulated by a variety of solution conditions, including but not limited to ionic concentrations, pH, temperature, polymers, and proteins and other biomolecules, and the full solution phase space of ACP is still open to investigation. However, such studies are often complicated because of the transient nature of ACP and the diversity of calcium-phosphates species which all fall under the category of ACP. In this thesis, we will

add to the understanding of some of these open questions as we develop the experimental platform to test the Quantum Brain theory, further developing our understanding of the phase diagram in Fig. 2.1.

2.4 Posner molecules and calcium phosphate nanoclusters

As noted in the previous section, it has become well established that ACP formation involves the formation and aggregation of nanometric calcium phosphate prenucleation clusters (Fig. 2.1, stage II). There are two primary proposals for the stoichiometry of these prenucleation clusters: 1) some form of ionic calcium triphosphate (such as $[Ca(H_2PO_4)_{1.04})(HPO_4)_{1.76}]^{2.56-}$) [101, 123, 102], and 2) the Posner molecule ($Ca_9(PO_4)_6$) [78, 100, 99]. Given that the solution conditions used in different experiments are vastly varied, with differences in pH, temperature, calcium and phosphate concentrations, and additional salts, it is also entirely possible that these two clusters exist in equilibrium, with the exact solution conditions dictating which prenucleation nanocluster is preferred. Here we will review the experimental and theoretical work on each of these proposed prenucleation clusters, beginning with the calcium triphosphate species, before moving onto the Posner molecule.

The first proposal for calcium triphosphate as the prenucleation cluster of ACP came in 2013, from a study using a range of techniques including cryogenic transmission electron microscopy (cryo-TEM), pH measurements, free Ca^{2+} ion measurements, and Fourier transform infrared spectroscopy. The solution conditions encouraged the formation of ACP with a Ca/P ratio of 1.33, indicating that some phosphate groups remained protonated during ACP formation. Based on the pH and free Ca^{2+} measurements, they

proposed prenucleation species with a Ca/P ratio of $\sim 0.3-0.4$, which then incorporated additional Ca^{2+} ions en route to forming spherical ACP units. However, these prenucleation species were not observed free in solution, but rather their size of $\sim$ 1.2 nm was extrapolated as a function of defocus when imaging the already formed aggregates with cryo-TEM. Thus, while this work presents evidence for a calcium triphosphate-like structure based on the initial changes in pH and $[Ca^{2+}]$, it was unable to show that these structures exist in free solution.

An additional work on calcium triphosphate used dissolution dynamic nuclear polarization, where the sample is hyperpolarized via dynamic nuclear polarization before being rapidly melted and monitored in solution NMR [123]. They proposed that they indirectly observed a calcium triphosphate prenucleation cluster en route to the formation of brushite by considering the linewidth of their NMR signal and assuming a relaxation mechanism of chemical shift anisotropy. While this study is a nice proof of concept for this experimental technique, we would not expect that the prenucleation clusters formed here would correspond to those involved in ACP or HAp growth since these conditions promoted brushite formation instead.

A recent 2021 study also proposed the calcium triphosphate cluster by using a combination of NMR experiments, cryo-TEM, and free Ca^{2+} measurements [102]. This work used a more complex solution that contained a number of other ions including multivalent ions such as carbonate and magnesium that are known to interact with calcium phosphate. They found evidence for a slowly forming (over the course of several hours) nanometric calcium triphosphate species. Unlike previous studies of calcium triphosphate, they were able to make direct measurements on the size of the cluster free in solution, confirming its nanometric size, and proposed that phosphate ions in this nanocluster were in exchange with free phosphate ions for up to 10 hours. However, these solutions never showed significant growth of ACP and did not ever precipitate, raising

the question of whether these observed nanoclusters are prenucleation species.

In total, there is some evidence that under specific solution conditions, calcium triphosphate may be the preferred calcium phosphate nanocluster. However, none of the above-mentioned studies showed that calcium triphosphate was a prenucleation cluster for stoichiometric (Ca/P ratio of 1.5) ACP. Thus, it appears that while the calcium triphosphate cluster should be considered as a potential nanocluster under certain solution conditions, it may not be the primary prenucleation cluster involved in ACP growth.

We now turn our attention to the Posner cluster, the originally proposed ACP prenucleation cluster, as well as potential biological qutrit in the Quantum Brain theory. The Posner cluster was first hypothesized by Posner and Betts, who found short-range order on the scale of 0.95 nm in ACP in a x-ray diffraction study [99, 89, 65]. Given that ACP has a Ca/P ratio of 1.5, they considered what size cluster would produce the observed short-range order, and found that a spherical cluster of 9 calciums and 6 phosphates, would explain their observation.

Because of the small size of the Posner cluster and its tendency to aggregate in solution to form ACP, it was 20 years before its presence in solution was suggested experimentally. In the late 1990s, a group in Japan used dynamic light scattering on simulated body fluids (SBF), simple solutions of calcium chloride, phosphoric acid, potassium chloride, and potassium hydroxide designed to roughly simulate intercellular concentrations and pHs, and found evidence for a nanometric calcium phosphate cluster [78, 100]. Given that these solutions promoted the formation of hydroxyapatite, and building off the work of Posner and Betts, they proposed these nanoclusters to be Posner clusters. However, the exact size and populations of these particles (let alone their atomic composition and structure) was difficult to extract due to limitations posed by the apparatuses available for DLS at the time. Nonetheless, this work presented evidence for the existence of free calcium phosphate nanoclusters in solution en route to hydroxyapatite growth, supporting the

prenucleation cluster proposal of Posner and Betts. In Chapter 4, we will build off of these studies using a state-of-the-art DLS apparatus to gain additional insights into calcium phosphate nanoclusters.

In the 2010s, as experimental techniques advanced to be able to better investigate nanometric species in solution, a number of additional studies probed prenucleation clusters in ACP growth. These studies utilized cryogenic transmission electron microscopy (cryo-TEM) [93], atomic force microscopy (AFM) [124], and x-ray absorption near-edge spectroscopy (XANES) [125, 126] to investigate early nucleation events in ACP formation. The cryoTEM and AFM studies used surfaces to induce calcium phosphate nucleation and ACP growth, and both observed the presence of calcium phosphate clusters of ~ 1 nm during this surface-induced growth process, with AFM also showing evidence for ~ 2 nm clusters. While these units were mostly visualized after already aggregating on a Langmuir monolayer of arachidic acid designed to mimic calcifiable surface *in vivo*, cryoTEM also visualized a few individual nanometric units free in solution [93] (AFM does not allow for the sizing of particles free in solution). Given these clusters size and their appearance during ACP growth, they were proposed to be Posner molecules.

XANES studies on calcium phosphate focused on the coordination chemistry of calcium ions in solution [125, 126]. One study on a simple calcium chloride - sodium phosphate system proposed an "idealized" cluster of a Posner cluster coordinated with 30 water molecules [125]. A follow up study by the same group included sucrose at 24 wt%, in order to increase viscosity and allow for more resolution of solution dynamics. This work found a significantly different calcium coordination, with a single calcium ion coordinating with multiple phosphates and water molecules, rather than in a Posner-type arrangement [126]. However, given the large amount of sucrose in the solution, it is not surprisingly that this system showed significantly different coordination, and thus the previous study is more likely to reflect the SBF conditions used by other groups that

observed calcium phosphate nanoclusters.

With experimentally evidence seeming to verify the prenucleation cluster theory for ACP, a number of density functional theory (DFT) studies were conducted to study the energetics of the Posner cluster as compared to other calcium phosphate nanoclusters of the form $(Ca_3(PO_4)_2)_n$ [127, 128, 129]. These studies verified that the Posner cluster was energetically favorable as a prenucleation cluster as opposed to smaller or larger clusters with the same 1.5 Ca/P ratio. There was also evidence that aggregation of the monomeric form $Ca_3(PO_4)_2$ could be a potential alternative hypothesis, but computational limitations meant that this was unable to be verified [128], and such a unit would also be much smaller than the experimentally observed diameter of ~ 1 nm. A Posner cluster with 6 protons attached to the phosphate groups, and 6 hydroxide ions incorporated for charge neutrality, was also found to be an energetically possible cluster [129]. However, due to the nature of these *ab initio* calculations, where water molecules have to be expressed in a mean-field approximation, it is difficult to accurately capture exact solution energetics for the even the simplest of SBFs that were experimentally studied.

A more recent *ab initio* DFT study of Posner conducted by Swift in collaboration with Fisher went into more depth on both spin dynamics and potential substitutions in Posner molecules and put forth a number of interesting findings [55]. One is that while the Posner molecule is not always symmetric, the deviations from a symmetric arrangement are on the order of thousandths of an Å, and thus would be washed out by thermal fluctuations, which is key given the importance of symmetry for quantum dynamical selection to function. The study confirmed that pair-binding of Posner molecules is favorable, supporting the prenucleation cluster theory, although the authors note that since solvent interactions are not taken into account in these DFT studies the energetics may be slightly different in solution.

This work made a prediction for the longitudinal relaxation time (T_1 of a ^{31}P spin in

a Posner molecule tumbling in water at 300 K under the assumption that the relaxation is induced by dipolar coupling with an exterior proton, and found a relaxation time of 21 days. Compared with "normal" molecules and ions, which often show T_1 times on the order of seconds, with T_1 of tens of seconds considered "long," this predicted T_1 is extremely long. While 21 days is an idealized estimate regarding potential relaxation mechanisms, given that there would be many protons, and potentially also paramagnetic agents, in the vicinity of biological Posners, this finding suggests that ^{31}P nuclear spins within the Posner molecule could be particularly well-suited for maintaining spin coherence, and thus quantum information, for times that could be relevant to computing and brain function. An additional study on ^{31}P relaxation for spin singlets between two Posner molecules found an upper limit of 37 minutes for the intermolecular spin entanglement [130]. This type of coherence is different than the T_1 time calculated by Swift, but 37 minutes is still a "long time" in the world of nuclear spin relaxation.

Another implication from Swift's study was that it is enthalpically favorable to swap the central calcium ion for certain other cations, most notably two lithiums ions. This is particularly interesting given that lithium has been found to be a potent medication for bipolar disorder [131, 132], and multiple studies on animal behaviors have indicated that the two stable lithium isotopes (with different nuclear spins) have differential impacts on animal mania [133, 134]. Given that the mechanism for lithium's impact on brain behavior is unknown, Fisher proposed that this isotopic difference could be caused by different nuclear spin coupling to Posner molecules, thereby disturbing the pseudospin of the molecules that was introduced in Chapter 1 [51]. Differential lithium isotope effects are therefore a useful tool in probing the Quantum Brain theory, as the two isotopes have similar chemistries but different pseudospin couplings which could then impact Posner aggregation. This idea is expanded upon in Chapter 5 with experimental work aimed at investigating lithium isotope effects on calcium phosphate growth and stability.

There have also been some molecular dynamics (MD) studies on calcium phosphate nanoclusters, with the same group looking into both the stability of both calcium triphosphate [135] and Posner molecules [136]. In the former, calcium triphosphate was found to be energetically favorable when compared to a single calcium atom coordinated with one or two phosphate groups, but there was no discussion of how this nanocluster compared to a Posner molecule, beyond the observation that two such clusters could coordinate additional calcium ions to form a Posner molecule as a sort of secondary prenucleation cluster. The latter study found Posner-like clusters were stable at pH 7, although they found that many clusters retained protonated phosphate groups and would sometimes incorporate sodium ions into the place of the outer calcium ions. However, they did not go to slightly higher pHs, which are more biologically relevant and might lead to additional phosphate deprotonation, as MD simulations often struggle to deal with non-neutral pH solutions.

While we see that there have been great strides in our understanding of calcium phosphate prenucleation nanoclusters over the past 20+ years, there are still a number of open questions. From a solution chemistry perspective, such questions include: What conditions promote Posner molecules as opposed to calcium triphosphate? What causes these clusters to sometimes be stabilized in solution as opposed to rapidly aggregating into ACP or other larger calcium phosphates? And how does this behavior differ in a crowded biological environment such as mitochondria, where a number of proteins may also directly interact with Posner molecules?

There are also the questions about ^{31}P nuclear spins within Posners that directly relate to Fisher's Quantum Brain theory: What are the ^{31}P nuclear spin dynamics in Posner molecules - estimate for T_1 span multiple orders of magnitude? Can the ^{31}P states influence bonding rates of Posner molecules, as predicted by QDS? And how are these spin dynamics affected by the substitution of other atoms, such as lithium isotopes?

While this thesis will not be able to answer all of these questions, over the past six years significant effort has been put towards building an experimental platform capable of investigating Posner molecules and their properties. Thus, some of these questions will be directly addressed and answers proposed in the following chapters. In the final chapter, I will return to the outstanding questions that remain unanswered, and put forth future research directions to further probe the Quantum Brain theory.

Chapter 3

Phosphates form spectroscopically dark state assemblies in common aqueous solutions

3.1 Introduction

As a first step towards understanding the formation and behavior of Posner molecules, we studied the behavior of phosphate ions in aqueous solution. Beyond their importance in the Quantum Brain theory as a unit of the Posner molecule and a vehicle of ^{31}P nuclear spins, phosphates play a number of biological roles. Phosphate containing species are in constant flux throughout the phosphorus cycle and accumulate within the cells of all living organisms. Cellular energy is primarily harvested through the dynamical formation and breakage of phosphoanhydride chemical bonds of adenosine phosphates [137, 138]. Free phosphates and their subsequent assembly are also involved in bone formation and growth when complexed with calcium [139, 140, 141], but these assemblies processed are not fully understood, as discussed in depth in Chapter 2. Thus, an understanding

of the equilibrium between free phosphates and higher-order phosphate assemblies in the form of polyphosphates and phosphate clusters would provide further insight into the mechanisms involving biological energy storage and/or the engineering of biological structures, as well as shedding light on the feasibility of the Quantum Brain theory and informing the current understanding of the prenucleation behavior of ACP.

^{31}P nuclear magnetic resonance (NMR) offers useful information about the composition, dynamics, and structural properties of lipid membrane interfaces [142, 143, 144], phosphorylated biomolecules [145, 146, 147], polyphosphates [148, 149] and precursors of bone formation [123]. Additionally, understanding the behavior of ^{31}P nuclei in phosphate ions is the first step towards understanding the ^{31}P spin dynamics within the Posner molecule, which are hypothesized to be novel (in their long relaxation times) and therefore difficult to probe.

We performed ^{31}P NMR to investigate the native state of phosphate species as a function of temperature with the initial intent to gain a basic understanding of ^{31}P spin relaxation in phosphates and then subsequently study the formation processes of calcium phosphate clusters. In this process, we encountered peculiar ^{31}P NMR line broadening with increasing temperature of aqueous solution of pure phosphates. Such characteristics cannot be explained by the usual temperature dependent T_2 relaxation due to increasing molecular tumbling of small molecules with increasing temperature. ^{31}P NMR line broadening as a function of pH, phosphate concentration, and counter cation species has been described in the literature [150, 151, 152], however line broadening with increasing temperature has not been reported before.

Underscoring these unexpected observations, we present experimental results showing that phosphate containing species, including orthophosphate, pyrophosphate, and adenosine diphosphate assemble into hitherto unreported spectroscopically 'dark' species, whose fractional population increases with increasing temperature. This observation is

shown to be consistent with the dehydration entropy-driven formation of dynamic phosphate assemblies. ^{31}P NMR Chemical Exchange Saturation Transfer (CEST) reveals that phosphates assemble into species with broad spectroscopic signatures, whose population is in exchange with NMR-detectable phosphate species. A sub-population of these assemblies are also observed in cryogenic transmission electron microscopy (cryo-TEM) images to exhibit droplet-like spherical assemblies up to 50 nm in diameter. The discovery that common phosphate-containing molecules can readily assemble into higher order species in water under physiological conditions in the absence of biologically activated processes should be relevant to a variety of biological and biochemical processes that use phosphate containing species as building blocks, energy sources or reactants in an aqueous environment. These studies also reveal that ^{31}P spin relaxation within phosphates is much more complex than previously thought, adding to our understanding of the potential of the Posner molecule as a biological qutrit.

3.2 Results and Discussion

3.2.1 Unexpected NMR relaxation behavior

A series of ^{31}P NMR spectra were acquired of an aqueous solution of sodium orthophosphate at 10 mM concentration, pH 4.5 and as a function of temperature between 293 K and 343 K. Each spectrum consists of a single ^{31}P NMR line that shows significant broadening with increasing temperature, as shown in Fig. 3.1A. The full width at half maximum (FWHM) linewidth increases from 0.74 to 1.21 Hz, while the chemical shift only slightly changes from 0.14 to 0.58 ppm as referenced to 85% H_3PO_4 at 293 K. To test the consistency and generality of this observation, these measurements were repeated for solutions of orthophosphates at concentrations of 100 mM and 1 M, at varying pH

from 4 to 10, at field strengths corresponding to ^{1}H NMR frequencies of 400 MHz and 500 MHz, and for solutions of orthophosphates with sodium and potassium counterions, as shown in Fig. B.1, B.2, B.3, and B.4. Under every condition tested, the general trend of ^{31}P NMR line broadening with increasing temperature was observed.

To further explore this observation, we tested a series of phosphate-containing species in addition to orthophosphates, such as pyrophosphate, adenosine diphosphate (ADP) and adenosine triphosphate (ATP). While the extent of ^{31}P NMR line broadening with increasing temperature varies between the different species and solution conditions, the general trend of line broadening with increasing temperature persists for all phosphate containing species tested here (Fig. 3.1B), suggesting that there is a common underlying molecular mechanism for solvent-exposed phosphate groups.

This line broadening is surprising, as it is inconsistent with expected trends for small molecules, including ionic species. Increasing temperature should generally lead to motional narrowing of NMR resonances of small molecules as their tumbling rate increases. An exception to this trend would be a case where increasing chemical exchange rate leads to a transition from an intermediate to a faster exchange regime, where the chemical shifts of the two species significantly diverge, given that the linewidth is proportional to the square of the chemical shift difference. In such a case, however, one would normally observe the splitting of the broad line into additional narrow resonances at sufficiently high temperatures, which was not observed for any of the phosphate-containing species studied under a wide range of experimental conditions. An additional possibility is scalar relaxation of the second kind, which has been observed to lead to line broadening with increasing temperature [153]. However, for such a case the proton exchange rate should be of the same order of magnitude as the linewidth, i.e. on the order of a few Hz, which is not the case for our phosphate solutions, given that the second order rate constant for proton exchange between monobasic and dibasic phosphate is $1.45 * 10^{9}$ mole^{-1} l sec. $^{-1}$,

orders of magnitudes larger than Hz [154].

To further examine the nature of the underlying process leading to the observed line broadening and its temperature-dependence, we measured the ^{31}P NMR spin-spin relaxation rate, R_2, at varying temperatures from 293 K to 343 K. This allowed us to assess whether the ^{31}P NMR line broadening with increasing temperature originates from inhomogeneous broadening due to the presence of multiple distinct spectral components or lifetime broadening. The value for R_2 in Hz measured by the Carr-Purcell-Meibom-Gill (CPMG) [155, 156] sequence was compared to that extracted from the FWHM (following $R_2 = \pi \cdot$ FWHM) for a 10 mM and 100 mM solution of sodium orthophosphate, as shown in Fig. 3.1D. We found that the two showed comparable trends for broadening, with slightly higher (1-2 Hz) values for the FWHM-derived linewidth compared to that directly measured via R_2, likely due to field inhomogeneities and small temperature gradients. This observation verified that the phosphate linewidth is primarily broadened by the dynamical properties of a homogeneous spectral population. This correspondence was found consistently across all samples tested. The expected trend from Bloembergen-Purcell-Pound (BPP) theory [157] of decreasing R_2 with increasing molecular tumbling rate, i.e. temperature, is shown in Fig. 3.1C to contrast to the experimental trend shown in Fig. 3.1D.

The temperature-dependence of the spin-lattice relaxation rate, R_1, provides further information on the molecular-scale dynamical properties of these phosphate solutions. We measured R_1 for a serious of phosphate concentrations, and again, observed unexpected values and trends. As illustrated in Fig. 3.1C, small molecular species tumble in the 'fast' regime- where rotational correlation time is faster than the Larmor frequency- so that R_1 is expected to monotonically decrease with increasing temperature, and to be nearly identical with the R_2 values. Instead, we observe R_1 values for orthophosphates at concentrations from 10 mM to 100 mM that are as many as one to two orders of

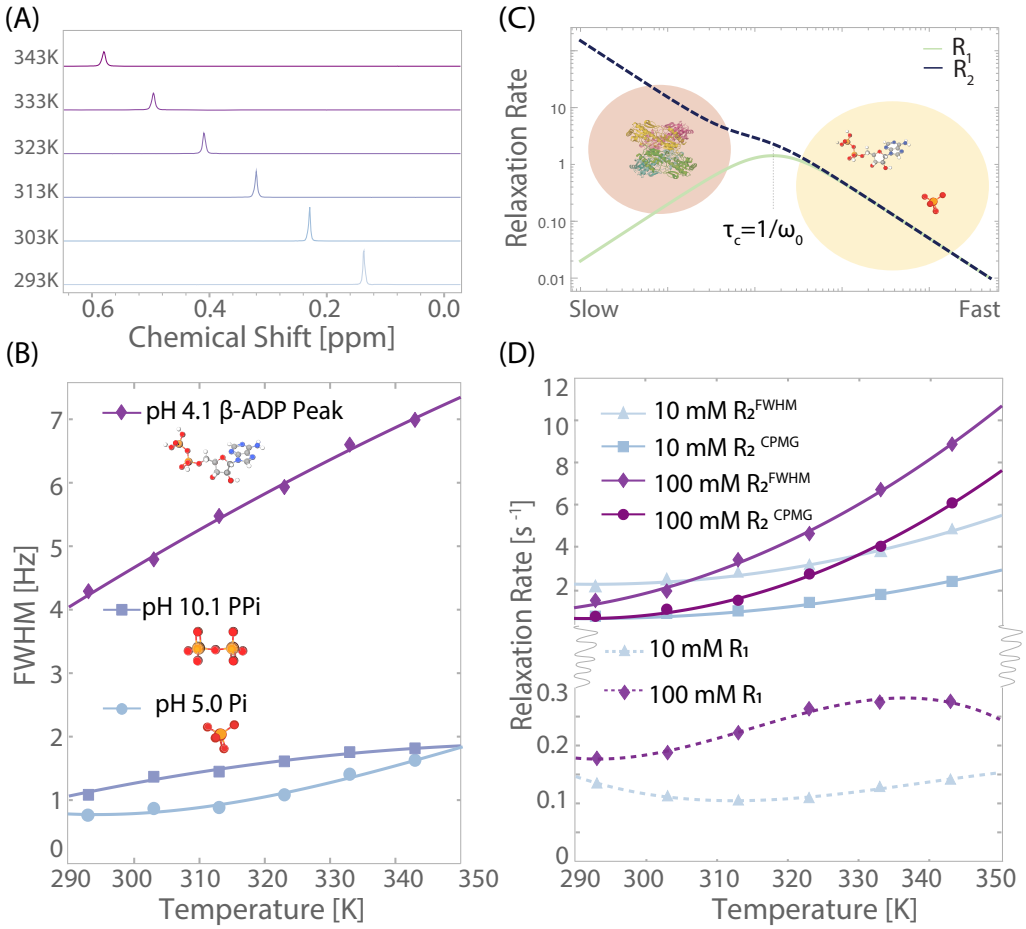

Figure 3.1: ^{31}P NMR results for phosphate-containing species. (A) 1D NMR spectra from 10 mM sample in (D) taken at every 10 K showing line broadening in orthophosphate. (B) Linewidths for orthophosphate, pyrophosphate, ADP, and ATP as a function of temperature showing monotonic increase with temperature. Solid lines are quadratic fits to data to guide the eye. (C) R_1 and R_2 curves as a function of molecular tumbling rate from Bloembergen-Purcell-Pound theory. Cartoons illustrate the approximate locations of ionic phosphate, ADP, and a standard protein based on tumbling rates. (D) R_2 as extracted from a CPMG pulse sequence and from FWHM for 10 mM and 100 mM monobasic sodium orthophosphate pH 4.5 as a function of temperature, showing monotonic increase in R_2 in each case. Solid lines are quadratic fits to data to guide the eye. R_1 for 10 mM, 100 mM, monobasic sodium orthophosphate pH 4.5 as a function of temperature showing different curve shapes as a function of concentration. Solid lines are cubic fits to data to guide the eye.

magnitude smaller than the R_2 values of the same samples. This observation suggests that the monitored phosphate species experience much slower dynamics than those of isolated orthophosphate monomers. Assuming a random field relaxation mechanism, the molecular tumbling correlation time would have to be larger than 10 ns, corresponding to a hydrodynamic diameter of larger than 4.4 nm according to the Stokes-Einstein relation in order to result in the observed difference between R_1 and R_2.

This consideration leads to the question of whether the states of phosphates giving rise to the observed properties correspond to phosphate assemblies. When examining the shape of change in R_1 with increasing temperature, we observed a subtle deviation from BPP theory for the solution of sodium orthophosphates at 10 mM concentration (Fig. 3.1D). The initial decrease of R_1 with temperature is expected, but not the observed increase at temperatures above 310 K. This latter observation is again consistent with a temperature-induced formation of larger phosphate assemblies, as such assemblies would lead to a lower rotational correlation time, effectively moving in the direction of the "slower" motion regime (towards the left of the x axis) as illustrated in Fig. 3.1C. A similar trend is observed for 10 mM potassium orthophosphate samples (see Fig. B.1).

The temperature dependence of R_1 for sodium orthophosphates at higher concentrations (100 mM) showed a local maximum with increasing temperature (Fig. 3.1D).This trend is again inconsistent with the dynamical properties of small molecules in solution. According to BPP theory, a local maximum in R_1 is expected only for species with rotational correlation times, τ_c, matching the inverse nuclear Larmor frequency, ω_0 (Fig. 3.1C). At 11.7 Tesla and a ^{31}P NMR frequency of $\frac{\omega_0}{2\pi}$ = 200 MHz, assuming a random field relaxation mechanism, we estimate τ_c = 800 ps following $\tau_c = \frac{1}{\omega_0}$. A rotational correlation time in this range implies a particle diameter of 2 nm for a spherical object according to the Stokes-Einstein relation. Regardless of the exact shape of the species, this size is several fold larger than that of monomeric orthophosphates [158].

The observed temperature-dependent trends in R_1 and R_2 are consistent with (a) the phosphate molecules assembling into larger species, whose tumbling rate lies in the slow motion regime, with correlation time τ_c exceeding ω_0, or (b) phosphate molecules being in exchange with spectroscopically invisible species that have much higher R_1 and R_2 rates. Explanation (b) would again be consistent with phosphate assemblies, since there are no other constituents than phosphate ions in the solution. Higher temperatures may facilitate the growth in population and size of such assemblies and/or accelerate the exchange, and hence enhance R_1 and R_2 of the detected ^{31}P NMR signal. It is also possible that monomeric phosphates coexist with spectroscopically invisible phosphate clusters across the temperature range tested, and that heating increases the relative abundance of this invisible species. Either scenario suggests the formation of larger phosphate assemblies, with enhanced populations and/or exchange rates at elevated temperatures, yielding much greater R_2 values compared to R_1 and consistent with our observed trends in relaxation with temperature. Notably, after cooling the sample that was heated back down to its initial temperature, the relaxation rates return to their initial values (Fig. B.5), suggesting that the assembly formation is reversible.

If larger assemblies are forming, it is important to consider their nature, and in particular the interactions leading to their formation. One possibility is that the new assemblies are polyphosphates formed by the enhanced formation of P-O-P bonds at elevated temperatures. The ^{31}P chemical shift for phosphates is known to shift by approximately -10 ppm with each P-O-P bond formed and by a maximum of 5 ppm from the unprotonated to triply protonated states [159, 160]. This is inconsistent with our observed chemical shifts that move systematically downfield, but only very slightly, by a maximum of 0.5 ppm when the temperature is increased from 293 K to 343 K. Hence, the observed chemical shift change is too small to be attributed to covalent P-O-P bond formation. The observed 0.5 ppm chemical shift change could instead be the result of changes in the

equilibrium P-O bond length, potentially induced by non-covalent association of phosphate molecules. Such changes could be mediated by hydrogen bond interactions that, in turn, can be modulated by changes in phosphate hydration. Notably, all four oxygens of the phosphate group can serve as hydrogen bond donors or acceptors, depending on the protonation, hydration and partial charge state of the group, hence allowing for multivalent interactions that can give rise to the formation of larger assemblies, while still maintaining rapid exchange with ionic phosphates and small clusters held together by weak interactions. In any case, the species forming must either have the same chemical shift as the orthophosphate ions and/or be so broad as to be rendered spectroscopically invisible.

3.2.2 Indirect observation of phosphate assemblies by ^{31}P CEST

To test whether the phosphate species are in exchange with a spectroscopically dark population, we performed chemical exchange saturation transfer (CEST) experiments. CEST typically provides a means of identifying signatures of exchangeable species with distinct chemical shifts from the visible species, but below the direct NMR detection limit. This effect is achieved by saturating a selected region in the spectroscopically invisible region of the spectrum, followed by the detection of the (visible) signal of a major species (in this case, monomeric phosphates) that is in exchange with the species below the NMR detection limit. Repeating these experiments with different saturation frequencies across the complete spectral region and saturation power permits scanning of an entire spectrum for potentially exchanging species. This procedure has been widely employed, for example, to identify weakly populated states of peptides and proteins whose protons are in exchange with water[161, 162], and in this context is often referred to as DEST (for dark state exchange saturation transfer)[163]. The sensitivity enhancement

effect for the dark species is achieved because exchange can occur many times during the saturation pulse, and thereby transfer saturation levels between the visible and invisible species repeatedly. In the CEST experiment of this study, we recorded ^{31}P NMR spectra of the visible ^{31}P NMR signals following rf irradiation (with nutation frequency of 150 Hz for 5 s) at a specified resonance frequency in what can be seen as a one-dimensional pump-probe experiment. Here, the pump frequency is stepped through a frequency range of approximately 8000 Hz, centered around the one visible ^{31}P NMR peak. In this fashion, CEST can test for the existence of spectroscopic dark states that are in exchange with phosphate species at frequencies within the scanned range. A plot of the detected intensity vs. saturation frequency offset is called a Z-spectrum.

Fig. 3.2B,C shows the both the measured (solid lines) and the simulated (dashed lines) Z-spectra as a function of temperature of a 100 mM orthophosphate solution. It is seen clearly that the widths of the dips in the Z-spectra increase with increasing temperature, which is consistent with the unexpected trend observed with the R_2 and linewidth data.

In the absence of exchange, one expects the width of the dip in the Z-spectrum (at half maximum) to be approximately a factor two times the rf nutation frequency (here 150 Hz) [164]. In all cases for CEST measurements (both as a function of temperature and as a function of irradiation power), we observed the dip widths to be significantly larger (a factor of 3-10 larger than the nutation frequency) than the expected two-fold the nutation frequency (see Fig. B.10). This finding is a clear sign that there must be significant underlying exchange processes with spectroscopically silent species, and that these processes change with temperature.

These results further corroborate the assumption that exchange occurs with a population exhibiting a broad spectroscopic signature, which is invisible to direct spectroscopic detection. The relative population of this spectroscopically 'dark' species may also be

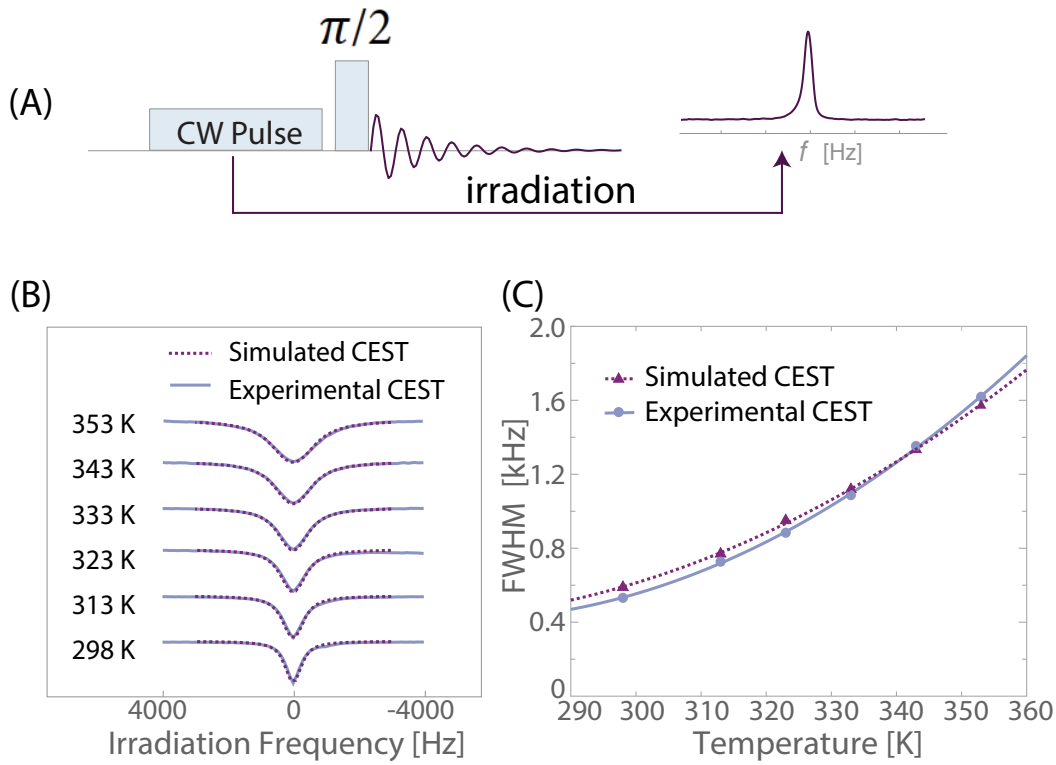

Figure 3.2: ^{31}P CEST results for 100 mM orthophosphate (pH=4.5). (A) CEST pulse sequence. (B) The experimental and simulated CEST Z-spectra as a function of temperature with 150Hz of the irradiation pulse power. (C) The width at half height of both the experimental and simulated Z-spectrum dips from (B) as a function of temperature. The solid and dashed line represent a quadratic fit to data as a guide for the eye.

increasing with increased temperature. When the solutions are cooled back down to 298 K after heating, the Z-spectrum dip width returns to the originally measured value (Fig. B.6), indicating reversible assembly formation. Similar CEST results were observed for a range of pH values of orthophosphate solutions (Fig. B.7) and for ADP (Fig. B.8), suggesting that this behavior is common among several phosphate-containing molecular species in aqueous solution.

In order to further substantiate the hypothesis and generate a potential model, simulations were performed that could simultaneously satisfy the values and temperature trends of R_2 and CEST data. For the simulation, a two-pool model was used, with A referring to the detectable pool (phosphate monomers) and B to the spectroscopically silent pool (the assemblies). The model used separate R_1 and R_2 for pools A and B, exchange rate constants for the forward and backward interconversion processes $A \longleftrightarrow B$, and the relative populations of the pools, considering first-order kinetics. The rate constants were assumed to be of Arrhenius type, and the forward rate constant was parameterized using an Arrhenius pre-factor k_0 and activation energy E_a. The change of enthalpy ΔH_{PA} and change of entropy ΔS_{PA} for assembly formation derived from this simulation were then used to find the assembly population, p_B, using the Boltzmann factor $p_B = \exp(-\Delta G_{PA}/(RT))/(1 + \exp(-\Delta G_{PA}/(RT)))$, where $\Delta G_{PA} = \Delta H_{PA} - T\Delta S_{PA}$. The temperature dependence entered through the $T\Delta S_{PA}$ term, while ΔH_{PA} and ΔS_{PA} were assumed constant. At each temperature, these relationships were used to calculate the forward and backward exchange rates, and the McConnell equations solved iteratively to satisfy the experimental R_2 and CEST data using the Spinach software package [165].

Simulations of the R_2 data as a function of temperature of the 100 mM NaH_2PO_4 sample (at pH=4) led to the following parameters to describe the exchange process: $\Delta H_{PA} = 25$ kJ/mol, $\Delta S_{PA} = 30$ J/(mol K), $k_0 = 20,000$ s^{-1}, and $E_a = 10$ kJ/mol. We

then calculated the relative fraction for the B population, p_B, as described earlier. The forward and backward exchange rates are obtained via $k_f = k_0 \exp(E_a/RT)$, and $k_b = k_f(1-p_B)/p_B$, in steady state. For CEST simulations, R_1 was set equal to the measured values (shown in Fig. 3.1) for both pools (after verifying that setting $R_1^B = 0.1R_1^A$ to $10R_1^A$ did not change the quality and results of the fit), and R_2^A set equal to R_1^A, assuming a fast motion regime for the small molecular entity. Modeling of the R_2 data indicated that $k_f \gg p_B \Delta R_2$ is likely, where $\Delta R_2 = R_2^B - R_2^A$. In this regime, $R_2 \approx p_B \Delta R_2$ [166]. We therefore used this expression to determine the R_2^B values for the CEST simulation by using the fitted p_B values, the experimental R_2 values and relying on $R_1^A = R_2^A$, i.e. by equating R_2^A to the experimental R_1 values. These values ranged from 450 to $1,000$ s^{-1} over the experimental temperature range (increasing with increasing temperature), corresponding to linewidths exceeding 1400 Hz that hence is easily beyond the detection limit.

Using this approach, a consistent model was found to fit concurrently the experimental R_2 and CEST data (see Fig. 3.2 and Fig. B.10). The key takeaway is that increasing temperature leads to either larger or less mobile assemblies, as reflected in increasing R_2^B with temperature (see Fig. B.11), an increase in both k_f with increasing temperature (see Fig. B.10A), with the rates spanning 350-660 Hz. Most critically, the model that describes the R_2 and CEST data finds the fractional population of the assemblies, p_B, to be very small, but to grow with temperature (Fig. B.10C), with $p_B = 0.0013$ of phosphates at 293 K and 0.0073 at 353 K. While the absolute value of p_B in a dilute solution of monophosphates is small, the size of the assembly (the B pool) may comprise of a very large number of monomers (the A species), as reflected in the extremely high R_2^B rates. Assemblies formation, even with a small p_B, can have a significant impact on biological assemblies between phosphate-containing species in closer proximity.

3.2.3 Cryo-TEM

While there is compelling evidence for assembly formation, the previous measurements did not provide direct observation of the assemblies due to their spectroscopically dark nature. We hence used cryogenic transmission electron microscopy (cryo-TEM) to determine whether the phosphates assemble into large and persistent enough clusters to be imaged. Cryo-TEM was performed on ADP solutions that were vitrified after heating for at least 48 hours. Phosphate-containing solutions tested showed evidence of assemblies forming at diameters ranging from 30-50 nm in diameter (Fig. 3.3A,B, Fig. B.12). This is in contrast to a 500 mM KCl control solution, where a majority of features were at diameters of 50 nm and greater, consistent with consensus within previous cryo-TEM literature establishing that the most abundant form of ice artifacts are at sizes >50 nm [167, 168]. Given that these samples were prepared under identical conditions, we take this difference in the 30-50 nm region of the particle size distributions between the phosphate-containing solutions and the KCl control to indicate the presence of phosphate assemblies. Amongst the conditions tested, the abundance of assemblies appeared higher in solutions heated at 343 K compared to solutions that are unheated or salt controls without phosphate present (Fig. B.13). Additionally, ADP samples from different sources, and prepared on different days, showed an abundance of these features (Fig. 3.3A,B and B.12). Such analysis of cryo-TEM micrographs cannot provide quantitative analysis of the whole sample, given the nature of the thin film of water that forms before vitrification that can affect which particles may be imaged. Still, this methodology provides evidence that these features are not artifacts of sample preparation. We also found that for samples of 100 mM and 1 M sodium monophosphate the size distribution of structures is independent of phosphate concentration (Fig. B.14), providing additional evidence that these are equilibrium structures. Notably, the entire phosphate-containing

population is part of or is in exchange with the assemblies, given the homogeneously broadened nature of the ^{31}P NMR line. This suggests that the monomeric ADP and monophosphate populations are at thermodynamic equilibrium with the assemblies that may exist as liquid droplets, given their spherical shape. The phosphate assembly may be driven by liquid-liquid phase separation. However, further validating such hypothesis is outside the scope of this study, given that the assemblies evade quantitative analysis.

3.2.4 Molecular Dynamics Simulations

We next used molecular dynamics (MD) simulations to probe whether monomeric phosphate species can form stable clusters under the relevant aqueous solution conditions. We simulated three different solutions of orthophosphates: HPO_4^{2-}, $H_2PO_4^-$, and a 1:1 mixture of HPO_4^{2-} and $H_2PO_4^-$ using a modified GAFF forcefield [170] and TIP3P water [171]. The simulated systems each contain 100 total orthophosphates, enough Na^+ ions to neutralize them (200, 100, and 150, respectively), and water molecules to solvate to approximately 1 M orthophosphate concentration (4759, 4852, 4801 water molecules, respectively). We also simulated two less concentrated systems (∼78 mM), comprising (1) 3 HPO_4^{2-} ions, 6 Na^+ ions, and 2149 water molecules and (2) 3 $H_2PO_4^-$ ions, 3 Na^+ ions, and 2149 water molecules to more carefully probe the temperature-dependent water-phosphate, phosphate-phosphate, and counterion-phosphate interactions. Additional details regarding the systems and simulation workflow are provided in Table B.1). At 343 K, the HPO_4^{2-} system shows a strong tendency to assemble, forming a cluster comprising all 100 phosphate ions in the simulation box. The cluster size distribution for the HPO_4^{2-} system, represented as the fraction, $P(N)$, of phosphate ions in clusters of size N_{clust}, is therefore peaked at the maximum number of HPO_4^{2-} ions of 100 (Fig. 3.3C). We hypothesize that the equilibrium cluster size is larger than accessible by atomistic

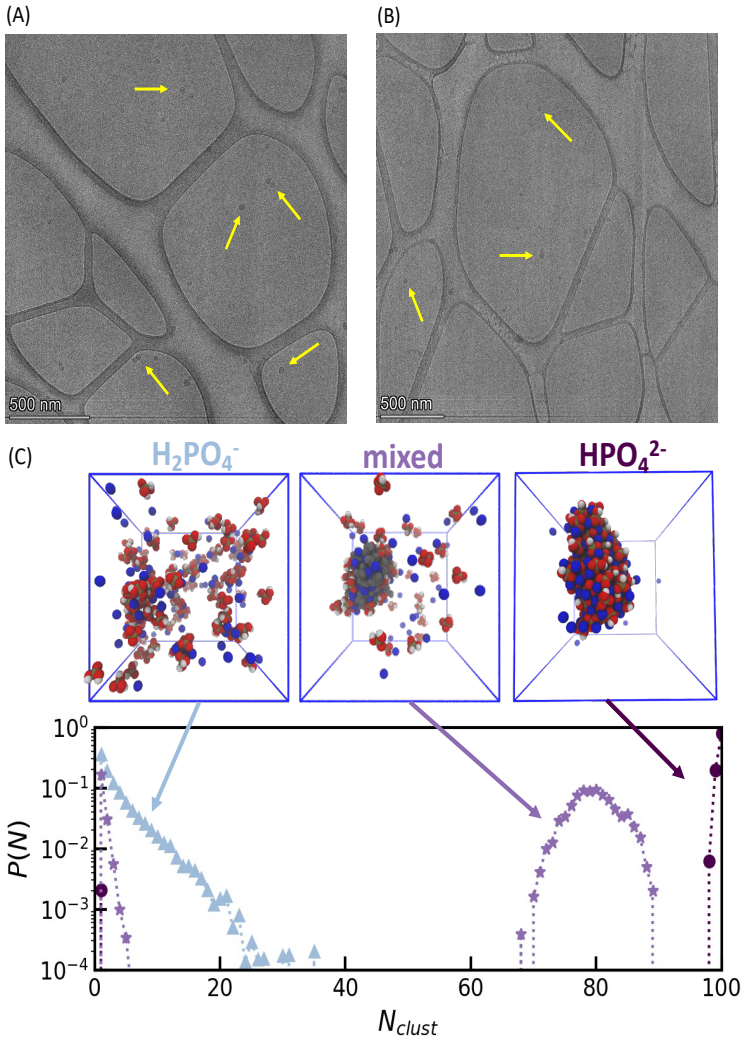

Figure 3.3: Evidence of phosphate assemblies from TEM and MD simulations. (A, B) TEM images of phosphate assemblies (yellow arrows) after heating phosphate solutions show droplet-like features forming at 25-50 nm in size. Samples were from different sources and prepared on different days. (A) 100 mM potassium ADP heated to 343 K before vitrification. (B) 100 mM sodium ADP heated to 343 K before vitrification. (C) Cluster size distributions from MD simulations at 343 K show the fraction, $P(N)$, of phosphate ions in a cluster of size N_{clust}. The insets show snapshots of phosphate assemblies (red and white) and sodium ions (blue) from the simulations. The cluster size distribution and snapshots show that HPO_4^{2-} strongly assembles in contrast to $H_2PO_4^-$. When $H_2PO_4^-$ is mixed with HPO_4^{2-}, the latter induces clustering of $H_2PO_4^-$. In this mixed system, the HPO_4^{2-} ions are grayed out to highlight the clustering of $H_2PO_4^-$. Simulation snapshots are visualized using Visual Molecular Dynamics.[169]

MD. This result is consistent with the observation of large phosphate assemblies visible to cryo-TEM, giving rise to distinct NMR spectral and relaxation properties. Interestingly, the $H_2PO_4^-$ system shows a much weaker tendency to assemble, with a peak in the cluster size distribution at $N_{clust} = 1$, indicating a preference to remain unaggregated at these conditions. However, in the mixed system, the presence of HPO_4^{2-} induces assembly of $H_2PO_4^-$ ions, and the system forms an assembly that comprises all 50 HPO_4^{2-} in the simulation box and some $H_2PO_4^-$ (Fig. B.16B-D). The three systems exhibit qualitatively the same behavior at 293 K (Fig. B.16A). The simulations are limited to system sizes smaller than the experimentally observed assemblies, as well as constant ionization state (as opposed to constant pH), which limits our ability to draw conclusions regarding the temperature dependence and size distributions of the observed clustering behavior. However, the MD simulations do confirm that orthophosphates cluster under comparable conditions as experimentally probed.

In addition, the sodium ions were observed to be involved in the phosphate assemblies by the MD simulations, and therefore the linewidth of sodium in the presence and absence of phosphate was investigated. While the ^{23}Na NMR line was found to narrow with increasing temperature, the ^{23}Na linewidth was broader for samples of NaCl with phosphate present as compared to NaCl without phosphates at both 298 K and 343 K (Fig. B.17). This observed increase in linewidth for ^{23}Na when phosphate is added to solution is consistent with the sodium ions also being incorporated into the phosphate assemblies. Although the ^{23}Na still narrows with temperature, this can be explained by the mechanisms that traditionally lead to line narrowing at higher temperature (such as larger fluctuations in electric field gradients and increased molecular tumbling rates) overcoming effects of a larger population of sodium ions being incorporated into assemblies. Since the relaxation mechanisms of the sodium, in monomer or assembled state, are quite different from the mechanisms for phosphates [172], the overall effect of increased

temperature on ^{23}Na NMR could still be line narrowing, but with different magnitudes of linewidths depending on whether phosphates are present to form assemblies.

3.2.5 DOSY NMR

Having established that larger phosphate assemblies exist in solution, we next explored the potential mechanisms of their assembly and, in particular, the temperature-dependent behavior. We performed pulsed field gradient (PFG) NMR, specifically Diffusion Ordered SpectroscopY (DOSY), to measure the self diffusion coefficients of the ^{31}P NMR signal-bearing species, and hence their hydrodynamic diameter. DOSY measurements were performed on a 100 mM sodium orthophosphate solution of pH 4.5 at 293 K, 343 K, and again at 293 K after cooling in order to assess the reversible formation of any structures at elevated temperatures. The results show that the phosphate species in solution diffuse with a single translational diffusion coefficient, as demonstrated by the linear relationship between Log(ψ) and the square of the gradient strength, where ψ is the signal attenuated by molecular motion along the gradient axis (Fig. 3.4A) [173]. This observation of a uniform diffusion coefficient did not change with increasing temperature. However, the diffusion coefficient significantly increased from $7.5 * 10^{-10}$ m^2/s at 293 K to $3.2 * 10^{-9}$ m^2/s at 343 K. We confirmed that this increase is not due to convection effects by comparing diffusion values measured with a convection-compensated pulse sequence (Fig. B.18), as well as in the presence and absence of capillaries added to the sample tube to disrupt convective flow (Fig. B.19) [174]. To convert these diffusion coefficients to hydrodynamic diameters, we used the Stokes-Einstein relationship to account for the increased thermal energy and the decreased viscosity of water at elevated temperature. The extracted (temperature-corrected) hydrodynamic diameters for orthophosphate ions show a reversible and significant decrease by $\sim$1.8 Å at 343 K compared to 293 K (Fig.

3.4B), suggesting partial dehydration of hydrated orthophosphate ions in water. Similar increases in the diffusion coefficient and decreases in the hydrodynamic diameter were observed for monophosphate ions in 100 mM and 1 M potassium phosphate samples and 1 M sodium phosphate samples (Fig. B.20 and B.21).

How do we reconcile the observation of assembly of orthophosphates according to ^{31}P NMR relaxation and CEST studies with the apparent decrease in the hydrodynamic radius of orthophosphate molecules, implying the partial dehydration of the detected phosphate ions at elevated temperatures? Presumably, the partially dehydrated phosphate groups can more strongly interact with other phosphate groups through stronger hydrogen bond formation. Hence, they may more readily assemble into, and exchange with, dynamic phosphate clusters. It is known that a single deprotonated orthophosphate moiety, the $H_2PO_4^-$ ion, carries 11 water molecules within its hydration shell at infinite dilution (the HPO_4^{-2} ion carries 20 water molecules) [175]. The ^{31}P DOSY result for samples of pH 4.2, where the large majority of the population is in the $H_2PO_4^-$ protonation state, suggests a decrease in the hydrodynamic diameter from 6 Å to 4.2 Å. This change in hydrodynamic radius is consistent with a decrease in hydrodynamic volume by 70 Å^3. Assuming a water radius of 1.4 Å[176], this result suggests a loss of 6 hydration water molecules upon heating, yielding a total of 5 remaining hydration water molecules per orthophosphate at 343 K. Given that the temperature dependent characteristics of ^{31}P NMR linewidth and relaxation data were observed across a wide pH range from 2 to 11, we expect both $H_2PO_4^-$ and HPO_4^{-2} ions to experience loss of hydration water with increasing temperature.

To further validate this experimental analysis based on DOSY, we performed MD simulations of less concentrated HPO_4^{2-} and $H_2PO_4^-$ systems discussed earlier. MD calculations show a decrease of water coordination from 13.4 to 13.1 per HPO_4^{2-} molecule and from 16.5 to 15.7 per $H_2PO_4^-$ with increasing temperature from 293 K to 343 K

(Fig. B.15C), corresponding to the range of temperatures experimentally probed. These results are qualitatively consistent with the trends observed experimentally. Although this average change is relatively small, it is being driven by very large changes in hydration for the phosphates forming assemblies. Additionally, the decrease in the hydration number of orthophosphates is less dramatic in the MD simulations, as the computational analysis does not probe hydrodynamic radii, but rather local density.

Is DOSY then detecting the phosphates within clusters directly? As discussed, phosphorus spins in these clusters undergo rapid relaxation due to their slower tumbling rates, and thus have very broad resonance lines, largely invisible to ^{31}P NMR. Thus, DOSY measurements should only be sensitive to the free phosphate ions that exist in equilibrium with these larger, spectroscopically dark, assemblies. The DOSY results reveal that free phosphate ions exchanging with the phosphate assemblies are more dehydrated at elevated temperatures, and hence potentially have a greater tendency to assemble into larger clusters.

3.2.6 Examining entropy-driven assembly

What then is the driving force for the formation of soluble, non-covalent, phosphate assemblies at equilibrium that are reversibly promoted at elevated temperature? Considering the Gibbs free energy for assembly, ΔG_{PA}, an increasing tendency to assemble ($\Delta\Delta G_{PA} < 0$) at higher temperature requires that ΔS_{PA} for assembly be positive, so that the entropic contribution lowers the free energy of assembly as temperature is increased, since generally ΔH increases (i.e. is less favorable) with increasing temperature [177]. The thermodynamic parameters found in fitting our experimental R_2 and CEST data of a $\Delta H_{PA} = 25kJ/mol$ and $\Delta S_{PA} = 30$ J/(mol K) is consistent with an entropy-driven assembly. However, considering the fit value of $\Delta H_{PA} = 25kJ/mol$ and a 0.6 % population

growth from 20 to 70 °C for a NaH_2PO_4 sample, the largest ΔH extracted would amount to only 0.002 J/°C/g solution for assembly formation of a 1 M potassium orthophosphate sample, rendering direct experimental verification of these thermodynamic values on our differential scanning calorimetry instrument unfeasible. Nonetheless, an extensive set of experimental data provided strong evidence for a favorable phosphate assembly with increasing temperature, implying that the phosphate assembly is enhanced by entropy gain with increasing temperature.

Possible sources for this putative entropy gain are depletion interactions, including excluded volume effects, counterion release, and/or dehydration of the phosphate moiety[178]. Excluded volume interactions between phosphates would not be expected to reduce the hydrodynamic diameters of individual phosphate monomers, and species with overlapping volume would co-diffuse, resulting in slower diffusion, neither of which effects are observed by DOSY. Another commonly expected source of entropy gain upon assembly of charged species is the release of bound counterions, however potassium and sodium ions are not strongly bound to phosphate, making its release a less likely source for significant entropy increase. This assessment is consistent with our MD simulation results, which show that there is no significant change in the number of counterions coordinated with HPO_4^{-2} and a slight increase in the counterion coordination number for $H_2PO_4^-$ in the less concentrated (∼78 mM) systems (Fig. B.15I). This analysis further supports our expectation that the phosphate-cation interaction is weak, making counterion release an unlikely driver of phosphate assembly. Furthermore, the observed changes in the hydrodynamic diameter of orthophosphates with increasing temperature as measured by DOSY are very similar between potassium and sodium phosphate samples (Fig. 3.4A and Fig. B.21). Since sodium and potassium ions are approximately 1 Å different in size [179], a difference in the change of the hydrodynamic diameter is expected if counterion release was a major contributor to these observed size changes of

orthophosphates.

Hence, the most likely source of increase in the total entropy is the shedding of water that is more strongly associated with the phosphate ions than with bulk water, also referred to as the hydration shell. Water forms networked hydrogen bonds and strongly solvates phosphate anions, offering ample opportunities for entropy increase upon its partial release. DOSY experiments and MD simulations confirm that water molecules are released to bulk when increasing the temperature from 293 to 343 K. In a recent study, dehydration-driven entropy increase has been shown to be a primary driver of liquid-liquid phase separation induced by polyelectrolyte assembly processes in water [180].

3.2.7 Manipulation of depletion interactions

Since the experimental results so far suggest dehydration entropy as the driver of phosphate assembly, we designed further experiments to deliberately modulate the phosphate-water interactions by known factors. Since we established a viable interpretation for the change in ^{31}P NMR linewidth and relaxation data, we rely on these readouts to evaluate phosphate assembly formation as a function of temperature.

One can amplify dehydration by the addition of hydrophilic molecular crowders or salting-out salts along the Hofmeister series. The introduction of molecular crowders is a common technique used to reduce the volume of water available for the other molecules of interest in aqueous solution, thus increasing the effective concentration of the dissolved molecule [180]. A commonly used molecular crowder is polyethylene glycol (PEG); its strong affinity for water over the temperature range of interest is known to drive dehydration and increase the effective concentration of other molecules in solution [181]. As expected, the ^{31}P NMR linewidth at temperatures ranging from 293 K to 343 K increased

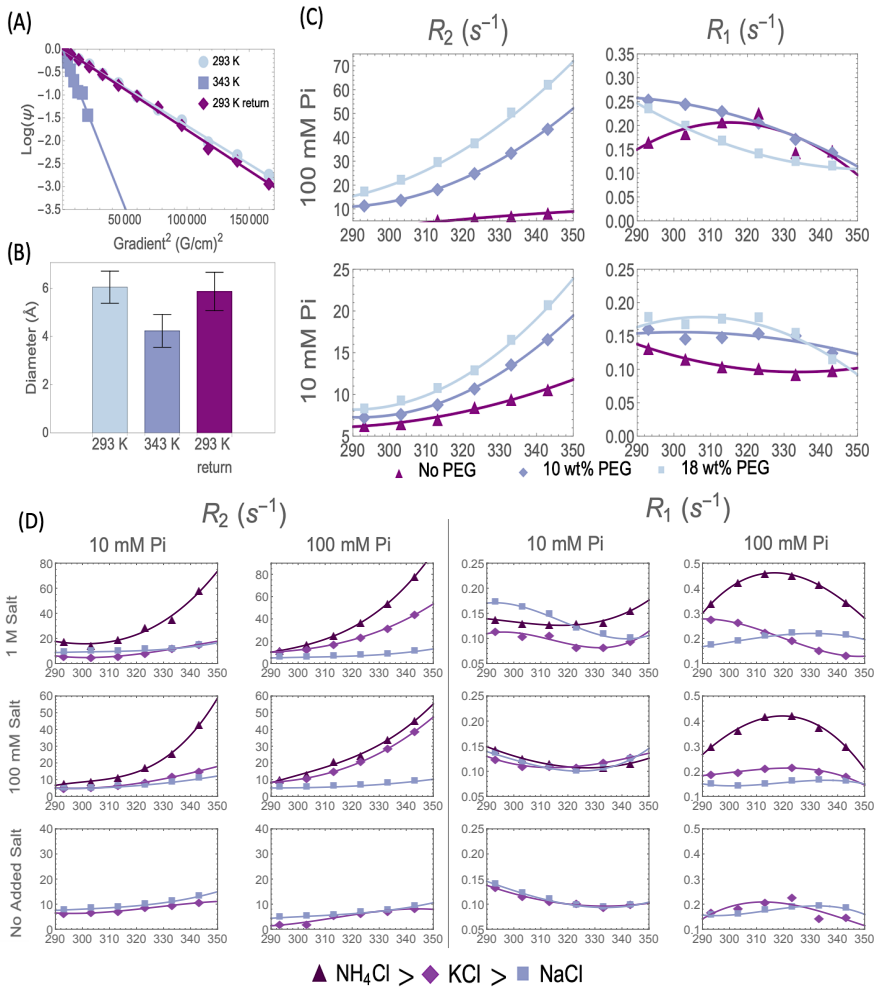

Figure 3.4: Evidence of entropically driven assembly. (A) 100 mM sodium phosphate at pH 4.2 ^{31}P DOSY fits of Log(ψ) vs gradient strength squared show a linear relationship, indicating that a single diffusion coefficient can describe behavior of phosphorous entities contributing to the observed NMR line. (B) Hydrodynamic diameters extracted from the diffusion coefficient from fits in (A). (C) R_2 and R_1 for potassium phosphate pH 4.5 in the presence of 6k MW polyethylene glycol (PEG) at varying PEG concentrations. Solid lines are quadratic fits to data to guide the eye. (D) R_2 and R_1 for orthophosphate pH 4.5 samples at 10 and 100 mM, with varying types of cationic salt chlorides and concentrations. Salt added samples are sodium phosphate salts, while no additional salt samples shown are monophosphate salts with the corresponding potassium or sodium cationic species. Solid lines are third order polynomial fits to data to guide the eye. The R_2 trends follow the predicted trends for the Hofmeister series, while R_1 shows little difference at 10 mM phosphate concentration, but significant differences for different salts at 100 mM.

for phosphate solutions at both 10 mM and 100 mM concentrations with increasing PEG concentrations at 10 wt% and 18 wt%. In order to evaluate whether these observed trends are due to a contrast in solution viscosity, R_2 relaxation extracted from FWHM for two samples of 100 mM potassium phosphate, with and without 18 wt% PEG, was plotted as a function of solution viscosity (Fig. B.22). The R_2 relaxation rates of the two samples are not superimposed, indicating that the observed increase in linewidth is not accounted for solely by changes in solution viscosity from the addition of PEG. This observation is consistent with the interpretation that PEG enhances dehydration of phosphates and facilitates phosphate clustering.

Dehydration can also be modulated by the addition of various salts according to the Hofmeister series [182]. This series is used in biological systems to induce salting-out (precipitation) or salting-in (dissolution) of proteins, with NH_4^+ on one salting-out end and Na^+ on the other salting-in end [183] of the series. While phosphate clusters under the here tested experimental conditions are not precipitated out of solution, the magnitude of dehydration, and thus the exchange with and/or formation of assemblies, should increase with salting-out salts and decrease with salting-in salts. To test our hypothesis of dehydration-driven phosphate clustering, we added a variety of cations that enhance the salting-out tendency in the order $NH_4^+ > K^+ > Na^+$. ^{31}P NMR linewidths were measured between 293 K and 343 K for orthophosphate solutions at 10 mM and 100 mM in the presence of added chlorine salt of three different cations at 100 mM and 1 M concentrations, as well as in the absence of added salts. The extracted linewidths show that the addition of NH_4^+ causes the greatest line broadening, followed by K^+ and then Na^+, at all phosphate concentrations, salt concentrations, and temperatures (Fig. 3.4D). These results are in agreement with the predicted trend of the Hofmeister series when considering line broadening as a proxy for dehydration-induced clustering. While the R_1 results are more difficult to interpret, given the non-monotonic trend, we see that

the salts clearly change the shape and magnitude of R_1 when phosphate and/or salt concentration is high enough (Fig. 3.4D). This finding is again in agreement with the hypothesis that the addition of salting-out salts impact the tendency of phosphates to form assemblies.

Molecular crowders and salting-out cations both serve to increase the total entropy of dehydration, further facilitated by elevated temperatures, consistent with the ^{31}P NMR results. While chemical exchange between phosphate species of different protonation states or scalar relaxation may potentially explain some of the observed anomalous ^{31}P NMR line broadening behavior with increasing temperature, these alternative hypotheses do not provide comprehensive explanations for the full range of results provided here. The proton exchange rate for a 100 mM phosphate sample is 10^7 Hz, many orders of magnitude larger than the strength of proton-phosphorus scalar couplings, indicating that scalar relaxation does not dominate. Similarly, a model of chemical exchange between differently protonated phosphate groups cannot explain the order of magnitude discrepancy between R_1 and R_2. This order of magnitude difference between R_1 and R_2 also indicates that paramagnetic impurities could not be causing the enhanced relaxation, as for phosphate and paramagnetic species tumbling freely in solution one would expect R_1 and R_2 to be close to identical. Additionally, these potential explanations fail to explain the other results shown, such as the broad CEST lines, the cryo-TEM images, or the multiple experiments indicating that phosphate dehydration plays a role in modulating ^{31}P NMR relaxation properties.

3.3 Conclusion

Taken together, our experiments present comprehensive evidence for the presence of phosphate assemblies in aqueous solutions in dynamic exchange with free phosphate. ^{31}P

NMR relaxation and CEST results both show signatures of the presence of these phosphate assemblies, whose population grows with increasing temperature. Cryo-TEM offers visual affirmation for the presence of large phosphate assemblies in both monophosphate and ADP solutions, with structures consistent with condensed spherical droplets. ^{31}P DOSY measurements, as well as the impact of PEG and cationic salts, indicate that dehydration of phosphate species is driving the formation of these assemblies. Even if the number of water molecules released per orthophosphate molecule was small, its effect on entropy gain driving the assembly formation can be very significant, given that the assembly consists of a large number of orthophosphates according to our model derived from R_2 and CEST data, cryo-TEM data and MD simulations.

Our results suggest that this dehydration-driven clustering of phosphates may be present in numerous species with exposed phosphate groups at a wide range of commonly used solution conditions, including those of biological relevance. Such clusters could have implications for biological phosphate transport and regulation, as well as aggregation events involving phosphates such as calcium phosphate nucleation and growth. Therefore, these assemblies should be added in the ACP phase diagram introduced in Chapter 2 and considered when seeking conditions that lead to the presence of stable Posner molecules, as well as in more general *in vivo* and *in vitro* experiments involving phosphate group-containing biomolecules. Initial investigations on the implications of these phosphate assemblies on calcium phosphate prenucleation behavior will be discussed in Chapter 7.

The presence of these assemblies also reveals complexity in phosphate ^{31}P spin relaxation. Since exchange with the assemblies induces faster spin relaxation, phosphate monomers may have longer spin relaxation times than previously measured. Such results add intrigue to the possibility of the Posner molecule, with its cage of spin 0 calcium atoms adding additional protection from relaxation, having long spin relaxation times that could allow it to function as a biological qutrit.

3.4 Materials and Methods

Potassium phosphate monobasic (MW 136.09) and sodium phosphate monobasic (MW 119.98) were acquired from Fisher Scientific. Sodium phosphate tribasic (MW 163.94) was acquired from Acros Organics. Potassium pyrophosphate (MW 330.34) was acquired from Sigma-Aldrich. Adenosine 5'-diphosphate orthopotassium salt dihydrate (MW 501.32) was acquired from Alfa Aesar. Adenosine 5'-triphosphate disodium salt hydrate (MW 551.14 anhydrous) was obtained from Sigma. Polyethylene glycol (MW 6K) was acquired from Fluka. Potassium chloride (MW 74.55), sodium chloride (MW 58.44), and ammonium chloride (MW 53.49) were acquired from Fisher Chemical. All samples prepared at room temperature. When not explicitly mentioned, the pH values were adjusted to 4.4 with HCl and NaOH to coincide with the native dissolved pH values found for monobasic orthophosphate. Every sample was dissolved in 600 to 700 uL of 90% Milli-Q water and 10% D_2O for locking purposes.

Adenosine 5'-diphosphate sodium salt (MW 427.20), sodium phosphate dibasic (MW 141.96), and coenzyme A sodium salt hydrate (MW 767.53) used for CEST were acquired from Sigma-Aldrich. All samples prepared at room temperature. The pH values of the solutions were adjusted to 4.4 with HCl and NaOH in order to make them coincide with the native dissolved pH values found for orthophosphate. The real concentrations of the solutions were determined from the absolute integrations of the ^{31}P peaks in the 1D NMR spectra.

3.4.1 NMR Experiments

Solution NMR relaxation experiments were performed on a Bruker Avance NEO 500 MHz spectrometer with a CryoProbe Prodigy BBO probe, using Wilmad-LabGlass 5 mm Thin Wall Precision NMR tubes. T_1 relaxation was measured with a standard inversion-

recovery pulse sequence and T_2 relaxation was measured using a CPMG sequence. Delays varied depending on sample conditions (temperature, pH, and concentrations of salts and polyethlyene glycol (PEG)).

T_1 and T_2 delays were experimentally modulated such that the final two points for T_1 curves fully recovered and the final point for T_2 curves were less than 5% of the initial intensity. T_1 relaxation times were determined by employing the TopSpin 4.0.6 T1/T2 dynamics module. T_2 relaxation times were determined by MestReNova monoexponential fitting. FWHM was determined by taking a 45°pulse and employing TopSpin 4.0.6 PEAKW command. For each spectrum, a single scan was acquired with 40000 data points to cover a spectral window of 10000 Hz (49.4 ppm). An AU program was created to ensure temperature equalisation uniformity which included a ten minute temperature equilibration time and autoshimming was applied continuously before and throughout acquisition.

Diffusion ordered spectroscopy (DOSY) measurements were taken on a 300 MHz SWB Bruker spectrometer with a single gradient along the z-axis. DOSY is an experimental that uses the Pulsed Field Gradient NMR (PFG-NMR) technique to extract diffusion coefficients for each NMR signal present in a sample. PFG-NMR measures particle diffusion by using a spin-echo pulse sequence in combination with a magnetic field gradient. As particles diffuse during the spin-echo sequence, they experience a slightly different field due to the gradient, and the spin-echo is unable to completely rephase the signal. This dephasing causes an attenuated signal intensity, which depend on the strength of the gradient, g, and the diffusion coefficient, D of the species as $\psi(g, D) = Exp(-Dg^2\gamma^2\delta^2(\Delta - \delta/3))$ where γ is the gyromagnetic ratio of the nucleus, δ is the width of the gradient pulse, and Δ is the time between gradient pulses [173]. By measuring this signal attenuation at several gradient strengths, one is able to fit the attenuation function to recover the diffusion coefficient of the associated species at each

NMR line.

Measurements were taken at 293 K, 343 K, and again at 293 K after the sample had cooled. Capillaries were used at elevated temperatures to suppress convection. To confirm there were not convection effects, a convection-compensated pulse sequence was compared to the standard sequence for one sample at 293 K and 343 K. At 293 K, 32 scans with a 90°pulse were acquired with 16384 data points to cover a spectral window of 6068 Hz (49.9 ppm) for gradient strength, and at 343 K, 64 scans with a 90°pulse were acquired for each gradient strength with the same spectral conditions as above. At each temperature, data was taken using 16 linearly spaced gradient strengths such that the final spectrum had an intensity less than 5% of the first's. These decays were then fit in the TopSpin 4.0.6 T1/T2 relaxation module to extract a diffusion coefficient. The Stokes-Einstein relation was then used to convert this to a hydrodynamic diameter.

NMR chemical exchange saturation transfer (CEST) experiments were performed on a Bruker 500 MHz (11.7 T) NMR spectrometer equipped with a broadband observe (BBO) probe. The 90° pulse duration ranged from 10 to 12 us depending on ionic strength of the solution. Saturation was performed by continuous wave (cw) irradiation of 5 s duration with field strengths of 1.16 μT to 8.69 μT (corresponding to nutation frequencies of 20 Hz to 150 Hz). The recycling delay was set to 5 s. Following cw irradiation, a 90° pulse is used for spectral readout. The temperature dependence of CEST measurements were taken with the irradiation power of 150 Hz at 298 K, 313 K, 323 K, 333 K, 343 K and 353 K, and the irradiation power dependence of CEST measurements were taken at 298 K with nutation frequencies of 20 Hz, 30 Hz, 50 Hz, 100Hz and 150 Hz. At each measurement, 8 scans with a 90°pulse were acquired. The scanned frequency ranged from -4000 Hz to 4000 Hz with a step size of 200 Hz.

Control experiments were performed to rule out the influence of temperature gradients or convection on the results. Relaxation rates were found to be the same in samples

containing capillaries (used to curb convection, if it exists), and chemical shift imaging was used to verify that the linewidths were the same in different z-positions in the sample.

3.4.2 cryo-TEM experiments

Phosphate solutions were prepared at room temperature and heated for at least 48 hours at 343 K before vitrification. Solutions were vitrified using an FEI Vitrobot Mark IV for vitrification in liquid ethane. 1.2 μL of sample was deposited on a lacey carbon support film on 200 mesh copper grid, blotted for one second, and immediately vitrified. The cryo-TEM was performed using Gatan 626 Cryo transfer holder with liquid nitrogen by ThermoFisher Talos G2 200X TEM/STEM at 200 kV with a Ceta II CMOS camera for bright field imaging.

Chapter 4

Evidence for free Posner molecules in simulated body fluids

4.1 Introduction

In Chapters 1 and 2, we established the importance of Posner molecules, nanometric calcium phosphate clusters, in the Quantum Brain theory and introduced the current understanding of their solution behavior. From a broader perspective, calcium phosphate nanoclusters appear to be important prenucleation species in the formation of amorphous calcium phosphate (en route to hydroxyapatite) [99, 89, 78, 100, 93] as well as octacalcium phosphate [101] and brushite [123]. Therefore, understanding the conditions that lead to the formation and aggregation of calcium phosphate nanoclusters is important in understanding the growth of a number of different calcium phosphate phases, with hydroxyapatite having particular biological relevance as the primary component of bone and teeth.

Within the Quantum Brain theory, Posner molecules function as a biological qutrit via their collective phosphorus nuclear spin states [51]. In order for the Posner molecule

to store, process, and output quantum information, it is imperative that free Posner molecules are stable within their biological "home" (we focus on the mitochondria as this potential location). The existence of such free Posner molecules (as opposed to aggregates or other calcium phosphate nanoclusters) is important for multiple reasons. For one, Posner molecules offer unique protection again ^{31}P spin decoherence. Compared to larger aggregates, their rapid tumbling blurs out environmental interactions, while the "cage" of spin-0 nuclei (in calcium and oxygen) provides spatial separation from source of spin relaxation. Additionally, the concept of pseudospin- the quantum degree of freedom in which the information is stored- only exists for small symmetric molecules with n-fold symmetry where $n > 2$ [54], which would not be the case for any form of aggregated Posners. Therefore, the Quantum Brain theory could function only if there are free Posner molecules in the mitochondrial matrix.

Unfortunately, imaging nanometer-sized clusters within mitochondria is currently infeasible. Cryogenic transmission electron microscopy (cryo-TEM) studies on mitochondria and the endoplasmic reticulum have found the presence of amorphous calcium phosphate granules with diameters ranging from $10 - 30$ nm [61, 30]. However, this size range of ACP is the current resolution limit due to the difficulties in sample preparation and imaging of relatively low contrast structures in biological samples. Attempts to use ^{31}P NMR on living mitochondria samples have revealed phosphate ion and adenosine phosphate signals, but such experiments are limited in their resolution due to the time constraints imposed by the necessity of mitochondrial respiration [184]. Additionally, the predictions for a long T_1 time for ^{31}P spins within a Posner molecule complicate potential NMR experiments. Since T_1 also dictates the time required for the spins in a sample to develop polarization for a NMR signal, solution NMR experiments on Posner molecules may require extremely long times to resolve a signal.

Given these difficulties, the *in vitro* isolation and characterization of Posner molecules

is the best current option for studying their behavior. First, it is important to confirm that Posner molecules are stable *in vitro* in simulated body fluids (SBFs), which use salt concentrations and pHs that mimic biological conditions. From this point, additional experimental characterization can take place, and open two different routes for testing of the Quantum Brain theory. For one, aspects of the theory- such as spin relaxation times, molecular symmetry, and studies on the impact of QDS on aggregation- can be examined *in vitro*. Secondly, once experimental signatures of Posner molecules have been established, such experiments might then be translatable to *in-vivo* biological systems.

Here, we use modernized dynamic light scattering (DLS), in combination with cryogenic transmission electron microscopy (cryo-TEM), pH measurements, and ^{31}P nuclear magnetic resonance (NMR) to study nanometer-sized entities in simulated body fluids containing calcium and phosphate. These systems have previously been inaccessible to high quality DLS measurements due to a combination of limitations relating to apparatus, experimental system, and data processing. Additionally, no prior studies have attempted to combine these different measurement techniques. These measurements provide the most accurate sizing of calcium-phosphate nanoclusters free in solution to date. The results suggest that multiple different calcium phosphate prenucleation clusters- not only Posner molecules but also other protonated calcium phosphate species, such as the hypothesized calcium triphosphate clusters [101, 123, 102], may form depending on solution conditions. This result unites previous experimental findings on calcium phosphate nanoclusters, and suggests that the solution phase behavior of calcium phosphate may be even more complex than previously believed.

4.2 Results and discussion

4.2.1 Sizing dilute nanometric particles with DLS

A full description of the theory of dynamic light scattering and data analysis can be found in Appendix A. Here we emphasize the importance of inline filtration and cross-correlation for sizing dilute particles at the single nanometer scale. We use a peristaltic pump that allows for inline filtration without exposing the sample to the atmosphere, removing any dust or larger particulates that would scatter much more strongly than nanometer-sized particles. The importance of removing these larger particles is demonstrated in Fig. A.1, which shows the scattering intensity of a particle at 1 μm, the typical size of dust, is $\sim 10^{10}$ that of a particle at 1 nm. A similar filtration setup was used by Ito et al. in their DLS studies that provided the first evidence of nanometric calcium phosphate species in solution [78, 100].

Our DLS setup also uses a state-of-the-art prototype cross-correlator developed by Brookhaven Instruments and tested and verified by us at UCSB. A schematic of the apparatus is shown in Fig. 4.1A. This cross-correlator utilizes parallel avalanche photodiodes to allow the experiment to access delay times as short as 75 ns. In contrast, the autocorrelator shows afterpulsing for delay times shorter than 1 μs (Fig. A.3), so that the cross-correlator allows us to access much earlier delay times in our autocorrelation function. These earlier times are key for resolving peaks at the nanometer and sub-nanometer size. The importance of using cross-correlation is demonstrated in Fig. A.3, where even for 4 nm diameter lysozyme proteins cross-correlation is necessary for accurate size measurements.

To confirm our ability to size dilute nanometer-scale species, the DLS apparatus and data processing was checked on a solution of α-cyclodextrin, an annular species with a theoretical diameter in vacuum of 1.46 nm [185] (Fig. 4.1B, right). The initial concen-

tration of α-cyclodextrin in solution was 1 mM before filtration. DLS experiments on α-cyclodextrin without filtration indicated a tendency for aggregates to form at > 100 nm. These aggregates were completely filtered out to allow for accurate measurements of individual α-cyclodextrin molecules, indicating that the concentration in the measured solution was less than the original 1 mM and in the μM range. Such concentrations are in the same approximate range of what we might expect for calcium-phosphate nanoclusters in simulated body fluids, as we describe below. Since α-cyclodextrin has a hydrophilic exterior, we would expect a strongly bound hydration shell that would increase the measured hydrodynamic diameter from the in-vacuum value. The resulting size distribution can be seen in Fig. 4.1B, with a peak at 1.77 nm, indicating that we are able to accurately measure sizes of relatively dilute nanometric species.

4.2.2 DLS Measurements on Simulated Body Fluids

With the confirmation that our experimental setup was able to size nanoparticles at concentrations in the μM range, we moved onto measurements of SBFs. We began with the system used previously [100], composed of 5 mM $CaCl_2$, 2 mM potassium phosphate buffer, and 250 mM KCl at pH 7.4 (buffered such that the pH was 7.4 after the addition of calcium). Full details on solution preparation can be found in the Methods and Materials section.

The autocorrelation function for this sample (light blue points), as well as the CONTIN fit (purple line), is shown in Fig. 4.2. The CONTIN algorithm is described in detail in Appendix A.3.2. Previous DLS studies by Ito et al., [78, 100, 186] were only able to observe one broad peak from this solution, in part because the autocorrelation function was already decaying at the earliest measurable delay times as they did not have access to a cross-correlating detector. While they were still able to find a peak around 1 nm, this

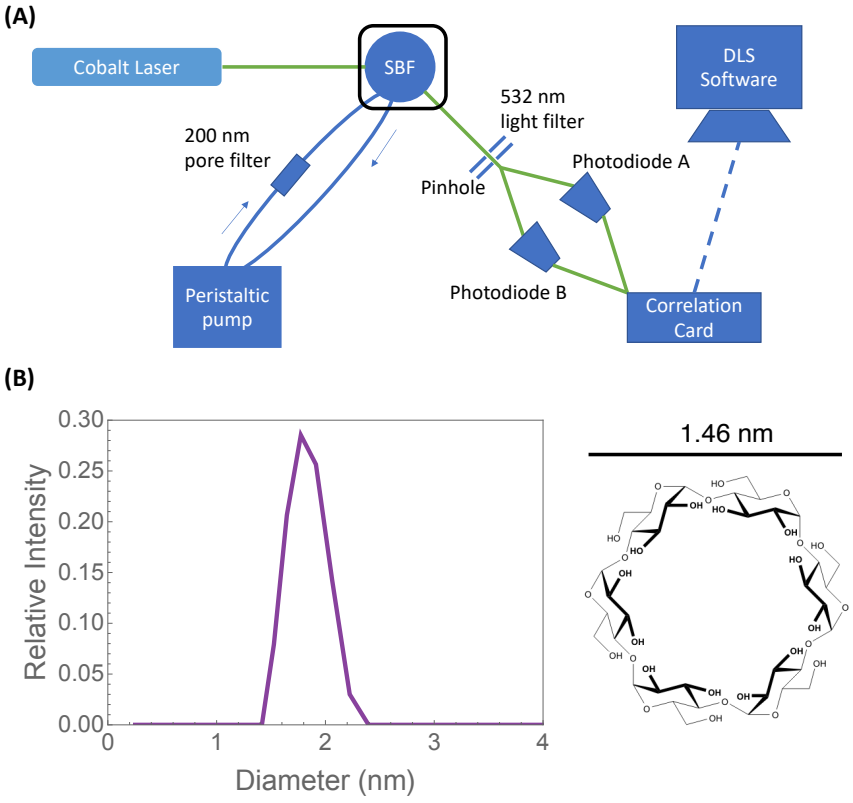

Figure 4.1: DLS setup for sizing nanoparticles. (A) Experimental setup used for DLS experiments. Of particular note is the cross-correlating detector, utilizing two separate avalanche photo diodes to remove afterpulsing effects and allowing the access of early delay times in the autocorrelation function. (B) Size distribution for α-cyclodextrin (structure shown on the right), indicating the ability of this DLS setup to size dilute nanoparticles.

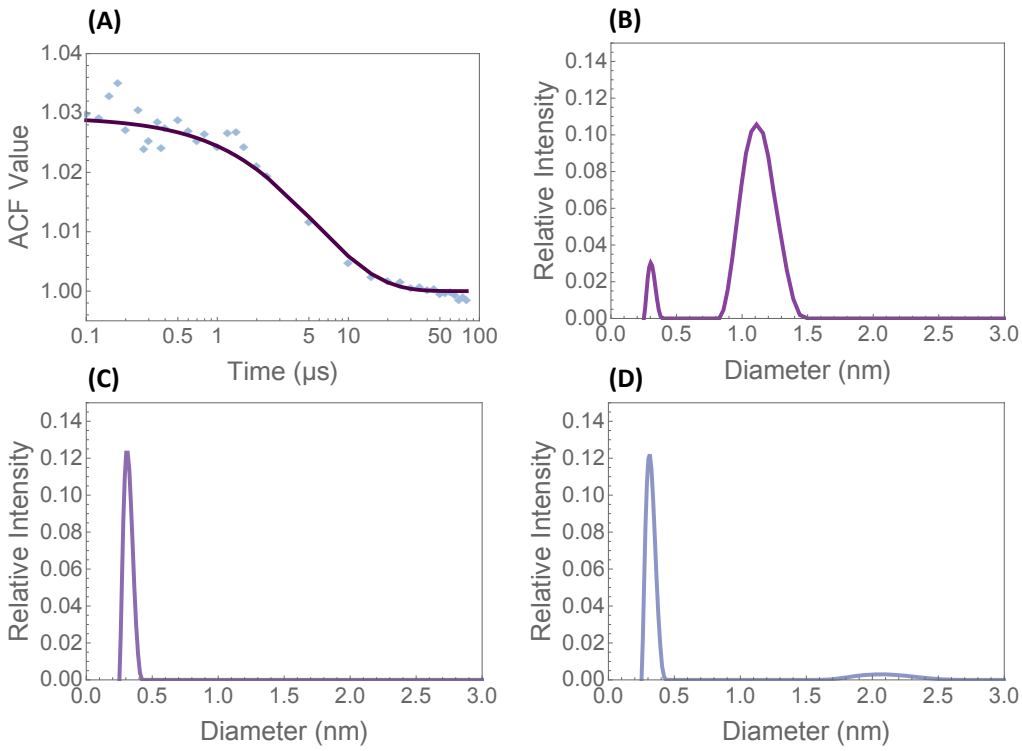

Figure 4.2: DLS results show evidence of a free calcium phosphate nanocluster in solution. (A) Autocorrelation function for a SBF, showing the raw data and the fit obtained from a CONTIN algorithm. (B) Size distribution extracted from the CONTIN fit of the autocorrelation function shown in (A). (C) Size distribution extracted for a SBF in the absence of phosphate. (D) Size distribution extracted for a SBF in the absence of calcium.

peak was broad and included contributions from ionic species in solution. This meant that they were unable to provide an accurate hydrodynamic diameter for these particles, and instead attributed all signal above 0.7 nm to nanoparticles, since no ionic species in the solution should be that large. Here, we find that we are able to resolve two separate peaks in our SBFs whose locations are robust to variations in fitting parameters.

The smaller peak, at a size of 0.3 nm, can be associated with free ions- primarily potassium and chloride because of their significantly higher concentrations. We also find a second distinct peak at a hydrodynamic diameter of 1.1 nm in the SBF (Fig. 4.2B). To determine the composition of the species contributing to this peak, we removed

either phosphate (Fig. 4.2C) or calcium (Fig. 4.2D) from the solution and extracted sizes. In these solutions, the ionic peak at 0.3 nm remains, but the peak at 1.1 nm has completely disappeared. We therefore identify the 1 nm peak as a free calcium phosphate nanocluster. (Note that the small peak at 2 nm in the solution without calcium is such low intensity that it is likely an artifact from the CONTIN fitting arising from noise in the measured autocorrelation function, as the location of this peak is highly sensitive to fitting parameters). This result improves upon previous studies by measuring a specific size of the calcium phosphate nanospecies in solution. Interestingly, this measured size aligns well with the theoretical size of a Posner molecule, which has a diameter of 0.95 nm in vacuum [55], and therefore would be expected to have a slightly larger hydrodynamic diameter when the molecule's hydration shell is also considered.

4.2.3 cryo-TEM Results

While the DLS results provide strong support for the presence of free calcium phosphate nanoclusters in the SBF mixture, we wanted to provide more direct evidence using cryo-TEM. Given the small size of the clusters, as well as the relatively low electron scattering contrast of calcium and phosphate against vitrified water, these species are at the limits of detection for cryo-TEM. Previous studies have claimed to image calcium phosphate structures at the single nanometer scale, but generally these structures are already aggregated [101, 93, 102]. In contrast, the DLS results confirm the lack of aggregates in our SBFs, so that any particles imaged at the nanometer scale would likely be free in solution.

We found that in this SBF we were able to resolve free nanometric clusters, as indicated by the yellow arrows in Fig. 4.3. While these species appear to be at the limit of

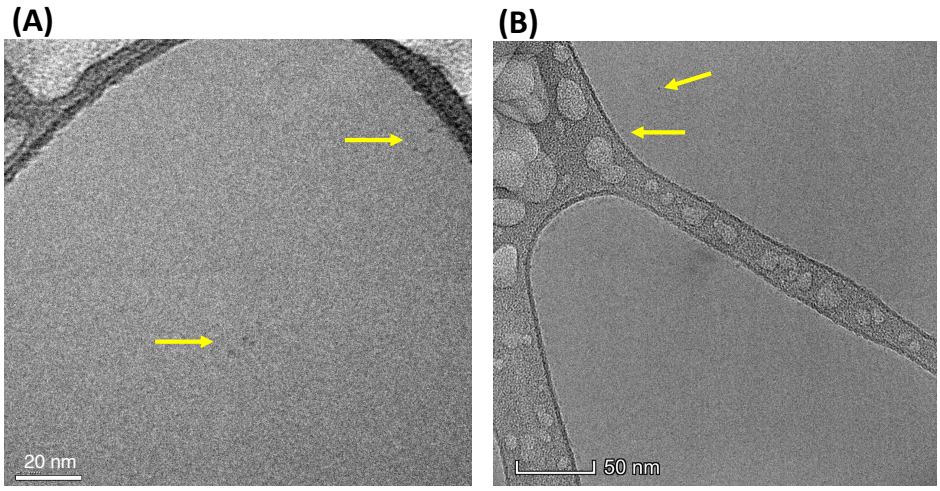

Figure 4.3: Cryo-TEM micrographs confirming the presence of nanoclusters in SBFs, indicated by yellow arrows. Sample in (A) were prepared and measured at a separate time from the sample shown in (B). Each sample showed evidence of nanometer-sized species in solution. Scale by in (A) is 20 nm and in (B) is 50 nm.

detection, the occurrence of multiple similar sized features across samples prepared on different days provides confidence that these features are not artifacts from preparation. Additionally, in cryoTEM ice artifacts that form during sample preparation and transfer are generally on the scale of > 50 nm, much larger than the features seen here [167, 168]. The size of these features, at just over 1 nm in diameter, agrees well with the results on the SBF from DLS, providing verification of the existence of free calcium phosphate nanoclusters in solution and our ability to use DLS to size them.

Unfortunately, hardware issues with this cryo-TEM setup meant that additional experiments were unable to be completed. However, the initial results on this SBF preparation verify our DLS results and indicate that this solution preparation is promising for future cryo-TEM experiments to collect further evidence of calcium phosphate nanospecies.

4.2.4 Exploring solution phase behavior of calcium phosphate nanoparticles

With cryo-TEM corroborating the ability of DLS to detect the presence and size of calcium phosphate nanoclusters in a SBF, we used DLS to explore how varying solution conditions can impact nanocluster formation. Given the strong pH dependence of calcium phosphate solubility and phase behavior [187, 188], we varied pH to see how this would affect the presence and population of nanoclusters. The ratio of phosphoric acid and sodium phosphate in our phosphate source was modified in order to maintain a constant phosphate concentration while changing pH without additional salts.

In this way, SBFs were monitored in the pH range 3.5 to 7.7 (after calcium addition). Higher pH values resulted in immediate precipitation of calcium phosphate from solution at these calcium and phosphate concentrations. Across this pH range, we observed two distinct peaks- one at 0.3 nm, attributed to free ions, and the other at just over 1 nm in size, which we identify as a calcium phosphate nanocluster (Fig. 4.4A,B). Note that at a lower pH of 2.4, we found no evidence for nanoclusters, and at higher pHs the precipitation of calcium phosphate prevented measurements of nanometric structures.

When monitoring the change in pH after the addition of calcium chloride, two distinct regimes are observed. At lower pHs, pH increases upon adding calcium chloride, whereas at higher pHs (>7), pH decreases upon adding calcium chloride (Fig. 4.4C). Since phosphate is the only salt present in the solution that would be likely to act as a buffer in binding/releasing protons (the other components being potassium, calcium, sodium, and chloride), we interpret these changes in pH as changes in the protonation state of phosphate. We thus note that at lower pHs, we infer that phosphates become more protonated upon calcium addition, leading to the observed increase of pH, while at higher pHs the phosphates are deprotonated after calcium addition. Since at higher

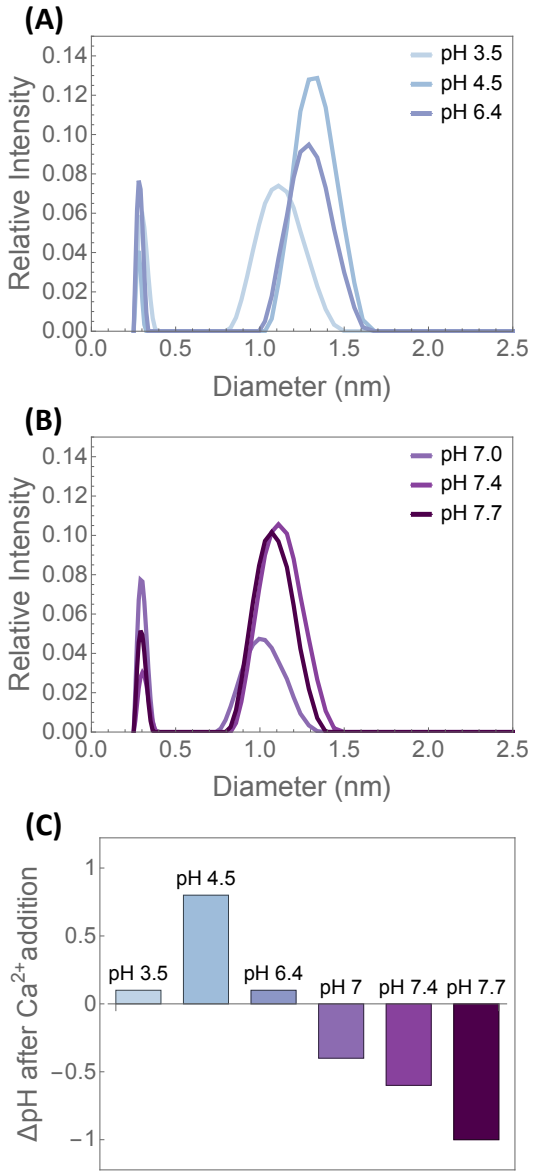

Figure 4.4: Size measurements and pH changes for simulated body fluids across a range of solution pHs. pH values shown represent the solution pH after the completion of the DLS experiment, while ΔpH is calculated by subtracting the pH before calcium addition from this final pH. (A) Size results for SBFs where the pH increased after calcium addition. (B) Size results for SBFs where the pH decreased after calcium addition. (C) Magnitude of pH change in solutions from (A) and (B) after calcium addition.

pH the phosphates were initially less protonated to begin with, the fact that these phosphates become additionally deprotonated rather than less indicates two distinct calcium-phosphate chemistries. At lower pH, the calcium ions appear to coordinate with protonated phosphate species, while at higher pHs, calcium coordinates with deprotonated phosphate species.

Given this result, we propose that there are two distinct calcium phosphate nanoclusters that can form in solution. Previous studies have argued for two nanocluster species- (1) Posner clusters, with stoichiometry $Ca_9(PO_4)_6$ such that the phosphates are fully deprotonated [99, 78, 125], and (2) Calcium triphosphate, where proposed stoichiometries vary from $Ca(HPO_4)_3^{4-}$ to $Ca(H_2PO_4)_3^{-}$ where each phosphate is at least singly protonated [101, 123, 102]. Our results here reveal that both of these species could be stable in solution. Additionally, the magnitude of ΔpH observed in the samples appear to reveal an equilibrium between these two nanocluster species rather than simply the formation of one or the other.

While here we have used pH to toggle this equilibrium, the results of previous studies show that other solution components, such as additional ions, can also shift the equilibrium between different species. For instance, studies on a more complex SBF that included magnesium, carbonate, and sulfate at concentrations in the mM range appeared to show a calcium triphosphate species at pH 7 that developed over the course of hours rather than minutes [102]. Such other salts may impact calcium phosphate nanocluster formation via direct interactions with calcium and phosphate ions, or by changing the population and dynamics of the phosphate assemblies discussed in Chapter 3. Thus, our result here, in concert with those of previous studies, indicate that the solution phase space of calcium phosphate nanoclusters is quite complex and highly influenced by a variety of factors.

4.2.5 ^{31}P NMR on simulated body fluids

Having established solution conditions that promoted the formation of calcium phosphate nanoclusters, we conducted ^{31}P NMR experiments on SBFs to look for a signal indicating the presence of these nanoclusters. A ^{31}P NMR signal from a Posner molecule would be of particular interest, given the importance of ^{31}P spin dynamics within the Posner in the Quantum Brain theory. However, a conventional ^{31}P signal is also a "double-edged sword" of sorts because this would likely require that the T_1 time for the Posner molecule is relatively short compared to the predictions.

We ran ^{31}P solution NMR on SBF samples prepared as previously introduced for DLS samples, including the inline filtration to remove any larger species or contaminants. During NMR experiments, solution aliquots were measured on DLS to confirm that no larger calcium phosphate species were forming. The result is shown in Fig. 4.5A for a SBF prepared at pH 7.7. Before calcium is added, there is a single ^{31}P peak that can be identified as ionic phosphate. After calcium is added and the solution is filtered, there is still a single peak, but with an upfield shift and a broadened line. Given the rapid tumbling expected of either a Posner molecule or a calcium triphosphate cluster, these species would not be expected to show any significant broadening compared with ionic phosphates. Considering the broadening of ^{31}P lines in phosphate due to the presence of spectroscopically dark assembles, the NMR signal may even be expected to narrow if the calcium phosphate species wasn't in exchange with the assemblies. (Note that it is entirely possible that calcium triphosphate species would be involved in the phosphate assemblies, given that other species with exposed phosphate groups, such as ADP, have been shown to assemble as well [64]).

Therefore, we investigated this result further by making SBFs with various calcium concentrations (from the same mother solution of 2 mM phosphate and 250 mM KCl at

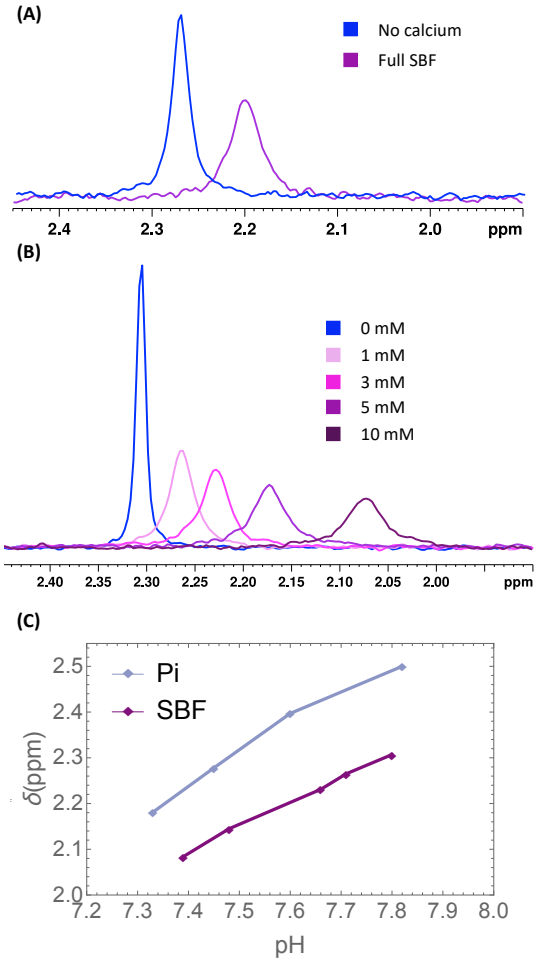

Figure 4.5: ^{31}P solution NMR results on simulated body fluids. (A) After 5 mM calcium is added to the SBF at pH 7.7, there is a shift in the linewidth and position. (B) Changing calcium concentration for a SBF with 2 mM phosphate and 250 mM KCl at pH 7.8 results in a progressively broader line and larger chemical shift difference from the original ionic phosphate peak. Legend indicates the calcium concentration used. (C) A comparison of the chemical shift for phosphate ions compared to the SBF as a function of pH.

pH 7.8) and measuring the ^{31}P signal. These results are shown in Fig. 4.5B. Note that the calcium concentration displayed is the concentration before filtration, so that the solution measured in NMR will have a lower actual calcium concentration since larger calcium phosphate species are removed during filtration. In these solutions, as the initial concentration of calcium increases, the peak progressively shifts upfield and broadens. This shifting and broadening indicates that there could be chemical exchange in the sample, and that as more calcium is added the equilibrium and exchange rate between species are changing. While it is difficult to know exactly which species are involved in this exchange, it appears likely to be some combination of phosphate ions, calcium phosphate nanoclusters, and small aggregates of calcium phosphate nanoclusters, as DLS confirmed that there are no large calcium phosphate species present in these solutions.

We emphasize here that the pH of these solutions also decreases monotonically with increasing calcium concentration. This decrease in pH causes the location of the ionic phosphate line to shift upfield, as shown in Fig. 4.5C. Therefore, the chemical shift difference between ionic phosphates and the ^{31}P signal from the SBFs actually becomes slightly closer as calcium concentration is increased. The fact that the chemical shifts are converging but the signal is broadening lends additional evidence to the possibility that there are several different species in a complex equilibrium that is shifting as a function of both pH and calcium concentration.

Given this result, it appears that isolating a ^{31}P solution NMR signal from a Posner molecule in these SBFs may not be feasible. Since there is only a single ^{31}P peak that is contributed to by multiple species, measuring parameters such as T_1 or T_2 would give a composite signal from the different species. Because we don't have information on the number of species that make up this signal, or their populations and exchange rates, extracting T_1 or T_2 is currently impossible.

However, if one were to vitrify a SBF, they would halt all dynamic processes and be

able to capture a snapshot of the solution. Indeed, dynamic nuclear polarization NMR (DNP-NMR) is a process in which solutions are vitrified, allowing for a single snapshot of solution conditions to be examined. Additionally, in DNP-NMR one uses polarization transfer from electron radicals in solution to the nuclei of interest to boost signal and allow for more complicated NMR techniques that are not available in solution state. This idea is explored more in Chapter 7 as a possible route for future experimental work.

4.3 Conclusions

While it is now generally agreed that calcium phosphate prenucleation clusters form in the initial stages of calcium phosphate aggregation, there has still been much debate over the composition and structure of these species. Here, we have directly sized these species, finding them to have hydrodynamic diameters of just over 1 nm. We have presented evidence that multiple distinct chemistries of prenucleation occur depending on the exact solution condition. Indeed, our results show that there appears to be an equilibrium in solution between Posner clusters and calcium triphosphate species. While we modulated the equilibrium between these species via solution pH, we recognize that other solution components, such as additional ions, temperature, and salt concentrations, are also likely to affect this equilibrium.

These results confirm that Posner molecules are likely able to exist in simulated body fluids. Of course, in a biological setting such as the mitochondrial matrix the environment would be significantly different, so future *in vivo* studies will be required to confirm the existence of Posners in that environment. However, these results indicate the possibility of doing further *in vitro* experiments and characterization on Posner molecules, which would be a key step towards potential *in vivo* experiments in the future.

4.4 Methods and Materials

4.4.1 Preparation of solutions

The simulated body fluids studied were a $CaCl_2$-H_3PO_4-Na_3PO_4-KCl-H_2O system, with a constant concentration of 250 mM KCl while varying concentrations of $CaCl_2$, H_3PO_4, and Na_3PO_4 to alter both the concentrations of calcium and phosphate and the pH of the solution. Sodium phosphate tribasic (MW 163.94) was acquired from Acros Organics. Potassium chloride (MW 74.55), calcium chloride dihydrate (MW 147.01), and ortho-phosphoric acid (85%) were acquired from Fisher Scientific. Milli-Q water was used for all solutions. Solutions were prepared and measured at 25 °C.

While a previous DLS study had used a 50 mM tris(hydroxymethyl)aminomethane buffer to modulate pH [78], we buffered instead with a mixture of phosphate solutions in order to remove the scattering signal from the tris. Solutions were thus prepared from stock phosphate solutions at 100 mM prepared by mixing H_3PO_4 and Na_3PO_4 solutions to achieve the desired pH. The accuracy of pH values reported for solutions is ± 0.05. Each solution had a volume of 15 mL and were prepared and measured in (information on glass vials). Solutions excluding calcium and/or phosphate were also prepared for comparison with the full simulated body fluid to confirm which signal corresponded to calcium-phosphate entities.

After mixing the solutions, an in-line filtration system was used to allow for constant filtration while in the DLS cell without exposure to air. Because of the strong radial dependence of scattered intensity ($I \propto r^6$), it is imperative to remove all dust and larger calcium-phosphate aggregates from the solution so that scattering signal from any nanometer-sized species can be registered. Thus, the system was filtered for 10 minutes using a peristaltic pump (Fisherbrand mini-pump variable flow peristalic pump) and a 200 nm pore-sized surfactant free cellulose acetate filter, which we found to be sufficient

to prevent intensity spikes that would correspond to large species in solution for the full length of the experiments. After this filtration the solution was allowed to settle for at least 5 minutes before beginning the DLS experiment to allow for the pH to equilibrate and to suppress any flows resulting from the pumping process. Solutions for cryo-TEM and NMR were prepared identically, except the exact time between end of filtration and beginning of experiment would vary from 5-15 minutes. However, DLS experiments showed no differences in the scattering signal over this time period (and for up to 4-5 hours), indicating that each experiment was accessing a similar solution state.

4.4.2 DLS data collection and processing

Dynamic light scattering was conducted with a BI-200SM Goniometer System with a cross-correlating TurboCorr correlator (Brookhaven Instruments) and a Cobolt Samba 500 mW laser at 532 nm (HÜBNER Photonics). The setup is shown in Fig. 4.1. After filtration, DLS measurements were performed at a 45° scattering angle at 25° C until noise was low enough that fitting was possible, generally over the course of 4-5 hours, or until there was evidence of aggregation in the samples (as seen by increasing scattering intensity), at which point experiments were stopped. Data was collected on $\sim$ 50 correlation channels with delays ranging from 75 ns to $\sim$ 100 μs, and samples rates of 25 ns to 5 μs, depending on channel delay. The exact number of channels used for each fitting was determined by finding a flat baseline of at least 8 channels.

DLS data was processed using a CONTIN algorithm implemented in MATLAB, based on a modified version of the rilt (Regularized Inverse Laplace Transform) code [189]. A full description of the CONTIN algorithm can be found in Appendix A. Values for the regularization parameter and the number and range of decay rates considered were varied for several sets of experimental data and were found to not qualitatively change

the resulting distributions, although the exact shapes of the resulting distributions did change.

4.4.3 NMR experiments

Solution NMR relaxation experiments were performed on a Bruker Avance NEO 500 MHz spectrometer with a CryoProbe Prodigy BBO probe, using Wilmad-LabGlass 5 mm Thin Wall Precision NMR tubes. Each 1D spectra was acquired with a 45 °pulse, 64 scans, a 15 s delay between scans, and a 1 s acquisition time. SBFs were prepared identically to DLS experiments but with 10% D_2O. After filtering, NMR experiments were begun within 10 minutes.

4.4.4 cryo-TEM

Simulated body fluids were prepared identically to DLS experiments. 10 minutes after filtering ended solutions were vitrified using an FEI Vitrobot Mark IV for vitrification in liquid ethane. 1.2 μL of sample was deposited on a lacey carbon support film on 200 mesh copper grid, blotted for one second, and immediately vitrified. The cryo-TEM was performed using Gatan 626 Cryo transfer holder with liquid nitrogen by ThermoFisher Talos G2 200X TEM/STEM at 200 kV with a Ceta II CMOS camera for bright field imaging.

4.4.5 pH measurements

pH measurements were made before calcium chloride addition, and after the DLS data had been collected- approximately 4.5 hours after calcium chloride. Measurements were made on a Fisherbrand accumet XL200 benchtop pH meter with a accuTupH Rugged Bulb electrode.

Chapter 5

A differential lithium isotope effect on the formation of amorphous calcium phosphate from solution

5.1 Introduction

In Chapter 1, we introduced the field of "quantum biology," where quantum mechanics is theorized to be non-trivially functional in biological systems, and noted some systems where there is evidence for quantum biological effects, including proton tunneling in proteins [1, 2], olfaction [3], photosynthesis [4, 5, 6], and magnetoreception in birds [7, 8, 9, 10]. Each of these systems utilizes quantum mechanics in different ways - for instance, the quantum theory of olfaction utilizes inelastic electron scattering to "measure" the vibrational spectra of a molecule, while in photosynthesis coherent electron states allow for ultra-fast energy transfer. One commonly considered area of interest within quantum biology is spin-based effects, ranging from singlet-triplet conversion in electron spin pairs [7, 4] to nuclear spin information storage [51], the latter of which is

the focus of this thesis. However, experimental tests of spin-based effects is complicated because conventional experiments that probe spins (electron paramagnetic resonance or nuclear magnetic resonance) will affect the state of the system and potentially alter any interesting quantum states.

Differential isotope effects offer a useful strategy for identifying spin-mediated cases of quantum biology, as the isotopes will have different spin-spin interactions but similar chemical interactions. Recently, a number of biological isotope effects have been discovered which cannot be readily explained by the classical mass-based kinetic isotope effect, including lithium isotope effects on mothering behavior [134] and the suppression of mania [133] in rats, a xenon isotope effect on xenon's anesthetic properties in mice [190], and a lithium isotope effect on mitochondrial calcium sequestration [191]. However, due to the complicated nature of biological systems, it is almost impossible to definitively place the origins of these isotope effects. Recently, experimental tests of Li isotope effects on key neuronal and enzymatic activities found no distinguishable differences [192] that link the observed effects on animal behavior and neurophysiology to differential uptake into cells, suggesting that the observed lithium isotope effects are due to functional differences between the isotopes. While the radical pair mechanism has been proposed for both xenon anesthesia and lithium mania suppression [193, 194], such modeling efforts are speculative in that they fail to link the spin dynamics to any biological function that would impact the observed behavior.

Lithium isotopes are of specific interest in the Quantum Brain theory because lithium has also been proposed to incorporate into Posner molecules and impact their binding dynamics in an isotope-dependent manner [51, 55, 54]. There is already biological evidence that lithium effects the growth and/or stability of calcium phosphate, as lithium has been implicated in the decalcification of teeth as an unwanted side-effect of lithium-based treatments [195], but this study did not have any isotope specificity. From the

perspective of brain function, lithium (often in the form of lithium carbonate) is a potent medication for bipolar disorder, but the mechanism behind its function is still unknown [131, 132]. As noted above, there are also studies showing a lithium isotope effect on specific aspects of rat behavior [134, 133]. Taken altogether, the calcium-phosphate-lithium system offers a model for establishing potential connections between calcium phosphates and brain function, thus probing aspects of the Quantum Brain theory. Additionally, the Quantum Brain theory predicts that there would be a lithium isotope effect on Posner molecule pair-binding not only *in vivo* but also *in vitro*. Evidence for an *in vitro* lithium isotope effect would also have broader implications within quantum biology, as it would demonstrate that *in vitro* systems are a useful tool for the systematic investigation of potential quantum effects *in vivo*.

In Chapter 2, we introduced the previous understanding for the nucleation and growth of amorphous calcium phosphate. However, we have since established the existence of phosphate assemblies in aqueous solutions in Chapter 3, and shown evidence for the presence of multiple different calcium phosphate nanoclusters in Chapter 4. Therefore, we have updated the nucleation and growth pathway for ACP, as is shown in Fig. 5.1 [196, 93, 197, 101, 64, 124]. Before calcium phosphate nucleation, phosphate ions are in exchange with phosphate assemblies, liquid-like clusters of phosphates that form in aqueous solution [64] (stage I). Solution conditions such as ion concentration, temperature, and pH then encourage the formation of prenucleation species from soluble ions, which nucleate into calcium phosphate prenucleation clusters. At stage II, there appears to be an equilibrium between some form of ionic calcium triphosphate (such as $[Ca(H_2PO_4)_{1.04})(HPO_4)_{1.76}]^{2.56-}$)[101, 123] and Posner molecules ($Ca_9(PO_4)_6$) [198, 100]. These prenucleation clusters then form calcium phosphate clusters at the scale of 50-100 nm [93, 90] (stage III). These ACP particles then aggregate into larger ACP colloids [93] and in time (minutes to hours depending on solution conditions) undergo phase trans-

formation into crystalline hydroxyapatite, the thermodynamically favored phase [79, 77].

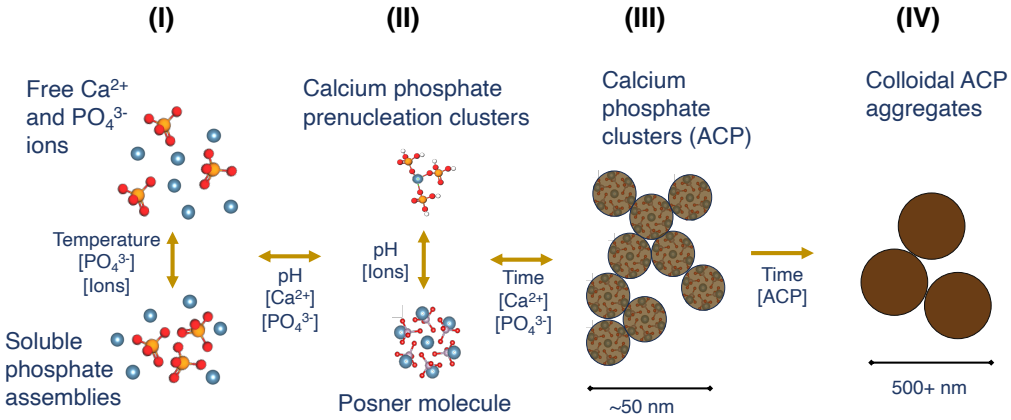

Figure 5.1: Proposed nucleation and growth pathway for the formation of amorphous calcium phosphate (ACP), showing four proposed stages and the transitions between them. Soluble calcium and phosphate ions (I) initially form prenucleation nanoclusters (II), which then rapidly form calcium phosphate clusters at 50-100 nm in diameter (III). These ACP clusters then aggregate into larger colloidal structures at several hundred nanometers in size (IV)). Over time, these metastable ACP aggregates undergo phase transformation to hydroxyapatite.

Within the framework of the Quantum Brain theory, it is posited that one might observe a differential lithium isotope effect on the aggregation of Posner molecules, arising from different couplings between the spins of the two lithium isotopes, ^{6}Li and ^{7}Li, and the ^{31}P spin states within the Posner molecules. Since the collective ^{31}P spin states are proposed to be linked to binding rates of Posner molecules [55, 54], such an isotope effect may manifest on larger scales by altering the aggregation of Posner molecules into larger calcium phosphate species (stage II to III). ACP growth might then display lithium isotope-dependent kinetics. Given that ^{6}Li and ^{7}Li have nearly identical electronic states, and thus chemistries, and that their diffusion rate in water differs by only 0.6% [199], any observable lithium isotope effect on ACP growth would be classically unexpected. Thus, ACP growth in the presence of lithium isotopes offers an experimental system where one can test a fundamental prediction of the Quantum Brain theory.

Here, we present results that show a measurable differential lithium isotope effect on

the *in vitro* formation of ACP in aqueous solutions that are mildly supersaturated with respect to calcium phosphate. Dynamic light scattering measurements of ACP growth in the presence of ^{6}Li and ^{7}Li salts at biologically relevant pH and temperature reveal that while the size of ACP particles is insensitive to isotope, the concentration of large ACP particles is enriched in the presence of ^{7}Li. ^{31}P nuclear magnetic resonance (NMR) and mass spectrometry confirm lithium incorporation into ACP and show significant Li-P spin coupling. Given the biological importance of calcium and phosphate regulation, in both the Quantum Brain theory and in several established biological processes, these results could have wide implications for the interpretation of the milieu of differential lithium isotope effects that have been previously observed.

5.2 Dynamic light scattering shows differential lithium isotope effect

Dynamic light scattering (DLS) allows for the measurement of particle sizes in solution, ranging from 1 nm to several microns in diameter, and has previously been used to measure calcium phosphate structures both at prenucleation stages (Fig. 5.1, II) and of larger colloidal structures (Fig. 5.1, III and IV). [100, 200, 201, 122] Here, we used DLS to monitor the size and scattering intensity of calcium phosphate in solutions promoting ACP formation during the first 5 minutes of growth in 10 s intervals. A schematic for the preparation and measurement of these solutions is shown in Fig. C.1. Solutions were prepared with 250 mM LiCl (either 95% ^{6}Li or 99% ^{7}Li), 2 mM sodium phosphate, and 5 mM $CaCl_2$ at pHs of 7-9 (before calcium) and at 37°C. This is a similar composition to previous studies that have used DLS to examine calcium phosphates species, although these were done at 25 °C. These specific conditions were chosen due to their biological

relevance to the mitochondrial matrix (noting that the pH drops after calcium addition to the 7-8 range), given the mitochondria's importance in buffering intracellular calcium via storage in amorphous calcium phosphate [202, 61], and as a potential location of Posner molecules within the Quantum Brain theory.

Prior to calcium addition, the solutions were filtered using 0.2 μm cellulose acetate syringe filters and measured for 120 seconds in DLS to confirm the absence of large contaminant particles. After adding calcium, the average sizes and scattering intensities were measured over a 5-minute interval (Fig. 5.2). At both pH 7.4 and 8.1, the sizes of ACP measured in the presence of the two lithium isotopes were identical. At the lower pH of 7.4, the scattering intensities are also isotope-independent, but at pH 8.1 the scattering intensity in the presence of ^{7}Li is significantly higher, potentially indicating a lithium isotope dependence on the formation of ACP from solution.

To understand the significance of the different scattering intensities despite the similar average particle sizes between solutions containing the two different lithium isotopes, one can consider how scattering intensity scales with particle size and concentration. Drawing from previous observation [122], we consider the wide size dispersity of ACP particles, ranging from prenucleation clusters at the single nanometer scale to larger ACP colloids (Fig. 5.1 stages II-IV). Mie scattering theory (Fig. C.2) shows that, for particle sizes with diameters above the Rayleigh regime (i.e. having diameter $d > \lambda$, where λ is the wavelength of incident light, in this case 532 nm), the scattering intensity I scales approximately as $I \propto d^2$ [203], while in the Rayleigh regime ($d << \lambda$), the scattering intensity drops significantly, with intensity $I \propto d^6$ [204]. Thus, particles at smaller length scales (1-10 nanometers in diameter) will have negligible contribution to the total scattering intensity compared to the largest ACP particles (at several hundred nanometers in diameter).

Considering this size-intensity relationship, one can then infer information on the

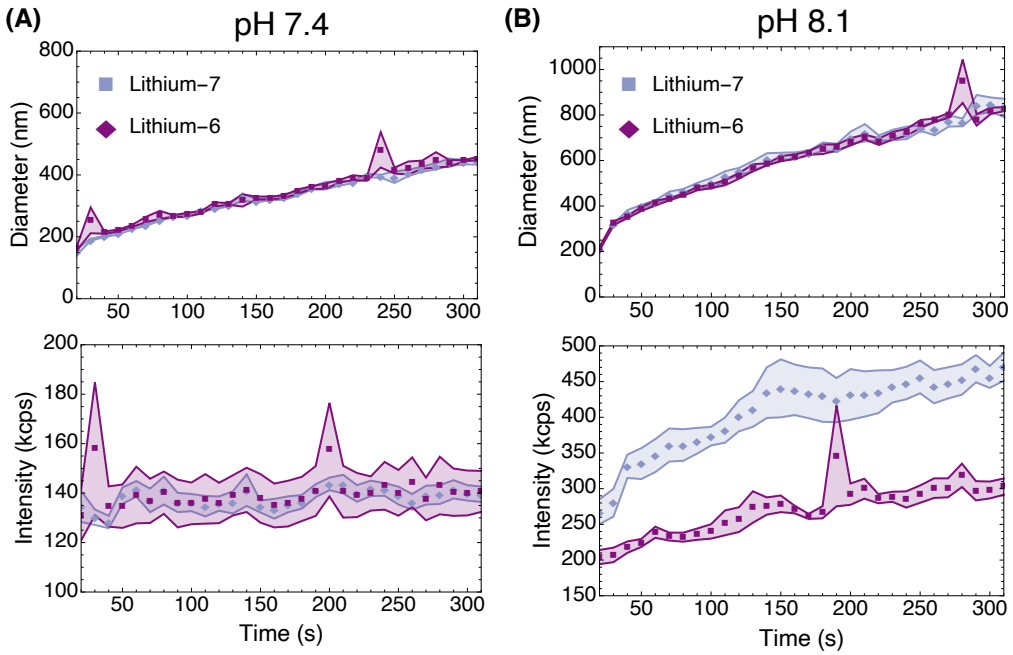

Figure 5.2: Dynamic scattering results of the first 5 minutes of ACP growth for a system of 5 mM $CaCl_2$, 2 mM $NaPO_4$, and 250 mM LiCl at 37 °C comparing ^{7}Li and ^{6}Li. (A) At pH 7.4, the sizes of calcium phosphate particles and their scattering intensities are the same, indicating no isotopic difference. (B) At pH 8.1, the sizes of calcium phosphate are the same, but the ^{7}Li solution shows greater scattering intensity, indicating a higher particle abundance of structures at large sizes. Each trace is the average result over 5 separate trials, with bands indicating the standard error of the mean. The pH was adjusted to the indicated value before calcium addition using 0.2 M NaOH.

distribution of particle sizes within the solutions containing each lithium isotope. Given that the cumulant average size is identical for both isotopes, it appears that the largest particles, which dominate the scattering signal, are forming at the same size in the presence of both isotopes. Therefore, the noted difference in scattering intensity can be attributed predominately to the abundance (concentration) of these largest particles, indicating that the ^{7}Li solution has a greater population of large particles. Given that the total molar concentrations of calcium and phosphate are identical, the ^{6}Li solution must have a more concentrated population of smaller ACP particles, prenucleation species, and/or ionic phosphate and calcium, which contribute minimally to the scattering signal,

leading to the observed intensity difference.

To further explore this apparent dependence of ACP formation on lithium isotopes, we explored the solution phase behavior of the LiCl-$NaPO_4$-$CaCl_2$ system to test whether the location of the phase boundaries is isotope-dependent. First, the solid-solution phase boundary was measured in a space of pH and [Ca^{2+}] phase space at fixed [PO_4^{3-}]. 35-minute absorbance measurements at 532 nm identified three distinct regions - a dissolved free ion phase, a metastable colloidal phase, where calcium phosphate particles formed and exhibited time-insensitive absorbance, and an unstable agglomeration phase, where absorbance traces steadily increase and ACP precipitation occurred within 45 minutes (Fig. C.4). The results (Fig. 5.3A) indicate no isotopic dependence on the location of these phase boundaries.

We then monitored ACP growth using DLS at a range of pH within the unstable agglomeration phase to search for the conditions where this isotope effect is present. We find (Fig. 5.3B) that the lithium isotope effect manifests in a specific range of supersaturation, whereas solutions too close to the agglomeration boundary or at too high of a supersaturation show little or no scattering intensity differential. This narrow window indicates that there may be a specific nucleation and growth pathway for ACP formation which experiences a differential lithium isotope effect, while other pathways show no effect.

5.3 Lithium acts on early stage calcium-phosphate nucleation

Having established a differential lithium isotope effect in a particular range of compositions *in vitro*, we designed experiments to investigate at what stage in the ACP

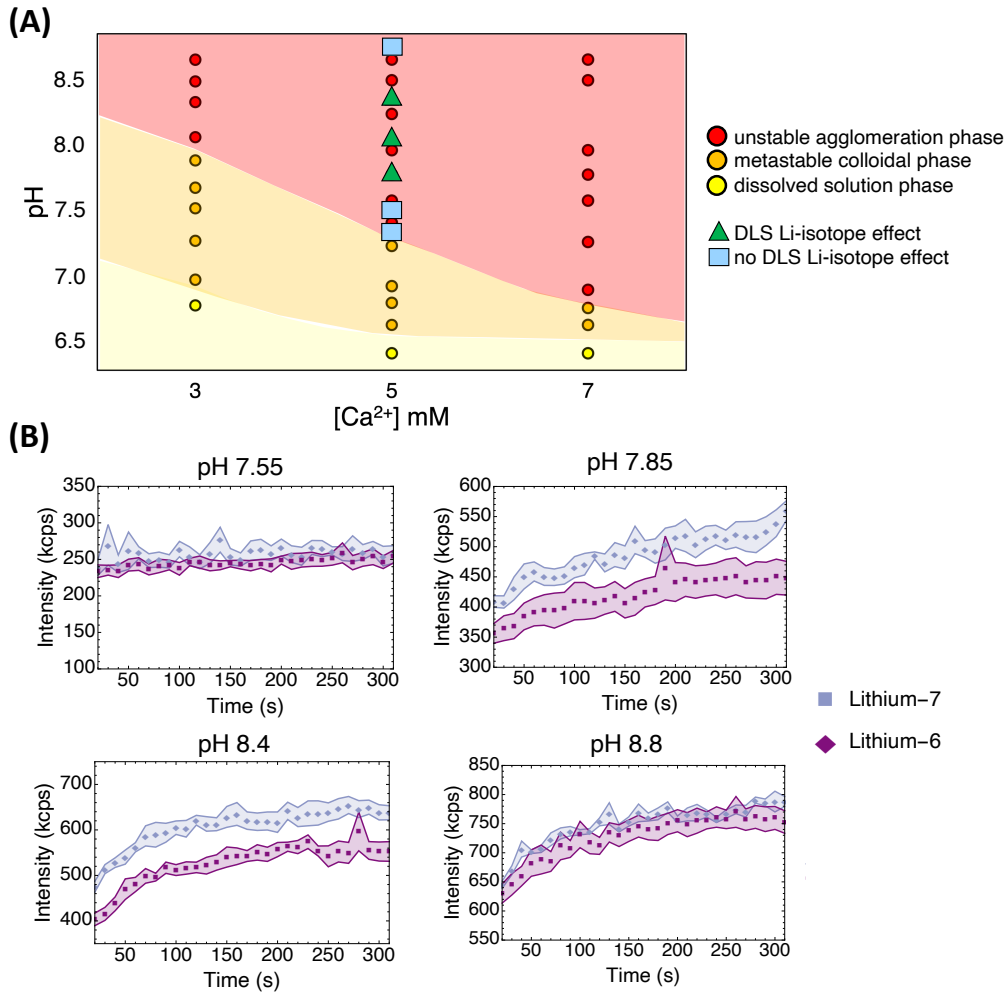

Figure 5.3: The solution phase behavior of calcium phosphate shows a specific region of active lithium isotope effect. (A) A phase diagram as a function of pH and calcium concentration reveals three distinct regions of ACP growth: 1) dissolved free ions, 2) metastable colloidal aggregates, and 3) unstable agglomeration of clusters. No isotope difference is found in the location of the boundaries between these regions. (B) Exploring pH within the unstable agglomeration phase reveals a distinct pH window where the lithium isotope effect on DLS scattering intensity on ACP growth is observable. All samples had identical sizes from DLS as shown in Fig. C.3.

formation pathway (Fig. 5.1) this effect manifests. Given that DLS is primarily sensitive to structures at several hundred nanometers in scale, any of the steps leading up to the formation of large ACP aggregates (stage IV) could be involved in the isotope effect. Therefore, we tested the possibility that a lithium isotope effect could occur at each stage of the ACP growth process.

First, we consider whether stage I, before any calcium phosphate structures have formed, could be differentially impacted. Such an effect could arise, for example, from different local water structuring around atoms of the two lithium isotopes, or due to a direct lithium-phosphate interaction (we assume no significant lithium-calcium interactions given they are both positively charged). As noted, ^{6}Li and ^{7}Li have aqueous diffusion coefficients that differ by $< 0.6\%$ [199]. This diffusion coefficient is proportional to the hydrodynamic diameter of the ions, which includes the bound water molecules around the ion. Thus, we expect no significant isotopic difference in the local water structuring.

To address the possibility of differential ionic lithium-phosphate interactions, we characterized solutions of lithium and phosphate using ^{31}P NMR before adding calcium. The resulting spectra (Fig. 5.4A) show nearly identical chemical shift and linewidth for phosphorus in the presence of ^{6}Li and ^{7}Li, indicating no significant difference in ionic lithium-phosphate chemistry. The small observed chemical shift difference of $\sim$0.01 ppm is of the order typically seen for isotopes, given that their different masses will change equilibrium bond length and therefore electron density at the phosphorus nucleus [205]. We conclude that the observed isotope effect is not likely to manifest during stage I of ACP growth.

To investigate the potential for an isotope effect on later stages of ACP growth, we first established whether lithium is incorporated into the resulting calcium phosphate phase in an isotope-dependent manner. ^{31}P NMR performed after calcium addition indicates a ^{31}P shift in line shift and linewidth compared to solutions containing no calcium (Fig.

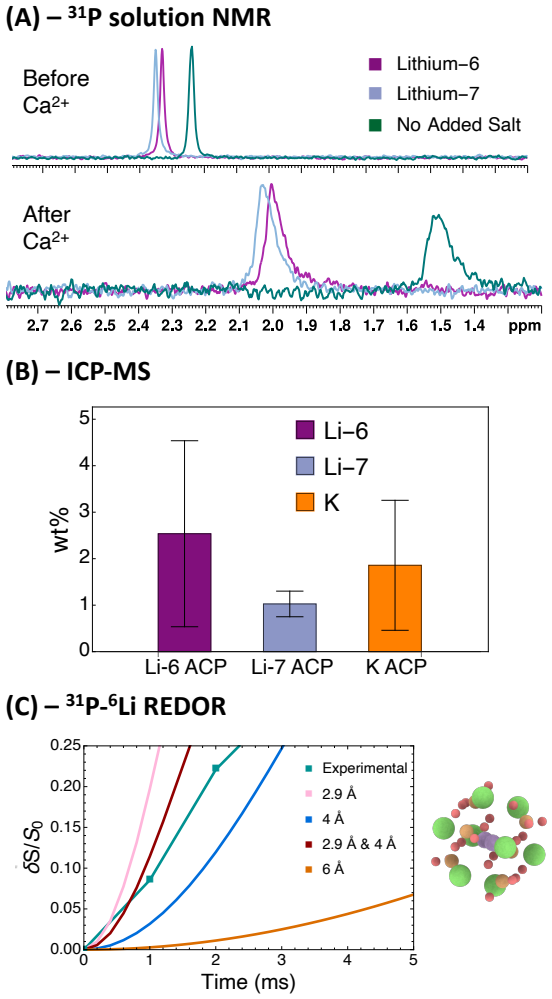

Figure 5.4: ^{31}P NMR and ICP-MS confirm the incorporation of lithium into ACP phase. (A) ^{31}P NMR on LiCl-$NaPO_4$-$CaCl_2$ solutions shows similar ^{31}P chemical shift in the presence of ^{7}Li and ^{6}Li both before and after the addition of calcium, indicating no isotopic difference in phosphate-lithium interactions and similar incorporation of both lithium isotopes into the ACP phase. (B) ICP-MS results on the incorporation of ^{6}Li, ^{7}Li, and K on ACPs synthesized in the presence of 250 mM ^{6}LiCl, ^{7}LiCl, and KCl. Both lithium isotopes are incorporated similarly into the ACP phase at ~ 1 wt%, with error bars indicating the standard error across 10 independent trials. Potassium is also incorporated at $\propto 1$ wt%, but given that potassium is 6-7 times as massive as lithium, its incorporation is much less favorable. (C) ssNMR REDOR on ^{31}P-^{6}Li coupling shows lithium-phosphorus distances of ≤ 4 Å. A fit with an equal mix of 2.9 Å and 4 Å distances, based on the DFT calculations for the geometry of a Posner molecule with two lithiums replacing the central calcium (shown on the right), shows agreement with the experimental curve.

5.4A), confirming that a new phase of calcium-phosphate forms which we identify as ACP. The ^{31}P signal for ACP in the presence of both lithium isotopes were again similar in linewidth and position, suggesting that lithium incorporates into the calcium phosphate aggregates in an isotope-independent manner.

The incorporation of lithium into the calcium phosphate phase was confirmed using inductively coupled plasma mass spectrometry (ICP-MS). An ACP powder was synthesized as described in the Materials and Methods section, such that initial calcium phosphate nucleation conditions were identical to those measured in DLS. Therefore, if lithium is incorporated in this synthesized powder, then we would also expect it to be present in the soluble structures that we measure using DLS. ^{31}P and ^{6}Li spin counting experiments verified that this synthesized powder was ACP, and that there were no clumps of reprecipitated LiCl in the powder (Fig. C.5). ICP-MS traces for ACP powders synthesized in the presence of 250 mM ^{6}LiCl and ^{7}LiCl indicate that both isotopes were incorporated into the resulting phase at ~ 1 wt% (Fig. 5.4B), with the large error bars resulting from difficulties in ablating the solid powders and mass-dependent transport through the apparatus. Assuming that ACP is $\propto 20$ wt% water [65] and composed of a glass of Posner molecules of stoichiometry $Ca_9(PO_4)_6$, this concentration would corresponds approximately one lithium ion per Posner molecule. Although such "doping" of ACP with lithium has not been reported previously in experiments, previous DFT calculations on Posner molecules indicated an energetic preference for two lithium ions to replace the central calcium ion [55], providing a potential explanation for the observed lithium incorporation.

With the confirmation of lithium incorporation into ACP in an isotope *in*dependent manner, we consider whether later stages of ACP growth could be impacted by lithium addition in an isotope-dependent manner. For the growth of calcium phosphate clusters ($\sim 50 - 100$ nm in diameter) into larger aggregates (several hundred nm – several

microns), we expect that the colloidal aggregation of ACP particles in aqueous salt solution is dominated by Derjaguin-Landua-Verwey-Overbeek interactions, i.e. an interplay between short-range van der Waals attractions and longer-range electrostatic repulsion [206]. Since the lithium isotopes have the same charge and electronic structure, neither of these forces should show a strong isotope dependence, so it is unlikely that the lithium isotope effect arises at this stage. Additionally, we expect the size of metastable ACP particles to be primarily determined by the degree of supersaturation of calcium phosphate in solution. However, the calcium phosphate solid-state boundary shows no isotopic dependence (Fig. 5.3A). This is in agreement with the DLS results that show that there is no isotopic dependence of ACP size.

Given the above arguments, neither the earliest (ionic) nor latest stages (colloidal aggregation) of ACP growth seem likely to be the source of the observed isotope effect. Therefore, we propose that it is during the formation and aggregation of nanoclusters (stage II) of ACP growth that the differential lithium isotope effect must be operative.

5.4 A possible mechanism for a differential isotope effect

To understand a possible mechanism for the lithium isotope effect on calcium phosphate growth, we consider the physical differences between the properties of ^{6}Li and ^{7}Li ions within putative ACP prenucleation species (e.g. Posner molecules). Since the two isotopes of lithium have identical electronic structure, this would presumably rule out any chemical differences in interactions between lithium isotopes, and their nearly identical diffusivities in water indicate similar dynamics in solution. However, the spin properties of ^{6}Li and ^{7}Li differ significantly. ^{6}Li is a spin-1 nucleus, although due to its

small quadrupole moment, it is often considered an "honorary spin-$\frac{1}{2}$" nucleus, with a T_1 relaxation time on the order of minutes [207]. On the other hand, ^{7}Li is a spin-$\frac{3}{2}$ nuclei, with a quadrupole moment two orders of magnitude greater than ^{6}Li, and a T_1 on the order of seconds [207]. Therefore, we expect these two lithium isotopes could have significantly different spin coupling to the ^{31}P nuclei within the Posner molecule, and thus affect their aggregation dynamics, as will be expanded upon later.

To experimentally test whether lithium is proximal enough to phosphorus to have notable spin coupling between the two nuclei, we used the rotational-echo, double-resonance nuclear magnetic resonance (REDOR) sequence on an ACP synthesized in the presence of 250 mM ^{6}Li. Briefly, REDOR is an experiment that can measure dipolar coupling between two heteronuclear spins, from which an inter-spin distance can be extracted [208]. For these measurements ^{6}Li was chosen in the preparation of ACP over ^{7}Li due to its significantly slower relaxation rate, which aids in data acquisition and analysis. However, given that solution NMR and ICP-MS results show similar level of incorporation of ^{6}Li and ^{7}Li into ACP, we expect the results on the ^{6}Li system to also provide insight into the ^{7}Li system.

While REDOR can be difficult to fit to extract precise distances when there is a dispersity of inter-nuclei distances and multi-spin effects, the early time REDOR buildup curve can still indicate the smallest distances (and thus strongest dipolar couplings) in the system. The early-time ^{31}P-^{6}Li REDOR curve (Fig. 5.4C) shows a measurable signal buildup that indicates significant ^{31}P-^{6}Li spin coupling and ^{31}P-^{6}Li distances on the scale of 3-4 Å (The REDOR curve for a 6 Å distance is also shown to illustrate that even slightly farther distances produce large differences in the observed signal). DFT calculations on a Posner molecule with two lithium ions replacing the central calcium ion yield lithium-phosphorus distances of 2.9 Å for three ^{31}P's and 4 Å for the other three ^{31}P's (Fig. 5.4C, right), and a REDOR model based on this distance distribution

shows good agreement with the experimentally measured buildup curve. Regardless of specific distances, the near proximity of the two spins indicates a spin-coupling based mechanism for the differential isotope effect could be physically possible. Notably, this lithium-doped Posner molecule maintains three-fold symmetry within 0.05 Å (which we take to be sufficient given thermal fluctuations), the importance of which is expanded upon below.

Colloidal aggregation can be theoretically described as a diffusion-reaction process by which — for the case of pair binding — individual particles encounter one another by diffusive transport and bind through intermolecular and surface forces. In the case of Posner molecules, calculations on the energy landscape for pair binding have found an energetically preferred orientation of pair binding in which Posner molecules have their C_3 axes anti-aligned [55]. This suggests that there is significant coupling between the rate of pair binding to the orientational dynamics, and thus the relative angular orbital momentum states, of a binding pair of Posner molecules. This provides a potential link between colloidal aggregation and the ^{31}P states of Posner molecules, as follows.

Here we give a brief reminder of the theory behind quantum dynamical selection (QDS). QDS posits that the collective ^{31}P spin states within the Posner molecule function as a qutrit with a quantum number defined by the phase factor acquired during a symmetry-preserving rotation, which we call the "pseudospin." [54]. Due to the Fermi statistics of the spin-$\frac{1}{2}$ phosphorus nuclei under this rotation, the orbital angular momentum (and rotational dynamics) of the molecule is then constrained by this pseudospin. In this way, only certain spin sectors (that sum to zero) are able to access a real wave function (and stop relative rotation between molecules) which is a requirement to form a chemical bond between pairs of Posner molecules (Fig. 5.5A,B). In this way, the ^{31}P spin states of the Posner molecules are proposed to impact the apparent chemical reaction rates of Posner molecule pair-binding - and subsequently, downstream aggregation events

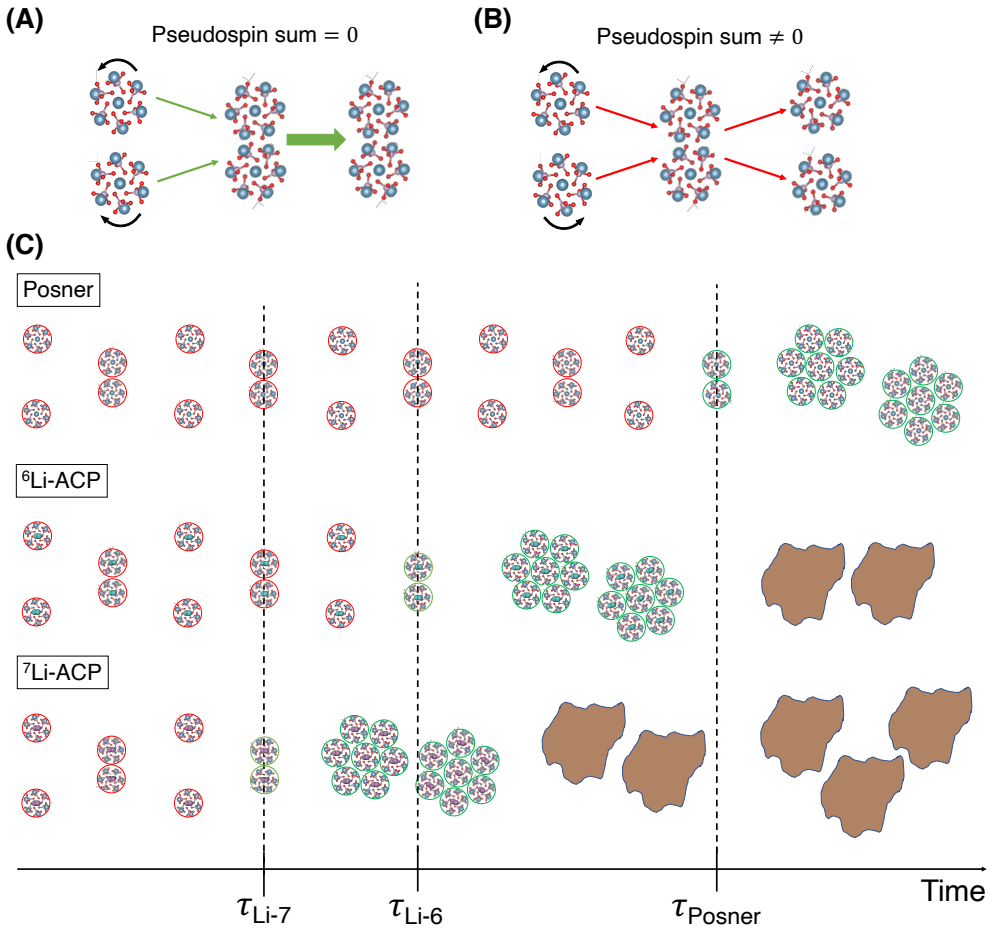

Figure 5.5: An illustration of a potential mechanism for the impact of pseudospin on Posner molecule pair binding. (A) Two anti-aligned Posner molecules with total pseudospin of 0 are able to access a real wave function that is required for bonding. Black arrows indicate that the pseudospins are opposite in this case. (B) Two anti-aligned Posner molecules with non-zero total pseudospin (black arrows in the same direction) are unable to form a real wave function, thus bond formation cannot occur. (C) The pseudospin coherence time, τ, would be shorter for Li-7 doped Posners compared to Li-6 doped or undoped Posners. After a pseudospin restricted binding attempt, the pseudospin would decohere fastest for Li-7 Posners, allowing them to make a new projective measurement onto pseudospin and bind. These bound pairs can then aggregate into larger ACP clusters, resulting in more clusters at the largest size in the presence of Li-7 as compared to Li-6.

in the growth of amorphous calcium phosphate. Note that while we focus on the Posner molecule here, quantum dynamical selection would hold for any calcium phosphate nanocluster with a three-fold or greater symmetry axis, such as the calcium phosphate dimer that has been proposed to have longer spin coherence times than the Posner [209].

This proposal is difficult to test directly because NMR is unable to probe the collective spin state of a molecule; instead measuring an ensemble of spin states across all spins within a given chemical environment. However, we can still consider what measurable consequences the theory would have. These collective spin states will eventually decohere, in a sort of analog to the conventional T_2 relaxation rate for a single spin in NMR, allowing for previously precluded binding to occur. The rate of this decoherence will depend on the coupling of the spins within whom the collective state is encoded (here ^{31}P) to the environment (including other spins within the molecule, such as lithium). Therefore, if two isotopes with different spins were to be incorporated into prenucleation species while preserving the molecular symmetry, one might expect the collective spin state lifetime to differ. In such a case, there might be an appreciable difference in pair-binding reaction rates between the two different isotopically doped species. This concept, and its potential implication on the formation of ACP aggregates, is demonstrated schematically in Fig. 5.5C, comparing a standard Posner molecule to Posners doped with ^{6}Li and ^{7}Li.

While the results we put forward here do not prove that QDS is active in this system, it is currently difficult to put forward any other potential explanation for the observed experimental finding. Our ^{31}P NMR, ICP-MS, and phase mapping results rule out ionic interactions, differential incorporation, or solid phase behavior as potential causes for this isotope effect. As such, it appears that the lithium isotope effect is manifesting during the formation and aggregation of prenucleation clusters, taken here to be Posner molecules for the solution conditions used. This result provides supporting evidence for a central hypothesis of the Quantum Brain theory- that Posner molecule binding is impacted by

nuclear spin states. Regardless of the exact mechanism behind the observed isotope effect, the discovery of an *in vitro* lithium isotope effect on ACP growth is an important step toward understanding the *in vivo* lithium isotope effects that have been observed in a wide range of biological systems.

5.5 Connections with lithium isotope effects in mitochondria

Here, we put forth a possible connection between our *in vitro* results on ACP growth and recent results on a differential lithium isotope in mitochondrial calcium handling [191]. This study treated mitochondria in buffers containing either ^{6}LiCl or ^{7}LiCl, and then exposed these mitochondria to boluses of calcium. It is understood that when mitochondria take up large amounts of calcium, it applies stress to the organelles, leading them to eventually undergo the mitochondrial permeability transition (MPT). At this point a number of correlated events occur, including a release of sequestered calcium [60]. Deline et al. found that the MPT onset in liver mitochondria treated with ^{6}Li was significantly later than those treated with ^{7}Li.

This study also went on to compare the maximum amount of calcium that could be uptaken by liver and brain mitochondria in the presence of ^{6}Li, ^{7}Li, and potassium (K) before they underwent the MPT. In the case of liver mitochondria, ^{7}Li led to the least amount of calcium accumulation before the MPT, followed by ^{6}Li and then K. However, this order was flipped for brain mitochondria, where ^{7}Li allowed for the greatest amount of calcium accumulation before the MPT, and K had the lowest amount of calcium accumulation. To test the origin of this effect, the study examined whether there was a differential uptake or cellular distribution of the two lithium isotopes, but found no

observable differences, indicating that the effect is arising from functional differences between the isotopes.

It has previously been established that calcium is stored within mitochondria in the form of ACP granules during these calcium loading events [61, 30]. Here, we have shown that there is a significant differential lithium isotope effect on ACP formation. Taking these together, one explanation for the observed lithium isotope effect in mitochondria is that the lithium isotopes are effecting the formation of ACP within the mitochondrial matrix in a similar manner to what we have observed *in vitro*. Thus, in the presence of ^{6}Li, there are fewer large ACP granules that are forming in the mitocohndrial matrix than in the presence of ^{7}Li. Since the presence of large ACP granules appear to induce stress on the mitochondria that lead to the MPT, liver mitochondria exposed to ^{6}Li undergo the MPT later than those exposed to ^{7}Li because the lower population of large ACP granules leads to lower mitochondrial stress.

However, because of the central role of calcium in neuronal cells, and the importance of mitochondria in regulating intercellular calcium concentrations, it is feasible that brain mitochondria react very differently to large calcium loads than liver mitochondria. In fact, Deline et al. found that they were unable to induce the MPT in brain mitochondria. Therefore, brain mitochondria may have evolved to be stable in the presence of a large number of calcium phosphate granules in order for them to be able to fulfill their role as neuronal calcium buffers. In that case, the promotion of large ACP granules by ^{7}Li relative to ^{6}Li would allow brain mitochondria to uptake more calcium in the presence of ^{7}Li, as the dense ACP granules would be the most efficient storage mechanism for calcium within the mitochondrial matrix. This increases in calcium uptake in brain mitochondria exposed to ^{7}Li is exactly what was found by Deline et al.

This result on mitochondrial calcium handling offers a remarkable connection between the *in vitro* lithium isotope effect on ACP growth and biologically observed lithium

isotope effects. While this is not confirmation that these isotope effects have the same origin, it is remarkable that these two unexpected results can be coherently explained within the framework of the Quantum Brain theory.

5.6 Conclusion

We have presented evidence for a differential lithium isotope effect on the *in vitro* formation of amorphous calcium phosphate at biologically relevant conditions. Dynamic light scattering experiments showed that while the size of ACP formed is identical in the presence of ^{6}Li and ^{7}Li, certain conditions promote a measurable difference in scattering intensity that indicates a difference in the abundance of nanoscale ACP clusters. ^{31}P NMR measurements confirm the incorporation of both lithium isotopes into the ACP phase and indicate the presence of Li-P spin couplings, indicating the possibility that the observed isotopic effect may be due to differing nuclear spin interactions between ^{6}Li and ^{7}Li and ^{31}P. The reported isotopic effect could potentially be explained by a quantum-based rule for symmetric pre-nucleation molecular binding, QDS, where the spins of the two lithium isotopes differentially impact the probability of Posner binding during early nucleation events.

Our experiments suggest the existence of an *in vitro* differential lithium isotope effect, which has previously only been seen in biological systems. These results offer a potential physical mechanism for previously observed *in vivo* lithium isotope effects, in particular on calcium handling in mitochondria, and is consistent with predictions by the Posner molecule-mediated Quantum Brain theory. Given these findings, we propose that additional investigations of differential isotope effects – both for lithium and other elements – on mineralization processes be undertaken both *in vivo* and *in vitro*. Across all systems, differential isotope effects can expand our understanding of putative quantum

phenomena in both biological and abiotic systems, while in calcium phosphate systems these studies can be used as further validation (or potentially refutation) of the Quantum Brain theory.

5.7 Materials and Methods

Phosphate stock solutions were made by mixing sodium phosphate tribasic (MW 163.94, Acros Organics, pure) and ortho-phosphoric acid (85%, Fisher Scientific) to reach pH 7. Calcium chloride dihydrate (FW 147.01, 99.7% purity) and potassium chloride (MW 74.55, 99-100.5 % purity) was acquired from Fisher Scientific. Lithium-6 chloride (MW 41.47, 95 atom %) and Lithium-7 chloride (MW 42.47, 99 atom %) were acquired from Sigma Aldrich, and ICP-MS confirmed no significant impurities. Sodium hydroxide (MW 40.00, 99% purity, EMD Millipore) was used to create 0.2 M NaOH solution for pH adjustment. Milli-Q water was used for all solutions.

5.7.1 DLS experiments

Dynamic light scattering was conducted with a BI-200SM Goniometer System with a TurboCorr correlator (Brookhaven Instruments) and a Cobolt Samba 500 mW laser at 532 nm (HÜBNER Photonics). DLS measurements were carried out at a 90° scattering angle with 200 correlation channels ranging from 100 ns to 100 ms and sampling rates of 25 ns, 5 ms, and 50 ms, depending on the channel delay.

Solutions were prepared by pH 7 sodium phosphate solution and lithium salt (^{6}LiCl or ^{7}LiCl) in milli-Q water, then adjusting pH to desired value with 0.2 M NaOH. Solutions were then filtered with an inline filtration system using a peristaltic pump and a 0.2 μm pore size cellulose acetate filter for 15 minutes. These solutions were then monitored for 120 with DLS to confirm that there were no significant sources of scattering that would

indicate contamination which could seed nucleation or affect scattering intensities during ACP formation. The solution pH was measured after filtering and heating to 37 °C to confirm that both lithium solutions were still at the same pH.

Once solutions were prepared, aliquots of 2.85 mL were prepared at 37 °C and 100 mM $CaCl_2$ was heated to 37 °C for at least 10 minutes to allow for equilibration. 150 μL of $CaCl_2$ was then added to the aliquots and after 2 seconds the solutions were vortex mixed for 5 seconds before being inserted into DLS sample cell. Samples were then left to sit for 8 seconds to suppress currents from mixing before data collection began, so that DLS data collection began 15 seconds after calcium addition.

DLS was collected in 10 second increments for 5 minutes at 90° scattering angle at 37° C. The z-average size for each 10 second period was found by fitting using the method of cumulants with a quadratic fit, and the intensity was measured in average counts per second at the detector over each 10 second period.

5.7.2 UV-visible spectroscopy

Optical density traces were monitored using a BioTek Synergy Multimode plate reader, with black clear-bottom 384-well plates. Plates were prepared by first setting up an array of solutions containing 250 mM lithium chloride and 2 mM sodium phosphate. The pH of each solution was adjusted to the desired values, ranging from 6.4 to 8.8, using 0.2 M NaOH. These solutions were then transferred into well plates and heated to 37 °C using an Eppendorf Thermomixer, with 3 replicate wells per solution condition. After temperature equilibration for 15 minutes, calcium chloride was added to each well at appropriate volumes to achieve 3 mM, 5 mM, and 7 mM calcium concentrations, followed by rapid mixing for 5 seconds. Absorbance measurements were carried out at 532 nm wavelength over a period of 35 minutes.

5.7.3 Solid ACP synthesis

For solid ACP synthesis, 500 mLs of solution of 2 mM sodium phosphate and 250 mM lithium chloride or potassium chloride were prepared and brought to pH 7.8. Calcium chloride was then added to bring the final calcium concentration to 5 mM. The solution was then let sit for 5 minutes, to allow for initial nucleation events to mimic the conditions used in DLS. 15 mLs 0.2 M NaOH was then added to each sample to cause ACP to precipitate. A Buchner funnel under vacuum with filter paper was used to capture precipitate which was then washed with milli-Q water. The resulting ACP paste was removed from the filter paper and lyophilized for 72 hours to form dried powder and stored at -4 °C.

5.7.4 NMR Experiments

Solution NMR relaxation experiments were performed on a Bruker Avance NEO 500 MHz spectrometer with a CryoProbe Prodigy BBO probe, using Wilmad-LabGlass 5 mm Thin Wall Precision NMR tubes. Solutions were prepared identically to DLS experiments, except with 10% D_2O instead of all milli-Q water. 1D ^{31}P spectra were acquired with a 90 degree pulse and 16 scans, with a delay of 10 second between pulses and a 1 second acquisition time at 37 ° C. Chemical shifts were referenced to 1 M H_3PO4.

Solid state NMR experiments were performed on a Bruker ASCEND DNP-NMR spectrometer (9.4 T) at room temperature and employing a 3.2 mm MAS DNP-NMR triple resonance broadband X/Y/H probe (Bruker) with ^6Li on the Y channel at 10 kHz MAS. REDOR experiments were executed following pulse sequence protocol found in Gulion [208], with cross polarization from ^1H to ^{31}P and power variation on the ^6Li channel. A relaxation delay of 5 s, ^1H $\frac{\pi}{2}$ of 3.92 μs at 50 W, ^{31}P $\frac{\pi}{2}$ of 5.3 us at 100 W, and ^6Li $\frac{\pi}{2}$ of 15.2 us at 250 W were used. Distance simulations were completed

using SIMPSON 4.1.1. Double quantum and triple quantum filtering, along with spin counting experiments, were completed using the same pulse sequence found in Nowotarski et al. (submitted 2023). ^{1}H-^{6}Li and ^{1}H-^{31}P cross polarization was used for spin counting experiments, with a relaxation delay of 5 s and 8 ms mixing time. For ^{6}Li spin counting, a $\frac{\pi}{2}$ pulse of 11.3 μs at 100 W was used, and for ^{31}P, a $\frac{\pi}{2}$ pulse of 5.1 μs at 100 W was used

5.7.5 ICP-MS

ICP-MS experiments were performed with laser ablation on solid powders using the Photon Machines Excite laser and the Agilent 7700X quadrupole ICP-MS. The procedures used followed [210]. Samples were synthesized as described above. ^{7}Li and ^{6}Li signals were calibrated using NIST Standard Reference Material 610.

Chapter 6

Quantum dynamic selection in the TMA-FMO3-TMAO system

6.1 Introduction

Enzyme-catalyzed reactions are ubiquitous in biology, and were conventionally thought to be primarily classical in nature. Recent advances in our understanding of enzymes have revealed that they do utilize quantum phenomena (i.e. quantum tunneling) in navigating potential energy barriers [211]. Enzymatic reactions can also show kinetic isotope effects unrelated to tunnelling, via changes in atomic mass that can impact binding, but these are not fundamentally quantum in that a classical description can still capture the behavior [212].

The proposed theory of quantum dynamical selection states that there could be quantum effects in the binding of symmetric substrates to enzymes [54]. To recall, quantum dynamical selection posits that due to the exchange statistics between fermionic particles (in our case these will be spin $\frac{1}{2}$ nuclei), the allowed orbital angular momentum states of a molecule are linked to the collective spin states of the fermionic nuclei within the

molecule. Specifically, one can look at the phase that these spin states pick up under a symmetric rotation, called a "pseudospin", and only certain pseudospin values would allow the molecule to reach a zero orbital angular momentum state (which allows for a real wave function to be constructed) so that the molecule could form a covalent bond or undergo other processes that require relative motion to stop. Such quantum binding effects would also be operational in any binding process involving small symmetric molecules with three-fold or greater symmetry, but enzyme-catalyzed reactions present an interesting and practical case study in that there is a clearly predicted hypothesis that is experimentally accessible to testing.

Choosing a single substrate enzyme-catalyzed reaction provides the advantage of utilizing the well understood framework of kinetics put forth by Michaelis and Menton[213]. Such kinetics can be characterized by two parameters- V_{max}, the maximum rate of substrate conversion by the enzyme at substrate-saturated conditions, and K_m, the concentration of substrate at which the reaction rate is half of V_{max}, which provides a measure of the binding affinity between the substrate and enzyme. Additionally, in the single substrate system complications such as competing substrates and inhibition can be ignored, allowing for a clear prediction from quantum dynamical selection (a full derivation of this prediction will be shown in the following section).

To find the proper enzymatic system to test the quantum dynamical selection hypothesis, a few conditions must be met. For one, the substrate should be three-fold symmetric (higher-fold symmetries would also be fine, but we focus on three-fold symmetry because of this is the proposed symmetry of Posner molecules). Second, a symmetric rotation of the molecule must spatially swap identical fermionic atoms (i.e. having a fermionic nucleus at the center of rotation is not enough). Third, we must be able to remove the symmetry of the molecule by an isotopic exchange that does not involve a proton. Since the mass change between a proton and deuteron are significantly different, it would be

difficult to interpret any observed effect as QDS-based rather than mass-based. And fourth and finally, we need to have a means of monitoring the enrichment/depletion of the asymmetric molecule as opposed to the symmetric molecule.

While these conditions do not immediately seem highly stringent, it is actually quite difficult to find in the literature enzymatic systems that can fulfill these requirements. However, we have found two such (closely related) systems that are able to meet the criteria. One is the reduction of trimethylamine N-oxide (TMAO) to trimethylamine (TMA) by the recombinant human mitochondrial amidoxime reducing component hmARC1 [214], and the other the oxidation of TMA to TMAO by the human flavin-containing monooxygenase FMO3 [215]. In each case, the substrate has a central nitrogen surrounded by three methyl groups, with TMAO also containing an oxygen bound to the aforementioned nitrogen atom. Structures for TMA and TMAO are shown in Fig. 6.1. A three-fold rotation would swap methyl groups and thus protons within, leading to the required exchange of fermionic nuclei. Additionally, a ^{13}C could replace a ^{12}C in the methyl groups to remove symmetry. Conveniently, the 1% natural abundance of ^{13}C allows one to look for asymmetric effects without requiring a synthetic route to isotopically dope the substrate. Since ^{13}C is NMR active, we can also use a combination of ^{1}H and ^{13}C to monitor the reaction and products. The scope of this work is focused on the oxidation of TMA to TMAO, while another collaborator is testing the QDS hypothesis in the reduction of TMAO. Notably, the theoretical predictions described below are not dependent of which molecule is the substrate and which is the product.

In the following chapter, we introduce Michaelis-Menton kinetics, and characterize the kinetics for the oxidation of TMA via this framework. Subsequently, we derive the quantum dynamical selection prediction for the enrichment of asymmetric (^{13}C-containing) TMA. We then present a NMR-based technique for testing the QDS prediction, and characterize TMA and TMAO to define the parameters to be used to monitor any ^{13}C

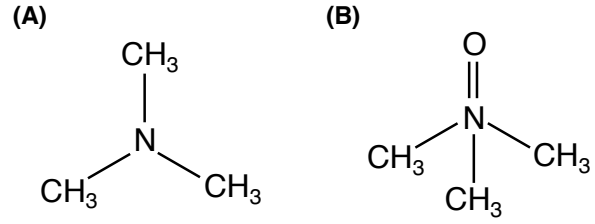

Figure 6.1: Structures of (A) trimethylamine (TMA) and (B) trimethylamine oxide (TMAO).

enrichment in the product. These results lay out a framework for a stringent test of QDS on a three-fold symmetric molecule, which will be a key experiment for verifying or refuting the Quantum Brain theory.

6.2 Michaelis-Menton kinetics

For a single substrate reaction, one can represent the process of events as

$$\mathrm{E} + \mathrm{S} \underset{\mathrm{k_-}}{\overset{\mathrm{k_+}}{\rightleftharpoons}} \mathrm{ES} \xrightarrow{\mathrm{k_{cat}}} \mathrm{E} + \mathrm{P} \tag{6.1}$$

where E is the enzyme, S the substrate, P the product, and with the different kinetic rates for substrate binding, unbinding, and catalyzed product formation given by k_+, k_-, and k_{cat}, respectively. The rate of product formation, v, can be calculated working under the assumptions that the enzyme concentration is much less than the substrate concentration, $[E] << [S]$, and that the substrate and enzyme are freely diffusing through the solution (both of which will be met in our system). The Michaelis-Menton equation states the rate of product formation, v, is

$$v = \frac{d[P]}{dt} = \frac{V_{max}[S]}{K_m + [S]} \tag{6.2}$$

with V_{max} the maximum rate of product formation and K_m the substrate concentration

at which the rate is half of the maximum [213]. A Michaelis-Menton curve is shown in Fig. 6.2 illustrating these values graphically. As one might expect, V_{max} should increase linearly with enzyme concentration (staying within the regime $[E] << [S]$), while K_m is be independent of enzyme or substrate concentration.

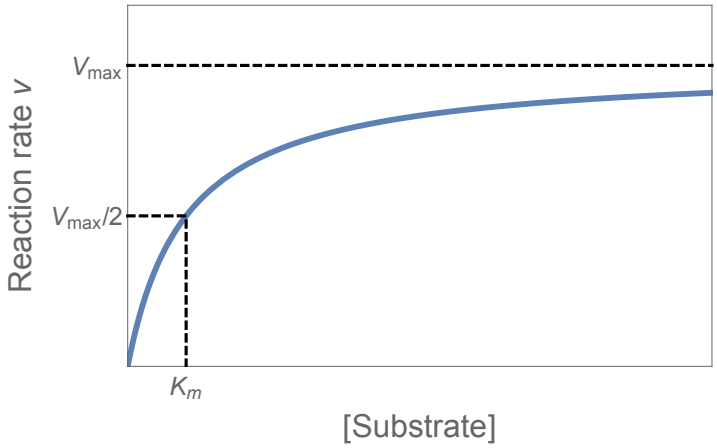

Figure 6.2: Generic Michaelis-Menton curve illustrating V_{max} and K_m.

To determine the parameters V_{max} and K_m, one varies the initial substrate concentration and measures the initial rate of product formation (before the substrate concentration has significantly changed). A non-linear regression model can then be used to fit these data and extract V_{max} and K_m, as will be done for our TMA-FMO3-TMAO system below.

In our case, it will also be useful to integrate this equation in order to characterize the reaction extent as a function of time, defined as $R(t) = \frac{[P]}{[S]_0}$, where $[S]_0$ is the initial substrate concentration. This function is 0 at $t = 0$, and will go to 1 at long times once all of the substrate has been converted into product. The exact closed-form solution to the Michaelis-Menton equation is given by [216]

$$[S(t)] = K_m * W\left(\frac{[S]_0}{K_m} * exp(\frac{[S]_0 - V_{max}t}{K_m}\right) \tag{6.3}$$

where $W(x)$ is the Lambert W-function. One can then convert $[S(t)]$ to $R(t)$ by noting that $[S(t)] = [S]_0 - [P(t)]$. Thus, once the parameters V_{max} and K_m have been experimentally determined, we can determine the reaction extent for a system as a function of time.

6.3 Quantum dynamical selection

Now we shift from classical enzyme kinetics to a derivation of the expected effect of quantum dynamical selection on the product formation from symmetric vs. asymmetric substrate. In this case, we can represent the reaction pathways by

$$\mathrm{E} + \mathrm{S_{sym}} + \mathrm{S_{asym}} \underset{\mathrm{k_-}}{\overset{\mathrm{k_{sym}}}{\rightleftharpoons}} \mathrm{ES_{sym}} + \mathrm{S_{asym}} \xrightarrow{\mathrm{k_{cat}}} \mathrm{E} + \mathrm{P_{sym}} + \mathrm{S_{asym}} \tag{6.4.1}$$

$$\mathrm{E} + \mathrm{S_{sym}} + \mathrm{S_{asym}} \underset{\mathrm{k_-}}{\overset{\mathrm{k_{asym}}}{\rightleftharpoons}} \mathrm{ES_{asym}} + \mathrm{S_{sym}} \xrightarrow{\mathrm{k_{cat}}} \mathrm{E} + \mathrm{P_{asym}} + \mathrm{S_{sym}} \tag{6.4.2}$$

where S_{sym}, S_{asym}, P_{sym}, and P_{asym} are the symmetric and asymmetric substrate and product, respectively. Note that while the binding rates are different for the symmetric and asymmetric substrates, the unbinding rates and enzyme-catalyzed rate of product formation do not depend on substrate symmetry. For a substrate with λ-fold symmetry, QDS states that the binding rates for the two forms of substrate will be related by [54]

$$k_{asym} = \lambda k_{sym} \tag{6.5}$$

since only one of the λ pseudospin states will be able to form a real wave function and bind to the enzyme, while the asymmetric substrate has no such restrictions.

One can then consider the equations governing the rate of change for each species and the conservation of the total amount of enzyme and substrate-plus-product, giving

$$\frac{dS_{sym}}{dt} = k_{-}ES_{sym} - k_{sym}E * S_{sym} \tag{6.6.1}$$

$$\frac{dS_{asym}}{dt} = k_{-}ES_{asym} - k_{asym}E * S_{asym} \tag{6.6.2}$$

$$\frac{dES_{sym}}{dt} = k_{sym}E * S_{sym} - k_{-}ES_{sym} - k_{cat}ES_{sym} \tag{6.6.3}$$

$$\frac{dES_{asym}}{dt} = k_{asym}E * S_{asym} - k_{-}ES_{asym} - k_{cat}ES_{asym} \tag{6.6.4}$$

$$\frac{dP_{sym}}{dt} = k_{cat}ES_{sym} \tag{6.6.5}$$

$$\frac{dP_{asym}}{dt} = k_{cat}ES_{asym} \tag{6.6.6}$$

$$\frac{dE}{dt} = k_{-}(ES_{sym} + ES_{asym}) + k_{cat}(ES_{sym} + ES_{asym}) - k_{sym}E * S_{sym} - k_{asym}E * S_{asym} \tag{6.6.7}$$

$$E + ES_{sym} + ES_{asym} = E_0 \tag{6.7.1}$$

$$S_{sym} + ES_{sym} + P_{sym} = S^0_{sym} \tag{6.7.2}$$

$$S_{asym} + ES_{asym} + P_{asym} = S^0_{asym} \tag{6.7.3}$$

where equations 6.7.1-6.7.3 define the initial enzyme, symmetric substrate, and asymmetric substrate concentrations, respectively. Combining equations 6.6.1-6.6.4 with equation 6.6.7, we get

$$\frac{dS_{sym}}{dt} = k_{-}ES_{sym} - k_{sym}(E_0 - ES_{sym} - ES_{asym}) * S_{sym} \tag{6.8.1}$$

$$\frac{dS_{asym}}{dt} = k_{-}ES_{asym} - k_{asym}(E_0 - ES_{sym} - ES_{asym}) * S_{sym} \tag{6.8.2}$$

$$\frac{dES_{sym}}{dt} = k_{sym}(E_0 - ES_{sym} - ES_{asym}) * S_{sym} - k_{-}ES_{sym} - k_{cat}ES_{sym} \tag{6.8.3}$$

$$\frac{dES_{asym}}{dt} = k_{asym}(E_0 - ES_{sym} - ES_{asym}) * S_{asym} - k_{-}ES_{asym} - k_{cat}ES_{asym} \tag{6.8.4}$$

so that we now have a system of four equations for four unknowns ($S_{sym}, S_{asym}, ES_{sym}$, ES_{asym}). We also know our initial $t = 0$ and our final $t \to \infty$ (i.e. the reaction has run to completion) conditions are

$$S_{sym}(0) = S^0_{sym} \tag{6.9.1}$$

$$S_{asym}(0) = S^0_{asym} \tag{6.9.2}$$

$$ES_{sym}(0) = ES_{asym}(0) = 0 \tag{6.9.3}$$

$$S_{sym}(t \to \infty) = S_{asym}(t \to \infty) = ES_{sym}(t \to \infty) = ES_{asym}(t \to \infty) = 0 \tag{6.10.1}$$

$$P_{sym}(t \to \infty) = S^0_{sym} \tag{6.10.2}$$

$$P_{asym}(t \to \infty) = S^0_{asym} \tag{6.10.3}$$

We now make the assumption that enzyme-substrate complex is quasi-stationary, since we have $[S(t)] >> [E]$ for almost all of the course of the reaction. Therefore we can set

$$\frac{dES_{sym}}{dt} = \frac{dES_{asym}}{dt} = 0 \tag{6.11}$$

allowing so that the left hand side of equations 6.8.3 and 6.8.4 is 0, giving

$$ES_{sym} = \frac{E_0 S_{sym}}{S_{sym} + \frac{k_{sym}}{k_{asym}} S_{asym} + \frac{k_- + k_{cat}}{k_{sym}}} \tag{6.12.1}$$

$$ES_{asym} = \frac{E_0 S_{asym}}{S_{asym} + \frac{k_{asym}}{k_{sym}} S_{sym} + \frac{k_- + k_{cat}}{k_{asym}}} \tag{6.12.2}$$

Combining equations 6.6.5 and 6.6.6 with equations 6.12.2 and 6.12.1 gives

$$\frac{dP_{sym}}{dt} = -\frac{dS_{sym}}{dt} = \frac{V_{max} S_{sym}}{S_{sym} + \frac{k_{sym}}{k_{asym}} S_{asym} + \frac{k_- + k_{cat}}{k_{sym}}} \tag{6.13.1}$$

$$\frac{dP_{asym}}{dt} = -\frac{dS_{asym}}{dt} = \frac{V_{max}S_{asym}}{S_{asym} + \frac{k_{asym}}{k_{sym}}S_{sym} + \frac{k_- + k_{cat}}{k_{asym}}} \tag{6.13.2}$$

where $V_{max} = k_{cat}E_0$ is the same value a introduced in equation 6.2 for Michaelis-Menton kinetics.

We now make the assumption that $S_{asym} << S_{sym}$, i.e. that the amount of asymmetric substrate is much smaller than the amount of symmetric substrate. While this may not be the case for all systems, for our TMA-FMO3-TMAO system we are using the natural abundance of ^{13}C to cause asymmetry in our substrate. Given that the natural abundance of ^{13}C is $\sim$1.1%, we expect $\sim$1 in 33 TMA molecules will have a ^{13}C on one of the methyl groups, and therefore be asymmetric. In this limit, we can write equations 6.13.1 and 6.13.2 as

$$\frac{dS_{sym}}{dt} = -\frac{V_{max}S_{sym}}{S_{sym} + \frac{k_- + k_{cat}}{k_{sym}}} \tag{6.14.1}$$

$$\frac{dS_{asym}}{dt} = -\frac{V_{max}S_{asym}}{S_{sym} + \frac{k_- + k_{cat}}{k_{sym}}} * \frac{k_{asym}}{k_{sym}} \tag{6.14.2}$$

where we have factored out the term $\frac{k_{asym}}{k_{sym}}$ from equation 6.14.2 in order to make the denominators of the two equations equivalent. Now, dividing equation 6.14.2 by 6.14.1, we get

$$\frac{dS_{asym}}{dt} / \frac{dS_{sym}}{dt} = \frac{k_{asym}}{k_{sym}} * \frac{S_{asym}}{S_{sym}} \tag{6.15.1}$$

from which follows

$$\frac{d}{dt}ln(S_{asym}) = \frac{k_{asym}}{k_{sym}}\frac{d}{dt}ln(S_{sym}) \tag{6.15.2}$$

We now recall equation 6.5 to substitute λ for $\frac{k_{asym}}{k_{sym}}$, and integrate equation 6.15.2 to find

$$ln(\frac{S_{asym}(t)}{S^0_{asym}}) = \lambda * ln(\frac{S_{sym}(t)}{S^0_{sym}}) \tag{6.16}$$

which yields

$$\frac{S_{asym}(t)}{S^0_{asym}} = \left(\frac{S_{sym}(t)}{S^0_{sym}}\right)^{\lambda} \tag{6.17}$$

Now, we note that our substrate is much more abundant than our enzyme, i.e. $S^0 >> E_0$, for both the symmetric and asymmetric substrates (this same limit is applied in Michaelis-Menton kinetics). For our specific system, the enzyme concentration will be on the order of 100 nM, while the substrate will be on the order of 1 mM, so this condition is satisfied for almost the entire reaction (even at 99% completion our substrate will still be x100 more abundant). This also gives

$$ES_{sym} << S_{sym} \tag{6.18.1}$$

$$ES_{asym} << S_{asym} \tag{6.18.2}$$

allowing so that equations 6.7.2 and 6.7.3 can be written as

$$P_{sym}(t) \approx S^0_{sym} - S_{sym}(t) \tag{6.19.1}$$

$$P_{asym}(t) \approx S^0_{asym} - S_{asym}(t) \tag{6.19.2}$$

From equations 6.17, 6.19.1, and 6.19.2, as well as our definition of reaction extent $R(t) = \frac{P}{S^0}$, we get

$$1 - \frac{P_{asym}(t)}{S^0_{asym}} = (1 - R(t))^{\lambda} \tag{6.20}$$

where $S_{asym} << S_{sym}$ and $P_{asym} << P_{sym}$ so that the reaction extent can be approximated as $R(t) = \frac{P_{sym}}{S^0_{sym}}$. Dividing by $R(t) = \frac{P_{sym}(t)}{S^0_{sym}}$ (noting that the result is valid only once some amount of product has been formed), we get

$$\frac{P_{asym}(t)}{S^0_{asym}} / \frac{P_{sym}(t)}{S^0_{sym}} = \frac{1 - (1 - R(t))^{\lambda}}{R(t)} \tag{6.21}$$

Finally, we can define an enrichment factor, or selectivity, of asymmetric product, $Enr(t)$, as

$$Enr(t) = \frac{P_{asym}(t)}{P_{sym}(t)} / \frac{S^0_{asym}}{S^0_{sym}} \tag{6.22}$$

that describes the preference for creating asymmetric product over symmetric product. Substituting $\lambda = 3$ for our specific case of three-fold symmetric substrate, this gives

$$Enr(t) = \frac{1 - (1 - R(t))^{\lambda}}{R(t)} \tag{6.23}$$

We compare this QDS-predicted enrichment factor to the classical case, where there is no expected difference between the symmetric and asymmetric substrates (or equivalently that $\lambda = 1$, so that $k_{sym} = k_{asym}$), in which case we expect no enrichment in our asymmetric product through the entire course of the reaction. This enrichment factor is shown in Fig. 6.3 for our TMA-FMO3-TMAO system, where the enrichment would be measurable by the ^{13}C content in the product.

Notably, QDS predicts a strong deviation from the classical theory for the amount of ^{13}C TMAO produced from our system. Thus, by measuring the ^{13}C content in TMAO as a function of the reaction extent, we should be able to rigorously test whether this

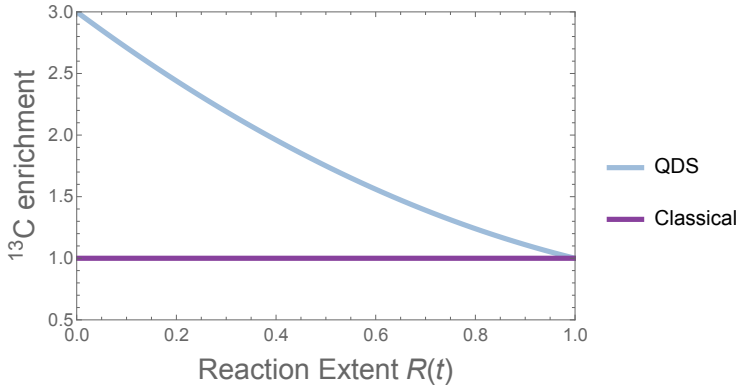

Figure 6.3: A comparison of the classical and QDS predictions for ^{13}C enrichment in TMAO produced from the TMA-FMO3-TMAO system as a function of the extent of reaction. At early extent of reaction, the ^{13}C enrichment in TMAO is up to x3 the classical prediction, while at at the end of the reaction the enrichment factors are identical, as all TMA (symmetric or asymmetric) has been converted to TMAO.

theory holds for this three-fold symmetric system.

6.4 Results on TMA-FMO3-TMAO system

6.4.1 Characterization of enzyme kinetics

The first step for a rigorous experimental test of the QDS-prediction in equation 23 is to find the kinetic parameters V_{max} and K_m for the TMA-FMO3-TMAO system, so that we can use equation 6.3 to find our reaction extent $R(t)$ as a function of time. In order to measure these parameters, we prepare a reaction mixture with the following components (excluding the enzyme) based on previous work using the FMO3 enzyme to run an oxidative reaction [217]: potassium phosphate buffer (pH 7.4, 100 mM), sodium chloride (150 mM), catalase (100 units/mL), superoxide dismutase (100 units/mL), bovine serum albumin (0.1 mg/mL), NADPH (0.1 mM), TMA (1 mM). In this system, NADPH is the reducing agent, donating it's electron for the oxidation of TMA to TMAO and resulting in $NADP^+$. When the full enzymatic reaction is studied, we will also add in a NADPH-

regenerating system consisting of glucose-6-phosphate dehydrogenase (2 units/mL) and glucose-6-phosphate (20 mM), so that NADPH is not depleted during the course of the reaction, which could cause the reaction rate is slow or go to zero at full depletion.

The advantage of having the NADPH depleted during these initial assays is that NADPH absorbs strongly at 340 nm, while $NADP^+$ does not. Therefore, we can measure the optical density at 340 nm as a proxy for the reaction rate, given that we should have a 1:1 relation of reduced NADPH to oxidized TMAO. As a first assay, we confirm NADPH reduction by measuring the optical density as a function of time after adding in FMO3 at 4 concentrations (0, 150, 300, and 600 nM). As shown in Fig. 6.4A, we have a time window for each concentration after FMO3 addition during which the optical density at 340 nm decreases linearly (with the exception when no enzyme is present, which serves as the control and no significant change in the optical density over time). From these optical density curves, we can convert to a rate of TMAO production by extracting the slope from a linear fit of the data, using the molar attenuation of NADPH at 340 nm of 6.22 mol^{-1} cm^{-1} and knowing the volume of reaction mixture and dimensions for each cell in the plate reader. We find that the rate of TMAO production goes linearly with the enzyme concentration, as is predicted by Michaelis-Menton kinetics (Fig. 6.4B).

We now use the same reaction mixture, but set the enzyme concentration constant at 300 nM and vary the substrate concentration, in order to measure our Michaelis-Menton plot and calculate V_{max} and K_m for this system. Using TMA concentrations of 0.01, 0.1, 0.5, and 1 mM, we conduct an identical spectrophotometric assay, measuring optical density at 340 nm to track NADPH reduction. The results are shown in Fig. 6.5A. The corresponding rate of TMAO production for each initial TMA concentration can then be extracted using the same method as above, producing the Michaelis-Menton curve in Fig. 6.5B. The resulting parameter values of the reaction mixture are $V_{max} = 7.17\mu M/s$ and a $K_m = 36.8\mu M$, allowing us to find the reaction extent $R(t)$ as a function of time.

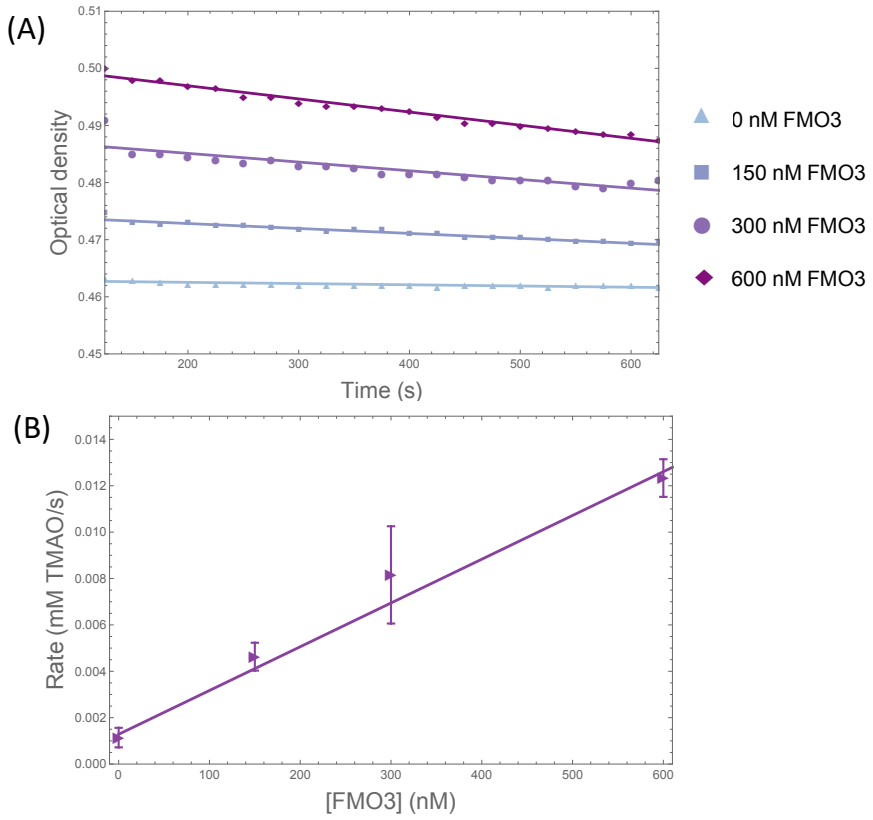

Figure 6.4: Spectrophotometric assay results for the reaction mixture showing the effect of different enzyme concentrations. (A) Optical density at 340 nm as a function of time after FMO3 addition, with linear fits shown in order to extract rates of NADPH reduction. Optical densities are the average of 3 trials. (B) Rates extracted from (A) and converted into TMAO production as a function of FMO3 concentrations, confirming a linear relationship between enzyme concentration and product formation for this enzyme concentration regime. Error bars are 95% confidence intervals from linear fits in (A).

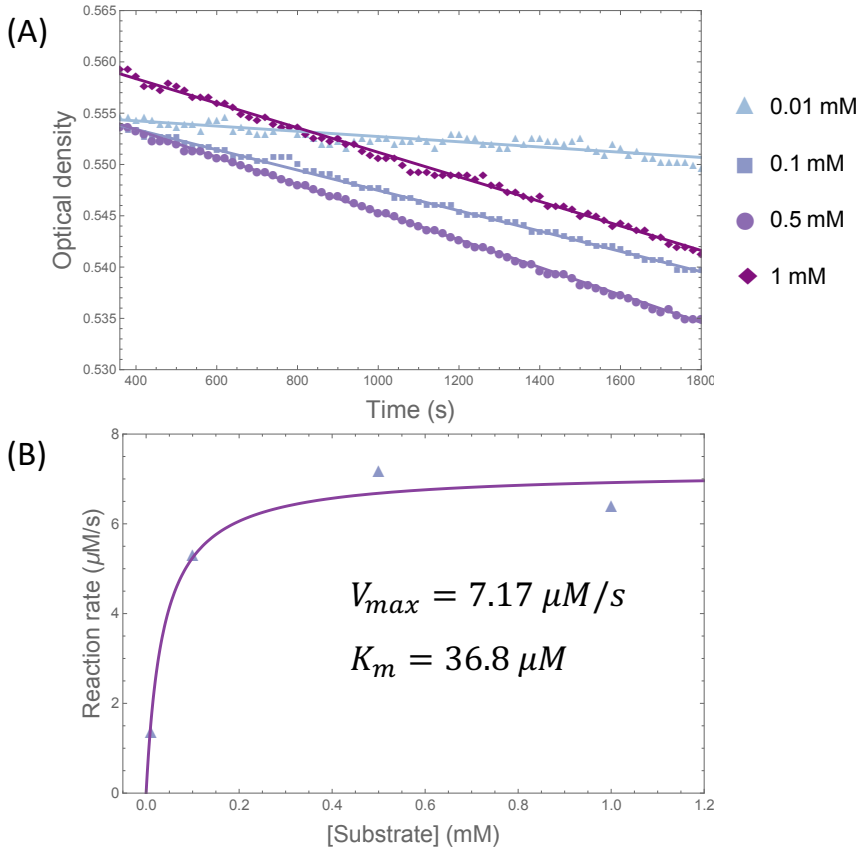

Figure 6.5: Michaelis-Menton kinetic curve for the TMA-FMO3-TMAO system found by varying TMA concentrations. (A) Optical density at 340 nm as a function of time after FMO3 addition for different TMA concentrations, with linear fits shown in order to extract rates of NADPH reduction. Optical densities are the average of 3 trials. (B) Reaction rates from (A) plotted as a function of initial substrate concentration, with the fitted Michaelis-Menton curve and corresponding parameter values for V_{max} and K_m.

6.4.2 NMR characterization of TMA and TMAO

We now shift to the ^{1}H and ^{13}C NMR characterization of TMA and TMAO. In order to monitor the potential enrichment of ^{13}C-containing TMAO, i.e. asymmetric product, (and corresponding depletion of ^{13}C-containing TMA) we will use both ^{1}H and ^{13}C NMR. This will allow for 2 different measurements of ^{13}C content. For one, we can compare the ^{13}C integral of TMA and TMAO at different points along our reaction extent, normalizing

by ^{1}H integral for each species. We note here that only the asymmetric substrate and product will contribute to the ^{13}C signal (except in the event of a molecule with three ^{13}C's, but we ignore this possibility given the 1% natural abundance of ^{13}C, so that this would only occur in 1 in 10^{6} molecules). However, all substrate and product molecules will contribute to the ^{1}H integral, so that this ratio will provide information on the relative abundance of ^{13}C within the substrate/product.

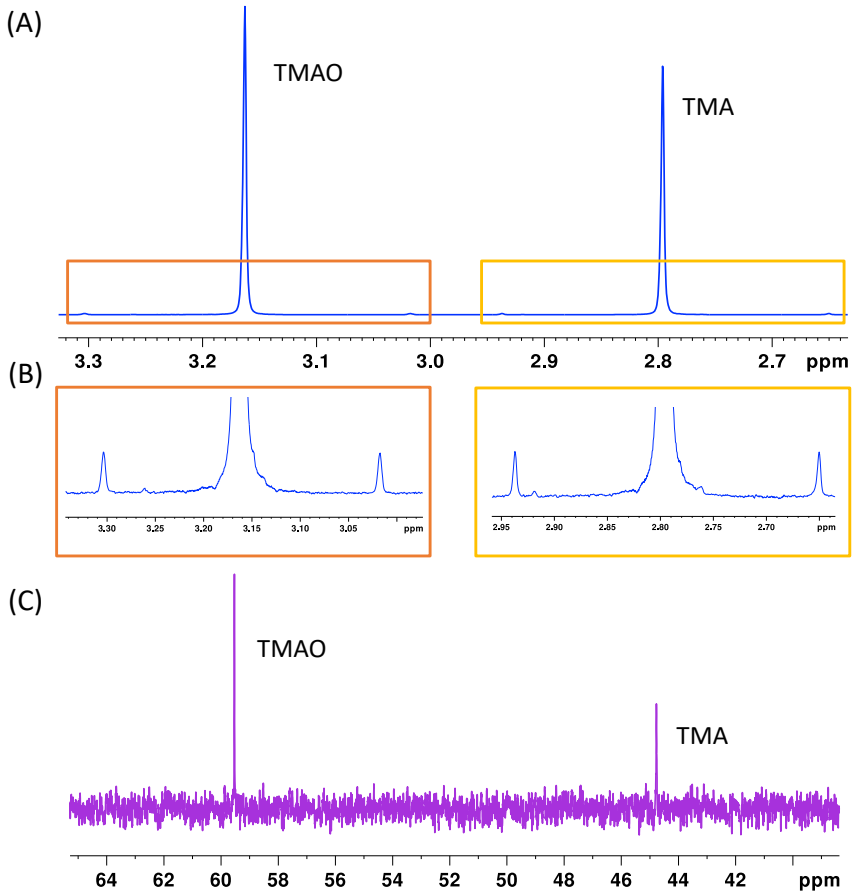

Figure 6.6: NMR spectra for 1 mM TMA and 1 mM TMAO showing (A) The full ^{1}H spectrum, (B) A zoom in on the 1:200:1 triplets in the ^{1}H spectrum, and (C) The ^{13}C spectrum. Spectra were acquired with the acquisition parameters described in the text.

The second means for quantifying the ^{13}C content is to utilize the scalar-coupling between a ^{13}C and the protons on the corresponding methyl group. As shown in Fig.

6.6B, there is scalar coupling of $70Hz$, leading to a $1:200:1$ triplet in the proton spectra for both TMA and TMAO, as would be expected given the 1% natural abundance of ^{13}C. Measuring this triplet ratio at different reaction extents thus provides a second measure of the ^{13}C content in both TMA and TMAO.

To make quantitative NMR measurements, it is important to first characterize the NMR signals for both TMA and TMAO to make sure that the lines are well resolved and to optimize NMR acquisition parameters. Additionally, we want to find the approximate error in the NMR integrals (by measuring several independently prepared samples), to confirm that we are able to measure these integrals with the necessarily precision to rigorously test the QDS hypothesis. As shown in Figures 6.6A and C, both the ^{1}H and ^{13}C signals for TMA and TMAO are well resolved and without overlap.

It is also important to characterize the ^{13}C T_1 times for both molecules to optimize our acquisition parameters. While the ^{1}H signal should be strong, given the 100% proton abundance and the high gyromagnetic ratio of protons, the ^{13}C, however, is much weaker due to both low abundance and low gyromagnetic ratio. ^{13}C T_1 was measured for both TMA and TMAO via an inversion recovery sequence and was found to be 8 s and 2.5 s, respectively. Given that our ^{13}C pulse program utilizes a 45° pulse, we can use the concept of the Ernst angle to optimize our signal. The Ernst angles defines the relationship between pulse angle, T_1, and time between pulses that will maximize the NMR signal in a set experiment time as $Cos(\theta_E) = Exp(-\frac{d1+at}{T_1})$, where $\theta_E = 45°$ is the pulse angle, $d1$ is the delay between pulses, and at is the FID acquisition time. Given our measured ^{13}C T_1 values, we find the optima $d1 + at$ for TMA and TMAO to be 2.77 s and 0.87 seconds, respectively. Therefore, we opt for the following ^{13}C acquisition parameters: 2048 scans, 45° pulse, $d1 = 1.5$ s, and $at = 1$ s, with a NOE sequence to help increase signal by transferring polarization from protons to ^{13}C. For ^{1}H, we use the following parameters: 64 scans, 90° pulse, $d1 = 7$ s, and $at = 2$ s, with a water suppression

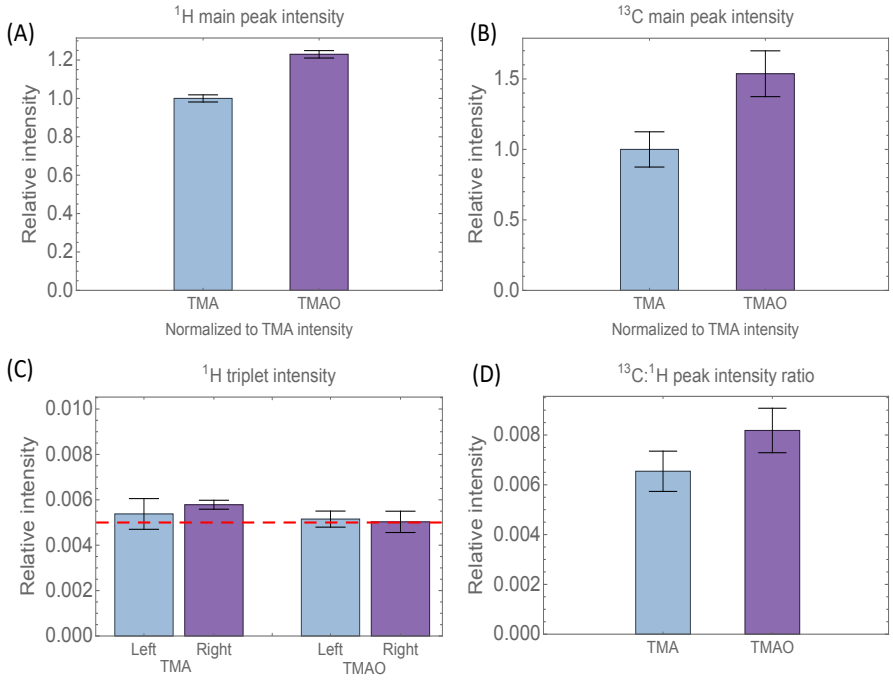

Figure 6.7: NMR characterization of error in ^{1}H and ^{13}C integrals for 1 mM TMA and 1 mM TMAO. Error bars represent the standard error over 5 independent trials. The relative error for the triplet intensities are $< 10\%$ of the signal, and for ^{13}C:^{1}H the relative errors are $< 20\%$ of the signal. Given that the QDS prediction is a factor of 3 different than the classical prediction, the predicted effect is well outside of the experimental error.

sequence that irradiates at the frequency of water to prevent the water proton signal from dominating the spectrum.

Using the above acquisition parameters, we measured the ^{1}H and ^{13}C signal for 5 independently prepared samples of 1 mM TMA and 1 mM TMAO in a 10% D_2O solution to measure the error that we expect in our integrals. Since we will be using 10 mM TMA in our full reaction mixture experiments, this should provide a good upper bound on the error we would expect if aliquots are taken between 10% and 90% of reaction extent. The results of these experiments are shown in Fig. 6.7, with error bars corresponding to the standard error across the five trials. From these error bars, we note that these NMR parameters should be fully sufficient to test the QDS prediction, given that the

error is $\sim 10 - 20\%$ of the integral, while QDS predicts an effect of up to 3-fold at short times, and greater than 1.1-fold up to 90% of reaction extent (Fig. 6.3). Therefore, our NMR characterization should provide a rigorous test of the QDS hypothesis in the TMA-FMO3-TMAO system.

6.4.3 Testing the QDS hypothesis

To test for QDS effects, the full reaction mixture is prepared, as introduced in section 6.4.1, and an initial 200 μL aliquot was removed. FMO3 is then added to initiate the reaction. At time points corresponding to 10%, 20%, 50%, and 90% extent of reaction, as calculated from equation 6.3 and the parameter values in Fig. 6.5, 200 μL aliquots were removed. Each aliquot is mixed with an equal volume of acetonitrile to quench the reaction at the desired time point. This quenching of the reaction is essential so that there is no additional product formation during the NMR experiments. Each aliquot is then diluted to 500 μL with milli-Q and then placed in a 10 kDA MW cutoff centrifuge filter and centrifuged at 4 °C until $> 90\%$ of the sample has been filtered. The filtrate is then removed and diluted with 10% D_2O and stored frozen until NMR analysis.

The ^{13}C and ^{1}H spectra can then be acquired for each aliquot using the acquisition parameters described above to test the enrichment of ^{13}C TMAO. Both measures of ^{13}C content (^{13}C integral and ^{1}H triplet integrals) can be extracted, to confirm that they are in agreement. From these integrals, one can plot the ^{13}C enrichment in TMAO as a function of reaction extent, and compare the measured values with the theoretical predictions presented in Fig. 6.3 for classical and QDS enzyme kinetics. Such an experiment should provide a strong test of whether QDS is active in for a three-fold symmetric substrate in an enzymatic system.

Here, we have laid out the theoretical predictions and experimental protocols nec-

essary for testing the QDS hypothesis. These experiments should be able to provide strong evidence for (or against) QDS effects on a three-fold symmetric substrate. Given the importance of QDS within the Quantum Brain theory, this work will be a key step towards testing the potential validity of the theory.

6.5 Material and Methods

Potassium phosphate buffer was made from potassium phosphate monobasic (FW 136.09, 99.9% purity) from Fisher Scientific and sodium hydroxide (FW 40.00, 99% purity) from EMD. Sodium chloride (FW 58.44, 99.5% purity) was purchased from Fisher Scientific. Trimethylamine N-oxide (MW 75.11, 95% purity), Trimethylamine hydrochloride (MW 95.57, 98% purity), NADPH (tetrasodium) (MW 833.4, 98% purity), catalase from bovine liver (aqueous suspension, 10,000-40,000 units/mg protein, 44 mg protein/ml), bovine serum albumin solution (30% in saline), D-glucose 6-phosphate disodium salt dihydrate (MW 304.1 (anhydrous basis), 98% purity), superoxide dismutase powder (recombinant, expressed in E-Coli, 3010 units/mg protein, 90% purity), glucose-6-phosphate dehydrogenase from baker's yeast (lyophilized, 200-400 units/mg protein), and flavin-containing monooxygenase-3, microsomes human (recombinant, expressed in baculovirus infected insect cells, buffered aqueous solution), and acetonitrile were purchased from Sigma Aldrich.

6.5.1 Spectrophotometric Assays

Optical density traces were monitored using a BioTek Synergy Multimode plate reader, with black clear-bottom 384-well plates. The reaction mixture was prepared as described in the text and heated to 37 °C using an Eppendorf Thermomixer before FMO3 was added. After adding FMO3, solutions were pipette mixed. Absorbance mea-

surements were carried out at a 340 nm wavelength for one hour, and a linear region was selected to obtain reaction rates.

6.5.2 NMR Experiments

Solution NMR relaxation experiments were performed on a Bruker Avance NEO 500 MHz spectrometer with a CryoProbe Prodigy BBO probe, using Wilmad-LabGlass 5 mm Thin Wall Precision NMR tubes. 10% D_2O was used in all solutions. T_1 relaxation was measured with a standard inversion-recovery pulse sequence, and relaxation times were determined by employing the TopSpin 4.0.6 T1/T2 dynamics module with monoexponential fitting. Acquisition parameters for 1D ^{1}H and ^{13}C experiments are described in the text.

Chapter 7

Conclusions and Future Directions

7.1 Summary and Outlook

In this thesis we have put forward some of the experimental progress that has been made towards testing the Quantum Brain theory. This effort has also led to a greater understanding of the solution behavior of calcium phosphate species. We have established the existence of previously unknown 'dark state' phosphate assemblies, adding to our understanding of solution behavior of phosphates as well as revealing the complexity of ^{31}P spin dynamics. We have shown that calcium phosphate nanoclusters are stable in simple simulated body fluids, directly measured their size, and presented evidence for an equilibrium between different hypothesized nanocluster species. We have also uncovered a differential lithium isotope effect in the formation of amorphous calcium phosphate, which points towards the possibility of nuclear spins directly impacting early nucleation events, and connected our *in vitro* results with observed *in situ* results on mitochondrial calcium dynamics. Finally, we have laid out a platform for testing QDS directly in an enzymatic reaction involving a three-fold symmetric substrate, which should present strong experimental evidence for the existence (or lack thereof) of QDS effects.

While this work provides important answers regarding the feasibility of the Quantum Brain theory, there are still open fundamental questions that must be probed experimentally. Regarding Posner molecules, what is the ^{31}P spin relaxation time for stable monomers? And do Posners have the three-fold (or higher) order symmetry that is required by QDS? Additionally, direct evidence for or against QDS in systems with greater than two-fold symmetry should answer the question of whether nuclear spin states can be transduced into biochemical signals that could then impact neuronal function.

There are also important questions from a biological standpoint which are being investigated by collaborators with expertise in these areas. If Posner molecules are fundamental to brain function, and exist within mitochondria, then there are almost certainly proteins which interact with Posners (to stabilize, transport, or otherwise manipulate them) located within the mitochondrial matrix. Ongoing proteomics work is aimed at identifying candidate proteins that could interact with Posner molecules, which could create experimental opportunities for measuring their ^{31}P spin dynamics in solution. Additionally, experiments on lithium isotopes in neuronal cell signaling could help connect results on lithium isotope effects on *in vivo* calcium phosphate and *in situ* mitochondrial dynamics with observed behavioral impacts of rodents, and even humans. Even outside the context of the Quantum Brain theory, given the importance of lithium as a drug for bipolar disorder, a greater understanding of the functionality behind lithium as a medicine (and any differential impact between lithium-6 and lithium-7) would be an important advancement.

Hopefully these future experiments, in combination with the results put forth in this thesis, can help to provide a definitive answer on the potential validity of the Quantum Brain theory and the potential for Posner molecules to be biological units for the storage and processing of quantum information.

In this chapter, we will present some future research directions that build off of the

work in this thesis. Some of these directions will relate directly to the Quantum Brain theory, while others will focus on the solution behavior of calcium phosphates from a more general perspective.

7.2 Phosphate assemblies

In Chapter 3, we presented our discovery of phosphate assemblies in aqueous solution, which appear to be loosely-bound (potentially liquid-like) clusters of phosphates that exist in exchange with individual ions. This assembly process appears to be entropically-driven, with our hypothesis being that the release of bound waters in the phosphate hydration shell provides the entropic gain that leads to assembly formation. This discovery has opened up several questions, both about the nature of these assemblies and also what impact they may have on solution processes involving phosphates, such as calcium phosphate formation.

In regard to the first question, ongoing work has aimed at more direct detection of the assemblies. While ^{31}P relaxometry and CEST, as well as cryo-TEM and MD studies, all showed evidence for the assemblies, their ^{31}P NMR signal was never directly observed. Towards this end, Lu, Straub, et al. (*submitted*) have used colder temperatures and more viscous solutions to slow down exchange enough to observe a CEST peak that can be attributed to the phosphate assemblies. By varying power and modeling the CEST spectrum, important physical parameters such as assembly population and monomer-assembly exchange can be extracted more accurately than was done in Chapter 3. This work provides a method for further detection and understanding of phosphate assemblies, with the potential to be applied to biological systems, where phosphates play several fundamental roles and these assemblies could be functionally important.

The presence of phosphate assemblies in solution is also likely to be important in ag-

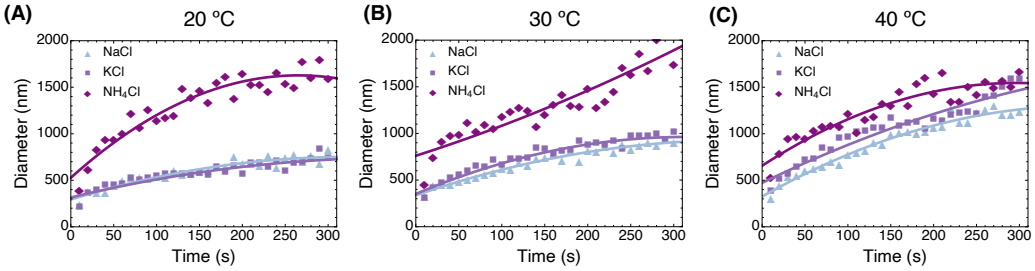

Figure 7.1: Impact of different salts on the formation of ACP as measured by DLS. Solutions consisted of 5 mM $CaCl_2$, 2 mM sodium phosphate, and 250 mM of the indicated salt at pH 7.8. Solid lines are quadratic fits to guide the eye. (A),(B),(C) ACP growth in the presence of different Hofmeister salts at 20 °C, 30 °C, and 40 °C, respectively.

gregation processes involving phosphates, such as calcium phosphate formation. Rather than building up prenucleation clusters or other nucleation seeds via ion by ion bonding, calcium ions encountering the assemblies could immediately coordinate with multiple phosphates, and additional calcium molecules could then join to make stoichiometric calcium phosphate species. In this sense, we began investigations on the impact of different assembly conditions on calcium phosphate. Because conditions such as temperature, pH, and phosphate concentration would have a large direct impact on both phosphate assemblies and calcium phosphate growth, we decided to monitor calcium phosphate formation and growth in the presence different salts from the Hofmeister series, which we previously showed to impact phosphate assembly using ^{31}P relaxometry.

The DLS results for ACP growth in solutions of 5 mM $CaCl_2$, 2 mM sodium phosphate, and 250 mM of either NH_4Cl, KCl, or NaCl at pH 7.8 and temperatures from 20 °C to 40 °C are shown in Fig. 7.1. According to the Hofmeister series, and our results in Fig. 3.4, we would expect that NH_4Cl would promote phosphate assemblies more than KCl or NaCl. If phosphate assemblies were then important in nucleating calcium phosphate particles, then the solution with NH_4Cl might show larger particle sizes. Indeed, we find that at each temperature tested, NH_4Cl promotes larger ACP particles, with the effect

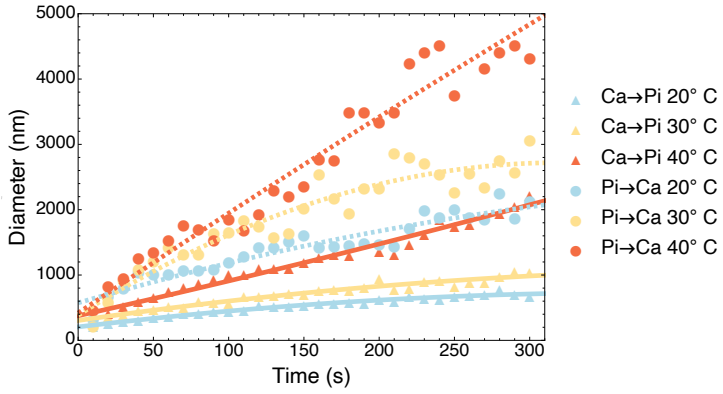

Figure 7.2: Impact of adding a concentrated calcium solution to a dilute phosphate solution vs. a concentrated phosphate solution to a dilute calcium solution. 100 mM $CaCl_2$ or sodium phosphate was added to the solution to reach final concentrations of 5 mM $CaCl_2$ and 2 mM sodium phosphate at pH 7.4 for each experiment. Lines are a quadratic fit to guide the eye. Triangles and solid fit lines indicate that calcium was added to dilute phosphate, and circles and dashed fit lines indicate that phosphate was added to dilute calcium.

most pronounced at lower temperatures. KCl and NaCl lead to the formation of very similar sized ACP, which agrees with our results in Fig. 3.4 where at lower phosphate concentrations (10 mM in that case) KCl and NaCl showed very similar relaxation rates (which is a proxy similar phosphate assembly behavior).

We also explored how adding a concentrated calcium solution (100 mM) to a dilute phosphate solution would differ from adding a concentrated phosphate solution (100 mM) to a dilute calcium solution. DLS results are shown in Fig. 7.2 for a range of temperatures in solutions with final concentrations of 5 mM $CaCl_2$ and 2 mM sodium phosphate. At each temperature adding the concentrated phosphate solution promotes significantly larger ACP than adding concentrated calcium to a dilute phosphate solution. Since a more concentrated phosphate solution would have a higher population of assemblies, this result points towards the presence of more phosphate assemblies helping to promote larger ACP.

It is important to note that the results in Figures 7.1 and 7.2 do not necessarily imply

that the phosphate assemblies are the reasons for the observed differences. Hofmeister salts each structure water differently, and this water structuring could be causing the observed differences rather than phosphate assemblies. Similarly, adding in concentrated phosphate solutions creates different concentration and pH gradients than concentrated calcium solutions, which could also be impacting how ACP nucleates and grows. Thus, more robust experiments with more independent trials are required to establish the statistical significance of these results. Nevertheless, given that these experiments indicate that solution conditions which promote a higher abundance of phosphate assemblies lead to larger ACP, we suggest that future studies examine the potential role of phosphate assemblies in calcium phosphate growth and other processes involving phosphates.

7.3 Future experiments on Posner molecules

In Chapter 4, we presented a combination of DLS, cryo-TEM, and ^{31}P results that indicated the existence of Posner molecules in SBFs. The verification that Posner molecules are stable *in vitro* is an important step towards characterizing their properties for testing Quantum Brain theory (in particular, the ^{31}P spin relaxation time and the molecular symmetry). However, the ^{31}P NMR indicated that there was chemical exchange in these SBFs between Posner molecules and other species, presumably phosphate ions and small ACP aggregates, that made it impossible to directly measure spin relaxation in these SBFs. Therefore, one direction of future research on Posner molecules is their stabilization in solution to allow for spin relaxation experiments. For this purpose, it may be important to add proteins or other additives (such as polymers) to the solution, which could then allow for stable Posner monomers to be tested.

With regards to proteins, we noted above that there are ongoing proteomic studies investigating calcium phosphate interacting proteins within the mitochondrial matrix. In

the literature, there have been claims based on small angle neutron scattering results that the protein fetuin (found in blood) stabilizes individual Posner molecules by binding them to the protein surface [114]. Casein phosphopeptides have also been shown to stabilize ACP nanoclusters at 3-4 nm in diameters by complexing with their surface [112]. These studies suggest the potential for individual Posner stabilization if the proper proteins can be discovered and isolated. Although such protein-calcium phosphate complexes would affect the ^{31}P spin dynamics by altering the rotational dynamics of the Posner and potentially putting protons near ^{31}P spins that would induce relaxation, it would still be a great step forward to be able to measure any ^{31}P spin relaxation time for a Posner molecule.

Polymers also offer an interesting potential route for Posner molecule stabilization. While proteins offer much more specificity in their binding and function, polymers can still significantly impact water structure and solution dynamics, and offer a means of simulating the crowded, viscous intercellular environment *in vitro*. To this end, we began exploring the impact of varying polymer type and wt% on the formation of ACP and transition into HAp using ^{31}P NMR. Note that DLS is no longer able to accurately provide sizes, as it is difficult to disentangle the scattering signal of the polymer from calcium phosphate particles. Therefore, we used the shifting of ^{31}P to try to understand the underlying phases and transformations. Because of the presence of the polymers, it is difficult to assign specific species based on chemical shift. Instead we use the shifting of line positions and widths to monitor the formation and subsequent transformation of calcium phosphate species. An initial change directly after calcium addition indicates that calcium phosphates are forming. If this signal then shows no changes over time, we assume this phase to be stable so that there is not a metastable phase forming. Given that Posner clusters seem to be involved in the formation of metastable ACP, the ideal conditions would be those that seemed to promote the formation of a metastable phase

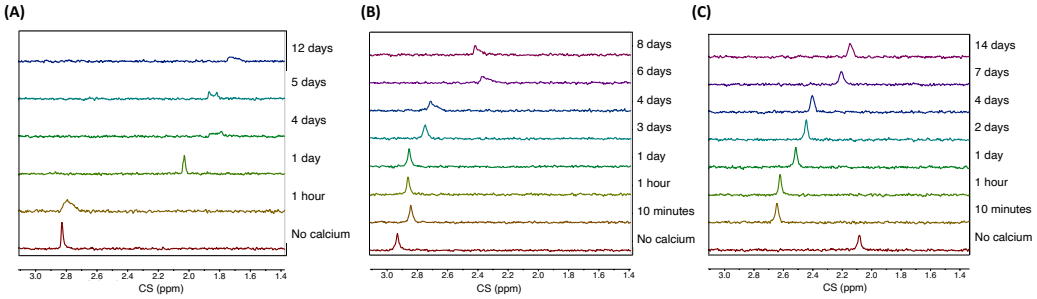

Figure 7.3: Impact of polymers on the formation and subsequent evolution of metastable calcium phosphate phase in solutions containing 5 mM $CaCl_2$ and 2 mM sodium phosphate at pH 7.4 and 25 °C. (A) In a standard SBF, the line broadens after calcium addition, indicating ACP formation, and subsequent transition into hydroxyapatite within 1 day. After several days the line is broadened due to precipitation. (B) In a solution with 5 wt% of 35,000 MW PEG, the initial formed calcium phosphate lasts for 3 days before transitioning to a different phase. (C) In a solution with 10 wt% 70,000 MW ficoll, a metastable phase forms and slowly transitions over the course of two weeks.

but a slow transformation into a thermodynamic phase.

We investigated four different polymers with varying hydrophilicity (ordered by increasing hydrophilicty)- polyvinylpyrrolidone (MW 8000), ficoll (MW 70,000), polyethylene glycol (PEG) (varying MW), and dextran (MW 70,000), with wt% from 5-40%. For both polyvinylpyrrolidone and dextran, there was no evidence for the formation of a metastable phase. Polyvinylpyrrolidone showed a line shift after calcium addition, but this line was sharp and never shifted, indicating that there was immediate formation of a crystalline calcium phosphate phase. In the presence of dextran there was no line shift after calcium addition.

However, both PEG and ficoll showed potential for stabilizing a metastable phase. We found that longer chain PEG (MW 35,000) was more successful than shorter chain (MW 600 and 6000), and that for both ficoll and PEG wt%'s ranging from 5-10% led to the longest lifetime for the metastable phase. Fig. 7.3 compare the ^{31}P time evolution of a standard SBF with PEG and ficoll solutions that showed the most promising results for

metastable phase stabilization. While the standard SBF transitions out of its metastable phase within a day, for the solutions containing PEG and ficoll this transition takes place over several days.

Taken together, these results indicate that relatively low wt%, high molecular weight polymers with a sort of "goldilocks" hydrophilicity may be the most promising route for ACP stabilization. While the solution phase space is extremely large- there is polymer type, MW, and wt%, but also calcium and phosphate concentrations, pH, temperature, and other salts- the work here puts forth a place to begin further exploration with the long-term goal of stabilization of ACP and potentially Posner molecules. Such studies would have important implications not only for the Quantum Brain theory, where the ^{31}P spin dynamics of individual Posner molecules within solution could be tested, but also in the field of synthetic biomaterials, where control over the ACP-HAp transformation is key for structure and function.

In addition to work towards stabilizing Posner molecules in solution, it is key to confirm the symmetry of Posner molecules in order that QDS would be operational on their pair-binding events. Solid-state NMR allows for the measurement of 3D structures via multidimensional correlation experiments [218], offering a route for measurements of the Posner symmetry. Although one cannot prepare a solid powder of Posner molecules, a sample containing Posner molecules could be vitrified, freezing them in a native state and allowing measurements with solid-state NMR. However, because of the low abundance of nuclear spins in an aqueous solution (when compared to a powder), such vitrification experiments generally employ dynamic nuclear polarization (DNP) to enhance the signal. DNP utilizes the much higher gyromagnetic ratio of free electrons (>1000 fold that of ^{31}P nuclei) to enhance signal by transferring polarization from electron to nuclei [219], thereby making solid-state NMR experiments on vitrified samples feasible.

However, for DNP-NMR, one cannot just vitrify a standard aqueous sample and run

experiments. Rather, there needs to be an electron source (such as TEMPOL at ∼10 mM) and a glassing agent, often glycerol at 60% v/v, to ensure that the water in the sample does not crystallize during vitrification and to allow for coherent transfer of the electron polarization to the nucleus of interest. Additionally, samples often use a 3:1 ratio of D_2O:H_2O. Therefore, the solution conditions that are required for DNP solution preparation are fundamentally different than the SBFs that we have found to promote Posner formation.

Initial experiments show that glycerol significantly shifts the phase space of calcium phosphate by increasing their solubility, and multiple attempts to prepare SBFs for DNP-NMR showed no ^{31}P spin clustering, suggesting that no calcium phosphate species were forming. As noted above in discussions on polymer-SBF samples, the scattering from the glycerol makes it is impossible to use DLS to scan for conditions that promote calcium phosphate nanoclusters. Additionally, the large amount of glycerol in these solutions means that the filtration process that was previously used on SBFs to isolate calcium phosphate nanoclusters is not possible on these samples. Therefore, the glycerol (or other additive) must be added after the preparation of a solution containing Posner molecules, so it is important that the additives do not cause significant dissolution or aggregation of calcium phosphate.

Because of the difficulty using glycerol as a glassing agent, we began exploration of other possible glassing agents. Dimethylsulfoxide at 77% v/v is another commonly used glassing agent for DNP-NMR, but was found to promote significant calcium phosphate aggregation. However, based on the results on polymers stabilizing ACP, long chain PEG (MW 10,000) was also investigated as a potential glassing agent. Differential scanning calorimetry confirmed that PEG-D_2O-H_2O solutions formed a glassy solid when cooled to temperatures required for DNP (∼90 K). DLS confirmed that there was no significant aggregation (even in the presence of polymers, one can use DLS to monitor the formation

of larger species on the scale of >100 nm based on intensity changes), and solution ^{31}P NMR confirmed that there was formation of calcium phosphates based on line shifts after calcium introduction.

Therefore, a PEG-SBF sample was prepared for DNP-NMR. The SBF preparation was identical to samples in Chapter 4, using 5 mM calcium chloride, 2 mM sodium phosphate, and 250 mM KCl at pH 7.8, and filtering after calcium addition, except that the solvent was 75% D_2O and 25% H_2O. This sample was then mixed with 40% v/v PEG (MW 10,000) and 10 mM TEMPOL and vitrified. Initial double-quantum and triple-quantum filtering experiments showed signal, indicating the presence of networks of at least 3 dipolar couple phosphorus nuclei. Unfortunately, difficulties with the apparatus meant that spin counting experiments to look for higher order phosphorus networks were not feasible on this sample (ideally, a Posner would give signal for a network of up to, but not above, 6 phosphorus nuclei). However, these initial experiments indicate that DNP-NMR experiments on SBFs containing Posner molecules could be possible, and that these solution conditions laid out here should be investigated more in the future.

Altogether, we see that there are a number of interesting routes to explore for future experiments on Posner molecules. One route will be exploring the proteins that are implicated to interact with calcium phosphates in the ongoing mitochondrial proteomic studies. Another route that appears promising for both solution NMR and DNP-NMR experiments is introducing polymers into SBFs. Although the introduction of polymers adds further complications to the already complex solution phase space of calcium phosphates, the preliminary results and experiments discussed above show that polymer-SBF solutions could be promising for measurements of both the spin dynamics and symmetry of Posner molecules.

7.4 Non-classical isotope effects

In Chapter 5, we introduced a differential lithium isotope effect in the formation of ACP that appeared to be unexplainable by the classical mass-based kinetic isotope effect. We proposed that the observed difference in ACP growth - where ^{7}Li promoted a higher abundance of large ACP particles than ^{6}Li - could relate to couplings between the lithium nuclear spins and the nuclear spins in Posner molecules, whereby the ^{7}Li led to more rapid decoherence of the phosphorus pseudospin states. This decoherence in turn led to more Posner binding events, manifesting in the observed difference in light scattering intensity.

This lithium isotope effect is particularly interesting in two regards - for one, it could be an explanation for observed biological lithium isotope effects observed in mitochondria, neuron function, and rat behavior. But secondly, it indicates that isotope effects could be operational in other nucleation and growth processes, whether in calcium phosphates or other species. On this point, other nucleation and growth processes that involve nanometric prenucleation clusters and fermionic nuclei, such as calcium carbonate and iron-oxyhydroxide [220, 221, 222], should be investigated for potential isotope effects that could impact growth via QDS.

In the case of calcium phosphate and Posner molecules, we can consider what other isotopes might be used to modulate nucleation events via QDS. Considering other dopant elements such as lithium, Swift found that iron, magnesium, and sodium were the next most enthalpically favorable elements to substitute the central calcium in a Posner molecule [55]. However, iron and magnesium both form their own solid phases, complicating the interpretation of any such experiments, and sodium has only a single stable isotope, so that varying isotopes to modulate QDS effects would not be possible.

Posner molecule symmetry could also be removed by substituting isotopes of calcium,

phosphorus, or oxygen. While phosphorus has only one stable isotope, both calcium and oxygen have multiple stable isotopes. In theory, isotope replacement of oxygens on phosphorus groups could remove molecular symmetry- however, oxygen isotopes might then exchange with oxygens in water, adding complication to interpretation of experimental results as the amount of symmetric vs. asymmetric Posner molecules would be difficult to quantify. Thus, the most promising route in this regard appears to be modulating calcium isotopes. Two calcium isotopes appear particularly promising- ^{44}Ca (the second highest natural abundance, at 2%, and therefore easiest to isolate and acquire) and ^{43}Ca (the only stable calcium isotope with non-zero nuclear spin at $\frac{7}{2}$).

Here we propose some experiments of interest involving these two calcium isotopes. First, we consider DLS to monitor ACP growth in the presence of ^{44}Ca, where the nuclear spin is 0 (the same ^{40}Ca), similar to the lithium isotope experiments in Chapter 5. In the case of pure ^{44}Ca, the nucleation and growth processes should be almost identical to a ^{40}Ca solution, although there may be slight differences due to classical mass based isotope effects. More interestingly, in solutions with a mix of ^{40}Ca and ^{44}Ca there would be a mixture of asymmetric and symmetric Posner molecules. While the symmetric molecules would be affected by QDS, the asymmetric molecules would not, so that solutions with a higher proportion of asymmetric Posners should show more rapid initial nucleation events. This dependence on the proportion of symmetric Posner molecules would be expected to manifest similarly to the lithium isotope effects, where the abundance of large ACP particles was impacted. Different ratios of ^{40}Ca to ^{44}Ca could then change the ratio of symmetric to asymmetric Posner molecules and impact calcium phosphate growth. Additionally, by doing symmetric ratios (e.g. both 1:3 ^{40}Ca:^{44}Ca and 3:1 ^{40}Ca:^{44}Ca), one could test whether any observed effect was mass-based or symmetry-based.

One can also consider doing a similar titration of ^{40}Ca and ^{44}Ca while also looking for lithium isotope effects. In this case, one might expect to toggle the lithium isotope

effect via the proportion of symmetric Posner molecules. In the case of a single calcium isotope, the Posner molecules are symmetric, and the lithium isotope effect would still active. However, when mixing the two calcium isotopes, we introduce a degree of asymmetry to the Posners. Since incorporation of the different lithium isotopes into an asymmetric Posner should lead to negligible differences in their binding dynamics, the isotope effect should be less pronounced the greater the degree of asymmetry. Similar to above, one could do different ratios of the calcium isotopes to introduce different amounts of asymmetry and confirm that any effects were not related to the different calcium masses.

In the case of ^{43}Ca, with nuclear spin $\frac{7}{2}$, the calcium atom itself would lead to pseudospin decoherence via its coupling to ^{31}P spins. Therefore, we could compare the growth of ACP in a solution with ^{43}Ca to both ^{40}Ca and ^{44}Ca. In the case of ^{43}Ca, we would expect faster growth/higher abundance of ACP because of the rapid pseudospin decoherence compared to the other two isotopes. Since the mass of ^{43}Ca is between that of ^{40}Ca and ^{44}Ca, any observed difference would likely be related to nuclear spin rather than mass.

Because of its non-zero nuclear spin, ^{43}Ca is also NMR active. This is of particular importance for the DNP-NMR experiments described above for testing Posner molecule symmetry. With a spin 0 calcium nuclei, only the ^{31}P nuclei can be confirmed to be in a symmetric arrangement. However, symmetry of the entire molecule must be confirmed, and probing the calcium spins would give a more complete 3D picture of the molecule. Unfortunately, if QDS is active, then DNP-NMR solution preparations that work in the presence of ^{40}Ca might not work for ^{43}Ca, where the Posners binding dynamics would be impacted. Nonetheless, it is still worth considering experiments that would aim to vitrify solutions of Posners composed with ^{43}Ca because of the importance of verifying the symmetry of the Posner molecule.

7.5 Quantum dynamical selection

In Chapter 6, we have laid out a model enzymatic system (the TMA-FMO3-TMAO system) for testing whether QDS is active for a three-fold symmetric molecule. While the lithium isotope effect on ACP growth observed in Chapter 5 is proposed to be related to QDS, the TMA-FMO3-TMAO system offers a strong quantitative prediction and should give definitive experimental evidence on whether QDS is active. Given the fundamental role of QDS within the Quantum Brain theory, this experiment will answer a key question regarding the viability of the theory.

If there is a positive result in the TMA-FMO3-TMAO system, then there are a whole range of experiments to investigate other QDS effects. One experiment would involve synthesizing TMA substrates with either 0, 1, 2, or 3 ^{13}C molecules. In the case of either 0 or 3 ^{13}C's, the substrate is symmetric and we would expect QDS effects, while in the case of 1 or 2 ^{13}C's, the substrate is asymmetric. This experiment would rule out that any observed differences were due to mass-based isotope effects, as the heaviest and lightest substrate (both symmetric) would be expected to show similar behavior compared to the middle two masses (both asymmetric).

Other enzyme systems with symmetric substrates that contain fermionic nuclei could also be investigated. (However, as noted in Chapter 6, such systems are rare in the literature). In these cases, it would be of particular interest to look for QDS in systems with greater than three-fold symmetry, to confirm that the theory holds in such cases. Much like the TMA-FMO3-TMAO system, single substrate enzymatic reactions are ideal for testing QDS because of the clear prediction on reaction rates.

Outside of enzymatic systems, QDS effects could also be investigated in growth processes that involve the aggregation of small, symmetric clusters containing fermionic nuclei. In the previous section, we noted other potential mineralization systems to in-

vestigate, as well as a range of additional isotope experiments on calcium phosphate growth. While QDS does not offer precise predictions for these experiments like it does for enzymatic reactions, any observed effects would still be exciting and novel.

7.6 Closing remarks

We hope and believe that the work and efforts described in this thesis have helped to build and utilize an experimental platform for testing the Quantum Brain theory. Such revolutionary theories, and the experiments that confirm or refute their validity, are fundamental to the progress of science and our understanding of the world. While we have not yet been able to provide a definitive answer on whether our brain may be some form of quantum computers, we are excited to see the future progress on this question and wish luck to all the researchers involved in this endeavor.

Appendix A

Dynamic Light Scattering Theory

A.1 Introduction

Dynamic light scattering (DLS) is an experiment that uses the intensity fluctuation of scattered light from particles within solution to extract diffusion coefficients, and thus sizes. DLS is a technique that is widely used across the biophysical sciences due to its ability to size particles ranging from a single nanometer to a few microns in diameter. Additionally, DLS is highly advantageous in that it is non-destructive of samples, with short experimental times (often on the scale of a couple minutes), and bench-top apparatuses widely available.

Here we describe the general experimental principle behind DLS, and then go into more depth on the theoretical background and data analysis. Briefly, an incident laser is directed at a solution in which the solutes are undergoing diffusive Brownian motion. When these particles diffuse into the beam path, they will scatter light, which is collected by a detector. Eventually, these particles will diffuse out of the beam path and no longer scatter light onto the detector. The detector is connected to a correlator, which quantifies the change in scattering intensity as a function of time, encoding information on the

diffusion rate of the particles in solution. This diffusion rate can be extracted from the decaying correlations in intensities, and diffusion rate can then be converted into particle size. A simple schematic of this experimental apparatus can be found in Fig. C.1.

A.2 DLS Theory

A.2.1 The autocorrelation functions

We will not give here the full mathematical theory behind DLS, which can be found elsewhere [223], but we will present the key concepts required to understand and process the experimental data. As noted above, DLS monitors changes in scattering intensity as a function of delay time, τ, which are used to calculate a normalized autocorrelation function $g^2(\tau)$ for the intensity of scattered light $I(t)$, defined as

$$g^2(\tau) = \frac{\langle I(t)I(t+\tau)\rangle}{\langle I(t)\rangle^2} \tag{A.1}$$

At small τ, correlated scattering will lead $g^2(\tau)$ to be greater than 1, while at long τ, once there is no more correlation in the scattered intensity, $g^2(\tau)$ will decay to 1.

This second-order autocorrelation function can then be expressed by using the Siegert relation in terms of first-order autocorrelation function $g^1(\tau)$ as

$$g^2(\tau) = 1 + \beta|g^1(\tau)|^2 \tag{A.2}$$

where β is a constant based on the experimental setup and scattering contrast between the particles and solvent. Except for samples where the solvent scattering is comparably large to the solute (generally only the case for very dilute, very small particles), β is roughly inversely proportional to the number of different coherence areas, A_{coh} that are

imaged onto the detector. This can be understood by considering two different regions within the scattering volume. Within each region, or coherence area, scattered light will be coherent with itself, but between regions, the scattered light is not necessarily coherent. This leads to destructive interference between light scattered from different regions, decreasing the overall scattering signal. For a typical experiment where solid angle Ω is imaged onto the detector and with incident wavelength λ, the coherence area is $A_{coh} \approx \frac{\lambda^2}{\Omega}$.

(Outside of atmospheric effects, this is why stars twinkle but planets do not. Because stars are so distant, the solid angle for light emitted from stars is very small. Thus, their coherence area is very large, so even though stars are much larger than planets, they still compose only a single coherent area. On the other hand, planets are much closer with a much larger solid angle for emitted light, so that they are composed of multiple coherence areas. Thus, we see the coherent fluctuations in intensity from stars, while in planets these fluctuations are averaged out over the many coherence areas we are observing.)

The first-order autocorrelation function $g^1(\tau)$ has a characteristic decay rate Γ so that it can be expressed in the form of an exponential decay

$$g^1(\tau) = Exp(-\Gamma\tau) \tag{A.3}$$

This decay rate can then be related to a particle's translational diffusion coefficient, D_t, by

$$\Gamma = D_t \left(\frac{4\pi n}{\lambda} \sin\theta/2 \right)^2 \tag{A.4}$$

where n is the index of refraction of the solvent, λ is the incident wavelength of the scattered light, and θ is the scattering angle. Given that these are all known quantities for a DLS experiment, measuring the decay rate Γ allows one to extract D_t, the translational

diffusion coefficient. D_t can then be related to a particle's hydrodynamic diameter, d, by the Stokes-Einstein relation [224]

$$d = \frac{kT}{3\pi\eta D_t} \tag{A.5}$$

where k is the Boltzmann constant, T is the solution temperature, and η is the dynamic viscosity of the solution, which are all known quantities for a given experiment. Therefore, by determining the decay constant Γ of the first-order autocorrelation function, we are able to extract a hydrodynamic diameter for our solute. Note here that we have assumed the solute to be roughly spherical. For other well defined aspect ratios, such as narrow rods, the theory is slightly different, and is covered in [223].

If there are multiple particle sizes appearing in the solution, then the first-order autocorrelation function is expressed as a weighted integral over the distribution of decay rates G(Γ),

$$g^1(\tau) = \mathcal{L}^{-1}[G(\Gamma)] = \int_0^\infty G(\Gamma) Exp(-\Gamma\tau) d\Gamma \tag{A.6}$$

where $\mathcal{L}^{-1}[G(\Gamma)]$ indicates the inverse Laplace transform of $G(\Gamma)$. The procedure for inverting this equation to extract $G(\Gamma)$, and thus the intensity averaged distribution of hydrodynamic diameters of particles in solution, will be discussed in A.3 below.

Here we emphasize the two assumptions made in the above theory. First, the solutions are composed of dilute particles, meaning there is a low probability that the light scattered from a particle will be scattered by another particle before reaching the detector. If these "multiple scattering" processes are common in a solution, then the relation A.4 between decay rate and translational diffusion coefficient no longer holds, and particles size distributions will be distorted to appear broader and at smaller sizes. Because of this, DLS samples should never be visually turbid.

Second, the solutions are composed of non-interacting particles, meaning their motion can be described completely by Brownian motion. If there are inter-particle interactions, then relation A.4 will again not be true. Additionally, this is the reason for the upper size limit for DLS- once particles are larger than a few microns, they will begin to sediment in solution, and their motion will no longer be Brownian.

A.2.2 Rayleigh and Mie Scattering

As noted above, DLS often makes the assumption that the particles in the solution are spherical. In this case, the scattering of light is described by Mie Theory [203], which gives a full mathematical description of the scattering of an electromagnetic plane wave by a uniform sphere in the form of an infinite series. Solutions to such problems are generally found via computational techniques and series truncation at the appropriate order, and open source software is available for arbitrary wavelength, particle size, and refractive index.

However, for small particle sizes, appropriate approximations allow for a closed form description of the scattering intensity. One can consider the so-called size parameter

$$x = \frac{2\pi r}{\lambda} \tag{A.7}$$

where r is the radius of the particle and λ is the wavelength of the incident light. Note that for $x >> 1$, we are in the macroscopic regime, and Mie scattering theory is no longer appropriate. At such large sizes, the scattering is geometric, and objects scatter light according to their shape. (There is also a breakdown of the Brownian motion approximation due to sedimentation). At $x \simeq 1$, Mie theory describes the scattering, and one uses computational techniques as mentioned above.

However, at $x << 1$, the scattering is known as Rayleigh scattering, and the scattered

intensity from a particle can be described as [204]

$$I = I_0 \frac{1 + cos^2(\theta)}{2R^2} \left(\frac{2\pi}{\lambda}\right)^4 \left(\frac{n^2 - 1}{n^2 + 2}\right)^2 \left(\frac{d}{2}\right)^6 \tag{A.8}$$

where I_0 is the incident laser intensity, θ is the scattering angle, R is the distance from the particle to the detector, λ is the incident wavelength, n is the index of refraction of the particle, and d is the particle diameter. The total scattering intensity for a solution will then be a sum of the contributions of each particle in the solution.

Notably, the scattering intensity for Rayleigh scattering scales as d^6, so that small particles will have their scattering signal completely swamped by large particles. (For example, consider a solution with x1000 the concentration of 1 nm particles as 10 nm particles. The scattering intensity from the 1 nm particles will still only be 0.1% the scattering intensity of the 10 nm particles, meaning that it is unlikely that the 1 nm particles will even be detected.)

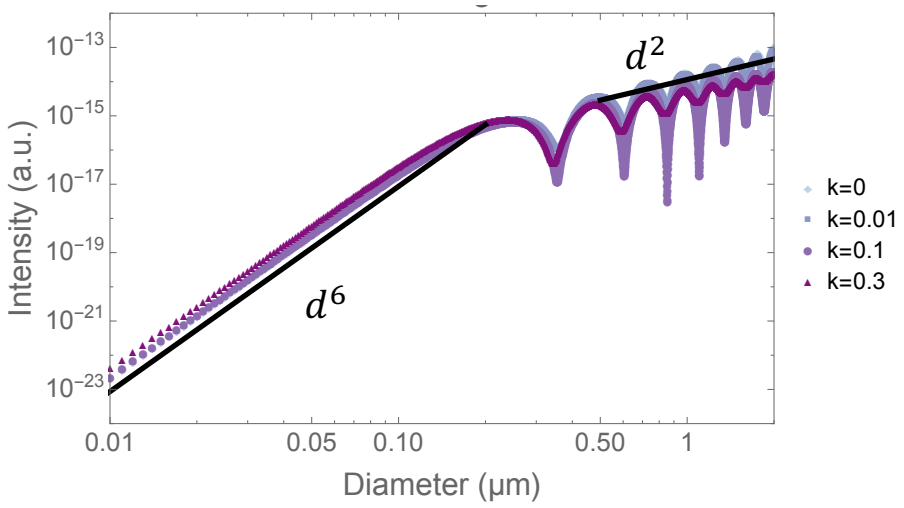

Figure A.1: Scattering intensity vs. diameter for particles with refractive index $n = 1.626$ and varying extinction coefficient k for 532 nm incident light. Notably, in the Rayleigh regime defined by diameter $d << \lambda$, the intensity I scales as $I \propto d^6$, while for sizes greater than the Rayleigh regime we have $I \propto d^2$.

It is also useful to note that the general trend for Mie scattering intensity with particle

size for objects with $x \simeq 1$ is $I \propto d^2$, although there is not a closed form and the scattering does not monotonically increase with size. An example intensity-size relationship is shown in Fig. A.1, where we note the difference in scaling in the Rayleigh and Mie regimes. Some of the consequences of these intensity-size relationships will be discussed in more detail below.

A.3 Data Processing

As noted in equation A.6, the general process of data analysis in DLS involves the extraction of a decay rate distribution, G(Γ), by solving the inverse Laplace transform

$$g^1(\tau) = \int_0^\infty G(\Gamma) Exp(-\Gamma\tau) d\Gamma \tag{A.9}$$

In this case, we have experimentally extracted $g^1(\tau)$ by directly measuring $g^2(\tau)$ and using equation A.2 to convert to $g^1(\tau)$. However, this type of integral is known as a Fredholm integral of the first kind, a mathematically ill-posed problem in that infinitesimally small amounts of noise can lead to large fluctuations in the resulting solution. Given that all experimental data will be subject to noise, one can see that finding $g^1(\tau)$ for a real system is non-trivial. To alleviate this pathology, a number of different fitting techniques are used in analyzing DLS data. These include expanding the $g^1(\tau)$ as a power series (known as the method of cumulants) [225, 226], Bayesian inference [227], wavelet methods [228], and Tikhonov regularization [229, 230]. Herein we focus on the method of cumulants and the regularization algorithm CONTIN, the two most popular techniques in DLS, while recognizing that there are additional techniques that can produce good size distributions given the appropriate data.

A.3.1 Method of Cumulants

The moment-generating function $M_X(t)$ for a random variable X is defined as [231]

$$M_X(t) = E[e^{tX}] \tag{A.10}$$

where E represents the expectation value operator. The origin of the name "moment-generating function" can be seen by considering a power series expansion, and recognizing that E is a linear operator, thereby giving

$$M_X(t) = E[e^{tX}] = 1 + tE[X] + \frac{t^2E[X^2]}{2!} + \frac{t^3E[X^3]}{3!} + ... \tag{A.11}$$

We note that the nth derivative of $M_X(t)$ evaluated at $t = 0$ will give the nth moment about the origin. (Noting the similarities between equations A.3 and A.10, we see that for the variable Γ the moment generating function is our first order autocorrelation function $g^1(\tau)$.)

The cumulant generating function is then defined as the natural logarithm of the moment generating function

$$K_\Gamma(-\tau) = Ln\ M_\Gamma(-\tau) = Ln\ g^1(\tau) \tag{A.12}$$

where we noted that we have converted from a generic random variable and time to the specific form of $g^1(\tau)$ with random variable Γ. We now consider a power series expansion of K

$$K_\Gamma(-\tau) = \sum_{m=1}^{\infty} K_m(\Gamma)\frac{(-\tau)^m}{m!} \tag{A.13}$$

where $K_m(\Gamma)$ is defined as the mth cumulant of Γ. Note that for the case of a single

exponential decay in our correlation function, we have $Ln\ g^1(\tau) = -\Gamma\tau$ and $K_\Gamma(-\tau)$ is a linear function of τ, with $K_1(\Gamma) = -\Gamma$ and $K_{m\neq1}(\Gamma) = 0$. Higher order terms in our expansion will represent more complex distributions than a single decay rate (which would correspond to a δ-function at a single size).

One can express these cumulants as moments about the mean $\langle\Gamma\rangle$ of our decay rate distribution $G(\Gamma)$. Here we give the explicit form of the first four cumulants, which each have a well-defined physical meaning. Rarely does one consider higher orders in analyzing DLS data, but an explicit form for any order cumulant can be found at and a more detailed discussion can be found in [225]. These four cumulants are

$$K_1 = \langle\Gamma\rangle \tag{A.14}$$

$$K_2 = \langle(\Gamma - \langle\Gamma\rangle)^2\rangle \tag{A.15}$$

$$K_3 = \langle(\Gamma - \langle\Gamma\rangle)^3\rangle \tag{A.16}$$

$$K_4 = \langle(\Gamma - \langle\Gamma\rangle)^4\rangle - 3K_2^2 \tag{A.17}$$

and are measures of the mean, variance, skewness (asymmetry), and kurtosis (flatness), respectively. Notably, if $G(\Gamma)$ is a Gaussian distribution, all cumulants beyond order 2 are 0, and the distribution can be fully described by K_1 and K_2.

In the reporting of dynamic light scattering data, it is common to consider only the first two cumulants, thereby assuming a Gaussian distribution. In this case, the reported values are often in the form of the intensity-averaged mean diameter, found by converting $\langle\Gamma\rangle$ to $\langle d\rangle$ via equations A.4 and A.5 (also known as the Z-average size), and the polydispersity, often given as the dimensionless quantity $\sqrt{\frac{K_2}{K_1^2}}$, an analog to the standard deviation of a Gaussian distribution.

A.3.2 CONTIN

While the method of cumulants is an excellent method for sizing monodisperse solutions whose distributions can be well captured by a Gaussian or near-Gaussian approximation, for more complex shaped or multimodal distributions this analysis technique will fail to accurately describe the distribution. In such cases, one might introduce *a priori* knowledge, or use Tikhonov regularization. Tikhonov regularization is a technique used when the independent variables (in this case, the different decay rates) are highly correlated [232]. Given that we often expect physical size distributions (equivalent here to decay rate distributions) to be relatively smooth, this technique is appropriate for DLS fitting.

The introduction of regularization is able to remove the ill-posed nature of this inversion process at the cost of assumuptions on the smoothness of the distribution. For DLS, the most common algorithm is Provencher's CONTIN algorithm [229, 230], which minimizes the value of

$$\left|\mathcal{L}^{-1}[\tilde{G}] - \mathcal{L}^{-1}[G_{measured}]\right|^2 + \alpha \left|\omega - \Omega[\tilde{G}]\right|^2 \tag{A.18}$$

where $\tilde{G}$ is the desired decay rate distribution, $\mathcal{L}^{-1}[\tilde{G}]$ is the corresponding autocorrelation function, $\mathcal{L}^{-1}[G_{measured}]$ is the experimental data, α is a regularization parameter, ω includes any *a priori* knowledge about the distribution (often set to zero but included here for completeness), and Ω is a measure of curvature, often a second derivative operator.

This algorithm thus considers the residual norm in the first term while punishing high-curvature distributions for which $\left|\Omega[\tilde{G}]\right|^2$ is large, with the parameter α dictating the balance between these two contributions. It can be seen that the first term above is the standard non-negative least squares (NNLS) fitting, which is also sometimes used in DLS. However, because the regularization term removes the ill-fitted nature of the inversion

problem at almost no computation cost, it is much more common (and appropriate) to use the CONTIN algorithm than just a NNLS.

There are multiple ways to select a proper regularization value α for a set of experimental data. Note that there is often a range of α values that do an equally good job of capturing the distribution. Commonly, one might vary α with the goal of removing any trends in the fitting residuals. One can also implement a L-curve algorithm, which varies α and looks at the relatively contributions of each term in equation A.18 [233]. By plotting the magnitude of each term on the x- and y-axes, respectively, one will find a "L" shape, and optimized value for α is selected as the corner of this "L," thereby balancing the contributions from each term.

Equation A.18 is often minimized by considering discrete decay rates Γ_i, such that $\tilde{G}$ is a vector representing the different weights G_i for the contribution from each decay rate. The integral in equation A.9 then becomes a sum over the different weights

$$g^1(\tau) = \sum_i G_i Exp(-\Gamma_i \tau) \tag{A.19}$$

These decay rates are often chosen to be logarithmically spaced to promote symmetric size distributions. Limits on Γ_i's chosen such that there is no weight on minimal or maximal rates, as this would indicate that too narrow a range of rates had been selected. For the analysis described in this thesis, we have implemented this algorithm in MATLAB, using a modified version of the rilt (Regularized Inverse Laplace Transform) code [189]. For any CONTIN data shown in this thesis, values for the regularization parameter and the number and range of decay rates considered were varied for several sets of experimental data and were found to not qualitatively change the resulting distributions, although the exact shapes of the resulting distributions did change.

In Fig. A.2, we compare the method of cumulants and the CONTIN algorithm for

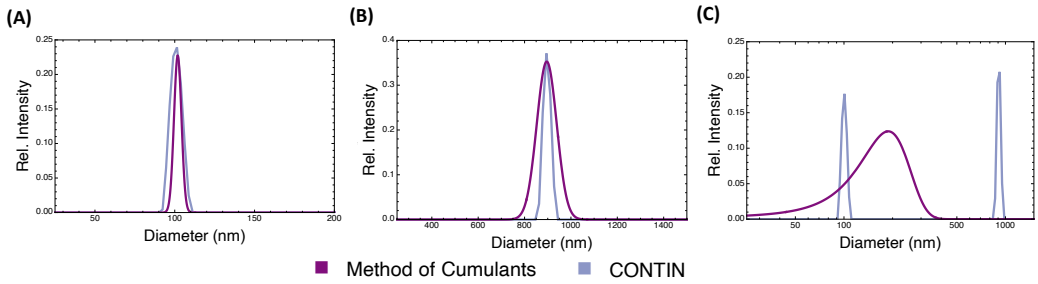

Figure A.2: Comparison of the method of cumulants and CONTIN algorithms for fitting DLS data. (A) For monodisperse 100 nm standards, both fitting methods capture the distribution peak and produce similar widths. (B) For monodisperse 900 nm standards, both fitting methods capture the distribution peak and produce similar widths. (C) For a 1:1 intensity mixture of 100 nm and 900 nm standards, CONTIN is able to reproduce the peak locations and relative intensities, while the method of cumulants gives a single very broad peak in between the two sizes. Note that the x-axis is logarithmic in (C). α was set to $5 * 10^{-8}$ for each fit. For (A) and (B), 100 sizes were considered, ranging from $25 - 250$ nm and $250 - 1500$ nm, respectively. For (C), 125 sizes were considered, ranging from $25 - 1500$ nm.

three different solutions- one with monodisperse 100 nm particles, one with monodisperse 900 nm particles, and a 1:1 intensity mixture of the two. For monodisperse solutions, the method of cumulants and CONTIN both capture the peak locations well, and the distribution widths are relatively similar, indicating that both algorithms are appropriate for fitting these data. However, for the bi-modal distribution, CONTIN still captures the peak locations and widths, the method of cumulants gives a very broad, skewed distribution in between the two sizes. For such multimodal cases, the method of cumulants is no longer appropriate, and CONTIN should be used.

A.3.3 Number vs. Intensity distributions

The above analysis techniques, as well as other DLS fitting algorithms, will produce a distribution of the *intensity* distribution by size. That is, the resulting size distribution will describe the contribution to the overall intensity signal, not the *number* distribution of particles. For example, if the distribution produced by CONTIN was centered at 100

nm, then this result states that 100 nm particles are the strongest source of scattering signal, not that 100 nm particles are necessarily the most abundant in solution. Since we are fitting the intensity profile of the scattering, it is natural that the information we can extract relates to the sources of that scattering intensity. Therefore, this intensity distribution by size is the most appropriate way to report DLS results, given that this directly relates to the measured signal.

However, sometimes it is informative to consider the number (or volume) distribution by size to get more direct information on the particle concentrations within a solution. As noted, in the Rayleigh regime, the scattering intensity scales as $I \propto d^6$, so that a conversion from intensity distribution to size distribution is done by scaling the distribution by the inverse of the diameter to the sixth power, and renormalizing. However, it is clear to see that this transformation will skew the distribution towards small sizes and while not actually adding any extra information about the particle size distribution. Additionally, in the event of multimodal distributions, this scaling will often make all peaks except the smallest size effectively zero, making the distribution appear monomodal.

Even in the case of Mie scattering, where the intensity scales as $I \propto d^2$ so that the weighting factor in going from the intensity distribution to the number distribution is not as extreme as in Rayleigh scattering, extracting a number distribution from the intensity distribution can skew the data in a way that doesn't add to our description of the solution. Additionally, since the size-intensity relationship for Mie scattering is not monotonic (Fig. A.1, a similar d^2 weighting is particularly inappropriate.

Overall, it is recommended that one be careful when converting between the intensity distribution to a number distribution, as this often leads to a distortion of the size distribution that doesn't accurately reflect the measured autocorrelation function. Generally, it is best practice to report the intensity distribution by size. However, using these size-intensity relationships to get a semi-quantitative relationship between concentrations of

particles within or between solutions is appropriate and can provide useful information on relative abundances.

A.4 Cross-correlation

When performing a DLS experiment on a customary apparatus, photons scattered at the detection angle are incident on an avalanche photo diode and create a pulse of electrons. This electron pulse is then directed to a correlation card. The correlation card is composed of a number of channels at different delay times, τ, where each channel calculates $\langle I_A(t)I_A(t+\tau)\rangle$ for its corresponding delay time to produce a discrete autocorrelation function as a function of τ. However, when an avalanche photo diode detects a photon there is a small probability (generally on the order of 1% or less, depending on the specific avalanche photo diode) that a second pulse will be generated from the same incident photon, a process known as afterpulsing. The result of this afterpulsing is erroneously large values for the autocorrelation function at short delay times, as it appears that there are two photons arriving in rapid succession when there was actually just one. Thus, for small, rapidly diffusing species where correlations are only observed at short delay times, afterpulsing significantly distorts the "true" autocorrelation function and makes accurate data analysis impossible. An example of the effects of afterpulsing on the autocorrelation function of egg white lysozymes, whose hydrodynamic diameter has been measured to be 4.4 nm for similar conditions [234], are shown in Fig. A.3. The large decay at times < 500 ns is a signal artifact from afterpulsing.

One option used in DLS to minimize the impact of afterpulsing is cross-correlation. In cross-correlation, scattered photons are directed to one of two avalanche photo diodes (here referred to as A and B) and each communicates with the same correlation card. Each channel on the correlation card then calculates $\langle I_A(t)I_B(t+\tau)\rangle$, so that correlations

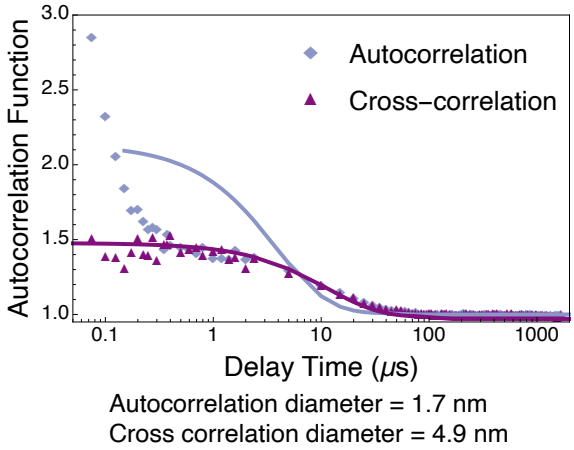

Figure A.3: Comparison of autocorrelation and cross correlation for a lysozyme sample. A sample of 5 mg/ml lysozyme was prepared at pH 4.5 in an aqueous solution with 0.5 M $NaCl_2$, and was then filtered using a peristaltic pump through 0.2 μm cellulose acetate filters to remove any aggregates or contaminants. Solid lines are the method of cumulants fits for each autocorrelation function, with the corresponding sizes extracted from the fit shown below.

are only measured between the different avalanche photo diodes. In this way afterpulsing events cannot be correlated with the incident photon that produced them. While there is still some small probability that afterpulsing on one avalanche photo diode could be correlated with a real signal from the other, this probability is becomes negligible. This is because both afterpulsing and detection of a photon within the period where afterpulsing occurs (on our apparatus found to be $\approx$ 500 ns) are already low probability events, so the probability that both occur simultaneously is effectively zero. Cross-correlation then eliminates the distortion of the autocorrelation function at short delay times, as is shown in Fig. A.3, and produces a much more accurate size for the 4.4 nm sized lysozymes. Thus, cross-correlation allows for accurate sizing of small species where the early time decay of the autocorrelation function is important for accurately fitting. In this thesis, this is of particular importance for sizing Posner clusters, given that their theoretical diameter is 0.95 nm in vacuum, so that the early delay times are key for accurate testing of their presence in solution.

Appendix B

Supporting Information for Chapter 3

Figures

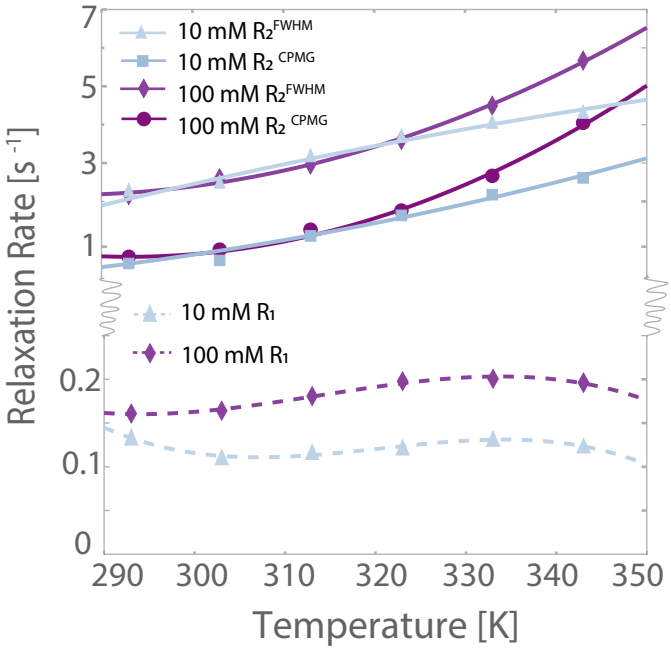

Figure B.1: R_2 as extracted from a CPMG pulse sequence and from FWHM for 10 mM and 100 mM potassium orthophosphate monobasic pH 4.5 as a function of temperature, showing monotonic increase in R_2 in each case. Solid lines are quadratic fits to data to guide the eye. R_1 for 10 mM, 100 mM, potassium orthophosphate monobasic pH 4.5 as a function of temperature showing the same curve shapes as a function of concentration. Solid lines are cubic fits to data to guide the eye.

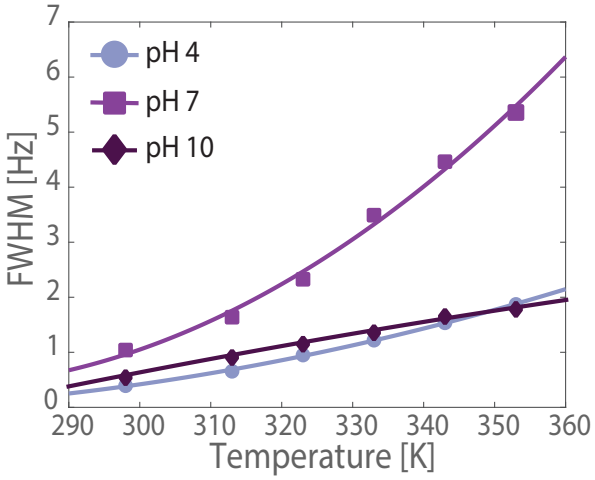

Figure B.2: FWHM of sodium phosphate dibasic solutions at pH 4, pH 7 and pH 10 showing line broadening. Solid lines are quadratic fits to data to guide the eye.

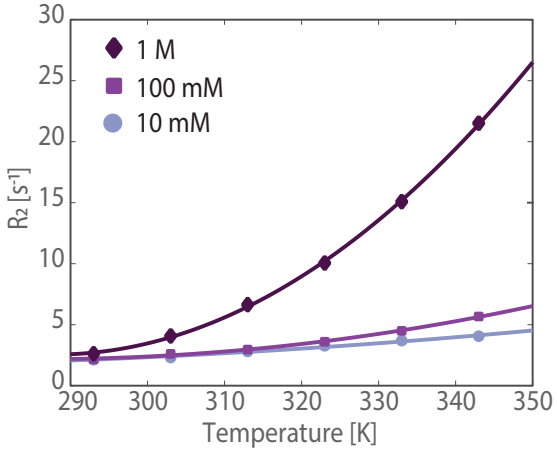

Figure B.3: R_2 rates calculated from FWHM for potassium phosphate solutions at pH 4.5 over a range of phosphate concentrations showing line broadening across a range of concentrations. Solid lines are quadratic fits to data to guide the eye.

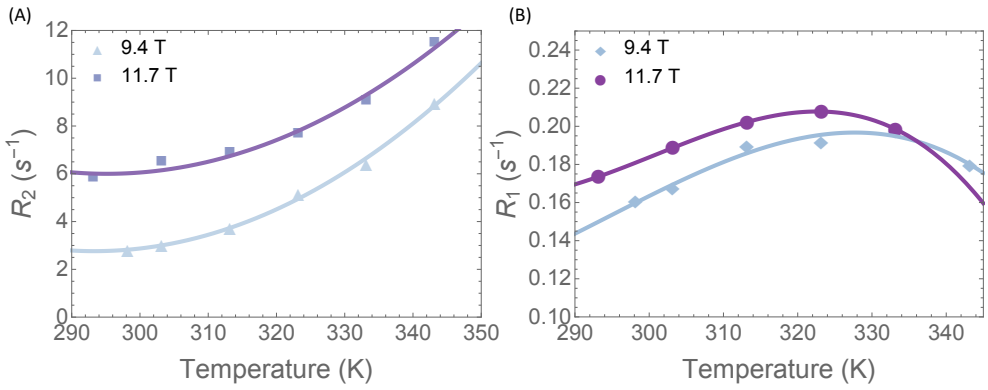

Figure B.4: Relaxation rates for 10 mM potassium phosphate at pH 4.5 from two different spectrometer strengths- 9.4 T ($\omega_0(^{31}P)$ =162 MHz) and 11.7 T ($\omega_0(^{31}P)$=202 MHz. (A) R_2 as calculated from FWHM shows increase with temperature at both spectrometer strengths. Solid lines are quadratic fits to data to guide the eye. (B) R_1 rate minimums shift to higher temperatures at greater field strength. Solid lines are third order polynomial fits to data to guide the eye.

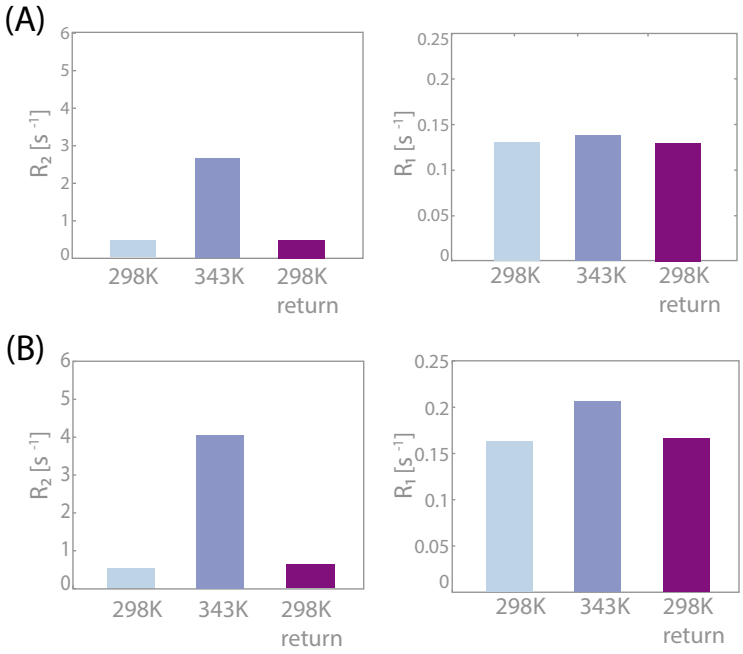

Figure B.5: Relaxation Rates for 10 mM and 100 mM sodium phosphate show reversibility after heating to 343K and cooling. (A) Relaxation rates for 10 mM sodium phosphate, (B) Relaxation rates for 100 mM sodium phosphate

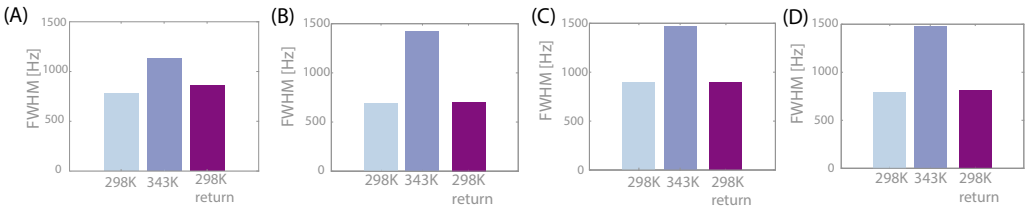

Figure B.6: ^{31}P CEST dip widths showing Reversibility at 298 K, 353 K and cooling back to 298 K. (A) 50 mM orthophosphate, (B) 100 mM orthophosphate, (C) 200 mM orthophosphate, (D) 300 mM orthophosphate.

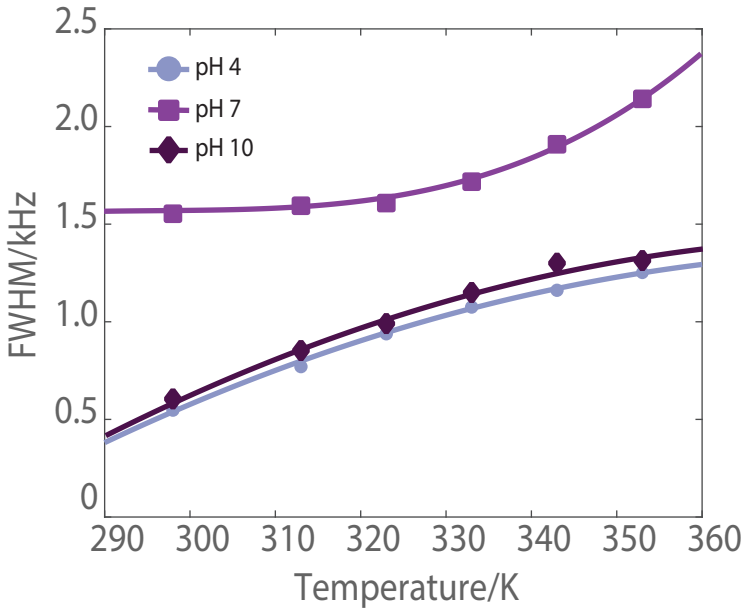

Figure B.7: ^{31}P CEST dip widths at half height of sodium phosphate dibasic solutions at pH 4, pH 7 and pH 10 showing line broadening as a function of temperature. Solid lines are quadratic fits to data to guide the eye.

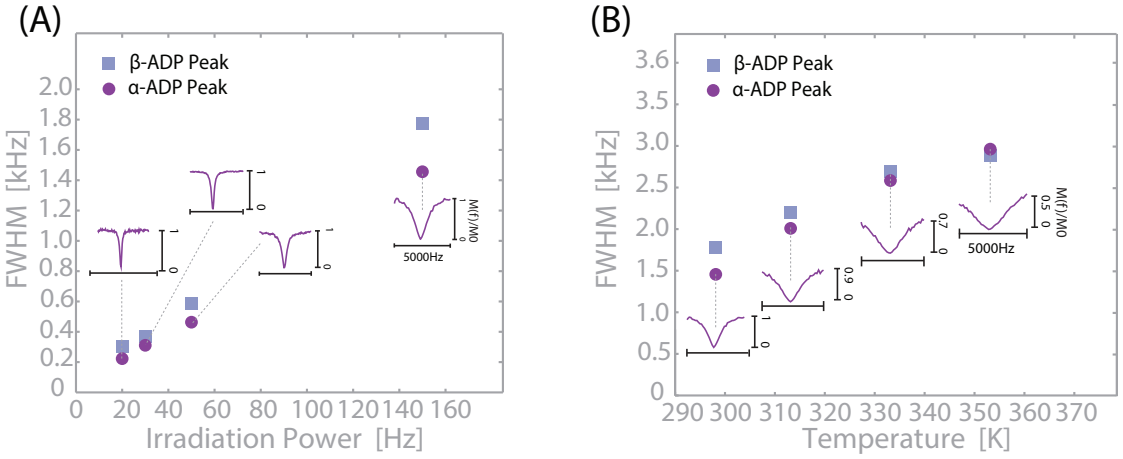

Figure B.8: ^{31}P CEST results for both phosphates in 100 mM ADP in D_2O at pH 3.9. (A) CEST dip width at half height as a function of CEST irradiation power of 20 Hz, 30 Hz, 50 Hz and 150 Hz at T=298.15 K, (B) CEST dip width at half height as a function of temperature of 298 K, 313 K, 333 K, 353 K.

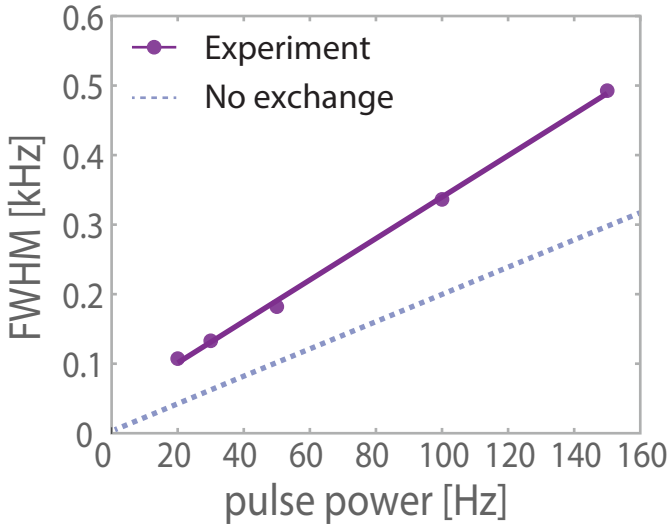

Figure B.9: ^{31}P CEST dip width at half height for 100 mM sodium phosphate as a function of CEST irradiation power of 20 Hz, 30Hz, 50 Hz, 100 Hz, and 150 Hz measured at 298 K. In the absence of exchange, one expects the width of the dip in the CEST spectrum to be approximately a factor two larger than the rf saturation power (expressed in Hz). However, the dip width ranging from 100 Hz to 500 Hz under exchange is over a factor three larger than the rf saturation power (expressed in Hz). The Solid lines are linear fits to guide the eye

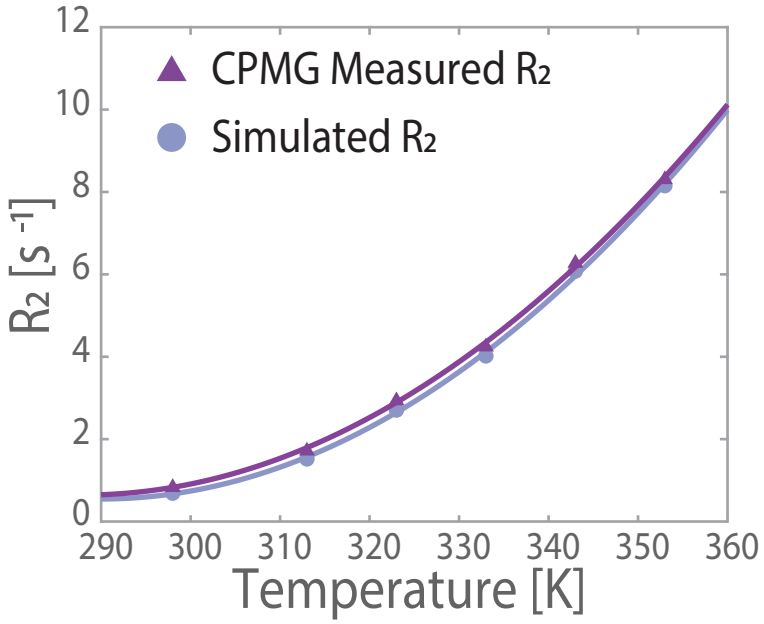

Figure B.10: The experimental and simulated ^{31}P R_2 rates for the 100 mM orthophosphate sample shown in Fig. 3.2B&C. Parameters used for this simulation were the same as used for the CEST simulations in Fig. 3.2B. Additional information on the modeling and physical interpretation is below.

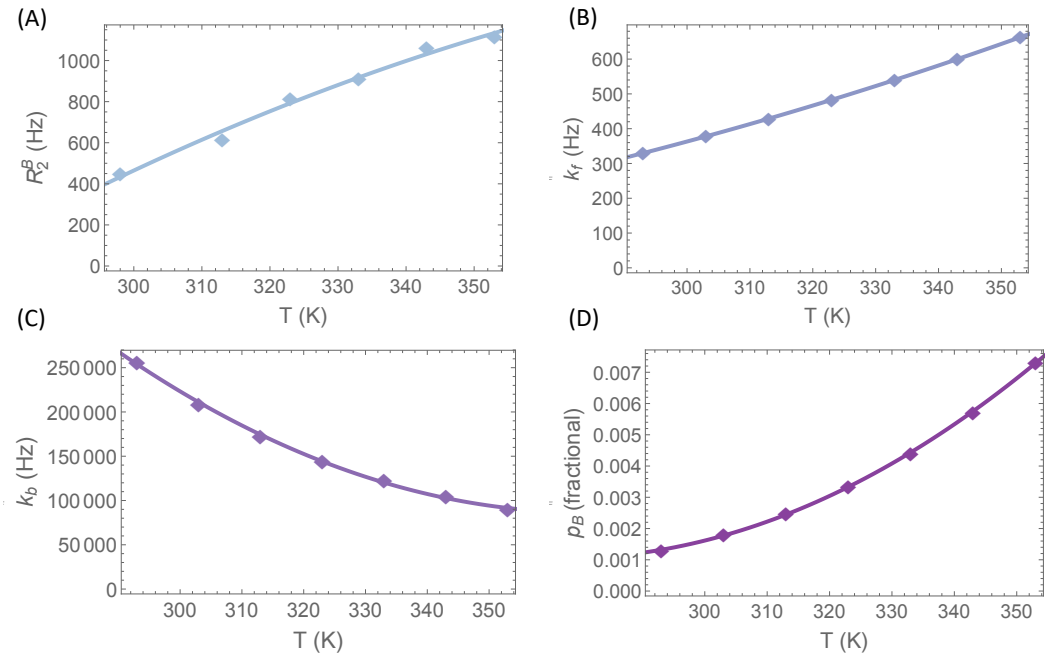

Figure B.11: Temperature dependence of R_2^B, kinetic parameters, and assembly population used for the simulated R_2 and CEST data shown in Fig. B.10 and 3.2B, respectively. Solid lines are quadratic fits to data to guide the eye. (A) The assembly relaxation rate R_2^B increases from 450 Hz to 1100 Hz between 298 K and 353 K. (B) The phosphate monomer to assembly rate (k_f) increases from 350 Hz to 600 Hz between 293 and 353 K. (C) The assembly to monomer rate (k_b) decreases from 250,000 Hz to 100,000 Hz between 293 and 353 K. (D) The fractional assembly population (p_B) increases from 0.0013 to 0.0073 between 293 K and 353 K.

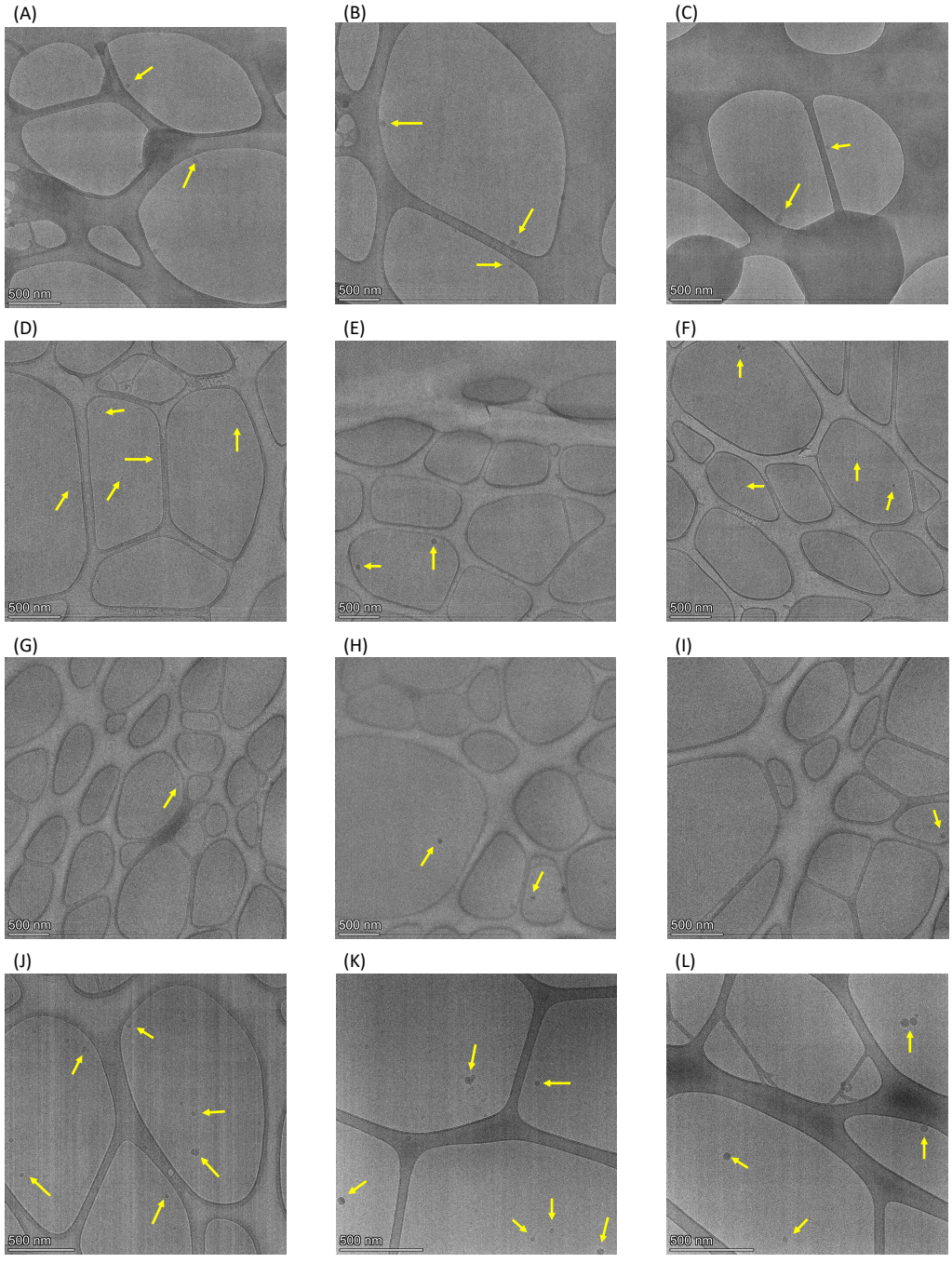

Figure B.12: Cryo-TEM micrographs from (A)-(C) 100 mM sodium ADP sample unheated, (D)-(F) 100 mM sodium ADP heated to 343 K, (G)-(I) 500 mM KCl heated to 343 K, and (J)-(L) 100 mM potassium ADP heated to 343 K. Yellow arrows indicate features in the size range of assemblies, although ice artifacts can appear at similar sizes. Samples in (A)-(I) are the samples used for the quantitative particle analysis.

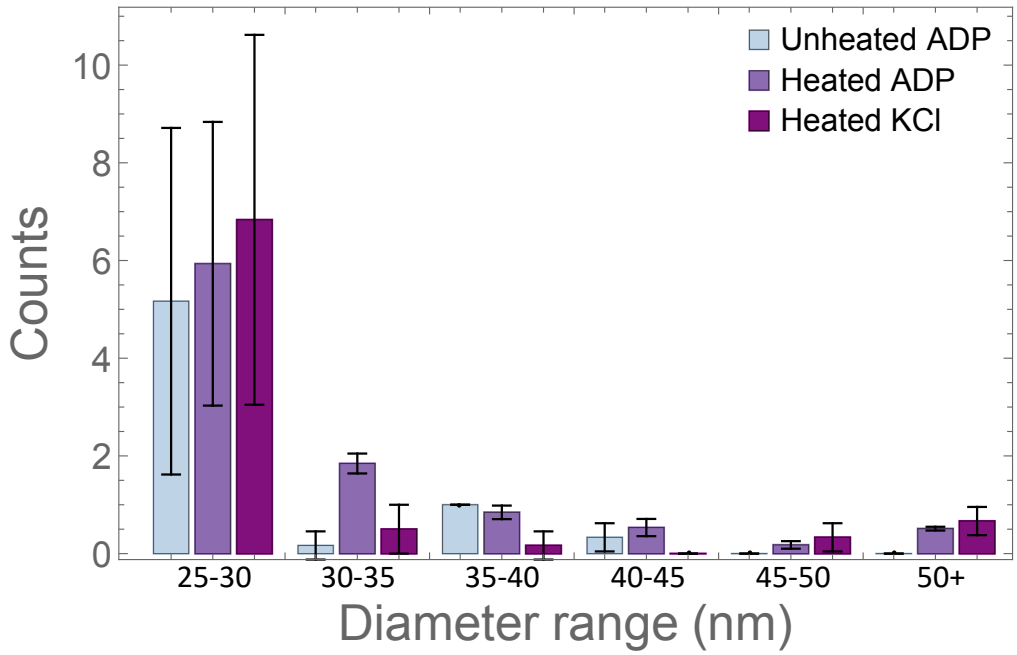

Figure B.13: Histogram of diameters for features detected per micrograph in selection of representative micrographs for sodium ADP at 298 K, sodium ADP heated at 343 K, and potassium chloride heated at 343 K. Only micrographs taken at the same magnification were compared, since the micrograph noise is primarily on pixel level. There were two, nine, and two micrographs, respectively, thus analyzed in the workflow described in SI. These results show a larger population of species in the two ADP samples, with the most in the heated ADP samples, except at the smallest and largest sizes, which can thus be attributed to erroneous features from the processing of the image analysis and ice artifacts, respectively, given that these are the only populations seen in the potassium chloride samples.

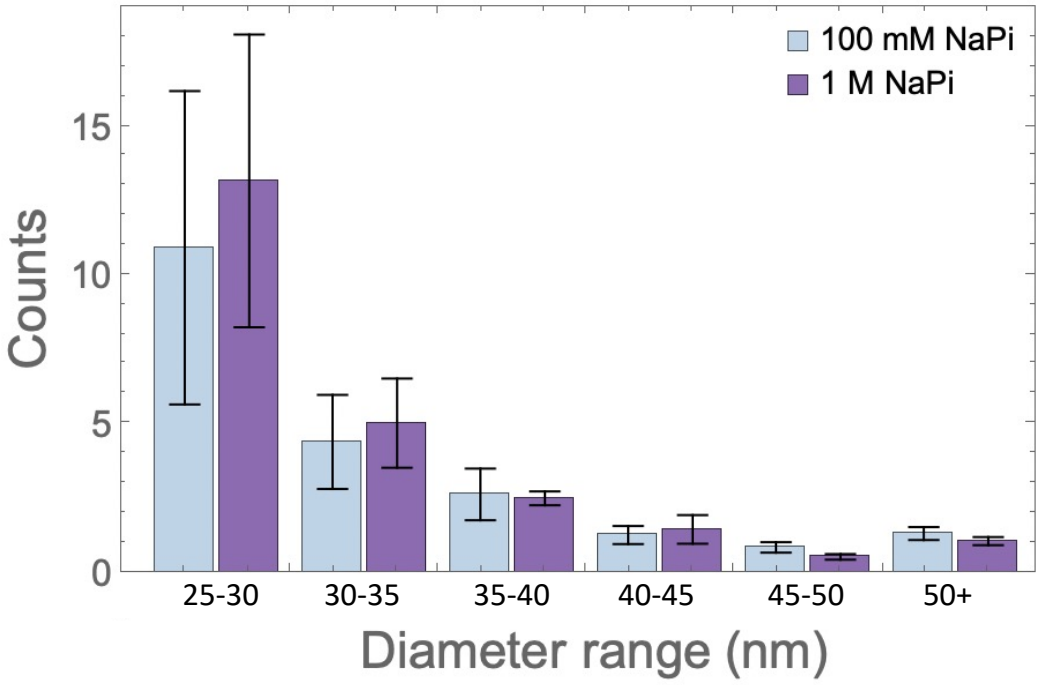

Figure B.14: Histogram of diameters for features detected per micrograph in selection of representative micrographs for sodium monophosphate at 100 mM and 1 M heated to 343 K before vitrification. Only micrographs taken at the same magnification were compared, since the micrograph noise is primarily on pixel level. Each sample incorporates data from 20 micrographs analyzed with the workflow described in SI. These results show that the size distribution of features is similar at both concentrations, which is consistent with equilibrium structures.

Cryo-TEM Image processing workflow

Microscopy analysis was conducted in Fiji Version 1.0. Images were first processed with a FFT bandpass filter, in order to smooth long-length scale variations in intensity to variations in camera pixel sensitivity, and to attenuate structures at small length scales that originate from pixel noise. Cutoffs for these filtering were varied, and found not to qualitatively affect the relative results. After filtering, pixels were autoscaled and saturated, before thresholding on the top 2-4 % of pixel intensity. The threshold was varied in this range to provide error bars for histogram results. After thresholding, the Close function was used to fill small regions of white pixels fully surrounded by black pixels. The Analyze Particles function was then used to select particles with an area of $200 - 2000$ pixels^2 and a circularity criteria of $0.6 - 1$, where circularity is defined as $4\pi * \frac{area}{perimeter^2}$. Results were then extracted and converted into area in nanometers for comparison between samples.

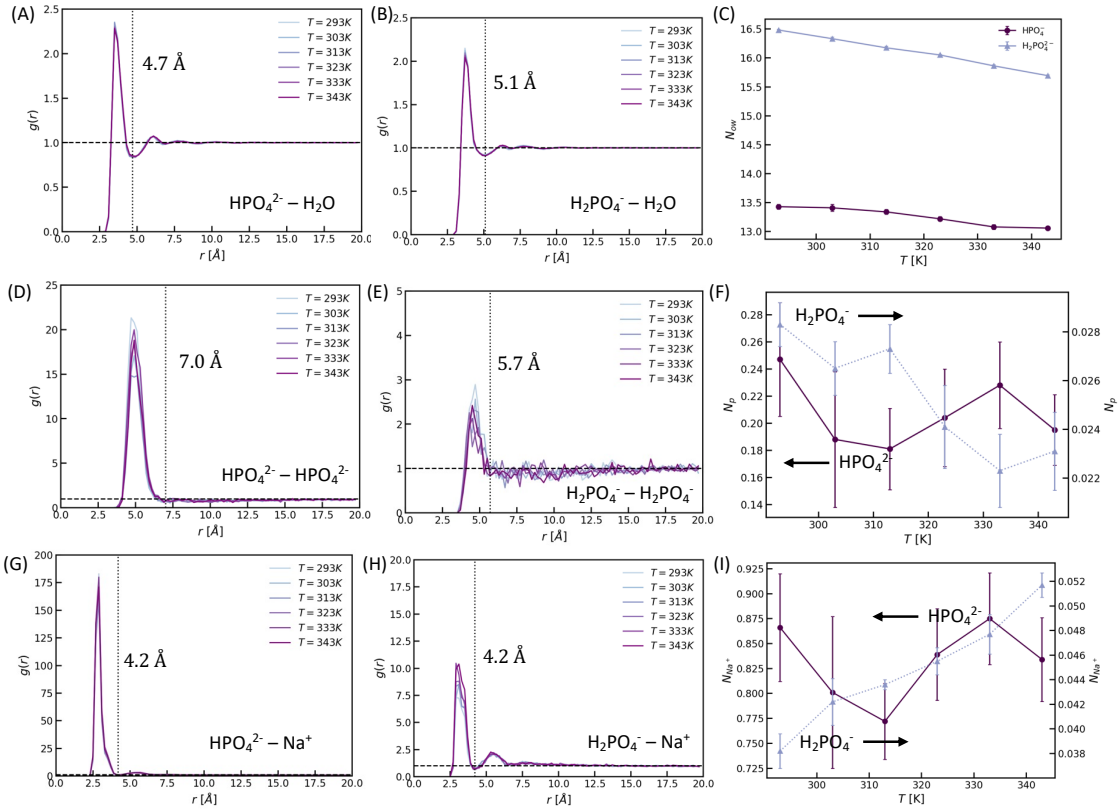

Figure B.15: Radial distribution functions (RDFs) and coordination numbers for water around phosphate ions, phosphate ions with each other, and Na^+ around phosphate ions. RDFs (A, B, D, E, G, H) are computed to a maximum distance of 20 Å with a bin size of 0.2 Å. The distances r are between (A, B) water oxygen atoms and phosphate phosphorous atoms, (D, E) phosphate phosphorous atoms with each other, and (G, H) sodium atoms and phosphate phosphorous atoms. The water-phosphate coordination number (C) is the average number of water oxygen atoms within 4.7 Å (HPO_4^{2-}) or 5.1 Å ($H_2PO_4^-$) of a phosphate phosphorous atom. The phosphate-phosphate coordination number (F) is the average number of phosphorous atoms within 7.0 Å (HPO_4^{2-}) or 5.7 Å ($H_2PO_4^-$) of a phosphorous atom. The sodium-phosphate coordination number (I) is the average number of sodium atoms within 4.2 Å of a phosphate phosphorous atom. The coordination number cutoffs are determined from the approximate location of the first minimum of the corresponding RDF (dotted lines, labeled with the exact cutoff). Error bars in (C), (F), and (I) are twice the standard error of the coordination numbers computed for each 200-ns block in the 1000-ns production simulation.

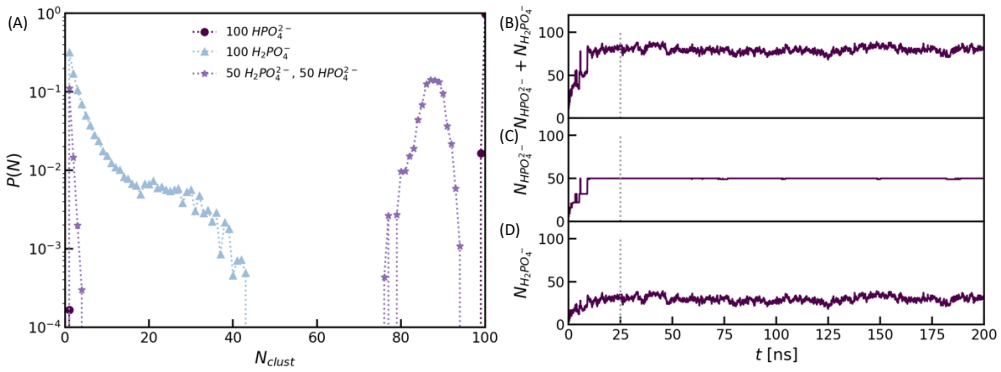

Figure B.16: (A) Cluster size distributions for the same systems as in Fig. 3.3C of the main text, but at 293 K. (B) Trajectory of the combined number of phosphate ions, both HPO_4^{2-} and $H_2PO_4^-$, in the largest cluster of the simulation of the mixed system at 343 K during the NPT equilibration and NPT production (separated by the dotted line). (C) Trajectory of the number of HPO_4^{2-} ions in that largest cluster. This trajectory is virtually constant at $N = 50$, the total number of HPO_4^{2-} ions in the box, during the entire production run, indicating that all HPO_4^{2-} ions in the box are in this large cluster. (D) Trajectory of the number of $H_2PO_4^-$ ions in that same cluster. Two phosphate ions are considered clustered if their phosphorous atoms are within 7.0 Å of each other. The 7.0 Å cutoff is chosen from the approximate location of the first minimum in the phosphate-phosphate RDF (Fig. B.13C).

MD simulation workflow and systems simulated

Systems are constructed using GROMACS 2016.1 [235, 236]. We perform the simulations using the OpenMM simulation engine [237]. Electrostatic interactions are computed using particle-mesh Ewald. Lennard-Jones nonbonded interactions are cut off at 10 Å. Hydrogen bonds are constrained with SHAKE [238] and water is kept rigid with SETTLE [239]. We use Langevin dynamics with an integration timestep of 2 fs and a friction coefficient of 0.1 ps^{-1}. We first perform a local energy minimization, followed by a 100-ps NVT equilibration. For the concentrated systems, we then perform a 25-ns NPT equilibration using a Monte Carlo (MC) barostat with 200 fs between MC moves and then perform a 175-ns NPT production, again using the MC barostat with the same conditions, saving configurations every 100 ps. For the dilute systems, we perform a 100-ps NPT equilibration using the MC barostat with the same conditions, followed by a 1000-ns NPT production, again using the MC barostat with the same conditions. The cluster size distributions, radial distribution functions, and coordination numbers are computed from the production simulations.

$N_{HPO_4^{2-}}$	$N_{H_2PO4^-}$	N_{Na^+}	N_{H_2O}	Temperatures simulated [K]
100	0	200	4759	293, 343
0	100	100	4852	293, 343
50	50	150	4801	293, 343
3	0	6	2149	293, 303, 313, 323, 333, 343
0	3	3	2148	293, 303, 313, 323, 333, 343

Table B.1: Systems simulated using molecular dynamics.

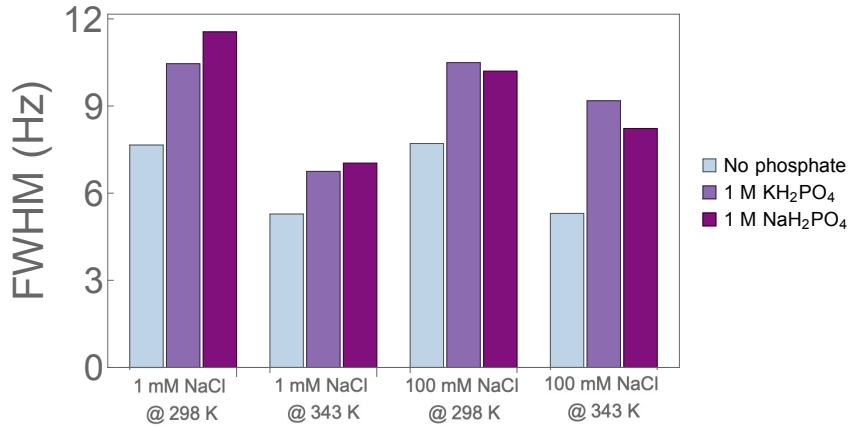

Figure B.17: Experimental ^{23}Na linewidth data for 1 mM and 100 mM NaCl in the absence of phosphates, and with 1 M KH_2PO_4 and 1 M NaH_2PO_4 at 298 K and 343 K. All solutions were adjusted to pH 4.1 with HCl. ^{23}Na linewidths are broader in the presence of phosphates at both temperatures and concentrations, indicating that sodium is incorporated into the assemblies.

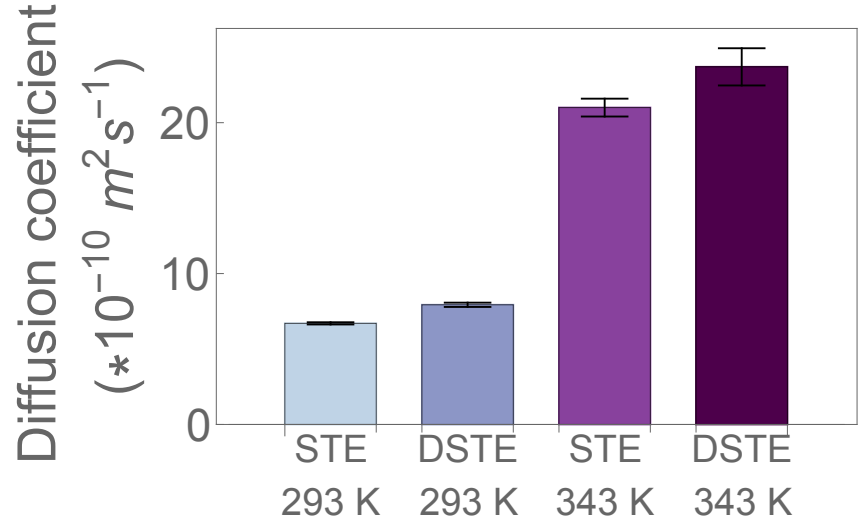

Figure B.18: Diffusion coefficients extracted from ^{31}P DOSY experiments for 1 M potassium phosphate at pH 4.2 using a stimulated echo (STE) and convection-compensated double stimulated echo (DSTE) sequence. Diffusion coefficients were found to be comparable at both 293 K and 343 K, indicating that the observed increased in diffusion coefficient with temperature is not a convection-based effect.

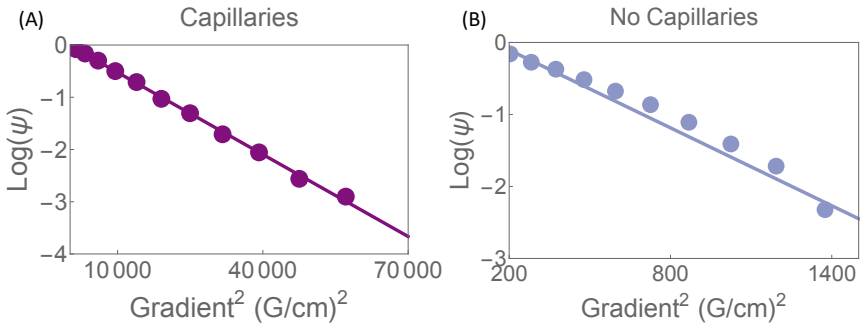

Figure B.19: ^{31}P DOSY fits of Log(ψ) vs gradient strength squared for a 1 M potassium phosphate sample in the presence (A) and absence (B) of capillaries at 343 K, where ψ is signal attenuation. Note that in the absence of capillaries, the relationship between Log(ψ) and gradient squared is non-linear due to convection-based dephasing effects, and that the gradient values are much lower because of the increased rate of particle motion. Capillaries were thus used for all high temperature samples.

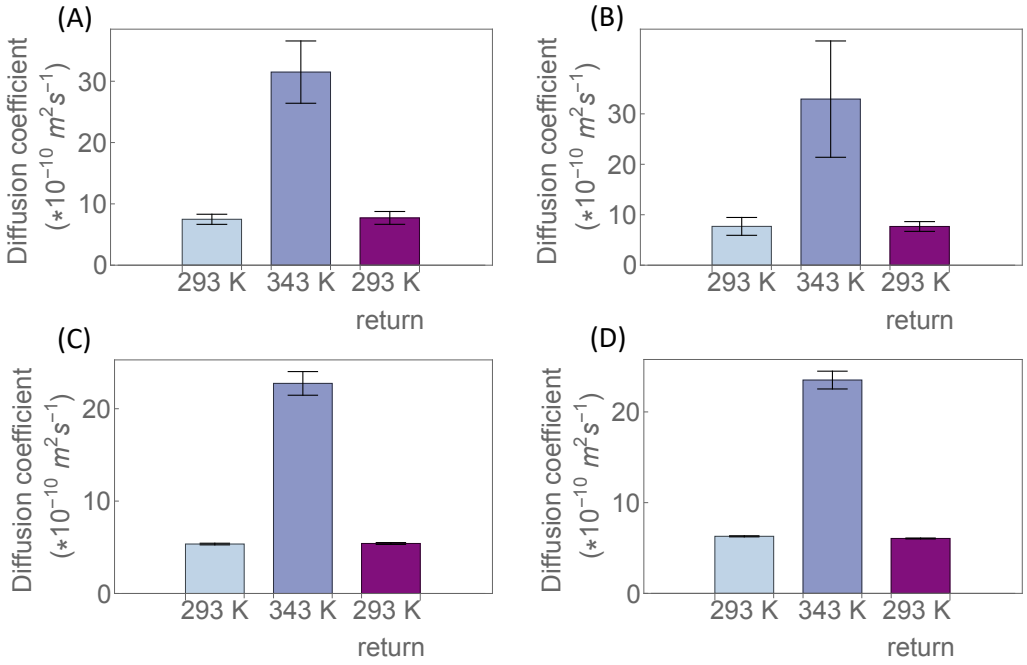

Figure B.20: Diffusion coefficients extracted from ^{31}P DOSY experiments. (A) 100 mM sodium phosphate at pH 4.2, (B) 100 mM potassium phosphate at pH 4.0, (C) 1 M sodium phosphate at pH 4.2, (d) 1 M potassium phosphate at pH 4.1.

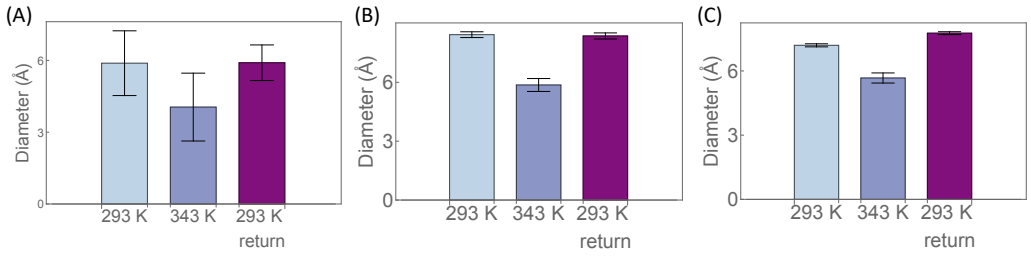

Figure B.21: Hydrodynamic diameters found by the Stokes-Einstein relaxation from diffusion coefficients in S5. (A) 100 mM potassium phosphate, (B) 1 M sodium phosphate, (C) 1 M potassium phosphate.

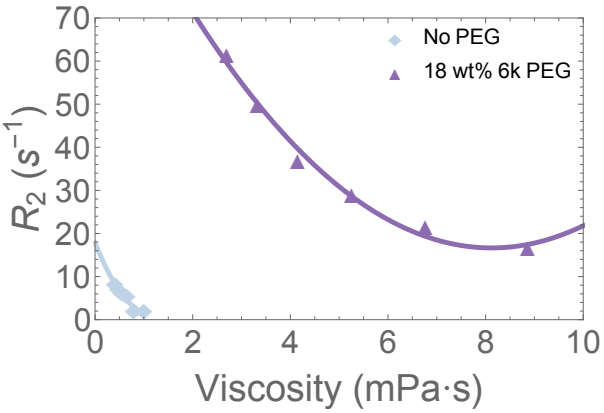

Figure B.22: R_2 relaxation rate as extracted from FWHM for 100 mM potassium phosphate at pH 4.5 in the absence of PEG and for a 18 wt% PEG solution as a function of viscosity [240], showing that viscosity alone cannot explain the effect of PEG on relaxation rates. Solid lines are quadratic fits to data to guide the eye.

Appendix C

Supporting Information for Chapter 5

Figures

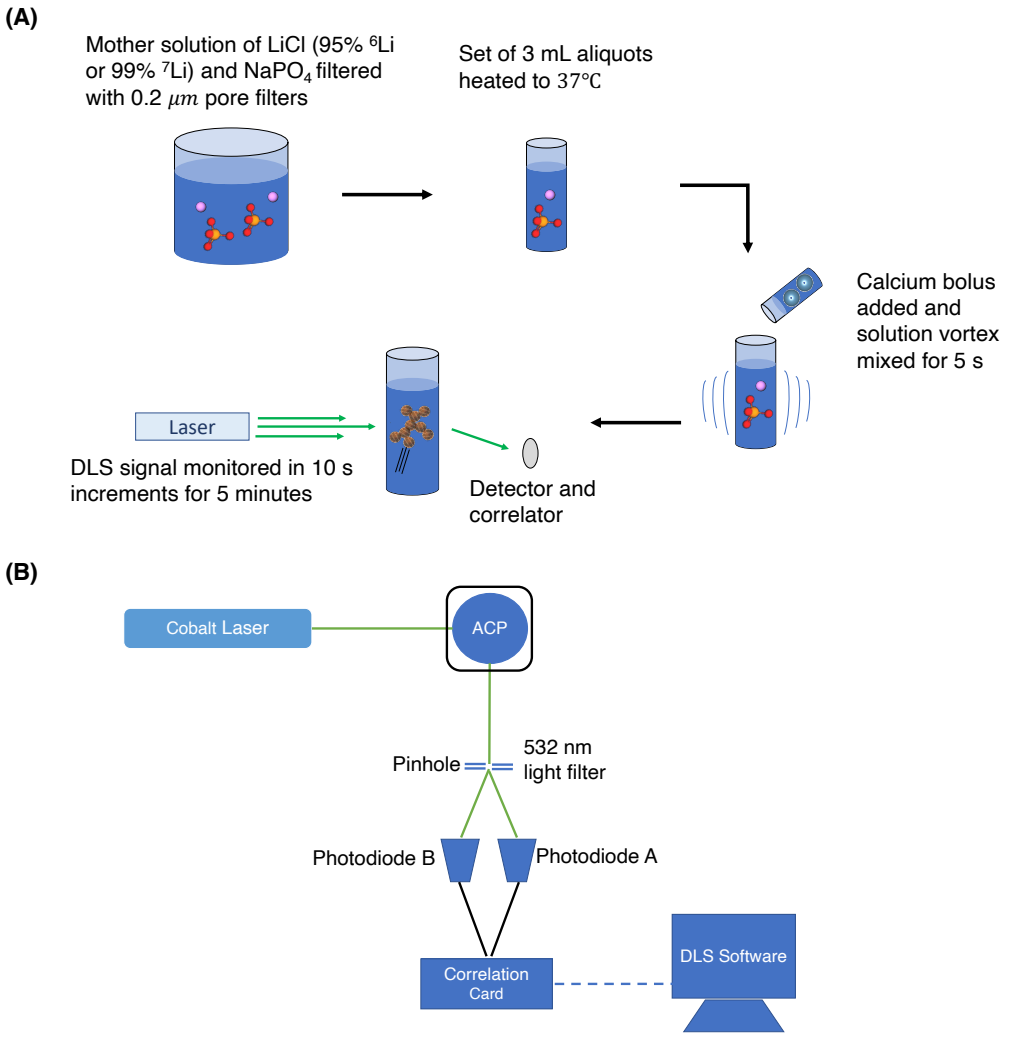

Figure C.1: Protocol and setup for DLS experiments. (A) Solutions of 2mM sodium phosphate and 250 mM lithium chloride were prepared and filtered to remove any contaminants. Aliquots were then heated to 37 °C, before adding calcium chloride (final concentration 5 mM) and rapidly vortex mixing. These solutions were immediately placed into the DLS and monitored for 5 minutes in 10 s blocks. (B) Setup for DLS experiments. Incident 532 nm light is scattered off of the sample and passes through a 532 nm filter. Scattered light then is split into two avalanche photodiodes which are connected to a correlation card that interfaces with DLS software provided by Brookhaven.

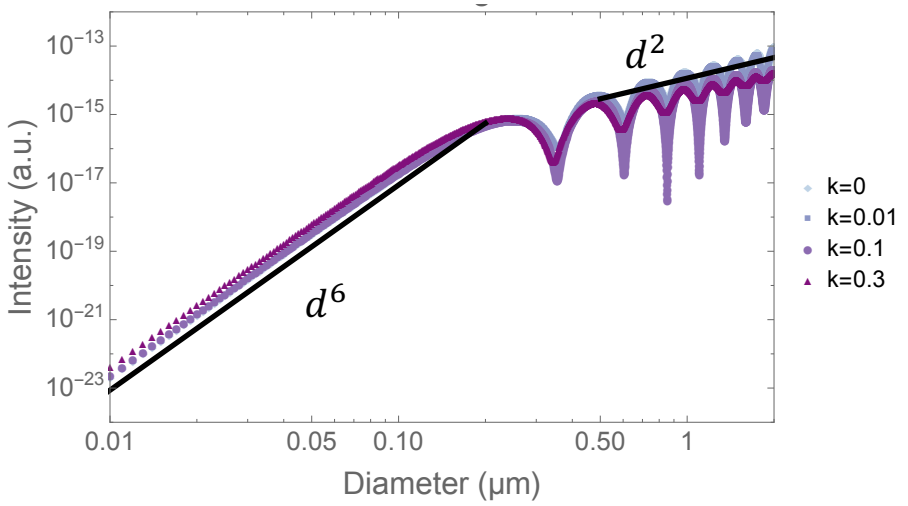

Figure C.2: Scattering intensity vs. diameter for calcium phosphate ($n = 1.626$) for 532 nm light. Notably, in the Rayleigh regime defined by diameter $d << \lambda$, the intensity I scales as $I \propto d^6$, while for sizes greater than the Rayleigh regime we have $I \propto d^2$. Difference curves show different values of the extinction coefficient, k, which is not quantified for ACP. Regardless of the specific value of k, the observed scaling is the same.

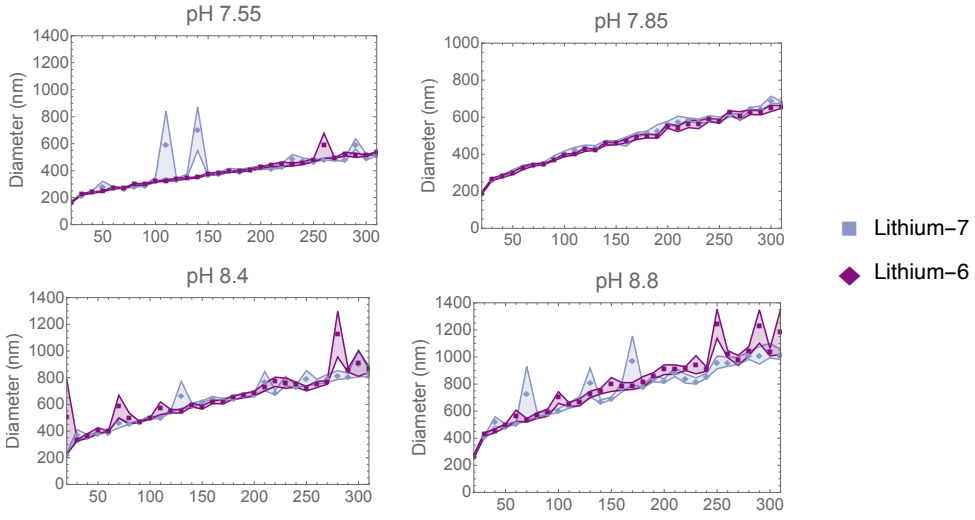

Figure C.3: DLS average diameter time series data at varying pH for samples whose intensity are shown in Fig. 5.3B. Average diameters show no lithium isotope dependence, indicating that the observed intensity difference in Fig. 5.3B is related to particle abundance.

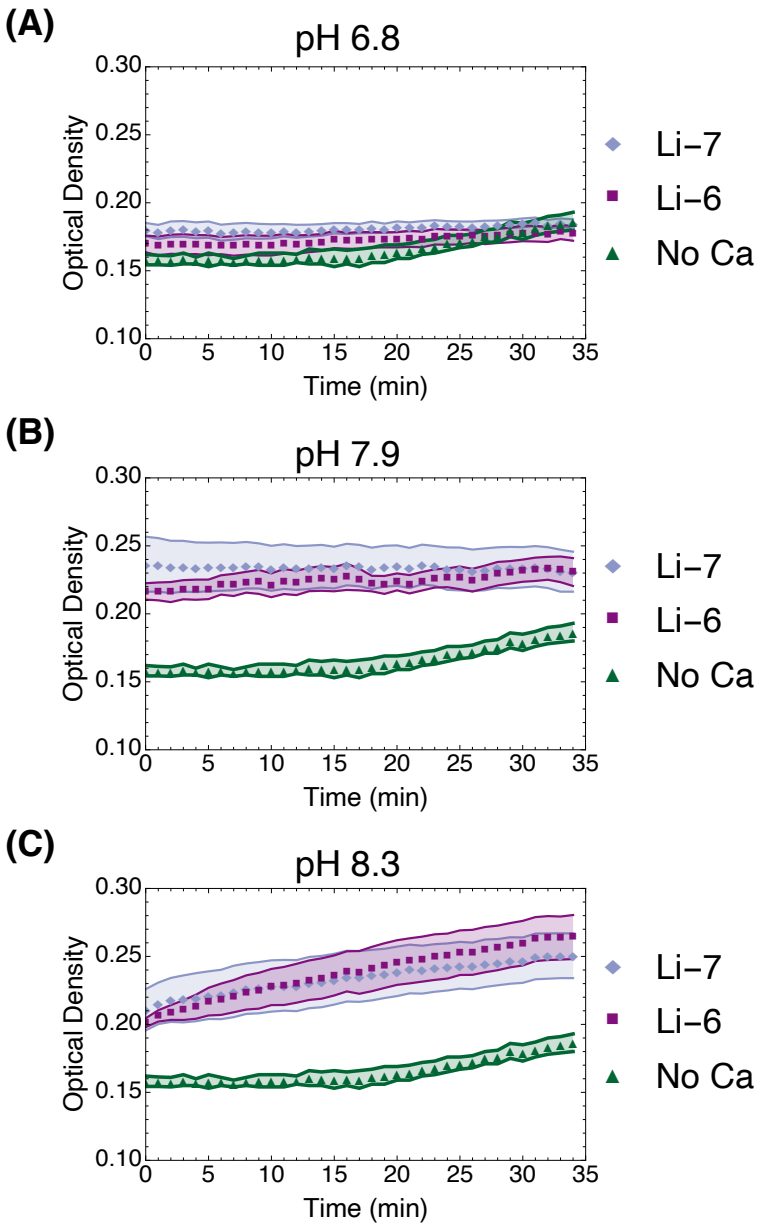

Figure C.4: 35-minute absorbance measurements at 532 nm wavelength identify three distinct stages of calcium phosphate growth in solution phase space. (A) At lower pH, solutions are indistinguishable from no-Ca control, corresponding to dissolved free ion phase. (B) At intermediate pH, solutions form metastable ACP colloids with constant absorbance traces. C) At higher pH, solutions immediately undergo agglomeration, indicated by steadily increasing absorbance. Error bars are the standard error from 4 independent trials.

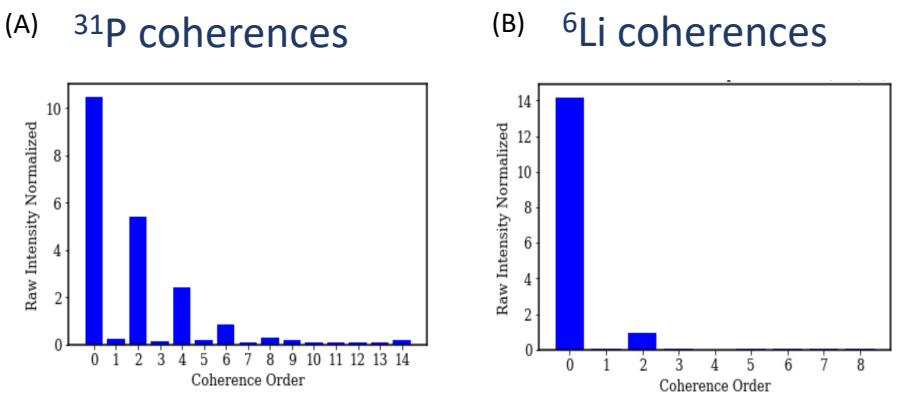

Figure C.5: Spin counting results on ^{6}Li-ACP powder used for ICP-MS and REDOR. (A) ^{31}P spin counting result confirms shows the same coherence orders as ACP, confirming that the phase of the powder. (B) ^{6}Li spin counting results show no coherences order over 2, as compared to ^{6}LiCl, which showed coherence orders up to 8. This suggests there are no large clumps of reprecipitated ^{6}Li in solution that would contribute to the ICP-MS ^{6}Li signal.

Bibliography

[1] P.-O. Löwdin, *Proton tunneling in dna and its biological implications*, *Rev. Mod. Phys.* **35** (Jul, 1963) 724–732.

[2] A. Kohen and J. P. Klinman, *Hydrogen tunneling in biology*, *Chemistry & biology* **6** (1999), no. 7 R191–R198.

[3] L. Turin, *A Spectroscopic Mechanism for Primary Olfactory Reception*, *Chemical Senses* **21** (12, 1996) 773–791, [https://academic.oup.com/chemse/article-pdf/21/6/773/1320021/21-6-773.pdf].

[4] C. C. Gradinaru, J. T. M. Kennis, E. Papagiannakis, I. H. M. van Stokkum, R. J. Cogdell, G. R. Fleming, R. A. Niederman, and R. van Grondelle, *An unusual pathway of excitation energy deactivation in carotenoids: Singlet-to-triplet conversion on an ultrafast timescale in a photosynthetic antenna*, *Proceedings of the National Academy of Sciences* **98** (2001), no. 5 2364–2369, [https://www.pnas.org/doi/pdf/10.1073/pnas.051501298].

[5] G. S. Engel, T. R. Calhoun, E. L. Read, T.-K. Ahn, T. Mančal, Y.-C. Cheng, R. E. Blankenship, and G. R. Fleming, *Evidence for wavelike energy transfer through quantum coherence in photosynthetic systems*, *Nature* **446** (2007), no. 7137 782–786.

[6] F. Fassioli, R. Dinshaw, P. C. Arpin, and G. D. Scholes, *Photosynthetic light harvesting: excitons and coherence*, *Journal of The Royal Society Interface* **11** (2014), no. 92 20130901, [https://royalsocietypublishing.org/doi/pdf/10.1098/rsif.2013.0901].

[7] K. Schulten, C. E. Swenberg, and A. Weller, *A biomagnetic sensory mechanism based on magnetic field modulated coherent electron spin motion*, *Zeitschrift fÃŒr Physikalische Chemie* **111** (1978), no. 1 1–5.

[8] W. Wiltschko and R. Wiltschko, *Magnetic orientation and magnetoreception in birds and other animals*, *Journal of Comparative Physiology A* **191** (2005), no. 8 675–693.

[9] H. Mouritsen and T. Ritz, *Magnetoreception and its use in bird navigation*, *Current Opinion in Neurobiology* **15** (2005), no. 4 406–414. Sensory systems.

[10] C. T. Rodgers and P. J. Hore, *Chemical magnetoreception in birds: The radical pair mechanism*, *Proceedings of the National Academy of Sciences* **106** (2009), no. 2 353–360, [https://www.pnas.org/doi/pdf/10.1073/pnas.0711968106].

[11] E. M. Kawamoto, C. Vivar, and S. Camandola, *Physiology and Pathology of Calcium Signaling in the Brain*, *Frontiers in Pharmacology* **3** (2012) 61.

[12] L. M. Grover and T. J. Teyler, *Two components of long-term potentiation induced by different patterns of afferent activation*, *Nature* **347** (1990), no. 6292 477–479.

[13] V. Y. Bolshakov and S. A. Siegelbaum, *Postsynaptic induction and presynaptic expression of hippocampal long-term depression.*, *Science* **264 5162** (1994) 1148–52.

[14] A. E. West, W. G. Chen, M. B. Dalva, R. E. Dolmetsch, J. M. Kornhauser, A. J. Shaywitz, M. A. Takasu, X. Tao, and M. E. Greenberg, *Calcium regulation of neuronal gene expression*, *Proceedings of the National Academy of Sciences* **98** (2001), no. 20 11024–11031.

[15] L. Redmond, A. H. Kashani, and A. Ghosh, *Calcium regulation of dendritic growth via cam kinase iv and creb-mediated transcription*, *Neuron* **34** (2002), no. 6 999–1010.

[16] M. J. Berridge, *Neuronal calcium signaling*, *Neuron* **21** (1998), no. 1 13–26.

[17] D. Tanaka, K. Nakada, K. Takao, E. Ogasawara, A. Kasahara, A. Sato, H. Yonekawa, T. Miyakawa, and J.-I. Hayashi, *Normal mitochondrial respiratory function is essential for spatial remote memory in mice*, *Molecular Brain* **1** (2008), no. 1 21.

[18] R. Tsien, D. Lipscombe, D. Madison, K. Bley, and A. Fox, *Multiple types of neuronal calcium channels and their selective modulation*, *Trends in Neurosciences* **11** (1988), no. 10 431–438.

[19] W. A. Catterall, *Voltage-gated calcium channels*, *Cold Spring Harbor perspectives in biology* **3** (2011), no. 8.

[20] M. Bertolino and R. R. Llinas, *The central role of voltage-activated and receptor-operated calcium channels in neuronal cells*, *Annual Review of Pharmacology and Toxicology* **32** (1992), no. 1 399–421.

[21] N. Burnashev, *Calcium permeability of glutamate-gated channels in the central nervous system*, *Current Opinion in Neurobiology* **6** (1996), no. 3 311–317.

[22] A. Verkhratsky, *Physiology and pathophysiology of the calcium store in the endoplasmic reticulum of neurons*, *Physiological Reviews* **85** (2005), no. 1 201–279, [https://doi.org/10.1152/physrev.00004.2004]. PMID: 15618481.

[23] G. E. Stutzmann and M. P. Mattson, *Endoplasmic reticulum ca2+ handling in excitable cells in health and disease*, *Pharmacological Review* **63** (2011), no. 3 700–727.

[24] M. Terasaki, N. Slater, A. Fein, A. Schmidek, and T. Reese, *Continuous network of endoplasmic reticulum in cerebellar purkinje neurons*, *Proceedings of the National Acadmey of Sciences* **91** (1994), no. 16 7510–7514.

[25] P. P. Carlotta Giorgi, Saverio Marchi, *The machineries, regulation and cellular functions of mitochondrial calcium*, *Nature Reviews Molecular Cell Biology* **19** (2018), no. 11 713–730.

[26] M. R. Duchen, *Mitochondria and calcium: from cell signalling to cell death*, *The Journal of Physiology* **529** (2000), no. 1 57–68.

[27] L. Contreras and J. Satrústegui, *Calcium signaling in brain mitochondria*, *J Biol Chem* **284** (2009), no. 11 7091–7099.

[28] G. Bustos, P. Cruz, A. Lovy, and C. CÃ¡rdenas, *Endoplasmic reticulumâmitochondria calcium communication and the regulation of mitochondrial metabolism in cancer: A novel potential target*, *Frontiers in Oncology* **7** (2017).

[29] R. J. Kaufman and J. D. Malhotra, *Calcium trafficking integrates endoplasmic reticulum function with mitochondrial bioenergetics*, *Biochim Biophys Acta* **1843** (2014), no. 10 2233–2239.

[30] C. Tang, Y. Wei, L. Gu, Q. Zhang, M. Li, G. Yuan, Y. He, L. Huang, Y. Liu, and Y. Zhang, *Biomineral precursor formation is initiated by transporting calcium and phosphorus clusters from the endoplasmic reticulum to mitochondria*, *Advanced Science* **7** (2020), no. 8 1902536.

[31] M.-m. Poo, M. Pignatelli, T. J. Ryan, S. Tonegawa, T. Bonhoeffer, K. C. Martin, A. Rudenko, L.-H. Tsai, R. W. Tsien, G. Fishell, C. Mullins, J. T. Gonçalves, M. Shtrahman, S. T. Johnston, F. H. Gage, Y. Dan, J. Long, G. Buzsáki, and C. Stevens, *What is memory? the present state of the engram*, *BMC Biology* **14** (2016), no. 1 40.

[32] D. O. Hebb, *The organization of behavior: A neuropsychological theory*. Wiley, New York, 1949.

[33] L. C. Katz and C. J. Shatz, *Synaptic activity and the construction of cortical circuits*, *Science* **274** (1996), no. 5290 1133–1138.

[34] T. V. Bliss and S. F. Cooke, *Long-term potentiation and long-term depression: a clinical perspective*, *Clinics (Sao Paolo)* **66** (2011) 3–17.

[35] H. Markram, J. Lübke, M. Froscher, and B. Sakmann, *Regulation of synaptic efficacy by coincidence of postynaptic aps and epsps*, *Science* **275** (1997), no. 5297 213–215.

[36] X. Liu, S. Ramirez, P. T. Pang, C. B. Puryear, A. Govindarajan, K. Deisseroth, and S. Tonegawa, *Optogenetic stimulation of a hippocampal engram activates fear memory recall*, *Nature* **484** (2012), no. 7394 381–385.

[37] S. Ramirez, X. Liu, P.-A. Lin, J. Suh, M. Pignatelli, R. L. Redondo, T. J. Ryan, and S. Tonegawa, *Creating a false memory in the hippocampus*, *Science* **341** (2013), no. 6144 387–391.

[38] F. Engert and T. Bonhoeffer, *Dendritic spine changes associated with hippocampal long-term synaptic plasticity*, *Nature* **399** (1999), no. 6731 66–70.

[39] A. Hayashi-Takagi, S. Yagishita, M. Nakamura, F. Shirai, Y. I. Wu, A. L. Loshbaugh, B. Kuhlman, K. M. Hahn, and H. Kasai, *Labelling and optical erasure of synaptic memory traces in the motor cortex*, *Nature* **525** (2015), no. 7569 333–338.

[40] H. David and L. Squire, *Protein synthesis and memory: a review*, *Psychological bulletin* **96** (1984), no. 3 518–559.

[41] T. J. Ryan, D. S. Roy, M. Pignatelli, A. Arons, and S. Tonegawa, *Engram cells retain memory under retrograde amnesia*, *Science* **348** (2015), no. 6238 1007–1013, [https://www.science.org/doi/pdf/10.1126/science.aaa5542].

[42] S. Tonegawa, M. Pignatelli, D. S. Roy, and T. J. Ryan, *Memory engram storage and retrieval*, *Current Opinion in Neurobiology* **35** (2015) 101–109. Circuit plasticity and memory.

[43] F. Crick and C. Koch, *Consciousness and neuroscience.*, *Cerebral Cortex* **8** (03, 1998) 97–107.

[44] F. Crick and C. Koch, *A framework for consciousness*, *Nature Neuroscience* **6** (2003), no. 2 119–126.

[45] E. P. Wigner, *Remarks on the Mind-Body Question*, pp. 247–260. Springer Berlin Heidelberg, Berlin, Heidelberg.

[46] R. Penrose, *The emperor's new mind*, *RSA Journal* **139** (1991), no. 5420 506–514.

[47] R. Penrose, *Shadows of the Mind: A Search for the Missing Science of Consciousness*. Oxford University Press, 1994.

[48] R. Penrose, *On gravity's role in quantum state reduction*, *General Relativity and Gravitation* **28** (1996), no. 5 581–600.

[49] S. Hameroff and R. Penrose, *Orchestrated reduction of quantum coherence in brain microtubules: A model for consciousness*, *Mathematics and Computers in Simulation* **40** (1996), no. 3 453–480.

[50] A. Ekert, R. Jozsa, R. Penrose, and H. Stuart, *Quantum computation in brain microtubules? the penroseâhameroff âorch orâ model of consciousness*, *Philosophical Transactions of the Royal Society of London. Series A: Mathematical, Physical and Engineering Sciences* **356** (1998), no. 1743 1869–1896, [https://royalsocietypublishing.org/doi/pdf/10.1098/rsta.1998.0254].

[51] M. P. A. Fisher, *Quantum cognition: The possibility of processing with nuclear spins in the brain*, *Annals of Physics* **362** (2015) 593–602.

[52] A. Abragam, *The Principles of Nuclear Magnetism*. International series of monographs on physics. Clarendon Press, 1961.

[53] M. Levitt, *Spin Dynamics: Basics of Nuclear Magnetic Resonance*. Wiley, 2013.

[54] M. P. A. Fisher and L. Radzihovsky, *Quantum indistinguishability in chemical reactions*, *Proceedings of the National Academy of Sciences* **115** (2018), no. 20 E4551–E4558.

[55] M. W. Swift, C. G. Van de Walle, and M. P. A. Fisher, *Posner molecules: from atomic structure to nuclear spins*, *Physical Chemistry Chemical Physics* **20** (2018), no. 18 12373–12380.

[56] M. Klingenberg, *The adp and atp transport in mitochondria and its carrier*, *Biochimica et Biophysica Acta (BBA) - Biomembranes* **1778** (2008), no. 10 1978–2021.

[57] G. C. Brown, *Control of respiration and ATP synthesis in mammalian mitochondria and cells*, *Biochemical Journal* **284** (05, 1992) 1–13.

[58] T. E. Gunter, D. I. Yule, K. K. Gunter, R. A. Eliseev, and J. D. Salter, *Calcium and mitochondria*, *FEBS Letters* **567** (2004), no. 1 96–102. Warsaw Special Issue.

[59] L. Contreras, I. Drago, E. Zampese, and T. Pozzan, *Mitochondria: The calcium connection*, *Biochimica et Biophysica Acta (BBA) - Bioenergetics* **1797** (2010), no. 6 607–618. 16th European Bioenergetics Conference 2010.

[60] A. P. Halestrap, *What is the mitochondrial permeability transition pore?*, *Journal of Molecular and Cellular Cardiology* **46** (2009), no. 6 821–831. Mitochondria Special Issue: From Basic Mitochondrial Biology to Cardiovascular Disease.

[61] S. G. Wolf, Y. Mutsafi, T. Dadosh, T. Ilani, Z. Lansky, B. Horowitz, S. Rubin, M. Elbaum, and D. Fass, *3d visualization of mitochondrial solid-phase calcium stores in whole cells*, *Elife* **6** (2017) e29929.

[62] D. Torralba, F. Baixauli, and F. Sánchez-Madrid, *Mitochondria know no boundaries: Mechanisms and functions of intercellular mitochondrial transfer*, *Frontiers in Cell and Developmental Biology* **4** (09, 2016).

[63] I. Scott and R. Youle, *Mitochondrial fission and fusion*, *Essays Biochem.* **47** (2010) 85–98.

[64] J. S. Straub, M. S. Nowotarski, J. Lu, T. Sheth, S. Jiao, M. P. A. Fisher, M. S. Shell, M. E. Helgeson, A. Jerschow, and S. Han, *Phosphates form spectroscopically dark state assemblies in common aqueous solutions*, *Proceedings of the National Academy of Sciences* **120** (2023), no. 1 e2206765120, [https://www.pnas.org/doi/pdf/10.1073/pnas.2206765120].

[65] A. S. Posner, N. C. Blumenthal, A. L. Boskey, and F. Betts, *Synthetic analogue of bone mineral formation*, *Journal of Dental Research* **54** (1975), no. 2_suppl 88–93.

[66] J. Jeong, J. H. Kim, J. H. Shim, N. S. Hwang, and C. Y. Heo, *Bioactive calcium phosphate materials and applications in bone regeneration*, *Biomaterials Research* **23** (2019), no. 1 4.

[67] R. Z. LeGeros, *Calcium phosphate-based osteoinductive materials*, *Chemical Reviews* **108** (11, 2008) 4742–4753.

[68] S. V. Dorozhkin and M. Epple, *Biological and medical significance of calcium phosphates*, *Angewandte Chemie International Edition* **41** (2002), no. 17 3130–3146.

[69] S. V. Dorozhkin, *Calcium orthophosphates in nature, biology and medicine*, *Materials* **2** (2009), no. 2 399–498.

[70] H. M. Myers, *Calcium phosphates in oral biology and medicine*, *Calcium Phosphate Biomaterials in Preventive and Restorative Dentistry. Farmington, CT: Karger* (1991) 154–71.

[71] J. Driver, D. Lijmbach, and I. Steen, *Why recover phosphorus for recycling, and how?*, *Environmental Technology* **20** (1999), no. 7 651–662.

[72] W. J. Schipper, A. Klapwijk, B. Potjer, W. H. Rulkens, B. G. Temmink, F. G. Kiestra, and A. M. Lijmbach, *Phosphate recycling in the phosphorus industry*, *Environmental Technology* **22** (2001), no. 11 1337–1345.

[73] J. Elliot, *Structure and Chemistry of the Apatites and Other Calcium Orthophosphates*. Elsevier Science B.V., 1994.

[74] S. V. Dorozhkin, *Amorphous calcium (ortho)phosphates*, *Acta Biomaterialia* **6** (2010), no. 12 4457–4475.

[75] M. D. Francis, R. Graham, G. Russell, and H. Fleisch, *Diphosphonates inhibit formation of calcium phosphate crystals in vitro and pathological calcification in vivo*, *Science* **165** (1969), no. 3899 1264–1266.

[76] N. Vidavsky, J. A. M. R. Kunitake, and L. A. Estroff, *Multiple pathways for pathological calcification in the human body*, *Advanced Healthcare Materials* **10** (2021), no. 4 2001271.

[77] K. He, M. Sawczyk, C. Liu, Y. Yuan, B. Song, R. Deivanayagam, A. Nie, X. Hu, V. P. Dravid, J. Lu, C. Sukotjo, Y. Lu, P. Král, T. Shokuhfar, and R. Shahbazian-Yassar, *Revealing nanoscale mineralization pathways of hydroxyapatite using in situ liquid cell transmission electron microscopy*, *Science Advances* **6** (2020), no. 47 eaaz7524, [https://www.science.org/doi/pdf/10.1126/sciadv.aaz7524].

[78] K. Onuma and A. Ito, *Cluster growth model for hydroxyapatite*, *Chemistry of Materials* **10** (11, 1998) 3346–3351.

[79] A. Lotsari, A. K. Rajasekharan, M. Halvarsson, and M. Andersson, *Transformation of amorphous calcium phosphate to bone-like apatite*, *Nature Communications* **9** (2018), no. 1 4170.

[80] J. A. Stammeier, B. Purgstaller, D. Hippler, V. Mavromatis, and M. Dietzel, *In-situ raman spectroscopy of amorphous calcium phosphate to crystalline hydroxyapatite transformation*, *MethodsX* **5** (2018) 1241–1250.

[81] R. Villa-Bellosta and W. C. O'Neill, *Pyrophosphate deficiency in vascular calcification*, *Kidney International* **93** (2018), no. 6 1293–1297.

[82] C. J. S. Ibsen and H. Birkedal, *Pyrophosphate-inhibition of apatite formation studied by in situ x-ray diffraction*, *Minerals* **8** (2018), no. 2.

[83] S. Kundu, A. J. Nathanael, Y. H. Seo, and T. H. Oh, *Pvp assisted synthesis of hydroxyapatite nanorods with tunable aspect ratio and bioactivity*, *Journal of Nanomaterials* **2015** (2015) 621785.

[84] K. Shin, J. E. Kent, C. Singh, L. M. Fujimoto, J. Yu, Y. Tian, W. Im, and F. M. Marassi, *Calcium and hydroxyapatite binding site of human vitronectin provides insights to abnormal deposit formation*, *Proceedings of the National Academy of Science* **117** (Aug., 2020) 18504–18510.

[85] J. L. Harding and M. D. Krebs, *Bioinspired deposition-conversion synthesis of tunable calcium phosphate coatings on polymeric hydrogels*, *ACS Biomaterials Science & Engineering* **3** (09, 2017) 2024–2032.

[86] S. Karthika, T. K. Radhakrishnan, and P. Kalaichelvi, *A review of classical and nonclassical nucleation theories*, *Crystal Growth & Design* **16** (2016), no. 11 6663–6681.

[87] W. Cui, X. Li, C. Xie, H. Zhuang, S. Zhou, and J. Weng, *Hydroxyapatite nucleation and growth mechanism on electrospun fibers functionalized with different chemical groups and their combinations*, *Biomaterials* **31** (2010), no. 17 4620–4629.

[88] P. Zhu, Y. Masuda, and K. Koumoto, *The effect of surface charge on hydroxyapatite nucleation*, *Biomaterials* **25** (2004), no. 17 3915–3921.

[89] A. S. Posner and F. Betts, *Synthetic amorphous calcium phosphate and its relation to bone mineral structure*, *Accounts of Chemical Research* **8** (08, 1975) 273–281.

[90] A. S. Posner, F. Betts, and N. C. Blumenthal, *Formation and structure of synthetic and bone hydroxyapatites*, *Progress in Crystal Growth and Characterization* **3** (1980), no. 1 49–64.

[91] M. Sleutel and A. E. S. V. Driessche, *Role of clusters in nonclassical nucleation and growth of protein crystals*, *Proceedings of the National Academy of Sciences* **111** (2014), no. 5 E546–E553.

[92] A. Levin, T. O. Mason, L. Adler-Abramovich, A. K. Buell, G. Meisl, C. Galvagnion, Y. Bram, S. A. Stratford, C. M. Dobson, T. P. J. Knowles, and E. Gazit, *Ostwald's rule of stages governs structural transitions and morphology of dipeptide supramolecular polymers*, *Nature Communications* **5** (2014), no. 1 5219.

[93] A. Dey, P. H. Bomans, F. A. Müller, J. Will, P. M. Frederik, G. de With, and N. A. Sommerdijk, *The role of prenucleation clusters in surface-induced calcium phosphate crystallization*, *Nature materials* **9** (2010), no. 12 1010–1014.

[94] J. Tao, H. Pan, J. Wang, J. Wu, B. Wang, X. Xu, and R. Tang, *Evolution of amorphous calcium phosphate to hydroxyapatite probed by gold nanoparticles*, *The Journal of Physical Chemistry C* **112** (09, 2008) 14929–14933.

[95] T. Tsuji, K. Onuma, A. Yamamoto, M. Iijima, and K. Shiba, *Direct transformation from amorphous to crystalline calcium phosphate facilitated by motif-programmed artificial proteins*, *Proceedings of the National Academy of Sciences* **105** (2008), no. 44 16866–16870.

[96] D. S. Seo and J. K. Lee, *Synthesis of hydroxyapatite whiskers through dissolutionâreprecipitation process using edta*, *Journal of Crystal Growth* **310** (2008), no. 7 2162–2167.

[97] R. Mathew, P. N. Gunawidjaja, I. Izquierdo-Barba, K. Jansson, A. García, D. Arcos, M. Vallet-Regí, and M. Edén, *Solid-state 31p and 1h nmr investigations of amorphous and crystalline calcium phosphates grown biomimetically from a mesoporous bioactive glass*, *The Journal of Physical Chemistry C* **115** (10, 2011) 20572–20582.

[98] C. Jäger, T. Welzel, W. Meyer-Zaika, and M. Epple, *A solid-state nmr investigation of the structure of nanocrystalline hydroxyapatite*, *Magnetic Resonance in Chemistry* **44** (2006), no. 6 573–580.

[99] F. Betts and A. Posner, *An x-ray radial distribution study of amorphous calcium phosphate*, *Materials Research Bulletin* **9** (1974), no. 3 353–360.

[100] A. Oyane, K. Onuma, T. Kokubo, and A. Ito, *Clustering of calcium phosphate in the system $cacl_2$-h_3po_4-kcl-h_2o*, *The Journal of Physical Chemistry B* **103** (09, 1999) 8230–8235.

[101] W. J. Habraken, J. Tao, L. J. Brylka, H. Friedrich, L. Bertinetti, A. S. Schenk, A. Verch, V. Dmitrovic, P. H. Bomans, P. M. Frederik, *et. al.*, *Ion-association complexes unite classical and non-classical theories for the biomimetic nucleation of calcium phosphate*, *Nature communications* **4** (2013), no. 1 1–12.

[102] L. M. Epasto, T. Georges, A. Selimović, J.-M. Guigner, T. Azaïs, and D. Kurzbach, *Formation and evolution of nanoscale calcium phosphate precursors under biomimetic conditions*, *Analytical Chemistry* **93** (2021), no. 29 10204–10211, [https://doi.org/10.1021/acs.analchem.1c01561]. PMID: 34251166.

[103] A. Boskey and A. Posner, *Magnesium stabilization of amorphous calcium phosphate: A kinetic study*, *Materials Research Bulletin* **9** (1974), no. 7 907–916.

[104] F. Abbona and A. Baronnet, *A xrd and tem study on the transformation of amorphous calcium phosphate in the presence of magnesium*, *Journal of Crystal Growth* **165** (1996), no. 1 98–105.

[105] C. J. S. Ibsen, D. Chernyshov, and H. Birkedal, *Apatite formation from amorphous calcium phosphate and mixed amorphous calcium*

phosphate/amorphous calcium carbonate, *Chemistry â A European Journal* **22** (2016), no. 35 12347–12357.

[106] R. E. Wuthier, S. Bisaz, R. G. G. Russell, and H. Fleisch, *Relationship between pyrophosphate, amorphous calcium phosphate and other factors in the sequence of calcificationin vivo*, *Calcified Tissue Research* **10** (1972), no. 1 198–206.

[107] H. Fleisch, R. G. G. Russell, S. Bisaz, J. D. Termine, and A. S. Posner, *Influence of pyrophosphate on the transformation of amorphous to crystalline calcium phosphate*, *Calcified Tissue Research* **2** (1968), no. 1 49–59.

[108] J. D. Termine and E. D. Eanes, *Comparative chemistry of amorphous and apatitic calcium phosphate preparations*, *Calcified Tissue Research* **10** (1972), no. 1 171–197.

[109] T. C. A. McGann, R. D. Kearney, W. Buchheim, A. S. Posner, F. Betts, and N. C. Blumenthal, *Amorphous calcium phosphate in casein micelles of bovine milk*, *Calcified Tissue International* **35** (1983), no. 1 821–823.

[110] E. Reynolds, *Casein phosphopeptide-amorphous calcium phosphate: The scientific evidence*, *Advances in Dental Research* **21** (2009), no. 1 25–29.

[111] E. Beniash, R. A. Metzler, R. S. Lam, and P. Gilbert, *Transient amorphous calcium phosphate in forming enamel*, *Journal of Structural Biology* **166** (2009), no. 2 133–143.

[112] K. Cross, L. Huq, and E. Reynolds, *Casein phosphopeptide-amorphous calcium phosphate nanocomplexes: A structural model*, *Biochemistry* **55** (07, 2016).

[113] P. A. Price and J. E. Lim, *The inhibition of calcium phosphate precipitation by fetuin is accompanied by the formation of a fetuin-mineral complex**, *Journal of Biological Chemistry* **278** (2003), no. 24 22144–22152.

[114] A. Heiss, V. Pipich, W. Jahnen-Dechent, and D. Schwahn, *Fetuin-a is a mineral carrier protein: Small angle neutron scattering provides new insight on fetuin-a controlled calcification inhibition*, *Biophysical journal* **99** (12, 2010) 3986–95.

[115] C. N. Rochette, S. Rosenfeldt, A. Heiss, T. Narayanan, M. Ballauff, and W. Jahnen-Dechent, *A shielding topology stabilizes the early stage proteinâmineral complexes of fetuin-a and calcium phosphate: A time-resolved small-angle x-ray study*, *ChemBioChem* **10** (2009), no. 4 735–740.

[116] M. H. Misbah, M. Espanol, L. Quintanilla, M. P. Ginebra, and J. C. RodrÃguez-Cabello, *Formation of calcium phosphate nanostructures under the influence of self-assembling hybrid elastin-like-statherin recombinamers*, *RSC Adv.* **6** (2016) 31225–31234.

[117] E. Moreno, K. Varughese, and D. Hay, *Effect of human salivary proteins on the precipitation kinetics of calcium phosphate*, *Calcified tissue international* **28** (1979), no. 1 7–16.

[118] M. Schweikle, S. H. Bjørnøy, A. T. van Helvoort, H. J. Haugen, P. Sikorski, and H. Tiainen, *Stabilisation of amorphous calcium phosphate in polyethylene glycol hydrogels*, *Acta Biomaterialia* **90** (2019) 132–145.

[119] S. Liu, W. Weng, Z. Li, L. Pan, K. Cheng, C. Song, P. Du, G. Shen, and G. Han, *Effect of peg amount in amorphous calcium phosphate on its crystallized products*, *Journal of Materials Science: Materials in Medicine* **20** (2009), no. 1 359–363.

[120] S. K. Hahn, R. Ohri, and C. M. Giachelli, *Anti-calcification of bovine pericardium for bioprosthetic heart valves after surface modification with hyaluronic acid derivatives*, *Biotechnology and Bioprocess Engineering* **10** (2005), no. 3 218–224.

[121] N. C. Blumenthal, F. Betts, and A. S. Posner, *Stabilization of amorphous calcium phosphate by mg and atp*, *Calcified Tissue Research* **23** (1977), no. 1 245–250.

[122] V. Čadež, I. Erceg, A. Selmani, D. Domazet Jurašin, S. Šegota, D. M. Lyons, D. Kralj, and M. D. Sikirić, *Amorphous calcium phosphate formation and aggregation process revealed by light scattering techniques*, *Crystals* **8** (2018), no. 6.

[123] E. M. M. Weber, T. Kress, D. Abergel, S. Sewsurn, T. Azaïs, and D. Kurzbach, *Assessing the onset of calcium phosphate nucleation by hyperpolarized real-time NMR*, *Analytical Chemistry* **92** (2020), no. 11 7666–7673, [https://doi.org/10.1021/acs.analchem.0c00516]. PMID: 32378878.

[124] L. Wang, S. Li, E. Ruiz-Agudo, C. V. Putnis, and A. Putnis, *Posner's cluster revisited: direct imaging of nucleation and growth of nanoscale calcium phosphate clusters at the calcite-water interface*, *CrystEngComm* **14** (2012) 6252–6256.

[125] L.-W. Du, S. Bian, B.-D. Gou, Y. Jiang, J. Huang, Y.-X. Gao, Y.-D. Zhao, W. Wen, T.-L. Zhang, and K. Wang, *Structure of clusters and formation of amorphous calcium phosphate and hydroxyapatite: From the perspective of coordination chemistry*, *Crystal Growth & Design* **13** (07, 2013) 3103–3109.

[126] Q. Zhang, Y. Jiang, B.-D. Gou, J. Huang, Y.-X. Gao, J.-T. Zhao, L. Zheng, Y.-D. Zhao, T.-L. Zhang, and K. Wang, *In situ detection of calcium phosphate clusters in solution and wet amorphous phase by synchrotron x-ray absorption near-edge spectroscopy at calcium k-edge*, *Crystal Growth & Design* **15** (05, 2015) 2204–2210.

[127] G. Treboux, P. Layrolle, N. Kanzaki, K. Onuma, and A. Ito, *Existence of posner's cluster in vacuum*, *The Journal of Physical Chemistry A* **104** (06, 2000) 5111–5114.

[128] N. Kanzaki, G. Treboux, K. Onuma, S. Tsutsumi, and A. Ito, *Calcium phosphate clusters*, *Biomaterials* **22** (2001), no. 21 2921–2929.

[129] X. Yin and M. J. Stott, *Biological calcium phosphates and Posner's cluster*, *The Journal of Chemical Physics* **118** (02, 2003) 3717–3723.

[130] T. C. Player and P. J. Hore, *Posner qubits: spin dynamics of entangled $ca_9(po_4)_6$ molecules and their role in neural processing*, *Journal of The Royal Society Interface* **15** (2018), no. 147 20180494.

[131] G. S. Malhi, M. Tanious, P. Das, C. M. Coulston, and M. Berk, *Potential mechanisms of action of lithium in bipolar disorder*, *CNS Drugs* **27** (2013), no. 2 135–153.

[132] J. R. Geddes, S. Burgess, K. Hawton, K. Jamison, and G. M. Goodwin, *Long-term lithium therapy for bipolar disorder: Systematic review and meta-analysis of randomized controlled trials*, *American Journal of Psychiatry* **161** (2004), no. 2 217–222.

[133] A. Ettenberg, K. Ayala, J. T. Krug, L. Collins, M. S. Mayes, and M. P. Fisher, *Differential effects of lithium isotopes in a ketamine-induced hyperactivity model of mania*, *Pharmacology Biochemistry and Behavior* **190** (2020) 172875.

[134] J. Sechzer, K. Lieberman, G. Alexander, D. Weidman, and P. Stokes, *Aberrant parenting and delayed offspring development in rats exposed to lithium*, *Biological Psychiatry* **21** (1986), no. 13 1258–1266.

[135] G. Mancardi, U. Terranova, and N. H. de Leeuw, *Calcium phosphate prenucleation complexes in water by means of ab initio molecular dynamics simulations*, *Crystal Growth & Design* **16** (06, 2016) 3353–3358.

[136] G. Mancardi, C. E. Hernandez Tamargo, D. Di Tommaso, and N. H. de Leeuw, *Detection of posner's clusters during calcium phosphate nucleation: a molecular dynamics study*, *J. Mater. Chem. B* **5** (2017) 7274–7284.

[137] J. R. Knowles, *Enzyme-catalyzed phosphoryl transfer reactions*, *Annual Review of Biochemistry* **49** (1980), no. 1 877–919, [https://doi.org/10.1146/annurev.bi.49.070180.004305]. PMID: 6250450.

[138] P. P. Dzeja and A. Terzic, *Phosphotransfer networks and cellular energetics*, *Journal of Experimental Biology* **206** (06, 2003) 2039–2047, [https://journals.biologists.com/jeb/article-pdf/206/12/2039/1244600/2039.pdf].

[139] N. Blumenthal and A. Posner, *Hydroxyapatite: Mechanism of formation and properties*, *Cal. Tis Res.* **13** (1973) 235–243.

[140] H. Schröder, L. Kurz, W. Müller, and B. Lorenz, *Polyphosphate in bone*, *Biochemistry (Moscow)* **65** (2000), no. 3 296–303. PMID:10739471.

[141] L. Wang and G. H. Nancollas, *Calcium orthophosphates: Crystallization and dissolution*, *Chemical Reviews* **108** (2008), no. 11 4628–4669, [https://doi.org/10.1021/cr0782574]. PMID: 18816145.

[142] A. McLaughlin, P. Cullis, M. Hemminga, D. Hoult, G. Radda, G. Ritchie, P. Seeley, and R. Richards, *Application of ^{31}P NMR to model and biological membrane systems*, *FEBS Letters* **57** (1975), no. 2 213–218.

[143] E. Burnell, P. Cullis, and B. de Kruijff, *Effects of tumbling and lateral diffusion on phosphatidylcholine model membrane ^{31}P-NMR lineshapes*, *Biochimica et Biophysica Acta (BBA) - Biomembranes* **603** (1980), no. 1 63–69.

[144] Y. Su, W. F. DeGrado, and M. Hong, *Orientation, dynamics, and lipid interaction of an antimicrobial arylamide investigated by ^{19}F and ^{31}P solid-state NMR spectroscopy*, *Journal of the American Chemical Society* **132** (2010), no. 26 9197–9205, [https://doi.org/10.1021/ja103658h].

[145] C. Ho, J. A. Magnuson, J. B. Wilson, N. S. Magnuson, and R. J. Kurland, *Phosphorus nuclear magnetic resonance studies of phosphoproteins and phosphorylated molecules. II. Chemical nature of phosphorus atoms in α_8-casein B and phosvitin*, *Biochemistry* **8** (1969), no. 5 2074–2082, [https://doi.org/10.1021/bi00833a044]. PMID: 5814938.

[146] M. H. J. Seifert, C. B. Breitenlechner, D. Bossemeyer, R. Huber, T. A. Holak, and R. A. Engh, *Phosphorylation and flexibility of cyclic-AMP-dependent protein kinase (PKA) using ^{31}P NMR spectroscopy*, *Biochemistry* **41** (2002), no. 19 5968–5977, [https://doi.org/10.1021/bi025509g]. PMID: 11993991.

[147] J. Ren, B. Yang, A. Sherry, and C. Malloy, *Exchange kinetics by inversion transfer: integrated analysis of the phosphorus metabolite kinetic exchanges in resting human skeletal muscle at 7 T*, *Magnetic resonance in medicine* **73** (2015), no. 4 1359–1369.

[148] M. Hupfer, R. Gtichter, and R. R. Ruegger, *Polyphosphate in lake sediments: ^{31}P NMR spectroscopy as a tool for its identification*, *Limnology and Oceanography* **40** (1995), no. 3 610–617, [https://aslopubs.onlinelibrary.wiley.com/doi/pdf/10.4319/lo.1995.40.3.0610].

[149] L. B. Staal, A. B. Petersen, C. A. Jørgensen, U. G. Nielsen, P. H. Nielsen, and K. Reitzel, *Extraction and quantification of polyphosphates in activated sludge from waste water treatment plants by ^{31}P NMR spectroscopy*, *Water Research* **157** (2019) 346–355.

[150] M. A. Swartz, P. J. Tubergen, C. D. Tatko, and R. A. Baker, *Experimental determination of pKa values and metal binding for biomolecular compounds using ^{31}P NMR spectroscopy*, *Journal of Chemical Education* **95** (2018), no. 1 182–185, [https://doi.org/10.1021/acs.jchemed.7b00508].

[151] Z. Szabó, *Multinuclear NMR studies of the interaction of metal ions with adenine-nucleotides*, *Coordination Chemistry Reviews* **252** (2008), no. 21 2362–2380. Applications of NMR to Inorganic and Organometallic Chemistry.

[152] R. K. Brow, C. C. Phifer, G. L. Turner, and R. J. Kirkpatrick, *Cation effects on ^{31}P MAS NMR chemical shifts of metaphosphate glasses*, *Journal of the American Ceramic Society* **74** (1991), no. 6 1287–1290, [https://ceramics.onlinelibrary.wiley.com/doi/pdf/10.1111/j.1151-2916.1991.tb04099.x].

[153] J. Iwahara, Y.-S. Jung, and G. M. Clore, *Heteronuclear nmr spectroscopy for lysine NH_3 groups in proteins: Unique effect of water exchange on ^{15}N transverse relaxation*, *Journal of the American Chemical Society* **129** (2007), no. 10 2971–2980, [https://doi.org/10.1021/ja0683436]. PMID: 17300195.

[154] Z. Luz and S. Meiboom, *Rate and mechanism of proton exchange in aqueous solutions of phosphate buffer*, *Journal of the American Chemical Society* **86** (1964), no. 22 4764–4766, [https://doi.org/10.1021/ja01076a006].

[155] H. Y. Carr and E. M. Purcell, *Effects of diffusion on free precession in nuclear magnetic resonance experiments*, *Phys. Rev.* **94** (May, 1954) 630–638.

[156] S. Meiboom and D. Gill, *Modified spin-echo method for measuring nuclear relaxation times*, *Review of Scientific Instruments* **29** (Aug., 1958) 688–691.

[157] N. Bloembergen, E. M. Purcell, and R. V. Pound, *Relaxation effects in nuclear magnetic resonance absorption*, *Phys. Rev.* **73** (Apr, 1948) 679–712.

[158] J. Fraústo da Silva and R. Williams, *The Biological Chemistry of the Elements: The Inorganic Chemistry of Life*. Oxford University Press, Oxford, 1997.

[159] J. P. Yesinowski, R. J. Sunberg, and J. J. Benedict, *pH control and rapid mixing in spinning NMR samples*, *Journal of Magnetic Resonance (1969)* **47** (1982), no. 1 85–90.

[160] T. R. Krawietz, P. Lin, K. E. Lotterhos, P. D. Torres, D. H. Barich, A. Clearfield, and J. F. Haw, *Solid phosphoric acid catalyst: A multinuclear NMR and theoretical study*, *Journal of the American Chemical Society* **120** (1998), no. 33 8502–8511, [https://doi.org/10.1021/ja9813461].

[161] N. J. Anthis and G. M. Clore, *Visualizing transient dark states by NMR spectroscopy*, *Quarterly Reviews of Biophysics* **48** (2015), no. 1 35–116.

[162] J. M. Edwards, J. E. Bramham, A. Podmore, S. M. Bishop, C. F. van der Walle, and A. P. Golovanov, *^{19}F dark-state exchange saturation transfer NMR reveals reversible formation of protein-specific large clusters in high-concentration protein mixtures*, *Analytical Chemistry* **91** (2019), no. 7 4702–4708, [https://doi.org/10.1021/acs.analchem.9b00143]. PMID: 30801173.

[163] P. Vallurupalli, G. Bouvignies, and L. E. Kay, *Studying invisible excited protein states in slow exchange with a major state conformation*, *Journal of the American Chemical Society* **134** (2012), no. 19 8148–8161, [https://doi.org/10.1021/ja3001419]. PMID: 22554188.

[164] I. A. L. Lim, X. Li, C. K. Jones, J. A. Farrell, D. S. Vikram, and P. C. van Zijl, *Quantitative magnetic susceptibility mapping without phase unwrapping using WASSR*, *NeuroImage* **86** (2014) 265–279.

[165] H. Hogben, M. Krzystyniak, G. Charnock, P. Hore, and I. Kuprov, *Spinach–a software library for simulation of spin dynamics in large spin systems*, *J Magn Reson* **208** (2011), no. 2 179–194.

[166] A. G. Palmer III, *Chemical exchange in biomacromolecules: past, present, and future*, *J Magn Reson* **241** (2014) 3–17.

[167] N. D. Burrows and R. L. Penn, *Cryogenic transmission electron microscopy: Aqueous suspensions of nanoscale objects*, *Microscopy and Microanalysis* **19** (2013), no. 6 1542–1553.

[168] H. Cui, T. K. Hodgdon, E. W. Kaler, L. Abezgauz, D. Danino, M. Lubovsky, Y. Talmon, and D. J. Pochan, *Elucidating the assembled structure of amphiphiles in solution via cryogenic transmission electron microscopy*, *Soft Matter* **3** (2007) 945–955.

[169] W. Humphrey, A. Dalke, and K. Schulten, *VMD: Visual molecular dynamics*, *Journal of Molecular Graphics* **14** (1996), no. 1 33–38.

[170] M. Golda-Cepa, K. Riedlová, W. Kulig, L. Cwiklik, and A. Kotarba, *Functionalization of the parylene c surface enhances the nucleation of calcium phosphate: Combined experimental and molecular dynamics simulations approach*, *ACS Appl. Mater. Interfaces* **12** (2020), no. 11 12426–12435.

[171] W. L. Jorgensen, J. Chandrasekhar, J. D. Madura, R. W. Impey, and M. L. Klein, *Comparison of simple potential functions for simulating liquid water*, *The Journal of Chemical Physics* **79** (1983), no. 2 926–935.

[172] I. Chubak, L. Alon, E. V. Silletta, G. Madelin, A. Jerschow, and B. Rotenberg, *Quadrupolar relaxation of $^{23}Na^{+}$ in solution beyond rotational models: Revealing a link with ultrafast collective dynamics by experiments and simulations*, .

[173] C. Johnson, *Diffusion ordered nuclear magnetic resonance spectroscopy: principles and applications*, *Progress in Nuclear Magnetic Resonance Spectroscopy* **34** (1999) 203–256.

[174] A. Jerschow and N. Müller, *Suppression of convection artifacts in stimulated-echo diffusion experiments. double-stimulated-echo experiments*, *Journal of Magnetic Resonance* **125** (1997), no. 2 372–375.

[175] A. Eiberweiser, A. Nazet, G. Hefter, and R. Buchner, *Ion hydration and association in aqueous potassium phosphate solutions*, *The Journal of Physical Chemistry B* **119** (2015), no. 16 5270–5281, [https://doi.org/10.1021/acs.jpcb.5b01417]. PMID: 25826464.

[176] M. Gerstein and C. Chothia, *Packing at the protein-water interface*, *Proceedings of the National Academy of Sciences* **93** (1996), no. 19 10167–10172, [https://www.pnas.org/content/93/19/10167.full.pdf].

[177] M. D'Agostino, R. Bougault, F. Gulminelli, M. Bruno, F. Cannata, P. Chomaz, F. Gramegna, I. Iori, N. L. Neindre, G. Margagliotti, A. Moroni, and G. Vannini, *On the reliability of negative heat capacity measurements*, *Nuclear Physics A* **699** (2002), no. 3 795–818.

[178] D. Marenduzzo, K. Finan, and P. R. Cook, *The depletion attraction: an underappreciated force driving cellular organization*, *Journal of Cellular Biology* **175** (2016), no. 5 681–686. PMID: 17145959.

[179] A. Bondi, *van der waals volumes and radii*, *The Journal of Physical Chemistry* **68** (1964), no. 3 441–451, [https://doi.org/10.1021/j100785a001].

[180] S. Park, R. Barnes, Y. Lin, B. Jeon, S. Najafi, K. Delaney, G. Fredrickson, J. Shea, D. Hwang, and S. Han, *Dehydration entropy drives liquid-liquid phase separation by molecular crowding*, *Communications Chemistry* **3** (2020), no. 1 83.

[181] S. Großhans, G. Wang, and J. Hubbuch, *Water on hydrophobic surfaces: mechanistic modeling of polyethylene glycol-indcued protein precipitation*, *Bioprocess and Biosystems Engineering* **42** (2019), no. 4 513–520.

[182] Y. Zhang and P. S. Cremer, *Interactions between macromolecules and ions: the hofmeister series*, *Current Opinion in Chemical Biology* **10** (2006), no. 6 658–663. Model systems / Biopolymers.

[183] H. I. Okur, J. Hladílková, K. B. Rembert, Y. Cho, J. Heyda, J. Dzubiella, P. S. Cremer, and P. Jungwirth, *Beyond the hofmeister series: Ion-specific effects on proteins and their biological functions*, *The Journal of Physical Chemistry B* **121** (2017), no. 9 1997–2014, [https://doi.org/10.1021/acs.jpcb.6b10797]. PMID: 28094985.

[184] M. L. Deline, M. Grashei, F. H. van Heijster, F. Schilling, J. Straub, and T. Fromme, *Adenylate kinase derived atp shapes respiration and calcium storage of isolated mitochondria*, *Biochimica et Biophysica Acta (BBA) - Bioenergetics* **1862** (2021), no. 7 148409.

[185] H. Dodziuk, *Cyclodextrins and Their Complexes: Chemistry, Analytical Methods, Applications*. 08, 2006.

[186] A. Oyane, K. Onuma, A. Ito, H.-M. Kim, T. Kokubo, and T. Nakamura, *Formation and growth of clusters in conventional and new kinds of simulated body fluids*, *Journal of Biomedical Materials Research Part A* **64A** (2003), no. 2 339–348.

[187] G. Nancollas, Z. Amjad, and P. Poutsoukos, *Calcium Phosphates—Speciation, Solubility, and Kinetic Considerations*, ch. 23, pp. 475–497. 1979.

[188] H.-B. Pan and B. W. Darvell, *Calcium phosphate solubility: The need for re-evaluation*, *Crystal Growth & Design* **9** (2009), no. 2 639–645, [https://doi.org/10.1021/cg801118v].

[189] I. Marino, *rilt*, 2018. MATLAB Central File Exchange.

[190] N. Li, D. Lu, L. Yang, H. Tao, Y. Xu, C. Wang, L. Fu, H. Liu, Y. Chummum, and S. Zhang, *Nuclear Spin Attenuates the Anesthetic Potency of Xenon Isotopes in Mice: Implications for the Mechanisms of Anesthesia and Consciousness*, *Anesthesiology* **129** (08, 2018) 271–277, [https://pubs.asahq.org/anesthesiology/article-pdf/129/2/271/381676/20180800_0-00017.pdf].

[191] M. Deline, J. Straub, M. Patel, P. Subba, M. Grashei, F. van Heijster, P. Pirkwieser, V. Somoza, J. Livingstone, M. Beazely, B. Kendall, M. Gingras, Z. Leonenko, C. Hoeschen, G. Harrington, K. Kuellmer, W. Bian, F. Schilling, M. Fisher, M. Helgeson, and T. Fromme, *Lithium affect mitochondrial amorphous calcium phosphate aggregation in a tissue and isotope dependent manner*, *Frontiers in Physiology* (2023).

[192] J. D. Livingstone, M. J. Gingras, Z. Leonenko, and M. A. Beazely, *Search for lithium isotope effects in neuronal ht22 cells*, *Biochemistry and Biophysics Reports* **34** (2023).

[193] J. Smith, H. Zadeh Haghighi, D. Salahub, and C. Simon, *Radical pairs may play a role in xenon-induced general anesthesia*, *Scientific Reports* **11** (2021), no. 1 6287.

[194] H. Zadeh-Haghighi and C. Simon, *Entangled radicals may explain lithium effects on hyperactivity*, *Scientific Reports* **11** (2021), no. 1 12121.

[195] C. de P. Eduardo, P. d. F. A. Simões, V. Arana-Chavez, J. Nicolau, and V. Gentil, *Dentin decalcification during lithium treatment: case report*, *Special Care in Dentistry* **33** (04, 2013) 91–95, [https://onlinelibrary.wiley.com/doi/10.1111/scd.12000].

[196] A. L. Boskey and A. S. Posner, *Conversion of amorphous calcium phosphate to microcrystalline hydroxyapatite. a ph-dependent, solution-mediated, solid-solid conversion*, *The Journal of Physical Chemistry* **77** (1973), no. 19 2313–2317.

[197] F. Grases, M. Zelenková, and O. Söhnel, *Structure and formation mechanism of calcium phosphate concretions formed in simulated body fluid*, *Urolithiasis* **42** (2014), no. 1 9–16.

[198] F. Betts and A. Posner, *An x-ray radial distribution study of amorphous calcium phosphate*, *Materials Research Bulletin* **9** (1974) 353–360.

[199] P. F. Renshaw, *A diffusional contribution to lithium isotope effects*, *Biological Psychiatry* **22** (1987), no. 1 73–78.

[200] K. Onuma, A. Oyane, K. Tsutsui, K. Tanaka, G. Treboux, N. Kanzaki, and A. Ito, *Precipitation kinetics of hydroxyapatite revealed by the continuous-angle laser light-scattering technique*, *The Journal of Physical Chemistry B* **104** (2000), no. 45 10563–10568, [https://doi.org/10.1021/jp002697g].

[201] J. R. de Bruyn, M. Goiko, M. Mozaffari, D. Bator, R. L. Dauphinee, Y. Liao, R. L. Flemming, M. S. Bramble, G. K. Hunter, and H. A. Goldberg, *Dynamic light scattering study of inhibition of nucleation and growth of hydroxyapatite crystals by osteopontin*, *PLOS ONE* **8** (02, 2013) 1–9.

[202] A. L. Lehninger, *Mitochondria and calcium ion transport.*, *Biochemical Journal* **119** (1970), no. 2 129.

[203] G. Mie, *Sättigungsstrom und stromkurve einer schlecht leitenden flüssigkeit*, *Annalen der Physik* **331** (1908), no. 8 597–614.

[204] L. Rayleigh, *On the scattering of light by spherical shells, and by complete spheres of periodic structure, when the refractivity is small*, *Proceedings of the Royal Society of London. Series A, Containing Papers of a Mathematical and Physical Character* **94** (1918), no. 660 296–300.

[205] C. J. Jameson, *Isotope Effects on Chemical Shifts and Coupling Constants*. John Wiley Sons, Ltd, 2007. https://onlinelibrary.wiley.com/doi/pdf/10.1002/9780470034590.emrstm0251.

[206] J. N. Israelachvili, *Intermolecular and surface forces*. Academic Press London ; San Diego, 2nd ed. ed., 1991.

[207] M. Mohammadi, S. Benders, and A. Jerschow, *Nuclear magnetic resonance spin-lattice relaxation of lithium ions in aqueous solution by nmr and molecular dynamics*, *The Journal of Chemical Physics* **153** (2020), no. 18 184502, [https://doi.org/10.1063/5.0026450].

[208] T. Gullion, *Introduction to rotational-echo, double-resonance nmr*, *Concepts in Magnetic Resonance* **10** (1998), no. 5 277–289.

[209] S. Agarwal, D. R. Kattnig, C. D. Aiello, and A. S. Banerjee, *The biological qubit: Calcium phosphate dimers, not trimers*, *The Journal of Physical Chemistry Letters* **14** (03, 2023) 2518–2525.

[210] A. R. C. Kylander-Clark, *Petrochronology by Laser-Ablation Inductively Coupled Plasma Mass Spectrometry*, *Reviews in Mineralogy and Geochemistry* **83** (08, 2017) 183–198.

[211] M. Sutcliffe and N. Scrutton, *Enzymology takes a quantum leap forward*. 2001.

[212] A. Sen and A. Kohen, *Enzymatic tunneling and kinetic isotope effects: chemistry at the crossroads*, *Journal of Physical Organic Chemistry* **23** (2010), no. 7 613–619, [https://onlinelibrary.wiley.com/doi/pdf/10.1002/poc.1633].

[213] L. Michaelis, M. L. Menten, *et. al.*, *Die kinetik der invertinwirkung*, *Biochem. z* **49** (1913), no. 333-369 352.

[214] J. Schneider, U. Girreser, A. Havemeyer, F. Bittner, and B. Clement, *Detoxification of trimethylamine n-oxide by the mitochondrial amidoxime reducing component marc*, *Chemical Research in Toxicology* **31** (06, 2018) 447–453.

[215] D. Lang, C. Yeung, R. Peter, C. Ibarra, R. Gasser, K. Itagaki, R. Philpot, and A. Rettie, *Isoform specificity of trimethylamine n-oxygenation by human flavin-containing monooxygenase (fmo) and p450 enzymes: Selective catalysis by fmo3*, *Biochemical Pharmacology* **56** (1998), no. 8 1005–1012.

[216] M. Goličnik, *Exact and approximate solutions for the decades-old michaelis-menten equation: Progress-curve analysis through integrated rate equations*, *Biochemistry and Molecular Biology Education* **39** (2011), no. 2 117–125, [https://iubmb.onlinelibrary.wiley.com/doi/pdf/10.1002/bmb.20479].

[217] L. Qian and P. R. Ortiz de Montellano, *Oxidative activation of thiacetazone by the mycobacterium tuberculosis flavin monooxygenase etaa and human fmo1 and fmo3*, *Chemical research in toxicology* **19** (2006), no. 3 443–449.

[218] B. Reif, S. E. Ashbrook, L. Emsley, and M. Hong, *Solid-state nmr spectroscopy*, *Nature Reviews Methods Primers* **1** (2021), no. 1 2.

[219] A. S. Lilly Thankamony, J. J. Wittmann, M. Kaushik, and B. Corzilius, *Dynamic nuclear polarization for sensitivity enhancement in modern solid-state nmr*, *Progress in Nuclear Magnetic Resonance Spectroscopy* **102-103** (2017) 120–195.

[220] D. Gebauer, A. Völkel, and H. Cölfen, *Stable prenucleation calcium carbonate clusters*, *Science* **322** (2008), no. 5909 1819–1822.

[221] D. Gebauer, M. Kellermeier, J. D. Gale, L. BergstrÃ¶m, and H. CÃ¶lfen, *Pre-nucleation clusters as solute precursors in crystallisation*, *Chem. Soc. Rev.* **43** (2014) 2348–2371.

[222] B. Das, *Theoretical study of small iron–oxyhydroxide clusters and formation of ferrihydrite*, *The Journal of Physical Chemistry A* **122** (01, 2018) 652–661.

[223] B. Berne and R. Pecora, *Dynamic Light Scattering: With Applications to Chemistry, Biology, and Physics*. Dover Books on Physics Series. Dover Publications, 2000.

[224] C. C. Miller and J. Walker, *The stokes-einstein law for diffusion in solution*, *Proceedings of the Royal Society of London. Series A, Containing Papers of a Mathematical and Physical Character* **106** (1924), no. 740 724–749.

[225] D. E. Koppel, *Analysis of Macromolecular Polydispersity in Intensity Correlation Spectroscopy: The Method of Cumulants*, **57** (Dec., 1972) 4814–4820.

[226] B. J. Frisken, *Revisiting the method of cumulants for the analysis of dynamic light-scattering data*, *Appl. Opt.* **40** (Aug, 2001) 4087–4091.

[227] L. A. Clementi, J. R. Vega, L. M. Gugliotta, and H. R. Orlande, *A bayesian inversion method for estimating the particle size distribution of latexes from multiangle dynamic light scattering measurements*, *Chemometrics and Intelligent Laboratory Systems* **107** (2011), no. 1 165–173.

[228] Y. Wang, J. Shen, X. Yuan, Z. Dou, W. Liu, and S. Mao, *Scale analysis of wavelet regularization inversion and its improved algorithm for dynamic light scattering*, *Applied Sciences* **8** (2018), no. 9.

[229] S. W. Provencher, *Contin: A general purpose constrained regularization program for inverting noisy linear algebraic and integral equations*, *Computer Physics Communications* **27** (1982), no. 3 229–242.

[230] S. W. Provencher, *A constrained regularization method for inverting data represented by linear algebraic or integral equations*, *Computer Physics Communications* **27** (1982), no. 3 213–227.

[231] J. H. Curtiss, *A note on the theory of moment generating functions*, *The Annals of Mathematical Statistics* **13** (1942), no. 4 430–433.

[232] G. H. Golub, P. C. Hansen, and D. P. O'Leary, *Tikhonov regularization and total least squares*, *SIAM journal on matrix analysis and applications* **21** (1999), no. 1 185–194.

[233] P. Hansen, *The l-curve and its use in the numerical treatment of inverse problems*, in *InviteComputational Inverse Problems in Electrocardiology*, WIT Press, 2000. InviteComputational Inverse Problems in Electrocardiology ; Conference date: 01-01-2000.

[234] M. Skouri, J.-P. Munch, B. Lorber, R. Giégé, and S. Candau, *Interactions between lysozyme molecules under precrystallization conditions studied by light scattering*, *Journal of Crystal Growth* **122** (1992), no. 1 14–20.

[235] M. J. Abraham, T. Murtola, R. Schulz, S. Páll, J. C. Smith, B. Hess, and E. Lindahl, *GROMACS: High performance molecular simulations through multi-level parallelism from laptops to supercomputers*, *SoftwareX* **1-2** (2015) 19–25.

[236] A. Bondi, *van der waals volumes and radii*, *The Journal of Physical Chemistry* **68** (1964), no. 3 441–451.

[237] P. Eastman, J. Swails, J. D. Chodera, R. T. McGibbon, Y. Zhao, K. A. Beauchamp, L.-P. Wang, A. C. Simmonett, M. P. Harrigan, C. D. Stern, R. P. Wiewiora, B. R. Brooks, and V. S. Pande, *OpenMM 7: Rapid development of high performance algorithms for molecular dynamics*, *PLoS Computational Biology* **13** (2017), no. 7 e1005659.

[238] H. C. Andersen, *Rattle: A "velocity" version of the shake algorithm for molecular dynamics calculations*, *Journal of Computational Physics* **52** (1983), no. 1 24–34.

[239] S. Miyamoto and P. A. Kollman, *Settle: An analytical version of the SHAKE and RATTLE algorithm for rigid water models*, *Journal of Computational Chemistry* **13** (1992), no. 8 952–962.

[240] M. Rahbari-Sisakht, M. Taghizadeh, and A. Eliassi, *Densities and viscosities of binary mixtures of poly(ethylene glycol) and poly(propylene glycol) in water and ethanol in the 293.15 - 338.15 K temperature range*, *Journal of Chemical & Engineering Data* **48** (2003), no. 5 1221–1224, [https://doi.org/10.1021/je0301388].